

Acid-Catalyzed Production of Hydroxymethylfurfural; Selectivity and Deactivation during Sugar Dehydration Reactions

Ana Jakob

University of Nova Gorica, Vipavska 13, SI-5000 Nova Gorica

Abstract

Hydroxymethylfurfural (HMF) is recognized to be one of the most important value added bio-based chemicals, which is most commonly produced from lignocellulosic biomass. Its further conversion allows us to produce a vast majority of green chemicals including advanced bio-fuels. Therefore, HMF represents a sustainable source of raw material with a tremendous potential in a carbon neutral future within a circular bio-economy. With a suitable pretreatment of biomass feedstock such as hydrolysis, it is possible to produce desirable furanic products. After successful hydrolysis, individual monosaccharide units become available for further conversion. Specifically, C6 sugars commonly obtained from cellulose and hemicellulose biomass fractions, can be further converted via dehydration into HMF. Thus far, acid-catalytic dehydration reactions have been the most studied method for the conversion of sugars to HMF. Simple model compounds such as glucose or fructose have been extensively studied aimed at determining precise reaction pathways, however, little is known when it comes to the unwanted side product formation and inhibiting factors that occur in more complex biomass mixtures. Since HMF tends to rehydrate and/or polymerize during the sugar dehydration reactions, the choice of reaction conditions, solvent and catalyst is of significant importance to avoid unwanted product formation. Therefore, researchers are investigating the influence of different parameters on the reaction route to limit the formation of unwanted products such as humins. This review will focus specifically on saccharide model compounds (glucose and fructose) as well as real biomass mixtures and the impact of lignin, humins and different sugar concentration (sugar loading) on activity and product (HMF) selectivity.

Keywords: Hydroxymethylfurfural, Lignocellulosic biomass, humin formation

1. Introduction

Rapid increase of the world population, growing demand of energy consumption and accelerating carbon footprint of each individual are resulting in a global warming and depletion of natural resources. Global energy supply is currently still being majorly based

Email address: ana.jakob@ki.si (Ana Jakob)

on the utilization of the fossil fuels, therefore their reserves are rapidly diminishing. To avoid the shortage and secure global energy supply, together with the reduction of CO₂ emission the replacement of fossil fuels with an alternative source of energy has become a necessity. In a search for a suitable natural source, biomass can efficiently replace non-renewable feedstock as an only sustainable carbon resource. Application and viability of bio-fuel and bio-based chemicals itself can be challenging due to not fully optimized and costly infrastructure and technologies [1]. Therefore development of efficient processes and cost effective feedstock utilization up-to-date remains essential, prior to widespread use of biomass. With yearly estimated 140 Gt of the lignocellulosic residues, lignocellulosic biomass is most abundant type of biomass, namely including agricultural residues, wood processing waste, switchgrass, miscanthus, cornstover etc. [2, 3]. As a nonedible, easily convertible raw material it is a feedstock with a remarkable potential. Suitable conversion of lignocellulosic biomass can enable production of value added bio-based platform green chemicals and advanced bio-fuels.

2. Lignocellulosic biomass structure

Lignocellulosic biomass is essentially composed out of three different fractions, cellulose, hemicellulose and lignin, where each individual fraction can be efficiently utilized and converted into value added products. Due to its high complexity chemical or/and physical pretreatment and isolation is usually needed for optimal production of final products [3]. The lignin fraction is an amorphous polymer, rich with oxygenated aromatic species, which can be efficiently utilized and converted into phenolic resins, bio-oils, bio-fuels and aromatics [3, 4]. With its rigid structure it surrounds both hemicellulose and cellulose fraction and it is physiologically serving as a mechanic support [3]. Molecular wise it is a polymer composed of methoxylated phenylpropane units, namely coumaryl, coniferyl and sinapyl alcohol [3, 5]. Due to the rigid structure of a lignin protected layer, different pretreatment processes can be applied in order to access (hemi)cellulose fraction, Figure 1 [3]. Cellulose, beta-glycosidic linked glucose polysaccharide is the largest fraction of lignocellulosic biomass [3, 6]. With its crystalline structure it is resistant to the hydrolysis and degradation [7], whereas hemicellulose fraction is an amorphous polysaccharide, composed mainly out of C5 sugars, xylose and arabinose and C6 sugars, mannose, galactose and glucose [3]. With its H-bonds linkage to cellulose fraction, it creates a sheathing, which can exacerbate and slow down the hydrolysis [7].

Complexity of lignocellulosic biomass currently demands fraction isolation/separation in order to efficiently produce desired final products. Commonly used pretreatment methods are unanalyzed steam explosion, hot liquid water treatment, dilute acid treatment, etc. [7]. Composition of the feedstock can play an important role, when aiming for the desired product. Types of lignocellulosic biomass vary in the composition, which can later, depending on their pretreatment method impact the conversion process. Lignocellulosic biomass is a nonedible type of biomass obtained from various sources including plants residue, wood waste, algae etc., therefore the proportion of individual fractions namely

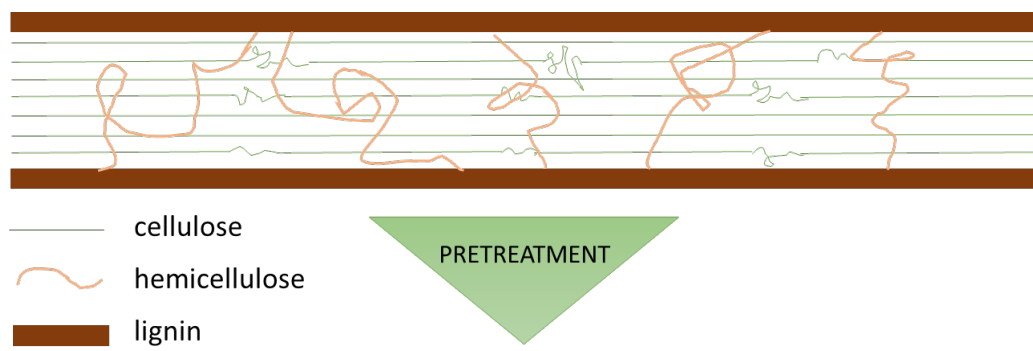


Figure 1: Structure of lignocellulosic biomass, adopted by [4].

hemicellulose, cellulose and lignin can vary between different sources. Generally it contains 25-35 % higher percentage of lignin compared to hardwood stem [8]. The variability in the feedstock composition can be vital parameter for the choice of suitable pretreatment and/or later product selectivity. Percentage of cellulose fraction can be crucial predisposition for later initial hexose concentration; precursor of 5-HMF, while presence of hemicelluloses, lignin and inorganic salts in reaction mixture can facilitate formation of humins or catalyst deactivation [8].

Table 1: Variability of feedstock of lignocellulosic biomass.

Feedstock	Celluloses	Hemicelluloses	Lignin	Reference
Sugarcane bagasse	44	29	20	[9]
Corn cob	30	37	33	[10]
Rice husk	28	28	24	[9]
Corn cob	50	31	15	[9]
Maple wood	41	18	24	[11]
Corn stover	33	23	16	[11]
Soft wood (pine)	31	19	29	[12]
Switchgrass	34	26	16	[12]

The lignin fraction is with its rigid structure serving as a mechanic support. The hemicellulose and cellulose fractions are surrounded and protected by a lignin outer layer, thus it is generally necessary to either break or remove it in order to obtain saccharide substrates for further conversion. Different physical (comminution, steam explosion, hydrothermol-

ysis) and chemical (acid, base or enzyme hydrolysis, pyrolysis, organosolv) pretreatment methods can be employed to alter the structure and the composition of lignocellulosic biomass [7, 8]. The variation of pretreatment result in different final composition of the feedstock, which later impact the dehydration reaction into 5-HMF. Therefore, due to the different pretreatment or the choice of one pot synthesis different amounts of lignin stays present in starting reaction mixture. Focusing on the conversion of (hemi)cellulose fraction, furanics; namely furfural and hydroxymethylfurfural are recognized as one of the most desired biomass value added platform chemicals, that can be transformed into different polyols, 2,5-furandicarboxylic acid, furfuryl alcohol, 5-etoxyethylfurfural. These can further serve as a precursors of several diverse products including biofuels, resins, polymers, fungicides and solvents [13], although current industrial production still remains a challenge.

3. Dehydration of biomass derived sugar

Hydroxymethylfurfural is a promising value added bio-based chemicals commonly produced from lignocellulosic biomass derived sugars. After hydrolysis of polysaccharides obtained from the (hemi) cellulose portion of biomass feedstocks, several different monomeric sugar units are available for further conversion. C5 sugars present in hemicellulose fraction of biomass are with dehydration reaction converted into furfural, whereas C6 sugars (present in cellulose and hemicellulose) are dehydrated into 5-HMF. 5-HMF can be in this reaction pathway recognized as an intermediate, which can be further rehydrated to levulinic acid and formic acid [13]. Along with the rehydration reaction, 5-HMF yield and selectivity can be reduced due to the other side reactions occurring via (cross) polymerization of 5-HMF and sugars. Frequently used starting feedstock for sugar dehydration into 5-HMF are biomass derived glucose and fructose. Using glucose as a reactant can appear to be more challenging due to the required additional step of isomerization, however, its lower cost makes glucose a more industrial relevant feedstock for the production of 5-HMF [14]. Acid-catalyzed dehydration is the most studied route for conversion of saccharides into 5-HMF. Exemplified reaction pathway and mechanism of acid-catalyzed carbohydrate conversion in Figure 2, includes 4 main steps; hydrolysis of polysaccharide, glucose-fructose isomerization, fructose dehydration and 5-HMF rehydration to levulinic and formic acid [15, 16]. Side reactions that can occur involve rehydration, cross-aldol condensation, C-C bond cleavage and polymerization which result in humin formation, an undesirable furanic polymer that greatly lowers the yield and selectivity towards HMF [14, 15, 16]. Several studies have been investigating various factors that can influence the reaction, including properties of different homogenous and heterogenous catalysts, solvent, feedstock composition and heating systems [8, 13, 16]. Thus, to minimize off-path reaction, the conditions must be carefully selected. Addition of polar aprotic solvents such as dimethylsulfoxide (DMSO), tetrahydrofuran (THF), methylisobutylketone (MIBK) to aqueous medium has so far shown a good conversion, with the limited side reactions and high 5-HMF yield, whereas a good catalytic performance towards 5-HMF was also shown with ionic liquids as a reaction media [13, 17]. Whit heterogeneous catalytic dehydration

of fructose preformed in DMSO Morales. et al. and Sajid et al., achieved 90 % molar yield of 5-HMF [18, 19]. Benefits of water/THF medium for lignocellulosic biomass conversion were presented by Li et al. [20], with the role of THF as a co-solvent in a monophasic and/or biphasic system. Nikolla et al. reported 57 % of 5-HMF from glucose feedstock in a THF-water biphasic system [21]. With a bifunctional porous coordination polymer (PCP) in THF/water medium Liang et al. achieved 65.9 % 5-HMF yield and 99.9 % conversion [18, 20]. Good performance of MIBK/water biphasic system was reported by Roman-Leshkov et al., where continuous in-situ extraction of 5-HMF resulted in 55 % yield from fructose feedstock [13, 23]. The choice of catalyst is another critical factor that can greatly influence 5-HMF selectivity during sugar dehydration. Therefore, various homogeneous and heterogeneous catalysts were investigated, trying to determine the role of Brønsted and Lewis acidity on saccharide conversion. As a homogeneous catalyst, mineral (HCl, H₂SO₄) and organic acid (acetic, formic, lactic etc.) are widely used Brønsted acids, facilitating hydrolysis and dehydration, while metal chlorides (AlCr₃, CrCl₂, SnCl₄) are with its Lewis acidity importantly contributing to isomerization step in the reaction pathway [13, 24]. Due to the easier catalyst separation, recyclability and non-toxicity heterogeneous catalysts are compared to homogeneous catalyst often more desired. Heterogeneous catalysts can also overcome some challenges that are associated when using biocatalysts such as higher cost and lower activity [15]. Commonly used solid acid catalysts for 5-HMF production are ion-exchange resins, namely Amberlyst-15 and Dowex-50, different types of zeolites, functionalized carbon and silica, metal oxides and phosphates [13, 15, 24].

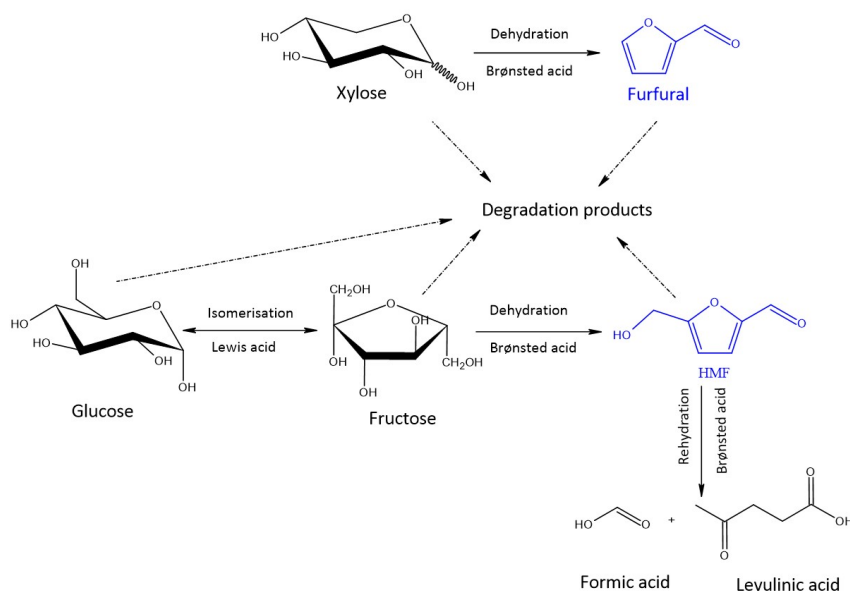


Figure 2: Sugar dehydration reaction pathway; hydrolysis of polysaccharide, glucose-fructose isomerization, fructose dehydration and 5-HMF rehydration to levulinic and formic acid.

4. Humin formation

Humins are identified as complex carbonaceous, heterogenous, polydisperse compounds [25, 26]. They are most likely formed under hydro-thermal, acid-catalyzed biomass (hemi)cellulose based sugar conversion, which negatively impacts the yield and selectivity of 5-HMF production [27]. This is usually accompanied with the loss of 10-50 of total carbon [28]. Due to their complexity and difficult analytical determination, the precise molecular structure of humins still remains relatively unknown. So far different humin formation pathways were proposed [26].

With suitable analytical techniques such as solid state NMR and FTIR, researchers are able to partially identify the structure of humins [25, 29]. Studies mostly agree that humins are based on polymerized furanics connected through aliphatic linkages with additional carboxyl, hydroxyl and carbonyl groups [25, 26, 29]. Based on the origin, starting substrate of dehydration there has been a few different structures proposed, knowingly humins are formed via aldol condensation, fructose, glucose and 5-HMF molecules derived humins are presented in Figure 3 [23, 25, 26, 31]. Humin formation not only is responsible for greatly reduced 5-HMF and furan yields, but can also contribute to reactor clogging and catalyst poisoning/deactivation [9, 30, 31, 34, 35]. Considering the aforementioned challenges, reaction conditions along with catalyst and sugar concentrations must be carefully selected to limit humin formation as it is mostly unavoidable during the acid-catalytic sugar dehydration. Extensive summary of work focusing mainly on the solvent and cat-

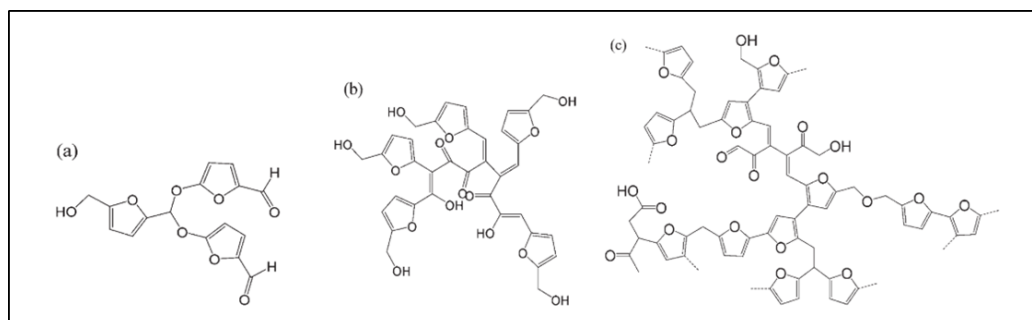


Figure 3: Scheme of proposed humin structure, a) fructose-derived humins, b) HMF-derived humins, c) glucose-derived humins, reprinted by [25].

alytic system was presented in the review papers [8, 13, 16], Figure 4. Yu et al. have reviewed and highlighted the mechanistic view of different catalyst and solvent performance used in biomass conversion to 5-HMF [13]. Zhang et al. in their review focused on heterogeneously catalyzed conversion of sugars including sugar dehydration reaction of C5 and C6 sugars to furfurals [15]. More information how lignocellulosic biomass composition and pretreatment impact on the production of 5-HMF and levulinic acid was summarized by Kang et al. [36]. Dashtban et al. briefly discussed the kinetics of 5-HMF production in different systems [17], and offered some important information, the goal of our review is to provide crucial information focusing on the reaction kinetics of sugar dehydration and

effect of humins and lignin on 5-HMF selectivity. So far studies majorly focused on the sugar dehydration reaction starting from sugar model compounds, fructose and glucose, respectively. With the implementation of the real lignocellulosic biomass mixtures, many more factors must be accounted for and the reaction becomes much more challenging to control, due to their complexity. Therefore it is of significant importance to optimize the reaction conditions and along with appropriate catalyst design reach the desired yields and selectivity. For that purpose, information provided with kinetic studies can be crucial for further development of the process. Kinetic studies with sugar model compounds are there for helping to provide better understanding with valuable information for process optimization and efficient catalyst design for simple systems. Different principles can be used for reaction kinetic modeling such as power-law approach and first order kinetic model. There has been various studies focused on kinetics of homogeneously catalyzed dehydration reaction, alternatively the studies conducting micro-kinetic modeling of heterogeneous system provides crucial first-principal information of liquid and as well as surface phase reactions [37]. Although an excess amount of studies conducted considering the kinetics of sugar model compounds have been reported, transferring, modifying and studying the kinetic models for real biomass streams, gives important information about the effect of several factors impacting the reaction. The review is aiming to understand and assess the optimal reaction condition and selection of catalyst through the information provided by kinetic studies. Knowing humins are unavoidable side product of sugar dehydration reaction, this review aims to provide information on the humin formation and reaction kinetics in order to more effectively suppress their formation. Focusing towards more efficient feedstock utilization, the impact of lignin on the selectivity and kinetics of catalytic dehydration reaction will be presented.

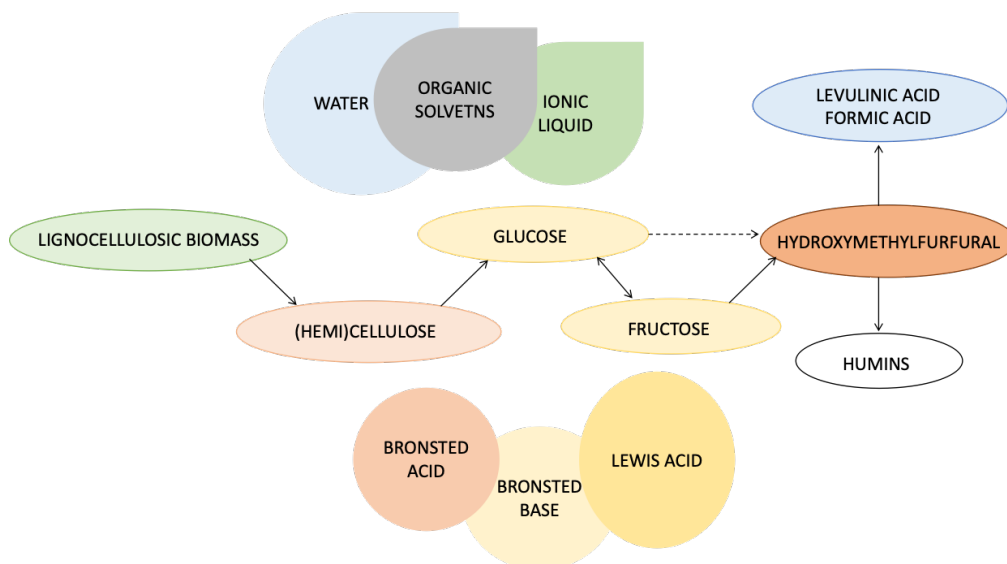


Figure 4: Pathway of lignocellulosic biomass valorization, adopted by [13].

5. Reaction Kinetics for Dehydration of Model compounds

Homogenous catalysis so far still remains one of the most commonly used and industrially applicable method for furanic production. In addition to being a non-recyclable catalysts that are difficult to separate from the desirable products, homogeneous catalysts pose an environmental risk due to being often highly corrosive [38]. Nonetheless, its continued use on the industrial scale lays in its higher yields and lower costs [13]. Mellmer et al. achieved 38 % and 40 % 5-HMF yield with fructose conversion in aqueous medium with H_2SO_4 and HCl , respectively [39], whereas Hansen et al. reported 53 % 5-HMF yield achieved under acid (HCl) hydrothermal microwave fructose conversion [40]. For acid-catalyzed dehydration of sugars, generally mineral acids such as sulfuric and hydrochloric acids together with some organic acids and metal chlorides are used. Most of the existing literature of sugar dehydration reactions is focused on the kinetics and mechanisms of homogeneously catalyzed reactions, with fructose and glucose commonly selected as model compounds. Reaction networks for reaction kinetic modeling usually consists of multiple consecutive steps including sugar dehydration, followed by 5-HMF rehydration and optional pathways of degradation and/or humin formation. In the cases of using a glucose (aldose) as a substrate, an additional isomerization step could also be included. Fachri et al. presented a kinetic model for fructose dehydration to 5-HMF catalyzed by sulfuric acid. Authors used a power law approach model considering side reactions of 5-HMF rehydration to levulinic and formic acid, and humin formation from both fructose and 5-HMF [41]. Regarding process condition, it was proposed that varying the initial concentration of fructose had no effect on its conversion. Increasing the temperature and acidity resulted in higher reaction rates, although lower acidity lead to higher 5-HMF yields. The fructose dehydration step was shown to be the fastest with the highest reaction rate constant and a relatively high activation energy. Humin formation from fructose resulted in highest activation energy (148 kJ/mol), indicating thermos-sensitivity of the reaction. The lowest activation energy was calculated for 5-HMF degradation to organic acid (92 kJ/mol), followed by 5-HMF derived humin formation [41]. Similar trends were reported for glucose conversion, with highest calculated apparent activation energies of dehydration reaction (152 kJ/mol) and glucose-derived humin formation (165 kJ/mol), whereas the model was limited to direct dehydration of glucose to 5-HMF and did not include glucose-fructose isomerization step [42]. When glucose was used as a starting feedstock slightly higher values were observed, possibly indicating higher reactivity of fructose [41, 42]. Furthermore, sulfuric acid was used as a catalyst in the study conducted by Van Putten et al. explaining the importance of hydroxyl group orientation in relation to reactivity of different ketoses [43]. Among fructose, sorbose and tagatose, the latter was the most reactive with significantly lower activation energy (89 kJ/mol) and higher reaction rate constant in comparison with sorbose (138 kJ/mol) and fructose (124 kJ/mol). Different reactivity is proposed to be a function of hydroxyl group orientation at C4 and C5 position, illustrated in Figure 5. The orientation of hydroxyl groups does not have the same effect on the reactivity of aldoses, which were found to result in lower 5-HMF selectivity and reaction rates [43]. W. Guo et al. developed a kinetic model for H_2SO_4 catalyzed aqueous conversion of fruc-

tose/glucose [44]. Comparing to glucose, higher reactivity was reported when reaction was conducted with fructose. The dehydration of glucose therefore demands more energy (156 kJ/mol) than fructose (133 kJ/mol) with a considerably lower reaction rate constant. Humins formation was also included in the reaction mechanism. Similarly to other studies, lower reaction rate constants of 5-HMF/sugar derived humins formation were determined in comparison to sugar dehydration. Lower reaction rates were accompanied with higher activation energies, implying that increased reaction temperatures could result in excess side product formation [44]. Hydrochloric acid is another mineral acid which, along with sulfuric acid, is among the most commonly used homogenous acid catalysts for carbohydrate dehydration reactions. Studying aqueous glucose conversion using HCl as a catalyst for levulinic acid production, activation energies and kinetic parameters were reported using a power law approach [45]. The model proposed direct glucose dehydration to 5-HMF, a reaction step with the highest energy barrier reported. Other reaction steps included reported lower activation energies; 5-HMF derived humins formation (142 kJ/mol) and 5-HMF rehydration (95 kJ/mol) and glucose derived humins formation with only 51 kJ/mol [45].

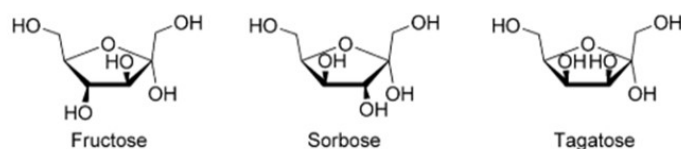


Figure 5: Ketoses, with different orientation of hydroxyl group at C4 and C5 position. Reprinted by reference [43].

An extensive reaction mechanism with 7 included parameters was proposed by Garces et al. while studying an aqueous phase conversion of glucose and fructose to HMF and levulinic acid [46]. The activation energy of fructose dehydration (88 kJ/mol) was lower compared to activated energy calculated for glucose dehydration to HMF (114 kJ/mol). Study also addressed fructose and glucose humins formation with calculation of apparent activation energy. The model, also included equilibrium reaction of glucose derived intermediate formation, such as isomerization to fructose, dimerization and anhydro-glucose formation [46]. Choudhary et al. proposed additional steps of open chain configuration when studying conversion of fructose. Proposed mechanism for fructose dehydration to 5-HMF included additional reversible intermediate formation presented in Figure 6 [47]. Reported values of activation energies are despite two step dehydration reaction in alignment with reported literature, with the lowest activation energy for 5-HMF derived humins formation 62 kJ/mol [47]. Yoshida et al. conducted a kinetic study of fructose decomposition catalyzed by hydrochloric acid in subcritical water [48]. The kinetic model considered formation of humins from both 5-HMF and fructose along with the degradation of formed levulinic and formic acid. The highest activation energy was reported for 5-HMF formation (161 kJ/mol), whereas the opposite was observed for rehydration (96 kJ/mol) of 5-

HMF [48]. For all humin and side product formation, the energy barrier can be compared to those studies which reported lower activation energy for 5-HMF and fructose derived humin production [45, 47]. Studying glucose conversion under hydrothermal acid catalysis, H_2SO_4 and H_3PO_4 resulted in higher 5-HMF yields, compared to HCl, while the highest yield of levulinic acid in supercritical water was achieved with HCl [49]. Comparing different inorganic Brønsted acids, authors have found that lower acidities (pH 2.5) favors higher 5-HMF yield, where rehydration is accelerated with increased acid concentration.

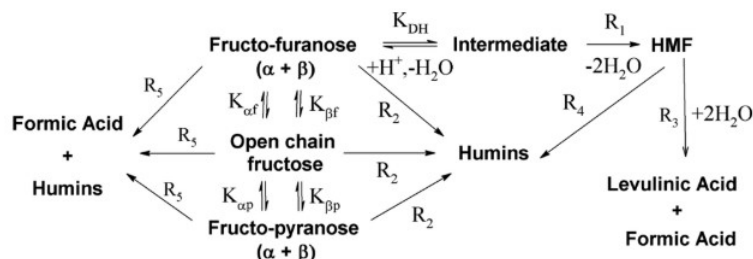


Figure 6: Fructose dehydration reaction network. Adopted by [47].

Considering small difference between activation energy denoted in Table 2, multiple pathways of side product formation could occur along with the desired 5-HMF synthesis.

Table 2: Homogeneously catalyzed monosaccharide dehydration to 5-HMF.

Feedstock	T [°C]	Catalyst	HMF Yield [%]	Solvent	References
Fructose	140–180	H_2SO_4	53	water	[41]
Glucose	140–200	H_2SO_4 (0.005–1M)	/	/	[42]
Fructose/Glucose	117–155	H_2SO_4	42	water	[44]
Fructose	90–130	HCl (0.05–0.25M)	57	water	[46]
Fructose	70–150	HCl	30	water	[47]
Glucose	140–180	HCl	/	water	[45]
Fructose	210–270	HCl	/	water	[48]
Fructose	100–130	pTSA	/	DMSO	[19]
Fructose	100–130	Oxalic acid	/	DMSO	[19]
Glucose	180–220	HTLW	32	water	[51]
Fructose	180–220	HTLW	/	/	[52]

When water is heated between 175 °C – 275 °C, the concentration of H^+ and OH^- ions are increased and can become catalysts for dehydration reactions [53]. With a reaction conducted in aqueous environment at elevated temperature (above 175 °C) 5-HMF yields of 47 % and 30 % can be achieved with fructose and glucose conversion, respectively [54]. Elevated temperatures and pressures can result in additional pathway of 5-HMF conversion, resulting in formation of trihydroxy benzene [8, 54]. Jing et al. proposed a reaction mech-

anism, addressing decomposition products formation from all compounds involved in a reaction including glucose, HMF and levulinic acid in the temperature range of 180 °C to 220 °C [51]. Apparent activation energies for glucose dehydration (108 kJ/mol), HMF rehydration (89 kJ/mol) and glucose and HMF humin formation (136 kJ/mol and 109 kJ/mol, respectively), and reaction rate constants, with the highest value for dehydration (at each temperature) were calculated. When studying decomposition of fructose consisting out of two consecutive reactions (dehydration to HMF and rehydration of HMF to levulinic acid) under a similar conditions in high-temperature liquid water, activation energy obtained without catalyst (127 kJ/mol) was higher than the one reported for glucose conversion [52]. Yu et al. discusses the effect of initial glucose concentration on its conversion in hot-compressed water (175 °C – 275 °C) [53]. The initial glucose concentration turned out to be of significant importance in the underlying reaction mechanism. With increased initial sugar loading, the apparent activation energy increased and the H⁺ ions overruled the effect of OH⁻ in the reaction of the dehydration, whereas lower initial concentration are more susceptible to the effect of OH⁻ ions. Latter lead to facilitated isomerization and retro aldol-condensation with a lower reported activation energy [53]. For glucose decomposition in high-temperature liquid water calculated parameters are in the arrangement with the previously reported values, where other homogenous catalyst (mineral acids) have been used. Considering that ions formed in water at elevated temperature can act as a catalyst, possible increased catalytic performance of other catalyst at higher temperatures should be considered, with a potential impact on the calculated kinetic parameters.

Compared to mineral acids, organic acids are less corrosive homogenous catalyst alternatives that provide Brønsted acidity necessary for sugar dehydration reactions [13]. De Souza et al. conducted fructose conversion in aqueous medium, with formic, acetic and lactic acid, achieving up to 64 % 5-HMF yield [55]. While studying fructose conversion in high-temperature liquid water, Li et al. discussed the influence of formic and acetic acid. The latter showed no effect on lowering the activation energy (126 kJ/mol), while the decrease of activation energy was more pronounced with formic acid (112 kJ/mol) [52]. Dussan et al. studied the conversion of hemicellulose sugars using formic acid as a catalyst [56]. Activation energy of glucose to 5-HMF dehydration (132 kJ/mol) was lower compared to studies conducted with mineral acid catalysts, similarly was also observed for glucose derived side products. The dehydration reaction under formic acid catalyst was therefore proposed to be less thermos-sensitive. Seemala et al. reported lignocellulose biomass conversion using levulinic acid as an acid catalyst [57]. Considering the carbohydrate dehydration reaction pathway, formic and levulinic acid can be formed via rehydration of 5-HMF. Therefore in-situ formed organic acids (levulinic and formic acid) could with its catalytic activity influence the reported reaction kinetics. Sajid et al. focused kinetics of fructose conversion in DMSO and water with five different organic acids; pTSA, oxalic acid maleic acid, succinic acid and malonic acid [19]. Based on the calculated reaction rate constants, the dehydration reaction was reported to be the fastest in all five organic acid systems, followed by significantly slower 5-HMF rehydration and humin formation. The reaction rate constants of fructose dehydration in water appeared to be as

followed: pTSA > oxalic acid > maleic acid > malonic acid > succinic acid. Changing the reaction media to DMSO resulted in significantly higher reaction rate constants and extremely lower activation energies for dehydration reactions and fructose derived humin formation (33.75 and 24.94 kJ/mol) catalyzed by pTSA. Authors have attributed that phenomenon to the higher acid concentrations, leading to lower temperature sensitivity of the reaction. This can also imply the difficulty of reaction kinetics comparison due to the difference in each individual reaction system and conditions.

Introducing Lewis acidity within homogeneously catalyzed water systems usually require addition of metal salts. So far different metal chlorides have been studied in terms of reaction kinetics, trying to understand what specifically effects individual reaction steps. Metal chlorides offers Lewis acidity, which provides a benefit when using glucose feedstock. Metal chlorides can provide good 5-HMF yields and selectivity in various solvent systems. Rasrendra et al. reported 54 % 5-HMF yield with CrCl₂ catalyzed glucose conversion in DMSO [58]. A kinetic study of Brønsted/Lewis acid catalyzed glucose dehydration was conducted using maleic acid and HCl for and AlCl₃ providing Lewis acidity [59]. The role of pH has been shown to influence the strength of the Lewis acidity of metal halides in aqueous environments [60]. Therefore, a combination of HCl and AlCl₃ resulted in the highest glucose-fructose isomerization reaction rate compared to when only AlCl₃ was present, although along with lower 5-HMF selectivity, the humin formation was also significantly increased. When AlCl₃ and maleic acid were utilized, humin formation was suppressed and resulted in the lowest reaction rate constant. 5-HMF selectivity was enhanced and humin formation was inhibited when maleic acid alone was used as catalyst, similarly when AlCl₃ was used in combination with maleic acid. The authors describe this phenomenon to be related to the possible intermediate formation between 5-HMF/fructose and maleic acid. Metal chlorides can be identified as either water sensitive or water compatible based on their hydrolysis constant, where water sensitive metal chlorides result in high hydroxylation [8, 60]. Hydrolysed metal ions in water can result in both Lewis and Brønsted acidity (hydronium ion) that can catalyze both isomerization and dehydration reactions [60]. Different metal chlorides have been investigated in aqueous glucose conversion reactions where smaller metal ion radius were correlated with increased reaction rates. Catalytic activity of water-sensitive and water-compatible metal chlorides followed the trend of LaCl₃ < DyCl₃ < YbCl₃ and InCl₃ < GaCl₃ < AlCl₃, respectively [60]. Higher activation energies of water-compatible metal salts were accompanied with lower reaction rates, whereas activation energies for glucose conversion calculated for water-sensitive salts showed no specific trends in relation to reaction rates, suggesting other factors can influence their activity. Starting with fructose as a feedstock, the same authors suggested the involvement of Lewis acid sites in fructose dehydration to 5-HMF. When comparing fructose dehydration conducted with HCl, AlCl₃ and YbCl₃, latter two resulted in higher reaction rates but lower 5-HMF selectivity. These findings imply that Lewis acidity can facilitate humin formation, resulting in lower 5-HMF selectivity. For glucose-fructose isomerization in aqueous media, a synergy of Lewis acidity and Brønsted basicity (-OH) is required [61]. Authors described the mechanism, denoted in Figure 7, where the Brønsted

base is responsible for deprotonation, which later enables the second step of intramolecular hydride shift which is Lewis acid catalyzed. Comparing homogeneously CrCl_3 , AlCl_3 and heterogeneously catalyzed Sn-beta isomerization, the latter was found to be the most effective. Carraher et al. investigated Brønsted base (trimethylamine) catalyzed isomerization

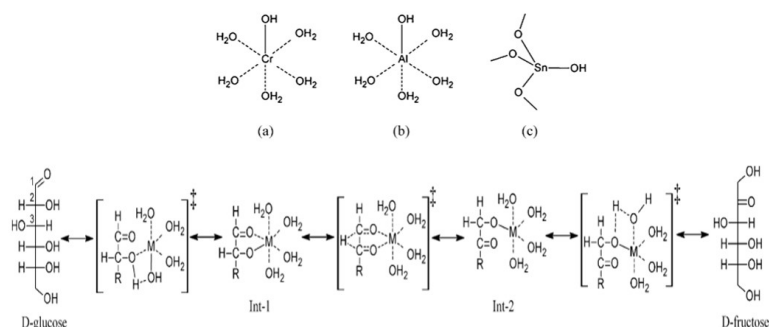


Figure 7: Scheme of active sites involved in aldose-ketose isomerization in aqueous media a) CrCl_3 , b) AlCl_3 , c) Sn-beta zeolite. Reprinted by [61].

reaction, where under strong alkali conditions the catalytic performance was comparable with other reported Lewis acid catalysts [62]. To conclude, sugar (glucose and fructose) derived humin formation and dehydration reaction are both Brønsted and Lewis acid catalyzed, while for the glucose to fructose isomerization requires specifically Lewis acidity [60, 61, 63].

Other widely used catalytic system for conversion of saccharides to 5-HMF are heterogeneous solid acid catalysis. These catalysts are easily recyclable and their use simplifies final product separation and offers a vast optimization range with possible basicity and acidity modulation [64]. Commonly used solid acid catalyst are alumina silicates, zeolites, heteropolyacids, functionalized carbon catalysts, different metal oxides and phosphates, denoted in Figure 8 [15, 65]. Ion exchange resins such as Amberlyst-15, with the presence of sulfonic group ($-\text{SO}_3\text{H}$) exhibit Brønsted acidity, needed for dehydration reaction, modulated with different metals can serve as efficient catalyst for saccharide conversion [66]. Zeolites are aluminosilicate porous solid acid catalysts, possessing Brønsted and Lewis acid sites, different types (ZSM, H-BEA, modernite etc.) of zeolite can result in different pore size and structure. With the pretreatment (calcination) the acid ration can be affected, while with a metal doping increase in Lewis acidity can be achieved [67]. The disadvantage of both zeolite and Amberlyst-15 catalyst is their instability in aqueous media at elevated temperatures, leading to leaching and fouling under these conditions [68, 69, 70, 71].

Although the homogeneous carbohydrate dehydration reaction to 5-HMF was extensively studied, to the best of our knowledge, there exists only limited data on the kinetics of heterogeneously catalyzed reactions. An important contribution for more in-depth understanding of its reaction kinetics was introduced by Moreau et al. [72]. The dehydration of fructose to 5-HMF was conducted using a solid acid catalyst, an H-modernite type of

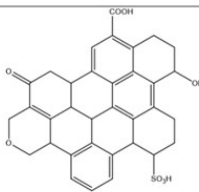
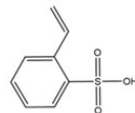
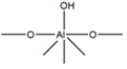
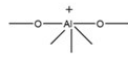
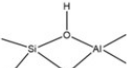
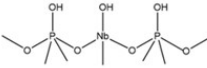
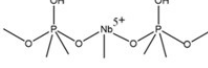
Catalyst	Brønsted acid	Lewis acid
Sulfonated carbon		Not available
Amberlyst-15		Not available
γ -Al ₂ O ₃		
Zeolite		
Niobium phosphate		

Figure 8: Commonly used solid acid catalysts. Reprinted by [15].

zeolite. In a biphasic MIBK/water solvent system, H-modernite catalysts with different Si/Al ratios were tested at a reaction temperature of 165 °C. Both the highest fructose conversion and 5-HMF selectivity along with the highest calculated initial rate constant of 7.6×10^6 mol/s was achieved with the Si/Al ratio of 11. A pseudo first-order approach was introduced for the kinetic modeling with a two-step reaction scheme: 1.) dehydration of 5-HMF and 2.) 5-HMF rehydration to formic and levulinic acid, where reported activation energies were 141 kJ/mol for the first step and 64 kJ/mol for the second one [72]. A kinetic study conducted by Lourvanij et al. contributed important information and helped to understand how different catalyst properties impacted reaction rates and product selectivity [73]. Among the important parameters such as catalyst acidity: acid strength and concentration, catalyst structure including pore size and geometry plays an important role when it comes to dehydration of glucose to HMF and other organic acids. To investigate how pore size of solid porous aluminosilicate catalysts effect selectivity and reaction rates, four different types of micro and mesoporous catalysts were selected with similar acidity: HY-zeolite, aluminum-pillared montmorillonite (APM), MCM-20 and MCM-41. The authors established a kinetic model based on 13 parameters, calculated reaction rate constants at 150 °C and activation energies in the range of 130 °C to 190 °C. Calculated activation energies for all three studied catalysts (HY-zeolite, APM and MCM-20) demonstrated the trend

that more energy is needed for either fructose or glucose (fructose produced by isomerization of glucose) dehydration (134-218 kJ/mol) whereas the reaction of HMF rehydration activation energy resulted in a significantly lower value (54 -80 kJ/mol). Based on the kinetic modeling results and calculated reaction rate constants, the study suggests that the mechanism for the formation of HMF via glucose-fructose isomerization pathway is more likely to occur in relation to direct glucose conversion to HMF. Comparing the forward rate constants (reaction rate constant of individual reactions per acidity on the catalyst), they concluded that the dehydration of fructose and glucose were fastest when the catalyst pore diameter was around 10 Å due to the size of the hydrated sugar molecule. Furthermore, reaction rate constants for 5-HMF rehydration and bond cleavage were, in all the studied cases, higher compared to dehydration reactions. The developed model also included coke formation suggesting formation of coke and insoluble humins can be enhanced when using microporous materials [73]. Similar conclusions were presented by Kruger et al. where furan selectivity was dependent on the size of sugars/furansics and catalyst pore diameter, as shown in Figure 9 [74].

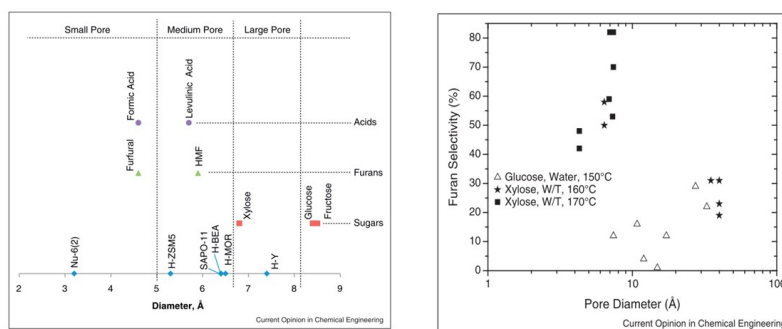


Figure 9: Comparison of catalyst pore size and size of sugars as substrates and furanics as end products. Reprinted by [74].

Along with the impact of catalyst structure, acidic properties are also considered of importance when it comes to conversion of sugars. Employing glucose as a starting material for 5-HMF production can be challenging when attempting to achieve high yields and selectivity due to the step of glucose-fructose isomerization. By introducing metal ions into aluminosilicate catalysts, it is possible to increase Lewis acidity and thus, facilitate this isomerization step. Based on the present literature, kinetic studies regarding sugar conversion to 5-HMF typically describe the dehydration step as slower and more energy demanding with a lower kinetic rate constant and higher activation energy in comparison to the subsequent rehydration step to HMF [41, 44]. The study conducted by Wei et al. exemplified that an increase in Lewis acidity can lead to faster dehydration of glucose when using 8 wt.% Cr/HZSM catalyst instead of undoped HZSM-5 [75]. With the addition of Cr, the reaction rate constant for glucose dehydration significantly increased and the activation energy lowered from 87 kJ/mol to 69 kJ/mol, whereas the decrease in the activation energy of HMF rehydration was not as significant (from 58 kJ/mol to 54 kJ/mol). Un-

fortunately, the model offers only limited information as it does not include reaction rate constants and activation energies for glucose-fructose isomerization and humin formation. However, the authors mentioned that an excessive increase of Lewis acidity in the case of higher Cr loading (16 % Cr/HZSM-5) can result in facilitated cross-polymerization and therefore, increased humin formation [75]. Ramli et al. has in the study of dehydration of glucose to levulinic acid over Fe/HY zeolite included additional kinetic parameter of reaction rate constants for humin formation [76]. Previously, they have conducted a study where they came to similar conclusions as the before mentioned authors. Introduction of Fe metal ion to the HY-zeolite catalyst surface increased the Lewis acidity and therefore, promoted glucose-fructose isomerization, which provided higher yields of the final product (levulinic acid) [67]. Similarly to Cr doped HZSM-5, increased loading of Fe resulted in higher Lewis acidity, causing excess humin and side product formation. As the Fe was added, change of pore diameter was detected. Authors proposed a theory where larger mesoporous size in an aqueous environment can lead to formation of H_3O^+ ions. This significantly increases the local acidity and can therefore promote unwanted side reactions of humin formation [67, 72]. A kinetic model was presented proposing that the reaction rate of 5-HMF decomposition to levulinic acid and humins is higher than its formation, which could explain the low HMF concentration that was achieved [76]. Activation energies for both glucose and HMF derived humin formation were higher compared to glucose dehydration, proposing that elevated temperatures could lead to lower 5-HMF selectivity. Reported activation energies of Fe/HY-zeolite are relatively lower compared to the ones [73] for the parent HY-zeolite, therefore it can be proposed that the addition of Lewis acidity effects the reaction kinetics by significantly lowering the activation energy of dehydration reaction, without effecting the activation energy of rehydration reaction. Swift et al. studied the conversion of fructose and glucose to HMF over H-BEA zeolites [69]. The reaction network implemented for the kinetic model contained 5 reaction rate constants including the equilibrium of glucose-fructose isomerization. This study is one of the only studies that takes into account both heterogeneous and homogeneous reactions. The developed model also distinguishes between the amount of Lewis and Brønsted acid sites present on the catalyst surface. The resulting TOF of H-BEA were lower compared to when homogeneous HCl catalyst was used. Authors also demonstrated that the high activation energy for fructose dehydration over H-beta zeolite (145 kJ/mol) can be significantly lowered by impregnation of the zeolite with Sn (89 kJ/mol) [69, 77]. There exists limited literature that provides the reaction kinetics of heterogeneous catalysts. Sairanen et al. reported calculated activated energies for dehydration of three different monosaccharides with and without activated carbon as catalyst [78]. Activated carbon has shown to efficiently lower the activation energy of both glucose and fructose dehydration reaction [78]. Carniti et al. used niobium phosphate (NBP) as a catalyst for fructose dehydration in a continuous flow reactor, where obtained activation energy in the temperature range from 90 – 110 °C was 66 kJ/mol [79]. The difference in the calculation of activation energy can also be attributed to a different temperature range and system condition, therefore they are often hard to directly compare. The data of kinetic parameters and reaction network studied in the each

individual is represented in a Table 3 below.

Table 3: Heterogeneously catalyzed monosaccharide dehydration to 5-HMF.

Feedstock	T [°C]	Catalyst	HMF Yield	Solvent	References
Glucose	120 –200	10 % Fe/HY zeolite	11.40%	water	[77]
Glucose	180	pTsa-Ca/AC	53%	MIBK/H ₂ O	[81]
Glucose	180 –220	Activated carbon	23%	water	[79]
Fructose	180 –220	Activated Carbon	69%	water	[79]
Glucose	160 –200	HZSM-5	/	water	[76]
Glucose	160 –200	Cr/HZSM-5	/	water	[76]
Fructose/glucose	110 –140	H-BEA-25	/	water	[70]
Fructose	90 –110	NBP	/	water	[80]
Fructose	165	H-form mordenite	/	MIBK/water	[73]
Glucose	130 –190	HY-zeolite, APM, MCM	water	water	[74]

6. From model compounds to real biomass feedstock kinetics

Proceeding from simple model compounds towards realistic biomass streams can be particularly challenging. Pedersen et al. established a kinetic model, with a reaction pathway for conversion of high fructose corn syrup (glucose and fructose mixture), with the hypothesis that sugars are the main source for humin formation [33]. Higher calculated activation energies (228 kJ/mol) for glucose derived humins, indicates that the reaction is more favorable at higher temperatures. In the year 1945, Saeman et al. studied biomass hydrolysis along with glucose decomposition and established a first systematic kinetic model [81]. Two step reaction mechanism that they proposed included cellulose hydrolysis with a glucose decomposition as a second step. Increased acid concentration and temperature resulted in higher rate of hydrolysis compared to glucose decomposition. The vast majority of kinetic studies were performed on cellulose conversion by acid hydrolysis to monomeric sugars, whereas the dehydration step to furfurals and/or to levulinic acid is often not included. Girisuta et al. studied acid-catalyzed hydrolysis of microcrystalline cellulose to levulinic acid and established a kinetic model using a power-law approach [82]. Hydrolysis of cellulose and glucose humin formation required the largest activation energies (175 kJ/mol and 165 kJ/mol, respectively), meaning these reactions will be facilitated at increased reaction temperatures. Based on the calculated kinetic parameters, authors proposed that lower temperatures and higher acid concentrations are favorable for higher selectivity towards levulinic acid. Therefore, the optimization of 5-HMF production appears to be more challenging. The same authors later transferred their established kinetic model to a real biomass sample containing water hyacinth plant by introducing specific correction factors. Hemicelluloses conversion to C5 sugars was found to proceed with a higher rate compared to cellulose decomposition to C6 sugars [83]. A study also demonstrated higher rate of pure cellulose conversion in comparison to the conversion of

the real biomass cellulose. This could be attributed to either different stage of cellulose crystallinity and/or the presence of lignin matrix. Pretreatment of hemicellulose fraction such as aqueous extraction and auto-hydrolysis can be successfully employed in converting hemicelluloses into polysaccharides, enabling acid hydrolysis and dehydration to proceed in order to obtain 5-HMF and furfural. A kinetic study conducted by Rivas et al. showed higher pentose reactivity compared to hexoses, which correlated with higher values of calculated reaction rate constants [84]. Assessment of kinetic coefficients (reaction rate constant) for 5-HMF and furfural conversion demonstrated higher rates for 5-HMF rehydration and formation of side products in comparison to furfural. Within the following study additional activation energies and reaction rates for hydrolysis of POS (poly/oligo saccharides) were systematically presented [85]. Hydrolysis reaction rates were shown to be significantly higher and strongly facilitated by increased temperature in comparison to dehydration reaction. Elevated temperatures facilitate the formation of sugar-derived degradation products at elevated temperatures, together with high 5-HMF rehydration rates and low activation energy (72 kJ/mol), leads to low 5-HMF yields. A study conducted by Girisuta et al. demonstrated relatively high reaction rate of C6 oligomer conversion, which was significantly affected by acid concentration, namely more acidic media lead to higher glucose yields [86]. The highest rate constants and lowest activation energy was attributed to 5-HMF rehydration reaction. Therefore as shown in studies previously conducted by Girisuta et al. [82] and Rivas et al. [85], difficulty in achieving higher 5-HMF yields can be attributed to the high activation energy of direct sugar humin formation (161 kJ/mol) and favorable rehydration reaction at lower temperatures and highly acidic media. Shen et al. studied conversion of cellulose under hydrochloric acid catalysis and proposed reaction of glucose dehydration to 5-HMF to be a rate controlling step, due to the lowest absolute reaction rate [87]. Instead of relying on commonly used dilute acid pretreatment to hydrolyze biomass streams, hydrothermal pretreatment can be implied for hemicellulose or cellulose decomposition in order to avoid the use of highly corrosive acids. Hydronium ions in hot compressed water can act as a catalyst and therefore hydrolyze (hemi)cellulose and/or dehydrate obtained monosaccharides further into value added products furanics [88]. Dos Santos Rocha et al. in their study present a kinetic model of sugarcane straw decomposition, separately evolving a kinetic model for conversion of hemicellulose to C5 sugar and furfural and cellulose to C6 sugar and HMF [88]. Hemicellulose – oligomer conversion was likely to be dominant at lower temperature, while further hydrolysis into monomers (220 kJ/mol) and their degradation to side products (146 kJ/mol) was strongly facilitated at higher temperatures. Similar trend was observed for the conversion of cellulose fraction. Observed trends tends to be similar to the ones reported when using dilute acid hydrolysis as a treatment of biomass [84, 85, 87]. As another environmentally friendly option ionic liquids can be implied as a solvent for one pot biomass conversion towards value added products. With the good solubility of cellulose fraction they create homogenous conditions, avoiding mass transfer limitations. Vanoye et al. preformed hydrolysis of lignocellulosic biomass, starting from cellobiose as a cellulose model compound [89]. Despite successfully transferred kinetic model to conversion pure

cellulose feedstock, predicted optimal conditions were not transferable to conversion of raw biomass sample (*Miscanthus* grass). Therefore in order to be able to obtain good fit for raw biomass samples additional modifications, including correction parameters needed to be introduced. Organosolv pulping process enables the separation of cellulose and lignin fraction leaving a liquid hemicellulose fraction available for further conversion to platform chemicals. Dussan et al. studied formic acid catalyzed dehydration of hemicellulose saccharides [56]. The evaluation of established kinetic models based on individual model compounds conversion, was successfully transferred to C6 and C5 sugar mixtures and real biomass samples (Wheat straw, *Miscanthus*, Norway spruce). Hemicellulose organosolv predominantly contains large amounts of C5 sugars, mainly xylose, whereas hexoses can be present in smaller amounts, therefore some kinetic studies doesn't always include HMF formation [90]. Studying hemicellulose organosolv conversion it was demonstrated doubled formation of humins in comparison to reaction conducted with model compounds alone. This can be associated with the presence of multiple hexoses, pentoses, organic acids and lignin residues, while reduction in humin formation can be achieved by addition of ethanol as a solvent to reaction mixture. [81]

The presence of various different compounds may affect the lignocellulosic biomass utilization and additional steps are necessary to optimize the process. Therefore, studies developing kinetic models using raw biomass as feedstock are of significant importance to obtain industrially transferable knowledge for the production of furanics.

The use of solid catalysts for a one pot conversion of lignocellulosic biomass material is not often reported in the literature. Gromov et al. recently published a study with a kinetic model of multistep hydrolysis-dehydration of cellulose as a starting material over solid sulfonated carbon catalyst. Findings reported cellulose solubilization and glucose-fructose isomerization as the main rate limiting steps in 5-HMF formation, without significant levulinic acid formation [92]. Jiang et al. have proven that acid sites present on the solid catalyst surface can donate a proton to a solid cellulose particle, resulting in protonated species, that can dissolve and degrade in water [93]. Since cellulose is a macromolecule it can also undergo the universal free radical degradation reaction. MCM-41, modified sulfuric acid catalyst facilitates cellulose degradation at increased temperatures. Using sulfonated MCM-41 authors observed fast decrease in the cellulose concentration at the start of the reaction, due to the degradation of amorphous cellulose fraction. Developed kinetic model also provides reaction rate constants and activation energies, where degradation of 5-HMF demonstrated the highest activation energy and reaction rates. The use of solid acid catalyst can be challenging due to possible deactivation and humin deposition [68, 94]. Trying to avoid these difficulties reaction media can be a crucial factor in suppressing undesired product formation. Atanda et al. optimized the catalytic performance of phosphated TiO_2 by using biphasic system by the addition of N-methyl-pyrrolidone (NMP), where the role of NMP was to stabilize 5-HMF and prevent the rehydration and humin formation [95]. Testing out glucose, cellulose, sugarcane bagasse and rice husk as a different starting material, the importance of cellulose structural composition has been emphasized. In order for cellulose to undergo the catalytic conversion it must dissolve in water, which can be

achieved by decrystallization and/or depolymerisation, using alkali pretreatment. Kinetic model included hydrolysis of cellulose with later glucose dehydration to 5-HMF, where hydrolysis (122 kJ/mol) had higher activation energy and reaction rates compared to the dehydration reaction (111 kJ/mol) [95]. Qing et al. studied SnCl₄ catalyzed conversion of corn cob, where the kinetic analysis shown lower activation energy for glucose dehydration into 5-HMF, compared to other homogenous catalysts (HCl, H₂SO₄) [96]. Similarly as reported for homogenous catalysis, [81, 85] reaction rate of cellulose hydrolysis increased with elevated temperature. When studying realistic stream mixtures it is important to consider their complex structure with possible presence of metal ion, which can be a defining factor for catalyst selection. Authors have reported the change in acidity of zeolite catalyst, based on metal-exchange study metal ions can be responsible for catalyst deactivation due to their possibility to exchange with the Brønsted acid sites [8, 97]. Proton exchange with metal ion in zeolite catalyst is denoted in Figure 10.

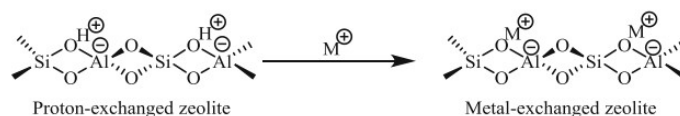


Figure 10: Proton exchange. Reprinted by [97].

7. Effect of lignin

The structure of lignocellulosic biomass is an important aspect when conducting reactions with real biomass samples, where the protective lignin layer can affect the surface accessibility cellulose and hemicellulose [8]. Based on the glucose decomposition study, Xiang et al. established a complex reaction network and discussed the effect of acid soluble lignin (ASL) on the degradation process [98, 99]. It has been proven that ASL in acid medium facilitates glucose conversion by formation of ALS-glucose or ALS-oligomer complexes [99]. A comprehensive kinetic study conducted by Yan et al. revealed the impact of cellulose crystallinity, in-situ formed ASL-glucose complex and humins on the reaction kinetics, [100]. Cellulose crystallinity significantly impacted the reaction rate of hydrolysis at the lower temperatures (140 °C – 160 °C), whereas it diminished with an increase in temperature. In-situ formed ASL-glucose complex and humins demonstrated a greater influence on the reaction kinetics at higher temperatures. Generation of ALS-glucose complex was facilitated by higher hydronium ion concentration in water medium, which negatively impacted 5-HMF yield. The third parameter of 5-HMF derived humin formation was negligible at lower temperature below 160 °C, whereas the increase in temperature resulted in lower 5-HMF and levulinic acid yields [100].

Raw lignocellulosic biomass is comprised of both C5 and C6 sugars, therefore the understanding of possible lignin interference and impact on conversion of both hexoses and

pentoses is crucial for process optimization, catalytic activity and yields of desired products. When studying acid catalyzed conversion of model compounds (xylose/ xylan) along with a real biomass sample, Yemisß et al. obtained higher furfural yield in straw biomass compared to pure model compound [101]. Interestingly, the study conducted by Daorattanachai et al. contrarily showed that the presence of Kraft lignin negatively impacted furfural yields from xylose and xylan [5]. The opposite has been proven for hexoses where lignin can promote glucose-fructose isomerization. It was proposed that the isomerization could be promoted by lignin originated organic acids under conditions of hot-compressed water, although in-situ formed organic acids were not mentioned. The impact of lignin on sugar conversion was studied at different acid concentrations, where the presence of lignin increased 5-HMF yield at concentration above 0.5 M H_3PO_4 [5]. This indicates a possible lignin neutralization capacity which was studied later by Lamminpää et al. where authors presented the impact of kraft lignin on xylose conversion [102]. Lignin has shown to highly impact the pH of the reaction media. Whereas the inhibition effect of lignin on xylose conversion and furfural yield was more pronounced using sulfuric acid in comparison to formic acid, ascribed to different acid strength and dissociation ability. Presence of neutralizing capacity could originate from cations (potassium, sodium, magnesium) present in biomass. Changes in pH could not fully explain the inhibition of xylose conversion proposing there are existing additional pathways in of xylose dehydration inhibition [102]. Gomes et al. investigated production of furanics from sugarcane bagasse and reported lower HMF and furfural yield when real biomass was used as a feedstock [103]. Authors have associated the inhibitory effect of lignin with barrier like effect of lignin as a macromolecule and/or possible catalyst ($ZnCl_2 / HCl$, $AlCl_3 / HCl$)-lignin interaction resulting in a deactivation and lower catalytic activity. Jongerius et al. studied the presence of lignin and lignin model compounds as a stabilizer of Pt / Al_2O_3 preventing alumina support to recrystallize to boehmite, the loss of Lewis acidity and sintering of metal particles [104]. It was evidenced that higher lignin concentration in the biomass stream can decrease furfural yield, along with an increase in degradation rate [105]. Alternatively, the addition of lignin model compounds to saccharide mixtures had no significant effect on either furfural or xylose degradation. Dussan et al. proposed the mechanism for xylose/furfural degradation in the presence of lignin. The authors proposed two possible pathways for lignin facilitated xylose/furfural degradation, which resulted in lower furfural yields. The first reaction pathway can be described by aldol condensation between a lignin carbonyl group and furfural. Another explanation for the low furfural selectivity can be due to the electrophilic behavior of xylose intermediates reacting with the lignin carbocation formed under acidic conditions. The results in the study also proposed no significant effect of lignin on glucose dehydration to 5-HMF or its degradation. An efficient method for feedstock purification was implemented by Liu et al. when studying the conversion of biomass hydrolysate containing high glucose concentrations into 5-HMF [106]. With the addition of activated charcoal (50 wt %), they were able to remove inhibitors such as lignin and furanics leading to higher yields of 5-HMF.

Binder et al. reported no negative effect of lignin and other macromolecules on the

HMF yield using DMA-LiCl (10 %) with ionic liquid as a reaction media for conversion of corn stover [107]. Similarly no interference of lignin present in biomass sample was observed when authors used GVL as a solvent. Other advantage of using solvent like GVL is its ability to dissolve lignin and huminic species that are formed during dehydration reaction [32]. It has been proven that lignin can react and form complexes with both C5 and C6 sugars, when biomass conversion is conducted under hydrothermal acidic catalysis, which can consequently lead to lower selectivity and yields of HMF and furfural, respectively. Considering lignin ability of neutralization, using acid catalyst in low concentrations can lead to neutralization and decreased acid concentration, effecting the catalyst activity. Regarding reaction condition optimization, the removal of lignin is not absolutely necessary for efficient lignocellulosic biomass saccharide dehydration.

8. Humins formation and its kinetics

Humins formation can be attributed to different substrates during dehydration reaction, including sugars, furanics (HMF or furfural) or intermediates. Sumerskii et al. studied formation of humins like substances (HSL) under industrial conditions of wood hydrolysis [31]. Authors proposed a reaction pathway of polycondensation of HMF derived ether or acetal, with possible integration of levulinic acid and incorporation of monosaccharide intermediates, considering the presence of lignin can also lead to lignohumic complex. Based on the analytic techniques (GC-MS pyrolysis-pyrogram, ^{13}C -NMR) the composition of HSL was suggested to be comprised of 60 % of furanic rings and 20 % of aliphatic linkers [31]. Horvat et al. showed the involvement of a highly reactive intermediate (2,5-dioxo-6-hydroxy-hexanal) DHH in the formation of 5-HMF derived humins [108]. The model was later expanded by Patil et al. proposing aldol addition/condensation between 5-HMF and DHH as a primary route for humins formation [30]. The reaction was reported to be first order, with activation energies of 89 and 94 kJ/mol for rehydration to LA and humins formation, respectively [30]. Comparison of glucose, fructose and 5-HMF humins formation revealed that direct the conversion of sugars into humins does not seem to be significant in relation to 5-HMF [109]. This contradicts the proposed mechanisms in most of the kinetic studies, which include direct humins formation from either fructose or glucose. Van Zandvoort et al. have later reported humins can be formed through additional reaction pathways [26]. The presented van Krevelen plot demonstrated participation of sugars, intermediates and furanics in humins formation. Alternatively, additional experiments and analytics (2D solid-state NMR and infrared (IR) spectroscopy, gel permeation chromatography (GPC)) confirmed that humins are mostly derived by 5-HMF [25] [29]. With ATR-FTIR spectroscopy, Scanning Electron Microscopy (SEM) and Dynamic Light Scattering (DLS) it was suggested that 5-HMF undergoes condensation reaction and/or nucleophilic attack, with levulinic acid being to some extent involved in a structural composition of humins [29, 110]. Acidic properties and possible incorporation of levulinic acid into the humins structure was also suggested by Whitaker et al. [111]. The authors later confirmed later by cation exchange titration of produced humins. Based on the mechanistic studies it can be concluded that 5-HMF represent key compound, whereas 5-HMF

can undergo either self-condensation or cross-polymerisation with partially dehydrated sugars and intermediates (DHH). Maruani et al. suggested formation of water soluble glucose oligomers under acidic hydrothermal conditions which could have a possible involvement in the humin formation [112]. The similar mechanism of oligomer formation via direct sugar dehydration was also proposed by Fu et al. [113]. Formation of the oligomeric species, described as a humin precursors was also proposed by 5-HMF and LA cross-polymerization and self-5-HMF condensation [114]. Soluble oligomers are formed via 5-HMF condensation where their size can later increase to a level where it overcomes its solubility, leading to the formation of primary particles. This theory was confirmed by a kinetic study regarding growth of humins [114].

Researchers have been during the last decade focusing on the mechanism of humin formation, proposing that the 5-HMF plays a key role in the reaction of condensation and or cross/self-polymerization, leading to humin formation. Literature does not agree on the involvement of partially dehydrated sugars or rehydration side products in the humin structure [115]. Although most of the kinetic studies are considering humin and/or side product formation directly from sugars, glucose and fructose, respectively. Alternatively, a lot of kinetic studies has proposed direct degradation of saccharides (fructose) to formic acid. This pathway was suggested due to the stoichiometric excess of detected formic acid during dehydration reactions in comparison to levulinic acid.

9. Influence of solvent and temperature on humin and side product formation

In order to achieve higher HMF yields, organic solvents often can be introduced to a reaction system. Mellmer et al. achieved 5-HMF yield above 70 %, when using H_2SO_4 and HCl in water-THF and water-dioxane reaction media [39]. Tang et al. investigated the effect of organic solvent addition on kinetics of dehydration reaction and 5-HMF yield and selectivity [63]. Based on the calculated reaction rates it was found that addition of organic solvent THF, suppressed undesired HMF conversion to humins. In comparison to pure aqueous systems, reverse (fructose-glucose) isomerization and formation of saccharide derived formic acid was found to be enhanced in THF-water reaction media, while glucose-fructose isomerization, fructose dehydration and HMF/fructose derived humin formation demonstrated lower reaction rates. With additional analysis by electron spin ionization mass spectroscopy (ESI-MS), it was proven that the presence of THF accelerates direct degradation of both sugars (fructose and glucose) to formic acid. Fu et al. studied suppression of unwanted oligomeric side products (humin precursors) by triphasic system of THF-water and CO_2 . THF was found to be responsible for the inhibition of cross/self-condensation of 5-HMF and LA, while CO_2 suppressed the sugar oligomer formation [113]. Due to the importance of solvent used as a reaction medium Fu et al. studied solvent effects on degradative condensation of fructose [115]. Polar aprotic solvents resulted in oligomer formation along with significant amounts of formic, acetic and levulinic acid. Individual solvents revealed to promote different side products, where THF and DIO lead to excessive formation of formic acid, MIBK facilitated formation of acetic acid and

significant amount of levulinic acid was formed in GVL and NMP, whereas DMSO specifically promoted formation of 5-HMF [115]. Important contribution to the field was done by Cheng, et al. by assessing the solubility of humins in various solvents, finding the correlation between solvent donor number and humins solubility, where THF and DMSO resulted in the highest concentration of solubilized humins. Vasudevan et al. provided additional information on glucose solvation using force-field molecular simulation [116]. It was proposed, that already small amount of co-solvent (DMSO, dimethylformamide (DMF), THF) added to the aqueous system can stabilize the glucose molecule (by stronger water-glucose interactions). Along with suppression of unwanted products formation it can promote sugar dehydration into 5-HMF. This theory can explain higher 5-HMF yields obtained in the reactions conducted with different polar aprotic co-solvents. Higher yields and selectivities of 5-HMF achieved in DMSO, attracted more attention to study the effect of DMSO on sugar dehydration reaction. Amarasekara et al. proposed the mechanism of DMSO promoting dehydration reaction by stabilizing fructose molecule in the furanose isomer form with a fructose dehydration through a cyclic intermediate [117]. Whitaker et al. similarly studied the impact of DMSO on the reaction mechanism [111]. Concluding, the main reason for higher 5-HMF yields and selectivity, lays in the stabilization, rather than other proposed option of DMSO to sulfuric acid degradation. Pedersen et al. conducted dehydration reaction from glucose/fructose mixtures in acetone-water solvent system, similarly to DMSO, acetone demonstrated an effect of HMF stabilization [33]. To achieve higher conversion and yields researchers also tried to implement a Simultaneous-Isomerization-and-Reactive-Extraction (SIRE) process for HMF production, where in order to increase HMF yield ketoses are extracted into acidic IL medium, whereas formed HMF is then further extracted into organic phase (THF). [86] Different organic solvents can be also added to aqueous medium in order to form a biphasic systems. Biphasic system enables, increase in 5-HMF yield due to transpiring in-situ extraction. Once HMF is formed, it is extracted to the organic phase where reactions leading to undesirable products, namely levulinic and formic acid and humins are suppressed, illustrated in Figure 11 [118]. Román-Leshkov et al. investigated biphasic system for fructose to 5-HMF conversion, the addition of MIBK as a water immiscible organic solvent was first introduced to increase fructose conversion and 5-HMF selectivity [23]. To further improve 5-HMF selectivity DMSO/PVP was added into water phase, resulting in better solubility in water phase, therefore low 5-HMF partitioning was corrected with 2-butanol. Due to the THF-water miscibility the addition of salt is needed in order to form biphasic system. By introducing NaCl to a system, isomerization reaction was suppressed, whereas addition of the NaCl facilitated FA formation from fructose and HMF rehydration. In terms of humin formation direct fructose to humin degradation was facilitated with the NaCl addition, but glucose to humin conversion was successfully suppressed. Importantly fructose to HMF dehydration was significantly facilitated [63]. Preforming reaction kinetic modeling for biphasic systems, several factors should be accounted, such as miscibility of selected solvents, partition coefficients, and extraction rate. W. Guo et al. first developed a kinetic model for fructose/glucose dehydration by using sulfuric acid as a catalyst in aqueous media and later expanded it further

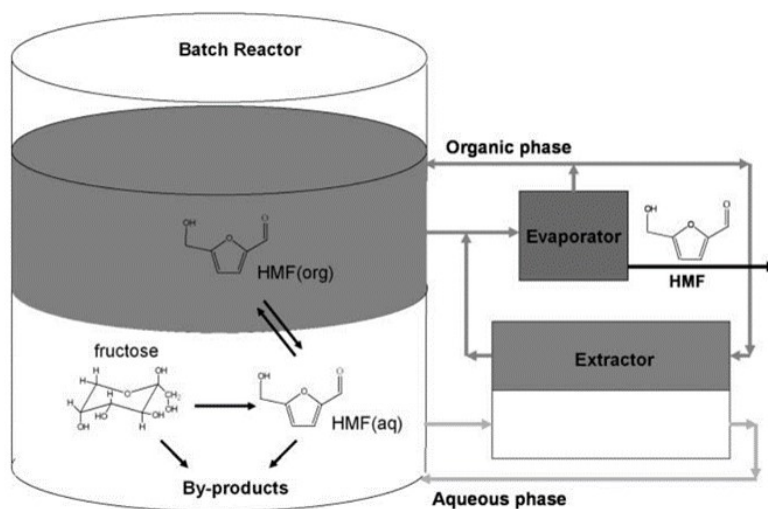


Figure 11: Fructose dehydration in biphasic system. Reprinted by [21].

to biphasic system of MIBK and water [44]. Recently authors have reported formation of insoluble humins (hydrochar) under microwave energy can increase the formation of humins and therefore by incorporating the HMF in their structure decrease its yield [119]. Eblagon et al. found severe humin formation at the temperature above 180 °C [120]. Similar was reported when studying production of HMF over HSO₃-ZSM-5 zeolite, where the mixture turn dark brown when temperature was increased over 150 °C [121].

10. Influence of initial feedstock and acid concentration on humin formation

Patil et al. reported humin formation from 5-HMF as a first order reaction; consequently higher amount of humins will be formed with 5-HMF higher concentration [30]. Van Zandvoort et al. ascribe the difference between glucose and fructose humin formation to higher yields of 5-HMF formed from fructose. With a systematic study it has been found that glucose concentration did not impact significant the humin formation, where temperature and to some extent also the acid concentration had more pronounce effect on the amount of humins formed via acid catalyzed dehydration reaction of glucose [26]. Tsilomelekis et al. have studied the impact of temperature and acid concentration on the growth kinetics, where increasing temperature and/or acid concentration resulted in higher growth rates [110]. Studying the humin growth kinetics, fructose concentration showed no affect the growth rate of humins (zero order), while opposite was observed for the initial concentration of 5-HMF [114]. Initial feedstock or substrate loading can due to the different reaction orders differently effect the formation of HMF, levulinic and formic acid and humins. Reaction of humin formation tend to be higher reaction order, due to the polymerization type of reaction [35]. Acidity can also affect formation of side products authors Körner et al. reported formation of acetic and lactic acid at higher pH, while levulinic

acid, 5-HMF and humins are more prone to form in more acidic conditions [122]. Studying the conversion of fructose in DMSO and water, the authors found no significant effect of organic acid (formic and levulinic acid) on the fructose conversion to 5-HMF, whereas relatively low presence of sulfuric acid can affect the conversion significantly [111]. Increased feedstock loading can lead to decreased furfural and HMF yield, where due to the previously proposed mechanisms furfural undergoes the fragmentation, resinification and cross-condensation and 5-HMF rehydrate further to levulinic and formic acid as well as polymerize in to unwanted huminic products [10, 123, 124, 125, 126]. To maximize the HMF yield it is important to start with the optimal concentration of initial substrate. Performing experiments varying a starting sugar concentration researchers reported a significant decrease of 5-HMF yield after exceeded optimal concentration due to the possible side reaction of humin formation [10, 106, 127, 128, 129, 130]. Sievers et al. confirmed that can presence of furanics in initial reaction mixture negatively impact final 5-HMF yield and result in increased amount of insoluble side products [131].

11. Catalyst deactivation in relation to humin formation

Regulation of humin formation is of significant importance especially when using heterogeneous catalysts [118]. Marzo et al. studied stability of niobic acid catalyst, where high acid density resulted in fast catalyst deactivation due to the humin deposition [34]. Catalyst ion doping decreased the acidity and increased long term catalyst activity. Humin formation can be promoted by both Lewis and Brønsted acid sites present on catalyst surface. Li et al. proposed that humin formation and rehydration to levulinic acid can be promoted by medium-to-strong Lewis acidity [132], while high amounts of Brønsted acid can facilitate aldol addition/condensation. Important parameter in solid catalyst is its structure and morphology. Recently a study using Fe/HY zeolite as a heterogeneous catalyst for a dehydration reaction discussed the impact of porosity on catalyst deactivation by humin deposits [94]. Time needed to deactivate catalyst was increasing with increased porosity up optimal value (0.2), while the further increase in catalyst porosity resulted in the glucose and 5-HMF diffusion in to the center of particle and earlier catalyst deactivation. 5-HMF yield and selectivity steadily decreased with increase in porosity. Due to the thermos-sensitivity higher temperatures lead to higher humin yield, and faster catalyst deactivation [94]. By adjusting acidic properties and porosity it is possible to limit humin formation. Despite the efforts of humin formation regulation, they are often an inevitable side product of sugar dehydration reaction, therefore there is still a need for a catalyst regeneration. Common methods refers to calcination [118] and catalyst washing, but authors have also discussed regeneration of catalyst under mild oxidation condition at low temperature of 70 °C, using Fenton's chemistry [133]. A technique showed promising results especially in removing the humin deposits, but unfortunately prior present acids sides could not be fully recovered.

12. Conclusion

Lignocellulosic biomass is an abundant feedstock, suitable for an industrial production of 5-HMF. Efficient 5-HMF synthesis requires pretreatment step, hydrolysis of polysaccharides and dehydration of individual sugar units, with additional glucose-fructose isomerization. Biomass composition is in this process of 5-HMF production one of the crucial factors, since can the presence of hemicelluloses and lignin severely affect the reaction kinetics. Additional steps are often necessary to optimize the process. Therefore, studies developing kinetic models using raw biomass as feedstock are of significant importance to obtain industrially transferable knowledge for the 5-HMF production. The major problem for inefficient lignocellulosic biomass utilization, can still be attributed to excessive humin formation. Based on the kinetic studies it can be concluded:

- Hydrolysis of cellulose and sugar humin formation on average required the largest activation energies, meaning these reactions will be facilitated at increased reaction temperatures, whereas lower temperatures and higher acid concentrations are favorable for higher selectivity towards levulinic acid. Therefore, the optimization of 5-HMF production appears to be more challenging.
- Most of the studies found that lignin and humins can significantly contribute and/or change the reaction kinetics, therefore several correction factors had to be employed for a better fit of the model.
- Suitable combination of reaction conditions, catalyst and solvent selection can considerably limit humin formation. Polar aprotic solvents and biphasic system were reported to be efficient in achieving high 5-HMF yield. Homogenous catalysts can be with the right acid concentration and temperature range be competently utilized for the dehydration into 5-HMF, whereas more environmentally friendly heterogeneous catalysts, can with the manipulation of Lewis and Brønsted acidity and porosity significantly improve 5-HMF yields.
- Several studies conducted the dehydration reaction using supercritical water as a catalyst, this could indicate a possible increased catalytic performance of other catalyst at higher temperatures and a potential impact on the calculated kinetic parameters.
- Considering the carbohydrate dehydration reaction pathway, formic and levulinic acid can be formed via rehydration of 5-HMF. Therefore in-situ formed organic acids (levulinic and formic acid) could with its catalytic activity influence the reported reaction kinetics.
- Researchers have been focusing on the mechanism of humin formation, proposing that the 5-HMF plays a key role in the reaction of condensation and or cross/self-polymerization. Literature does not agree on the involvement of partially dehydrated sugars or rehydration side products in the humin structure. Contradictory most of the kinetic studies are considering humin and/or side product formation directly from sugars, glucose and fructose, respectively.

References

- [1] S. Chakraborty, V. Aggarwal, D. Mukherjee, and K. Andras, "Biomass to biofuel: a review on production technology," *Asia-Pacific J. Chem. Eng.*, vol. 7, no. S3, pp. S254-S262, Aug. 2012, doi: <https://doi.org/10.1002/apj.1642>.
- [2] N. Tripathi, C. D. Hills, R. S. Singh, and C. J. Atkinson, "Biomass waste utilisation in low-carbon products: harnessing a major potential resource," *npj Clim. Atmos. Sci.*, vol. 2, no. 1, 2019, doi: [10.1038/s41612-019-0093-5](https://doi.org/10.1038/s41612-019-0093-5).
- [3] D. M. Alonso, J. Q. Bond, and J. A. Dumesic, "Catalytic conversion of biomass to biofuels," *Green Chem.*, vol. 12, no. 9, pp. 1493-1513, 2010, doi: [10.1039/c004654j](https://doi.org/10.1039/c004654j).
- [4] S. Laurichesse and L. Avérous, "Chemical modification of lignins: Towards biobased polymers," *Prog. Polym. Sci.*, vol. 39, no. 7, pp. 1266-1290, 2014, doi: [10.1016/j.progpolymsci.2013.11.004](https://doi.org/10.1016/j.progpolymsci.2013.11.004).
- [5] P. Daorattanachai, N. Viriya-empikul, N. Laosiripojana, and K. Faungnawakij, "Effects of Kraft lignin on hydrolysis/dehydration of sugars, cellulosic and lignocellulosic biomass under hot compressed water," *Bioresour. Technol.*, vol. 144, pp. 504-512, 2013, doi: <https://doi.org/10.1016/j.biortech.2013.06.124>.
- [6] F. Xu, J. Yu, T. Tesso, F. Dowell, and D. Wang, "Qualitative and quantitative analysis of lignocellulosic biomass using infrared techniques: A mini-review," *Appl. Energy*, vol. 104, pp. 801-809, 2013, doi: [10.1016/j.apenergy.2012.12.019](https://doi.org/10.1016/j.apenergy.2012.12.019).
- [7] N. Mosier *et al.*, "Features of promising technologies for pretreatment of lignocellulosic biomass," *Bioresour. Technol.*, vol. 96, no. 6, pp. 673-686, 2005, doi: [10.1016/j.biortech.2004.06.025](https://doi.org/10.1016/j.biortech.2004.06.025).
- [8] S. Kang, J. Fu, and G. Zhang, "From lignocellulosic biomass to levulinic acid: A review on acid-catalyzed hydrolysis," *Renew. Sustain. Energy Rev.*, vol. 94, no. March 2017, pp. 340-362, 2018, doi: [10.1016/j.rser.2018.06.016](https://doi.org/10.1016/j.rser.2018.06.016).
- [9] A. Chareonlimkun, V. Champreda, A. Shotipruk, and N. Laosiripojana, "Catalytic conversion of sugarcane bagasse, rice husk and corncob in the presence of TiO₂, ZrO₂ and mixed-oxide TiO₂-ZrO₂ under hot compressed water (HCW) condition," *Bioresour. Technol.*, vol. 101, no. 11, pp. 4179-4186, 2010, doi: [10.1016/j.biortech.2010.01.037](https://doi.org/10.1016/j.biortech.2010.01.037).
- [10] L. Zhang, G. Xi, J. Zhang, H. Yu, and X. Wang, "Efficient catalytic system for the direct transformation of lignocellulosic biomass to furfural and 5-hydroxymethylfurfural," *Bioresour. Technol.*, vol. 224, pp. 656-661, 2017, doi: [10.1016/j.biortech.2016.11.097](https://doi.org/10.1016/j.biortech.2016.11.097).
- [11] C. M. Cai, N. Nagane, R. Kumar, and C. E. Wyman, "Coupling metal halides with a co-solvent to produce furfural and 5-HMF at high yields directly from lignocellulosic biomass as an integrated biofuels strategy," *Green Chem.*, vol. 16, no. 8, pp. 3819-3829, 2014, doi: [10.1039/c4gc00747f](https://doi.org/10.1039/c4gc00747f).
- [12] C. L. Williams, T. L. Westover, R. M. Emerson, J. S. Tumuluru, and C. Li, "Sources of Biomass Feedstock Variability and the Potential Impact on Biofuels Production,"

Bioenergy Res., vol. 9, no. 1, pp. 1-14, 2016, doi: 10.1007/s12155-015-9694-y.

- [13] I. K. M. Yu and D. C. W. Tsang, "Conversion of biomass to hydroxymethylfurfural: A review of catalytic systems and underlying mechanisms," *Bioresour. Technol.*, vol. 238, pp. 716-732, 2017, doi: 10.1016/j.biortech.2017.04.026.
- [14] T. Wang, M. W. Nolte, and B. H. Shanks, "Catalytic dehydration of C6 carbohydrates for the production of hydroxymethylfurfural (HMF) as a versatile platform chemical," *Green Chem.*, vol. 16, no. 2, pp. 548-572, 2014, doi: 10.1039/c3gc41365a.
- [15] X. Zhang, K. Wilson, and A. F. Lee, "Heterogeneously Catalyzed Hydrothermal Processing of C5-C6 Sugars," *Chem. Rev.*, vol. 116, no. 19, pp. 12328-12368, Oct. 2016, doi: 10.1021/acs.chemrev.6b00311.
- [16] X. Zou, C. Zhu, Q. Wang, and G. Yang, "Catalytic dehydration of hexose sugars to 5-hydroxymethylfural," *Biofuels, Bioprod. Biorefining*, vol. 13, no. 1, pp. 153-173, 2019, doi: 10.1002/bbb.1932.
- [17] M. Dashtban, A. Gilbert, and P. Fatehi, "Recent advancements in the production of hydroxymethylfurfural," *RSC Adv.*, vol. 4, no. 4, pp. 2037-2050, 2014, doi: 10.1039/c3ra45396k.
- [18] G. Morales, J. A. Melero, M. Paniagua, J. Iglesias, B. Hernández, and M. Sanz, "Sulfonic acid heterogeneous catalysts for dehydration of C6-monosaccharides to 5-hydroxymethylfurfural in dimethyl sulfoxide," *Cuihua Xuebao/Chinese J. Catal.*, vol. 35, no. 5, pp. 644-655, 2014, doi: 10.1016/s1872-2067(14)60020-6.
- [19] M. Sajid, Y. Bai, D. Liu, and X. Zhao, "Organic acid catalyzed production of platform chemical 5-hydroxymethylfurfural from fructose: Process comparison and evaluation based on kinetic modeling," *Arab. J. Chem.*, vol. 13, no. 10, pp. 7430-7444, 2020, doi: 10.1016/j.arabjc.2020.08.019.
- [20] J. Li, W. Zhang, S. Xu, and C. Hu, "The Roles of H₂O/Tetrahydrofuran System in Lignocellulose Valorization," *Front. Chem.*, vol. 8, no. February, 2020, doi: 10.3389/fchem.2020.00070.
- [21] E. Nikolla, Y. Rom, M. Moliner, and M. E. Davis, "'One-Pot' Synthesis of 5-(Hydroxymethyl)furfural from Carbohydrates using Tin-Beta Zeolite," pp. 408-410, 2011.
- [22] F. Liang, D. Chen, H. Liu, W. Liu, M. Xian, and D. Feng, "One-Pot Synthesis of 5 - Hydroxymethylfurfural from Glucose by Brønsted Acid-Free Bifunctional Porous Coordination Polymers in Water," *ACS Omega*, vol. 4, pp. 9316-9323, 2019, doi: 10.1021/acsomega.9b00882.
- [23] Y. Román-Leshkov, J. N. Chheda, and J. A. Dumesic, "Phase Modifiers Promote Efficient Production of Hydroxymethylfurfural from Fructose," *Science (80-.)*, vol. 312, no. 5782, pp. 1933 LP - 1937, Jun. 2006, doi: 10.1126/science.1126337.
- [24] L. Zhu, X. Fu, Y. Hu, and C. Hu, "Controlling the Reaction Networks for Efficient Conversion of Glucose into 5-Hydroxymethylfurfural," *ChemSusChem*, vol. 13, no. 18, pp. 4812-4832, 2020, doi: 10.1002/cssc.202001341.
- [25] Z. Cheng, J. L. Everhart, G. Tsilomelekis, V. Nikolakis, B. Saha, and D. G. Vlachos,

- “Structural analysis of humins formed in the Brønsted acid catalyzed dehydration of fructose,” *Green Chem.*, vol. 20, no. 5, pp. 997-1006, 2018, doi: 10.1039/c7gc03054a.
- [26] I. Van Zandvoort *et al.*, “Formation, molecular structure, and morphology of humins in biomass conversion: Influence of feedstock and processing conditions,” *ChemSusChem*, vol. 6, no. 9, pp. 1745-1758, 2013, doi: 10.1002/cssc.201300332.
- [27] I. van Zandvoort, *Towards the Valorization of Humin By-products : Characterization , Solubilization and Catalysis*. 2015.
- [28] T. M. C. Hoang, L. Lefferts, and K. Seshan, “Valorization of humin-based byproducts from biomass processing - A route to sustainable hydrogen,” *ChemSusChem*, vol. 6, no. 9, pp. 1651-1658, 2013, doi: 10.1002/cssc.201300446.
- [29] I. Van Zandvoort, E. J. Koers, M. Weingarth, P. C. A. Bruijninx, M. Baldus, and B. M. Weckhuysen, “Structural characterization of ¹³C-enriched humins and alkali-treated ¹³C humins by 2D solid-state NMR,” *Green Chem.*, vol. 17, no. 8, pp. 4383-4392, 2015, doi: 10.1039/c5gc00327j.
- [30] S. K. R. Patil and C. R. F. Lund, “Formation and growth of humins via aldol addition and condensation during acid-catalyzed conversion of 5-hydroxymethylfurfural,” *Energy and Fuels*, vol. 25, no. 10, pp. 4745-4755, 2011, doi: 10.1021/ef2010157.
- [31] I. V. Sumerskii, S. M. Krutov, and M. Y. Zarubin, “Humin-Like substances formed under the conditions of industrial hydrolysis of wood,” *Russ. J. Appl. Chem.*, vol. 83, no. 2, pp. 320-327, 2010, doi: 10.1134/S1070427210020266.
- [32] D. M. Alonso, S. G. Wettstein, M. A. Mellmer, E. I. Gurbuz, and J. A. Dumesic, “Integrated conversion of hemicellulose and cellulose from lignocellulosic biomass,” *Energy Environ. Sci.*, vol. 6, no. 1, pp. 76-80, 2013, doi: 10.1039/c2ee23617f.
- [33] A. Toftgaard Pedersen, R. Ringborg, T. Grotkjær, S. Pedersen, and J. M. Woodley, “Synthesis of 5-hydroxymethylfurfural (HMF) by acid catalyzed dehydration of glucose-fructose mixtures,” *Chem. Eng. J.*, vol. 273, pp. 455-464, 2015, doi: 10.1016/j.cej.2015.03.094.
- [34] M. Marzo, A. Gervasini, and P. Carniti, “Improving stability of Nb₂O₅ catalyst in fructose dehydration reaction in water solvent by ion-doping,” *Catal. Today*, vol. 192, no. 1, pp. 89-95, 2012, doi: <https://doi.org/10.1016/j.cattod.2011.12.014>.
- [35] D. Jung, P. Körner, and A. Kruse, “Kinetic study on the impact of acidity and acid concentration on the formation of 5-hydroxymethylfurfural (HMF), humins, and levulinic acid in the hydrothermal conversion of fructose,” *Biomass Convers. Biorefinery*, 2019, doi: 10.1007/s13399-019-00507-0.
- [36] L. T. Mika, E. Cséfalvay, and Á. Németh, “Catalytic Conversion of Carbohydrates to Initial Platform Chemicals: Chemistry and Sustainability,” *Chem. Rev.*, vol. 118, no. 2, pp. 505-613, 2018, doi: 10.1021/acs.chemrev.7b00395.
- [37] B. Pomeroy and M. Grilc, “Catalyst structure-based hydroxymethylfurfural (HMF) hydrogenation mechanisms , activity and selectivity over Ni,” vol. 412, no. October 2020, 2021.
- [38] R. Karinen, K. Vilonen, and M. Niemelä, “Biorefining: Heterogeneously catalyzed

- reactions of carbohydrates for the production of furfural and hydroxymethylfurfural,” *ChemSusChem*, vol. 4, no. 8, pp. 1002-1016, 2011, doi: 10.1002/cssc.201000375.
- [39] M. A. Mellmer *et al.*, “Effects of chloride ions in acid-catalyzed biomass dehydration reactions in polar aprotic solvents,” *Nat. Commun.*, vol. 10, no. 1, pp. 1-10, 2019, doi: 10.1038/s41467-019-09090-4.
- [40] T. S. Hansen, J. M. Woodley, and A. Riisager, “Efficient microwave-assisted synthesis of 5-hydroxymethylfurfural from concentrated aqueous fructose,” *Carbohydr. Res.*, vol. 344, no. 18, pp. 2568-2572, 2009, doi: 10.1016/j.carres.2009.09.036.
- [41] B. A. Fachri, R. M. Abdilla, H. H. V. De Bovenkamp, C. B. Rasrendra, and H. J. Heeres, “Experimental and Kinetic Modeling Studies on the Sulfuric Acid Catalyzed Conversion of d -Fructose to 5-Hydroxymethylfurfural and Levulinic Acid in Water,” *ACS Sustain. Chem. Eng.*, vol. 3, no. 12, pp. 3024-3034, 2015, doi: 10.1021/acssuschemeng.5b00023.
- [42] B. Girisuta, L. P. B. M. Janssen, and H. J. Heeres, “GREEN CHEMICALS A Kinetic Study on the Conversion of Glucose to Levulinic Acid,” no. May, 2006, doi: 10.1205/cherd05038.
- [43] R. J. Van Putten *et al.*, “Dehydration of different ketoses and aldoses to 5-hydroxymethylfurfural,” *ChemSusChem*, vol. 6, no. 9, pp. 1681-1687, 2013, doi: 10.1002/cssc.201300345.
- [44] W. Guo, Z. Zhang, J. Hacking, H. J. Heeres, and J. Yue, “Selective fructose dehydration to 5-hydroxymethylfurfural from a fructose-glucose mixture over a sulfuric acid catalyst in a biphasic system: Experimental study and kinetic modelling,” *Chem. Eng. J.*, vol. 409, no. November 2020, p. 128182, 2021, doi: 10.1016/j.cej.2020.128182.
- [45] R. Weingarten, J. Cho, R. Xing, W. C. Conner, and G. W. Huber, “Kinetics and reaction engineering of levulinic acid production from aqueous glucose solutions,” *ChemSusChem*, vol. 5, no. 7, pp. 1280-1290, 2012, doi: 10.1002/cssc.201100717.
- [46] D. Garcés, E. Díaz, and S. Ordóñez, “Aqueous Phase Conversion of Hexoses into 5-Hydroxymethylfurfural and Levulinic Acid in the Presence of Hydrochloric Acid: Mechanism and Kinetics,” *Ind. Eng. Chem. Res.*, vol. 56, no. 18, pp. 5221-5230, 2017, doi: 10.1021/acs.iecr.7b00952.
- [47] T. D. Swift, C. Bagia, V. Choudhary, G. Peklaris, V. Nikolakis, and D. G. Vlachos, “Kinetics of homogeneous Brønsted acid catalyzed fructose dehydration and 5-hydroxymethyl furfural rehydration: A combined experimental and computational study,” *ACS Catal.*, vol. 4, no. 1, pp. 259-267, 2014, doi: 10.1021/cs4009495.
- [48] F. S. Asghari and H. Yoshida, “Kinetics of the decomposition of fructose catalyzed by hydrochloric acid in subcritical water: Formation of 5-hydroxymethylfurfural, levulinic, and formic acids,” *Ind. Eng. Chem. Res.*, vol. 46, no. 23, pp. 7703-7710, 2007, doi: 10.1021/ie061673e.
- [49] Y. Takeuchi, F. Jin, K. Tohji, and H. Enomoto, “Acid catalytic hydrothermal conversion of carbohydrate biomass into useful substances,” *J. Mater. Sci.*, vol. 43, no. 7, pp. 2472-2475, 2008, doi: 10.1007/s10853-007-2021-z.
- [50] K. Baugh and P. L. Mccarty, “Thermochemical Pretreatment of Lignocellulose to

- Enhance Methane Fermentation:,” 1986.
- [51] Q. JING and X. LÜ, “Kinetics of Non-catalyzed Decomposition of Glucose in High-temperature Liquid Water,” *Chinese J. Chem. Eng.*, vol. 16, no. 6, pp. 890-894, 2008, doi: 10.1016/S1004-9541(09)60012-4.
- [52] Y. Li, X. Lu, L. Yuan, and X. Liu, “Fructose decomposition kinetics in organic acids-enriched high temperature liquid water,” *Biomass and Bioenergy*, vol. 33, no. 9, pp. 1182-1187, 2009, doi: 10.1016/j.biombioe.2009.05.003.
- [53] Y. Yu and H. Wu, “Kinetics and mechanism of glucose decomposition in hot-compressed water: Effect of initial glucose concentration,” *Ind. Eng. Chem. Res.*, vol. 50, no. 18, pp. 10500-10508, 2011, doi: 10.1021/ie2011388.
- [54] M. Möller, F. Harnisch, and U. Schröder, “Microwave-assisted hydrothermal degradation of fructose and glucose in subcritical water,” *Biomass and Bioenergy*, vol. 39, no. 0, pp. 389-398, 2012, doi: 10.1016/j.biombioe.2012.01.036.
- [55] R. L. de Souza, H. Yu, F. Rataboul, and N. Essayem, “5-Hydroxymethylfurfural (5-HMF) Production from Hexoses: Limits of Heterogeneous Catalysis in Hydrothermal Conditions and Potential of Concentrated Aqueous Organic Acids as Reactive Solvent System,” *Challenges*, vol. 3, no. 2, pp. 212-232, 2012, doi: 10.3390/challe3020212.
- [56] K. Dussan, B. Girisuta, M. Lopes, J. J. Leahy, and M. H. B. Hayes, “Conversion of Hemicellulose Sugars Catalyzed by Formic Acid: Kinetics of the Dehydration of D-Xylose, L-Arabinose, and D-Glucose,” *ChemSusChem*, vol. 8, no. 8, pp. 1411-1428, Apr. 2015, doi: 10.1002/cssc.201403328.
- [57] B. Seemala, V. Haritos, and A. Tanksale, “Levulinic Acid as a Catalyst for the Production of 5-Hydroxymethylfurfural and Furfural from Lignocellulose Biomass,” *ChemCatChem*, vol. 8, no. 3, pp. 640-647, 2016, doi: 10.1002/cctc.201501105.
- [58] C. B. Rasrendra, J. N. M. Soetedjo, I. G. B. N. Makertihartha, S. Adisasmito, and H. J. Heeres, “The catalytic conversion of D-glucose to 5-hydroxymethylfurfural in DMSO using metal salts,” *Top. Catal.*, vol. 55, no. 7-10, pp. 543-549, 2012, doi: 10.1007/s11244-012-9826-y.
- [59] X. Zhang, B. B. Hewetson, and N. S. Mosier, “Kinetics of maleic acid and aluminum chloride catalyzed dehydration and degradation of glucose,” *Energy and Fuels*, vol. 29, no. 4, pp. 2387-2393, 2015, doi: 10.1021/ef502461s.
- [60] T. Wang, J. A. Glasper, and B. H. Shanks, “Kinetics of glucose dehydration catalyzed by homogeneous Lewis acidic metal salts in water,” *Appl. Catal. A Gen.*, vol. 498, pp. 214-221, 2015, doi: 10.1016/j.apcata.2015.03.037.
- [61] V. Choudhary, A. B. Pinar, R. F. Lobo, D. G. Vlachos, and S. I. Sandler, “Comparison of homogeneous and heterogeneous catalysts for glucose-to-fructose isomerization in aqueous media,” *ChemSusChem*, vol. 6, no. 12, pp. 2369-2376, 2013, doi: 10.1002/cssc.201300328.
- [62] J. M. Carraher, C. N. Fleitman, and J. P. Tessonnier, “Kinetic and mechanistic study of glucose isomerization using homogeneous organic brønsted base catalysts in water,” *ACS Catal.*, vol. 5, no. 6, pp. 3162-3173, 2015, doi: 10.1021/acscatal.5b00316.

- [63] J. Tang, L. Zhu, X. Fu, J. Dai, X. Guo, and C. Hu, "Insights into the Kinetics and Reaction Network of Aluminum Chloride-Catalyzed Conversion of Glucose in NaCl-H₂O/THF Biphasic System," *ACS Catal.*, vol. 7, no. 1, pp. 256-266, 2017, doi: 10.1021/acscatal.6b02515.
- [64] B. R. Caes, R. E. Teixeira, K. G. Knapp, and R. T. Raines, "Biomass to Furanics: Renewable Routes to Chemicals and Fuels," *ACS Sustain. Chem. Eng.*, vol. 3, no. 11, pp. 2591-2605, 2015, doi: 10.1021/acssuschemeng.5b00473.
- [65] R. Weingarten, G. A. Tompsett, W. C. Conner, and G. W. Huber, "Design of solid acid catalysts for aqueous-phase dehydration of carbohydrates: The role of Lewis and Brønsted acid sites," *J. Catal.*, vol. 279, no. 1, pp. 174-182, 2011, doi: 10.1016/j.jcat.2011.01.013.
- [66] S. Xu *et al.*, "Efficient conversion of glucose into 5-hydroxymethylfurfural using a bifunctional Fe³⁺ modified Amberlyst-15 catalyst," *Sustain. Energy Fuels*, vol. 3, no. 2, pp. 390-395, 2019, doi: 10.1039/c8se00499d.
- [67] N. A. S. Ramli and N. A. S. Amin, "Fe/HY zeolite as an effective catalyst for levulinic acid production from glucose: Characterization and catalytic performance," *Appl. Catal. B Environ.*, vol. 163, pp. 487-498, 2015, doi: 10.1016/j.apcatb.2014.08.031.
- [68] R. L. Johnson *et al.*, "Condensed Phase Deactivation of Solid Brønsted Acids in the Dehydration of Fructose to Hydroxymethylfurfural," *ACS Catal.*, vol. 9, no. 12, pp. 11568-11578, 2019, doi: 10.1021/acscatal.9b03455.
- [69] T. D. Swift, H. Nguyen, Z. Erdman, J. S. Kruger, V. Nikolakis, and D. G. Vlachos, "Tandem Lewis acid/Brønsted acid-catalyzed conversion of carbohydrates to 5-hydroxymethylfurfural using zeolite beta," *J. Catal.*, vol. 333, pp. 149-161, 2016, doi: 10.1016/j.jcat.2015.10.009.
- [70] I. Sádaba, M. López Granados, A. Riisager, and E. Taarning, "Deactivation of solid catalysts in liquid media: the case of leaching of active sites in biomass conversion reactions," *Green Chem.*, vol. 17, no. 8, pp. 4133-4145, 2015, doi: 10.1039/c5gc00804b.
- [71] J. S. Kruger, V. Nikolakis, and D. G. Vlachos, "Aqueous-phase fructose dehydration using Brønsted acid zeolites: Catalytic activity of dissolved aluminosilicate species," *Appl. Catal. A Gen.*, vol. 469, pp. 116-123, 2014, doi: 10.1016/j.apcata.2013.09.030.
- [72] C. Moreau *et al.*, "Dehydration of fructose to 5-hydroxymethylfurfural over H-mordenites," *Appl. Catal. A Gen.*, vol. 145, no. 1-2, pp. 211-224, 1996, doi: 10.1016/0926-860X(96)00136-6.
- [73] K. Lourvanij and G. L. Rorrer, "Reaction rates for the partial dehydration of glucose to organic acids in solid-acid, molecular-sieving catalyst powders," *J. Chem. Technol. Biotechnol.*, vol. 69, no. 1, pp. 35-44, 1997, doi: 10.1002/(SICI)1097-4660(199705)69:1<35::AID-JCTB685>3.0.CO;2-9.
- [74] J. S. Kruger, V. Nikolakis, and D. G. Vlachos, "Carbohydrate dehydration using porous catalysts," *Curr. Opin. Chem. Eng.*, vol. 1, no. 3, pp. 312-320, 2012, doi: 10.1016/j.coche.2012.06.003.
- [75] W. Wei and S. Wu, "Experimental and kinetic study of glucose conversion to levulinic

- acid in aqueous medium over Cr/HZSM-5 catalyst,” *Fuel*, vol. 225, no. April, pp. 311-321, 2018, doi: 10.1016/j.fuel.2018.03.120.
- [76] N. A. S. Ramli and N. A. S. Amin, “Kinetic study of glucose conversion to levulinic acid over Fe/HY zeolite catalyst,” *Chem. Eng. J.*, vol. 283, pp. 150-159, 2016, doi: 10.1016/j.cej.2015.07.044.
- [77] R. Bermejo-Deval *et al.*, “Metalloenzyme-like catalyzed isomerizations of sugars by Lewis acid zeolites,” *Proc. Natl. Acad. Sci. U. S. A.*, vol. 109, no. 25, pp. 9727-9732, 2012, doi: 10.1073/pnas.1206708109.
- [78] E. Sairanen, R. Karinen, and J. Lehtonen, “Comparison of solid acid-catalyzed and autocatalyzed C5 and C6 sugar dehydration reactions with water as a solvent,” *Catal. Letters*, vol. 144, no. 11, pp. 1839-1850, 2014, doi: 10.1007/s10562-014-1350-1.
- [79] P. Carniti, A. Gervasini, S. Biella, and A. Auroux, “Niobic acid and niobium phosphate as highly acidic viable catalysts in aqueous medium: Fructose dehydration reaction,” *Catal. Today*, vol. 118, no. 3-4 SPEC. ISS., pp. 373-378, 2006, doi: 10.1016/j.cattod.2006.07.024.
- [80] C. E. Bounoukta *et al.*, “Dehydration of glucose to 5-Hydroxymethylfurfural on bifunctional carbon catalysts,” *Appl. Catal. B Environ.*, vol. 286, no. December 2020, p. 119938, 2021, doi: 10.1016/j.apcatb.2021.119938.
- [81] J. F. Saeman, “Kinetics of Wood Saccharification - Hydrolysis of Cellulose and Decomposition of Sugars in Dilute Acid at High Temperature,” *Ind. Eng. Chem.*, vol. 37, no. 1, pp. 43-52, 1945, doi: 10.1021/ie50421a009.
- [82] B. Girisuta, L. P. B. M. Janssen, and H. J. Heeres, “Kinetic study on the acid-catalyzed hydrolysis of cellulose to levulinic acid,” *Ind. Eng. Chem. Res.*, vol. 46, no. 6, pp. 1696-1708, 2007, doi: 10.1021/ie061186z.
- [83] B. Girisuta, B. Danon, R. Manurung, L. P. B. M. Janssen, and H. J. Heeres, “Experimental and kinetic modelling studies on the acid-catalysed hydrolysis of the water hyacinth plant to levulinic acid,” *Bioresour. Technol.*, vol. 99, no. 17, pp. 8367-8375, 2008, doi: 10.1016/j.biortech.2008.02.045.
- [84] S. Rivas, M. J. González-Muñoz, C. Vila, V. Santos, and J. C. Parajó, “Manufacture of levulinic acid from pine wood hemicelluloses: A kinetic assessment,” *Ind. Eng. Chem. Res.*, vol. 52, no. 11, pp. 3951-3957, 2013, doi: 10.1021/ie3018725.
- [85] S. Rivas, M. J. González-Muñoz, V. Santos, and J. C. Parajó, “Acidic processing of hemicellulosic saccharides from pine wood: Product distribution and kinetic modeling,” *Bioresour. Technol.*, vol. 162, pp. 192-199, 2014, doi: 10.1016/j.biortech.2014.03.150.
- [86] B. Girisuta, K. Dussan, D. Haverty, J. J. Leahy, and M. H. B. Hayes, “A kinetic study of acid catalysed hydrolysis of sugar cane bagasse to levulinic acid,” *Chem. Eng. J.*, vol. 217, pp. 61-70, 2013, doi: 10.1016/j.cej.2012.11.094.
- [87] J. Shen and C. E. Wyman, “Hydrochloric Acid-Catalyzed Levulinic Acid Formation from Cellulose : Data and Kinetic Model to Maximize Yields,” vol. 58, no. 1, 2012, doi: 10.1002/aic.
- [88] M. S. R. dos Santos Rocha, B. Pratto, R. de Sousa, R. M. R. G. Almeida, and A. J. G.

- da Cruz, "A kinetic model for hydrothermal pretreatment of sugarcane straw," *Bioresour. Technol.*, vol. 228, pp. 176-185, 2017, doi: 10.1016/j.biortech.2016.12.087.
- [89] L. Vanoye, M. Fanselow, J. D. Holbrey, M. P. Atkins, and K. R. Seddon, "Kinetic model for the hydrolysis of lignocellulosic biomass in the ionic liquid, 1-ethyl-3-methylimidazolium chloride," *Green Chem.*, vol. 11, no. 3, pp. 390-39, 2009, doi: 10.1039/b817882h.
- [90] J. Köchermann, J. Mühlenberg, and M. Klemm, "Kinetics of Hydrothermal Furfural Production from Organosolv Hemicellulose and d -Xylose," *Ind. Eng. Chem. Res.*, vol. 57, no. 43, pp. 14417-14427, 2018, doi: 10.1021/acs.iecr.8b03402.
- [91] V. A. Online, "An improved kinetic model for cellulose hydrolysis to 5-hydroxymethylfurfural using the solid SO₄²⁻/Ti-MCM-41 catalyst," pp. 15216-15224, 2014, doi: 10.1039/c4ra00167b.
- [92] N. V. Gromov, O. P. Taran, C. Aymonier, and V. N. Parmon, "Kinetic modeling of the multistep hydrolysis-dehydration of cellulose to platform molecules over a solid carbon acid catalyst in pure water," *React. Kinet. Mech. Catal.*, vol. 130, no. 2, pp. 669-684, 2020, doi: 10.1007/s11144-020-01814-8.
- [93] C.-W. Jiang, X. Zhong, and Z.-H. Luo, "An improved kinetic model for cellulose hydrolysis to 5-hydroxymethylfurfural using the solid SO₄²⁻/Ti-MCM-41 catalyst," *RSC Adv.*, vol. 4, no. 29, pp. 15216-15224, 2014, doi: 10.1039/C4RA00167B.
- [94] S. Liu *et al.*, "Coking Prediction in Catalytic Glucose Conversion to Levulinic Acid Using Improved Lattice Boltzmann Model," *Ind. Eng. Chem. Res.*, vol. 59, no. 39, pp. 17462-17475, 2020, doi: 10.1021/acs.iecr.0c03635.
- [95] L. Atanda, M. Konarova, Q. Ma, S. Mukundan, A. Shrotri, and J. Beltramini, "High yield conversion of cellulosic biomass into 5-hydroxymethylfurfural and a study of the reaction kinetics of cellulose to HMF conversion in a biphasic system," *Catal. Sci. Technol.*, 2016, doi: 10.1039/C6CY00820H.
- [96] Q. Qing, Q. Guo, P. Wang, H. Qian, X. Gao, and Y. Zhang, "Kinetics study of levulinic acid production from corncobs by tin tetrachloride as catalyst," *Bioresour. Technol.*, vol. 260, no. January, pp. 150-156, 2018, doi: 10.1016/j.biortech.2018.03.073.
- [97] P. Bhaumik, A. K. Deepa, T. Kane, and P. L. Dhepe, "Value addition to lignocellulosics and biomass-derived sugars: An insight into solid acid-based catalytic methods," *J. Chem. Sci.*, vol. 126, no. 2, pp. 373-385, 2014, doi: 10.1007/s12039-014-0574-3.
- [98] Q. Xiang, J. S. Kiim, and Y. Y. Lee, "A Comprehensive Kinetic Model for Dilute-Acid Hydrolysis of Cellulose," *Appl. Biochem. Biotechnol.*, vol. 105, no. 1, pp. 337-352, 2003.
- [99] Q. Xiang, Y. Y. Lee, and R. W. Torget, "Kinetics of glucose decomposition during dilute-acid hydrolysis of lignocellulosic biomass," *Appl. Biochem. Biotechnol. - Part A Enzym. Eng. Biotechnol.*, vol. 115, no. 1-3, pp. 1127-1138, 2004, doi: 10.1385/ABAB:115:1-3:1127.
- [100] L. Yan, A. A. Greenwood, A. Hossain, and B. Yang, "A comprehensive mechanistic kinetic model for dilute acid hydrolysis of switchgrass cellulose to glucose, 5-HMF and

- levulinic acid,” *RSC Adv.*, vol. 4, no. 45, pp. 23492-23504, 2014, doi: 10.1039/C4RA01631A.
- [101] O. Yemiş and G. Mazza, “Acid-catalyzed conversion of xylose, xylan and straw into furfural by microwave-assisted reaction,” *Bioresour. Technol.*, vol. 102, no. 15, pp. 7371-7378, 2011, doi: 10.1016/j.biortech.2011.04.050.
- [102] K. Lamminpää, J. Ahola, and J. Tanskanen, “Acid-catalysed xylose dehydration into furfural in the presence of kraft lignin,” *Bioresour. Technol.*, vol. 177, pp. 94-101, 2015, doi: <https://doi.org/10.1016/j.biortech.2014.11.074>.
- [103] G. R. Gomes, D. S. Rampon, and L. P. Ramos, “Production of furan compounds from sugarcane bagasse using a catalytic system containing ZnCl₂/HCl or AlCl₃/HCl in a biphasic system,” *J. Braz. Chem. Soc.*, vol. 29, no. 5, pp. 1115-1122, 2018, doi: 10.21577/0103-5053.20180014.
- [104] A. L. Jongerius *et al.*, “Stability of Pt/γ-Al₂O₃ catalysts in lignin and lignin model compound solutions under liquid phase reforming reaction conditions,” *ACS Catal.*, vol. 3, no. 3, pp. 464-473, 2013, doi: 10.1021/cs300684y.
- [105] K. Dussan, B. Girisuta, M. Lopes, J. J. Leahy, and M. H. B. Hayes, “Effects of Soluble Lignin on the Formic Acid-Catalyzed Formation of Furfural: A Case Study for the Upgrading of Hemicellulose,” *ChemSusChem*, vol. 9, no. 5, pp. 492-504, Mar. 2016, doi: 10.1002/cssc.201501415.
- [106] L. Liu, H. Chang, H. Jameel, J.-Y. Park, and S. Park, “Catalytic Conversion of Biomass Hydrolysate into 5-Hydroxymethylfurfural,” *Ind. Eng. Chem. Res.*, vol. 56, no. 49, pp. 14447-14453, Dec. 2017, doi: 10.1021/acs.iecr.7b03635.
- [107] J. B. Binder and R. T. Raines, “Simple chemical transformation of lignocellulosic biomass into furans for fuels and chemicals,” *J. Am. Chem. Soc.*, vol. 131, no. 5, pp. 1979-1985, 2009, doi: 10.1021/ja808537j.
- [108] J. Horvat, B. Klaić, B. Metelko, and V. Sunjic, “Mechanism of levulinic acid formation in acid catalyzed hydrolysis of 2-(hydroxymethyl)furan and 5-(hydroxymethyl)-2-furancarboxaldehyde,” *Croat. Chem. Acta*, vol. 59, no. Copyright (C) 2015 American Chemical Society (ACS). All Rights Reserved., pp. 429-438, 1986.
- [109] S. K. R. Patil, J. Heltzel, and C. R. F. Lund, “Comparison of structural features of humins formed catalytically from glucose, fructose, and 5-hydroxymethylfurfuraldehyde,” *Energy and Fuels*, vol. 26, no. 8, pp. 5281-5293, 2012, doi: 10.1021/ef3007454.
- [110] G. Tsilomelekis *et al.*, “Molecular structure, morphology and growth mechanisms and rates of 5-hydroxymethyl furfural (HMF) derived humins,” *Green Chem.*, vol. 18, no. 7, pp. 1983-1993, 2016, doi: 10.1039/c5gc01938a.
- [111] M. R. Whitaker, A. Parulkar, P. Ranadive, R. Joshi, and N. A. Brunelli, “Examining Acid Formation During the Selective Dehydration of Fructose to 5-Hydroxymethylfurfural in Dimethyl Sulfoxide and Water,” *ChemSusChem*, vol. 12, no. 10, pp. 2211-2219, 2019, doi: 10.1002/cssc.201803013.
- [112] V. Maruani, S. Narayanin-Richenapin, E. Framery, and B. Andrioletti, “Acidic Hydrothermal Dehydration of d -Glucose into Humins: Identification and

- Characterization of Intermediates,” *ACS Sustain. Chem. Eng.*, vol. 6, no. 10, pp. 13487-13493, 2018, doi: 10.1021/acssuschemeng.8b03479.
- [113] X. Fu, J. Dai, X. Guo, J. Tang, L. Zhu, and C. Hu, “Suppression of oligomer formation in glucose dehydration by CO₂ and tetrahydrofuran,” *Green Chem.*, vol. 19, no. 14, pp. 3334-3343, 2017, doi: 10.1039/c7gc01115f.
- [114] Z. Cheng, K. A. Goulas, N. Quiroz Rodriguez, B. Saha, and D. G. Vlachos, “Growth kinetics of humins studied: Via X-ray scattering,” *Green Chem.*, vol. 22, no. 7, pp. 2301-2309, 2020, doi: 10.1039/c9gc03961a.
- [115] X. Fu *et al.*, “Solvent Effects on Degradative Condensation Side Reactions of Fructose in Its Initial Conversion to 5-Hydroxymethylfurfural,” *ChemSusChem*, pp. 501-512, 2019, doi: 10.1002/cssc.201902309.
- [116] V. Vasudevan and S. H. Mushrif, “Insights into the solvation of glucose in water, dimethyl sulfoxide (DMSO), tetrahydrofuran (THF) and N,N-dimethylformamide (DMF) and its possible implications on the conversion of glucose to platform chemicals,” *RSC Adv.*, vol. 5, no. 27, pp. 20756-20763, 2015, doi: 10.1039/c4ra15123b.
- [117] A. S. Amarasekara, L. T. D. Williams, and C. C. Ebede, “Mechanism of the dehydration of d-fructose to 5-hydroxymethylfurfural in dimethyl sulfoxide at 150 °C: an NMR study,” *Carbohydr. Res.*, vol. 343, no. 18, pp. 3021-3024, 2008, doi: 10.1016/j.carres.2008.09.008.
- [118] J. Zhang, L. Lin, and S. Liu, “Efficient production of furan derivatives from a sugar mixture by catalytic process,” *Energy and Fuels*, vol. 26, no. 7, pp. 4560-4567, 2012, doi: 10.1021/ef300606v.
- [119] Y. Shao *et al.*, “The formation of 5-hydroxymethylfurfural and hydrochar during the valorization of biomass using a microwave hydrothermal method,” *Sci. Total Environ.*, vol. 755, p. 142499, 2021, doi: 10.1016/j.scitotenv.2020.142499.
- [120] K. M. Eblagon, A. Malaika, K. Ptaszynska, M. F. R. Pereira, and J. L. Figueiredo, “Impact of thermal treatment of nb2 o5 on its performance in glucose dehydration to 5-hydroxymethylfurfural in water,” *Nanomaterials*, vol. 10, no. 9, pp. 1-24, 2020, doi: 10.3390/nano10091685.
- [121] P. H. Hoang, N. M. Dat, T. D. Cuong, and D. T. Tung, “Production of 5-hydroxymethylfurfural (HMF) from rice-straw biomass using a HSO₃-ZSM-5 zeolite catalyst under assistance of sonication,” *RSC Adv.*, vol. 10, no. 23, pp. 13489-13495, 2020, doi: 10.1039/d0ra02037k.
- [122] P. Körner, D. Jung, and A. Kruse, “Influence of the pH Value on the Hydrothermal Degradation of Fructose,” *ChemistryOpen*, vol. 8, no. 8, pp. 1121-1132, 2019, doi: 10.1002/open.201900225.
- [123] A. S. Dias, M. Pillinger, and A. A. Valente, “Mesoporous silica-supported 12-tungstophosphoric acid catalysts for the liquid phase dehydration of d-xylose,” *Microporous Mesoporous Mater.*, vol. 94, no. 1-3, pp. 214-225, 2006, doi: 10.1016/j.micromeso.2006.03.035.
- [124] M. J. Antal, T. Leesomboon, W. S. Mok, and G. N. Richards, “Mechanism of formation

- of 2-furaldehyde from d-xylose,” *Carbohydr. Res.*, vol. 217, pp. 71-85, 1991, doi: [https://doi.org/10.1016/0008-6215\(91\)84118-X](https://doi.org/10.1016/0008-6215(91)84118-X).
- [125] L. Qi, Y. F. Mui, S. W. Lo, M. Y. Lui, G. R. Akién, and I. T. Horváth, “Catalytic conversion of fructose, glucose, and sucrose to 5-(hydroxymethyl)furfural and levulinic and formic acids in γ -valerolactone as a green solvent,” *ACS Catal.*, vol. 4, no. 5, pp. 1470-1477, 2014, doi: 10.1021/cs401160y.
- [126] F. N. D. C. Gomes, L. R. Pereira, N. F. P. Ribeiro, and M. M. V. M. Souza, “PRODUCTION OF 5-HYDROXYMETHYLFURFURAL (HMF) VIA FRUCTOSE DEHYDRATION: EFFECT OF SOLVENT AND SALTING-OUT,” *Brazilian J. Chem. Eng.*, vol. 32, pp. 119-126, 2015, [Online]. Available: http://www.scielo.br/scielo.php?script=sci_arttext&pid=S0104-66322015000100119&nrm=iso.
- [127] X. Li, Y. Wang, X. Xie, C. Huang, and S. Yang, “Dehydration of fructose, sucrose and inulin to 5-hydroxymethylfurfural over yeast-derived carbonaceous microspheres at low temperatures,” *RSC Adv.*, vol. 9, no. 16, pp. 9041-9048, 2019, doi: 10.1039/C8RA10465D.
- [128] Y. Ma, L. Wang, H. Li, T. Wang, and R. Zhang, “Selective Dehydration of Glucose into 5-Hydroxymethylfurfural by Ionic Liquid-ZrOC12 in Isopropanol,” *Catalysts*, vol. 8, no. 10, p. 467, Oct. 2018, doi: 10.3390/catal8100467.
- [129] Q. Hou *et al.*, “An ionic liquid-organic solvent biphasic system for efficient production of 5-hydroxymethylfurfural from carbohydrates at high concentrations,” *RSC Adv.*, vol. 7, no. 75, pp. 47288-47296, 2017, doi: 10.1039/C7RA10237B.
- [130] L. Liu, X. Yang, Q. Hou, S. Zhang, and M. Ju, “Corn stalk conversion into 5-hydroxymethylfurfural by modified biochar catalysis in a multi-functional solvent,” *J. Clean. Prod.*, vol. 187, pp. 380-389, 2018, doi: 10.1016/j.jclepro.2018.03.234.
- [131] C. Sievers, I. Musin, T. Marzalletti, M. B. V. Olarte, P. K. Agrawal, and C. W. Jones, “Acid-catalyzed conversion of sugars and furfurals in an ionic-liquid phase,” *ChemSusChem*, vol. 2, no. 7, pp. 665-671, 2009, doi: 10.1002/cssc.200900092.
- [132] X. Li, K. Peng, X. Liu, Q. Xia, and Y. Wang, “Comprehensive Understanding of the Role of Brønsted and Lewis Acid Sites in Glucose Conversion into 5-Hydroxymethylfurfural,” *ChemCatChem*, vol. 9, no. 14, pp. 2739-2746, 2017, doi: 10.1002/cctc.201601203.
- [133] I. Agirrezabal-Telleria, N. Miletić, and P. L. Arias, “Regeneration of surface acid sites via mild oxidation on dehydration catalysts,” *Catal. Sci. Technol.*, vol. 6, no. 10, pp. 3367-3370, 2016, doi: 10.1039/C6CY00510A.

Recent advances in understanding dissolution of iridium-based catalysts for oxygen evolution reaction

Anja Lončar

University of Nova Gorica, Vipavska 13, SI-5000 Nova Gorica

National Institute of Chemistry, Hajdrihova 19, SI-1001 Ljubljana

Abstract

Widespread utilization of proton exchange membrane (PEM) electrolyzers is currently still uncertain, as it inevitably relies on the use of highly scarce iridium as the only viable catalyst for oxygen evolution reaction (OER), which is known to present the major energy losses of the process. The understanding of the origin of different stabilities of Ir-based catalysts is therefore crucial. It is known that structure importantly influences the dissolution, which is the main degradation mechanism and shares common intermediates with the OER. In this minireview, the state-of-the-art understanding of the dissolution phenomenon and its relationship with the structure of different iridium catalysts is gathered and correlated to different mechanisms of OER. In conclusion, the perspective on future investigation directions is presented.

Keywords: oxygen evolution reaction, iridium, dissolution

1. Introduction

Increasing interest in renewable energy sources, following the policies aiming to limit the anthropogenic changes of the climate, demands the development of innovative technologies that would mitigate the intermittence of solar and wind energy. Storing excessive energy in the form of chemical bonds, specifically as hydrogen, is currently seen as one of the best options, which can be confirmed by the increasing number of electrolyzer installations [1]. However, the efficient scale-up of this technology is currently still hindered by the low efficiency, arising predominantly from the sluggish kinetics of anodic oxygen evolution reaction (OER) and the high cost of materials that are able to resist the harsh, acidic conditions in the proton exchange membrane (PEM) electrolyzers. The material of choice for the OER catalysis is iridium, as it is the only metal that combines both sufficient stability and relatively high activity [2, 3]. To improve the performance of catalysts, the fundamental understanding of mechanisms, driving the reaction, is of great importance.

Email address: anja.loncar@student.ung.si (Anja Lončar)

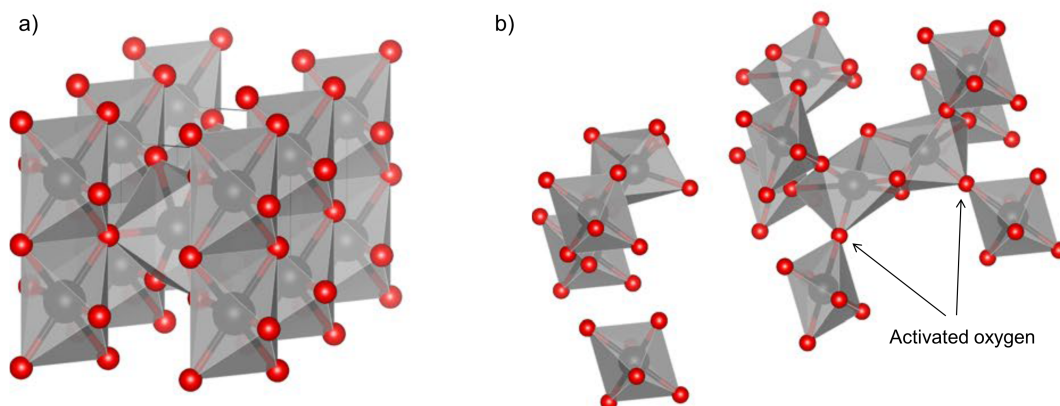


Figure 1: Structure of Ir-based catalysts: a) stable crystalline rutile IrO₂ with edge-sharing octahedra and b) less ordered amorphous oxide IrO_x. Gaps in amorphous oxide are filled with intercalated water molecules. Corner-sharing oxygen atoms, labelled as activated oxygen, can participate in the OER and thus accelerate the reaction [10].

The beginning of systematic studies on the OER mechanism on different noble metals goes back to the 50s, when the first kinetic studies were published [4]. The reaction has gained increasing interest since then, especially recently, when it is also exhibiting a widespread application potential. Mechanistic studies revealed various possible reaction pathways, which lead to different activity and stability of the Ir catalysts. The focus of the investigations on the Ir catalytic properties has only recently slowly shifted from the activity towards stability [5]. In this regard, the dissolution of active material is acknowledged as one of the predominant degradation mechanisms. Understanding of dissolution kinetics has advanced with the development of experimental techniques which combine electrochemical measurements with on-line detection of dissolved species, namely scanning flow cell connected to inductively coupled plasma mass spectrometer (SFC-ICP-MS) [6]. The dissolution kinetics are affected by both electrochemical parameters and physico-chemical properties of the catalytic material (its structure, etc). Specifically, in the case of iridium, less active crystalline rutile, with edge-sharing octahedra, IrO₂ (Figure 1a), is known to be stable under OER conditions, whereas its amorphous analogues with more corner-sharing octahedra with under-coordinated oxygen atoms and in the gaps intercalated water molecules (Figure 1b) exhibit higher activity for oxygen evolution, but also lower stability. Based on the dissolution studies, it is now generally accepted that OER and dissolution mechanisms are intertwined, either through a common intermediate [7] or via formation of oxygen from the oxide lattice [8, 9], which leads to destabilization of the structure and resulting dissolution.

This minireview aims to gather the state-of-the-art understanding of the dissolution mechanisms and their correlation to the OER. Special focus is given on the effect of the

structure of different Ir-based catalysts on both activity and stability. The summary of the latest literature is concluded with the perspective on the future challenges of the topic and strategies to overcome them.

2. Mechanism of Oxygen Evolution Reaction on Ir-based catalysts

OER is a complex electrochemical reaction involving four electron and proton transfers and at least two reaction intermediates [11]. First experimental studies on OER of different noble metals concluded that OER on iridium occurs via electrochemical oxide path [12], which was previously suggested by Bockris [4]. Since then, many studies tackled this problem, each using a different approach. Besides the mentioned classical electrochemical studies, based on Tafel analysis, they can be grouped into four additional categories:

1. X-ray photoemission and absorption spectroscopy (XPS, XAS) studies determining the oxidation state of the catalyst during the catalytic cycle [13, 14, 15, 16],
2. studies using spectroscopic methods (Raman, Infrared (IR) spectroscopy) aiming to detect reaction intermediates on the surface of the catalyst [17, 18, 19],
3. theoretical studies using density functional theory (DFT) calculations, microkinetics, molecular dynamics [20, 21, 22],
4. studies detecting reaction products and dissolved species [7, 23, 24].

Kötz et al. published one of the first ex-situ XPS studies of IrO₂ films and based on the constant ratio between oxygen and iridium at all studied potentials proposed a cationic catalytic cycle, following electrochemical oxide path, where iridium is oxidized to IrO₃ intermediate and is in the following reaction step reduced back to Ir^{IV} with a simultaneous release of oxygen molecule [25]. More recent in-situ XPS [13] and XAS [14] studies on iridium oxide nanoparticles and hydrated iridium oxide films, respectively have however on the contrary suggested Ir^V-Ir^{III} transition, with the presence of both oxidation states under OER conditions [14]. This mechanism was further confirmed by Sivasankar et al. who detected for the first time Ir-OOH intermediate using FT-IR spectroscopy by probing iridium oxide nanoclusters [17]. Cationic redox processes on which these studies were based have traditionally been thought to be the main source of charge storage. This view was challenged by the discovery of anion driven capacity storage in Li-ion battery technology [26, 27]. The idea of an anionic redox mechanism was soon applied to the field of electrocatalysis. Thermodynamic considerations proved that any metal oxide must become unstable under oxygen evolution conditions and the reason for that was found to be the instability of oxygen anion in the metal oxide lattice [9]. In another study, it was demonstrated that shifting the oxygen p-band closer to the Fermi level can trigger the redox activity of the lattice oxygen [28]. Anionic redox mechanism can exist in metal oxides with a highly covalent network. Activation of the oxygen ligand occurs if the transition metal's d-band penetrates the ligand's p-band. In that case, electrons from the oxygen's p-band are poured into the metal's d-band which leaves behind holes, that can be eventually attacked by water molecules and form peroxo species (Figure 2). Anionic redox

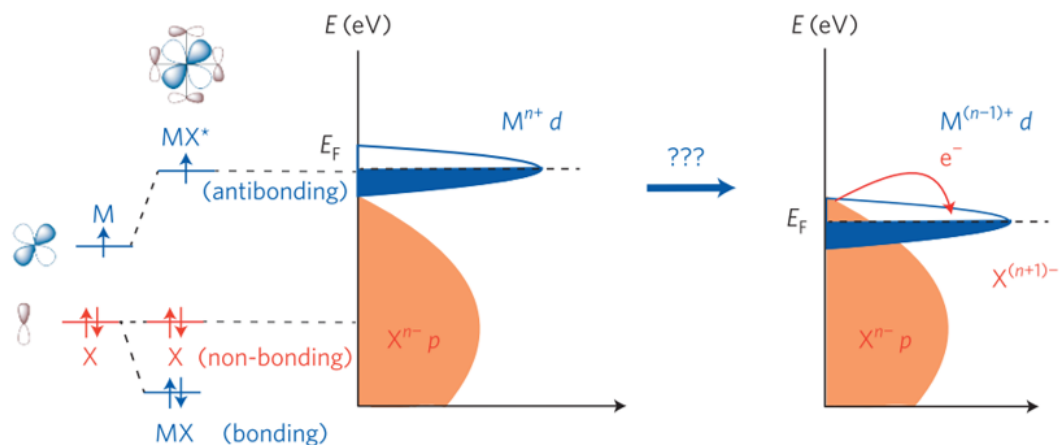


Figure 2: Activation of oxygen ligand for anionic redox mechanism in a highly covalent network. Here, the cationic d band penetrates the ligand's p band, which leads to the formation of holes, prone to the nucleophilic attack of water [31].

mechanism was experimentally confirmed in different studies [16, 29, 30]. Using near ambient pressure (NAP)-XPS and XAS, combined with *ab initio* calculations, Saveleva et al. aimed to reveal a universal mechanism by studying two different Ir-based catalysts, thermally oxidized IrO_2 and electrochemical amorphous iridium oxide nanoparticles [16]. The authors concluded that anionic lattice oxygen involvement in OER is operative on both, structurally rigid rutile and more flexible IrO_x nanoparticles and further questioned the possible presence of Ir in oxidation states above 4+.

The focus of the above-mentioned studies was on the operating OER mechanisms, however, none of them related them to the possible instability related issues. Only recently, a few papers, correlating different reaction mechanisms with the possible dissolution pathways, were published. These studies will be discussed below.

3. Mechanistic understanding of Ir dissolution under OER

One of the first dissolution studies comparing different noble metals, using then newly developed scanning flow cell (SFC) coupled to the inductively coupled plasma mass spectrometer (ICP-MS), showed that dissolution of all studied metals increases with the acceleration of OER, which directly interconnects activity and stability of OER catalysts [2]. The extent of dissolution was however very different, depending on the nature of the investigated metals. While OER did not significantly affect the dissolution of platinum, ruthenium, which is known to be among the most active catalysts for OER, displayed approximately three orders of magnitude higher dissolution. Iridium was found to have an

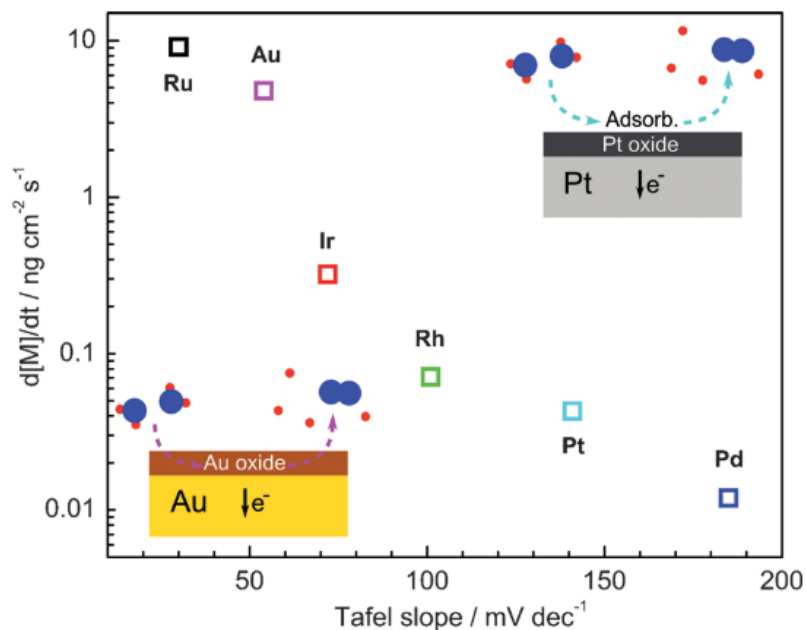


Figure 3: Correlation between stability of catalyst with Tafel slope and operating OER mechanism [2].

intermediate response, both in activity and stability. The authors have shown that stability can be estimated based on the Tafel slopes, which indicate different operating OER mechanisms. On the metals with high Tafel slope, such as platinum, OER is expected to go through an adsorbate route, which does not involve the participation of oxide lattice in the reaction and does not disturb the surface of catalysts, while on the contrary, on metals with lower Tafel slope, OER involves the participation of thick oxide layer, which results in its destabilization and higher dissolution of catalyst (Figure 3).

Dissolution of different iridium oxides was further tested to conclude which parameters render the improved stability of different oxides. It was shown that thermal treatment of either chemically [32] or electrochemically [33] prepared iridium oxides resulted in improved stability and decreased activity. The decrease in activity was explained by the changing of the stoichiometry of oxide with the initiated crystallization, which also leads to the lowering of accessible active sites and hindered ion insertion and mass transport due to the loss of hydration. They observed some discrepancies in the stabilization effect of different annealing temperatures. Interestingly, oxides, heat-treated between 100 and 300 °C exhibited lower both activity and stability. This was explained by the reduced hydration and conductivity, caused by the incomplete crystallization. Additionally, the formation of mixed oxide phase with the co-existence of both crystalline and amorphous phase, was recognized as the origin of the increased dissolution of iridium, as presence of conductive

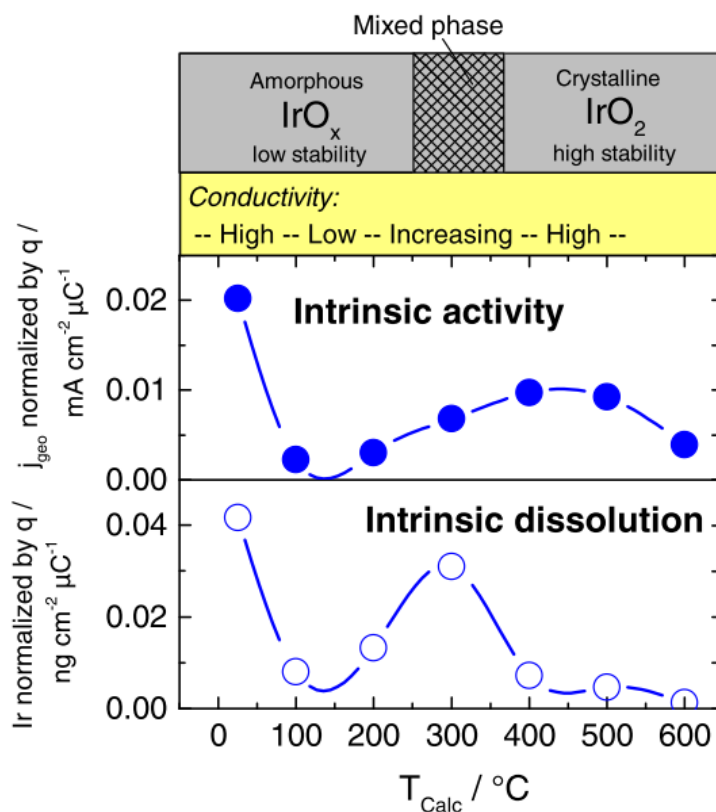
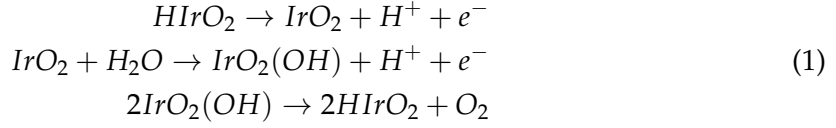


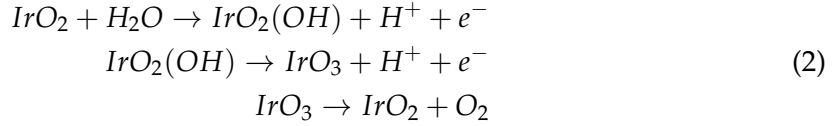
Figure 4: Effect of thermal treatment of hydrous iridium oxide films on their intrinsic activity and stability, obtained by normalization of current and dissolution rate by charge, which gives a rough estimation of the catalytically active surface area [33].

crystalline phase enhanced the dissolution of amorphous oxide. Further increase of the annealing temperature led to a complete crystallization, and thus to improved stability and lower activity (Figure 4). The effect of different crystal structures was further shown in a study investigating the activity and stability of iridium and ruthenium and their oxides [34].

A series of systematic examinations of dissolution of both bare metallic iridium disk and electrochemically grown iridium oxide were published the same year, aiming to further elucidate the dissolution of iridium in a broader potential range [35, 24]. It was shown that the dissolution of hydrous iridium oxide depends both on the potential of the electrode and oxide layer thickness; an increase in both parameters leads to enhanced dissolution. Based on the extensive literature review and data on the dissolution, the authors combined the state-of-the-art understanding of OER mechanism with the dissolution measurements and suggested a universal mechanism [35]:



If assuming that instead anhydrous oxide is used as catalyst, the catalytic cycle could be written with the second step of the cycle in Eq. 1 being the first step:



Mechanism suggested for active, hydrous oxide, where Ir^{III}-Ir^V switching of the oxidation state is predicted, was well in line with the observations reported by Minguzzi et al. [14]. Mechanism, proposed for anhydrous oxide, which was based on the observations made by Kötzt et al. [25], is however difficult to be experimentally confirmed, as IrO₃ intermediate was expected to be short lived.

Only recently, Kasian et al. published a study, where this high-oxidation-state iridium intermediate was detected for the first time [7]. Combining dissolution measurements using SFC-ICP-MS and detection of volatile intermediates and products of OER by online electrochemical mass spectrometry (OLEMS) on three different iridium anodes, namely metallic iridium, reactively sputtered and thermal iridium oxide, the authors were able to simultaneously measure the dissolved iridium and formation of O₂ and IrO₃ at 5, 10, 15 and 20 mA cm⁻². On thermal oxide, which displays lower reactivity towards OER, formation of volatile IrO₃ intermediate was detected already at the lowest current density, whereas on the other two, more active electrodes it was possible to detect it only at the highest current densities, after the potential on the anode exceeded 1.6 V. Based on that, already the above-mentioned mechanisms were confirmed and additionally combined into a potential dependent universal scheme, presented in Figure 5. Regardless of the material, the first step of OER, marked with blue arrows, is water discharge and adsorption of OH radical on the surface of catalyst, which is accompanied by the oxidation of iridium center and leads to the formation of Ir^VO₂(OH) intermediate. The next steps depend on the electrode potential, which is determined by the nature of the electrode. If OER is catalyzed by thermal oxide, required potential is high enough for further oxidation of iridium to Ir^{VI}O₃. This intermediate can then further either decompose to O₂ and IrO₂ to close the catalytic cycle or react with water and dissolve as IrO₄²⁻. Considering relatively low dissolution of the thermal oxide, it was suggested that hydrolysis is kinetically suppressed, which could explain the superior stability of crystalline iridium oxide. In the case of more active materials, the applied potential is not high enough to further oxidize iridium. Instead, OER cycle is closed by the decomposition of Ir^VO₂(OH) intermediate with evolution

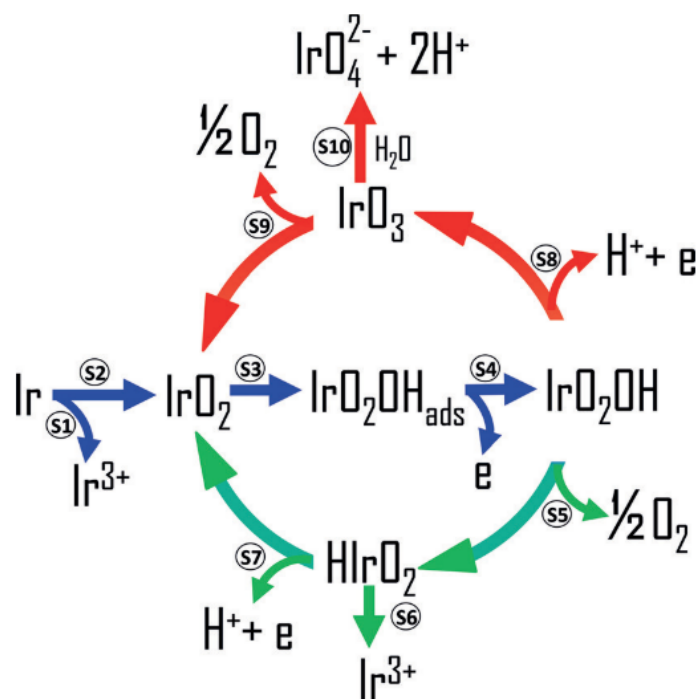


Figure 5: Universal mechanism correlating both OER and dissolution pathways, proposed by Kasian et al. [36].

of O₂ molecule and formation of HIr^{III}O₂ species, which can be further either dissolved or oxidized to IrO₂. Already in the study, published by Cherevko et al. [24], the formation of this Ir^{III} intermediate was suggested to be the origin of lower stability of metallic and hydrous iridium oxide catalysts. When current densities are high enough to exceed the potential required for oxidation of iridium further to Ir^{VI}, the pathway marked with red arrows, becomes relevant also for the more active catalysts. Here, dissolution via formation of IrO₄²⁻ - might however not be equally kinetically stabilized, as Geiger et al. showed that at potentials above 1.8 V, metallic iridium was completely dissolved already after 10 minutes [10].

Assuming that the proposed mechanism is operative, three different dissolution pathways are possible for different catalysts. First, dissolution of metallic iridium is inevitable under high anodic potentials, as it is accompanying the formation of protective passive oxide on the surface. The extent of dissolution depends on the nature of the metal, specifically on the cohesive energy and adsorption energy of oxygen, as was recently shown in the study by Speck et al. [37]. Second dissolution route involves the unstable Ir^{III} intermediate, which is formed on more active catalysts such as metallic iridium and reactively sputtered oxide. Involvement of this intermediate was experimentally proved many times [14, 15] and is usually assumed to be the reason for poor stability of these

materials. Based on the observed high dissolution, it was concluded that the dissolution of Ir^{III} has faster kinetics compared to the further oxidation to IrO₂. The third dissolution pathway involves the hydrolysis of IrO₃. The relevance of the proposed general mechanism was evaluated by ab initio molecular dynamics simulations [38]. The authors have confirmed the thermodynamic stability of Ir^V intermediate in relatively broad potential window, which is further transformed into IrO₃ at high anodic potentials and HIrO₂ at lower potentials. When further simulating the detachment of Ir^{III} intermediate from the surface, the authors found that iridium can either deposit back to the surface of oxide or dissolve as Ir(OH)₃, with the kinetics of redeposition being faster compared to the dissolution. Amorphization of the surface was experimentally observed and is thus in line with the calculations [39, 40]. When considering the third dissolution route via IrO₃ formation, it was shown that the reactivity of this intermediate towards OER was higher compared to IrO₂ (110) surface.

This mechanism could be applied also to the binuclear mechanism suggested by Steegstra et al. [41]. In this scenario, two neighboring iridium atoms are oxidized to Ir^V and further recombined with the release of oxygen molecule. If this mechanism is operative, the dissolved species should be instead Ir^V originating from the single iridium site, which at sufficient potential can dissolve, but cannot recombine without additional metallic center in the same oxidation state. Here the dissolution should be observed before the onset of OER, which was not detected in the previous studies on the noble metals [2].

Presence of unstable intermediates promotes the dissolution of catalysts during OER. Based on the presented possible reaction pathways, it can be concluded that both OER and dissolution are two parallel reactions with a common intermediate. Understanding this, it could be possible to suppress one without impacting the other. Still, the dissolution of either Ir^{III} or Ir^{VI} intermediate is not fully understood and it is not yet known whether the reaction is chemical or electrochemical. Nevertheless, the formation and lifetime of intermediates depends on the potential. With the progression of OER, the concentration of protons in the pores of oxide can significantly increase, which could lead to the enhanced dissolution of the less stable intermediates. Finding the environment where dissolution would be suppressed is therefore crucial in the forthcoming stability-related studies. This could be done, for example, with the change in pH of the electrolyte. Additionally, the stabilization of IrO₃ intermediate was experimentally already shown, specifically through a proton intercalation mechanism [42].

4. Lattice oxygen evolution reaction and its implications on the stability of Ir-based catalysts

The discussion above considered OER mechanism based on the cationic redox cycle. Assuming that another, anionic mechanism is also possible, lattice oxygen should be involved in the reaction. First attempt to prove this hypothesis was a study published by

Fierro et al., which combined differential electrochemical mass spectrometry (DEMS) and isotope labeling to detect oxygen, evolved from the oxide layer in Ti/IrO₂ [23]. Through the detection of species with m/z ratio 32 and 34, it was confirmed that oxygen is indeed partially evolved from the lattice. However, the study did not correlate this phenomenon with the possible destabilization of the structure via the formation of vacancies after the release of oxygen atoms. Only recently, two studies extended this experimental approach with additional simultaneous dissolution measurements [8, 10]. Geiger et al. examined the stability of different Ir-based catalysts, namely highly active perovskites, amorphous IrO_x, metallic iridium and rutile IrO₂. They found that the rate of dissolution depends on the structure of the catalyst. Non-noble elements present in the perovskites dissolved immediately after the immersion in the acidic electrolyte, leaving behind amorphous, highly hydrated structure or iridium oxide resulting from the collapse of the originally present iridium octahedral framework. The ordered structure with predominately edge-sharing oxygen atoms transformed into an amorphous structure with an increased number of corner-sharing oxygen atoms, which resulted in the enhanced dissolution of iridium. Additional isotope labeling experiments on rutile and hydrous iridium oxide thin films provided information on the involvement of the activated, corner-sharing oxygens in the mechanism of OER. The authors concluded that the involvement of lattice oxygen in the OER depends on the structure and that the overall stability of different oxides is determined firstly by the ratio between the edge- and corner-sharing iridium octahedra, which was also in line with the observations by Willinger et al. [43] and secondly, by the stability of intermediates could be higher for the rutile compared to the amorphous oxides. The S-number, which was introduced in this study as a stability metric, defined as the ratio between the number of evolved oxygen molecules and dissolved iridium atoms, explicitly shows the correlation between the activity and stability of different catalysts, and can be used to compare the different stabilities of newly designed materials.

4.1. Lattice oxygen evolution reaction and stability of amorphous IrO_x

A study by Kasian et al. further aimed to quantitatively assess the contribution of the oxygen evolved from the lattice to the overall OER [8]. The authors combined SFC-ICP-MS and OLEMS measurements with atomic scale structural characterization technique atom probe tomography (APT), which was previously used to unveil the structure of electrochemical metallic iridium oxide, grown under galvanostatic conditions [44]. As model systems in this study, hydrous Ir¹⁸O_x and reactively sputtered Ir¹⁸O₂ films were used. Results of the electrochemical experiment complemented with in-situ dissolution measurement and evolution of volatile products with m/z ratio 32, 34 and 36 are presented in Figure 6. Oxygen with m/z 32 evolved through a classical adsorbate route and does not involve lattice oxygen. Products with higher m/z on the contrary, contain one (34, O¹⁶O¹⁸) or two (36, O¹⁸O¹⁸) oxygen atoms from the lattice. Detection of the latter two molecules in measurements of hydrous oxide directly confirm the lattice oxygen participation, which results in the destabilization of oxide structure and its higher dissolution, compared to

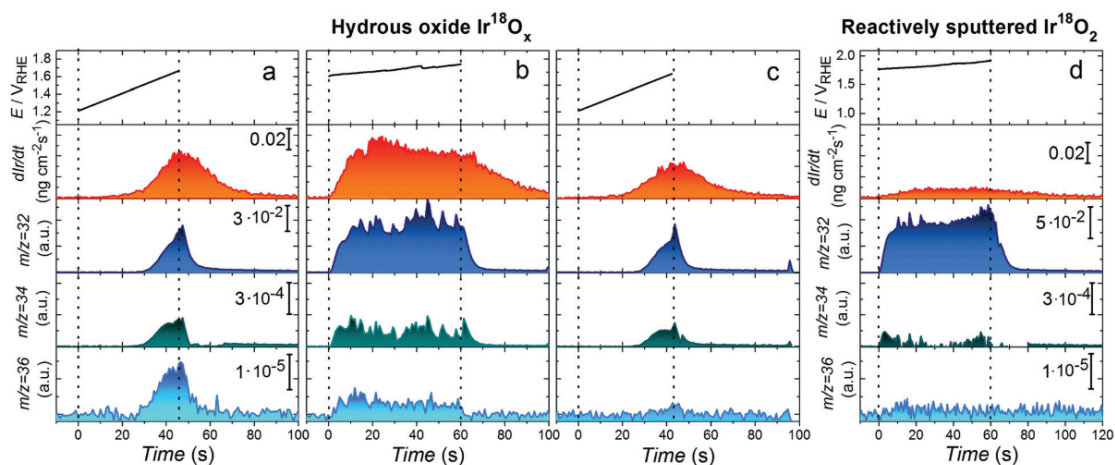


Figure 6: Electrochemical investigation of isotopically labelled hydrous iridium oxide and reactively sputtered iridium oxide with online dissolution of iridium and detection of oxygen molecule with m/z 32 ($O^{16}O^{16}$), 34 ($O^{16}O^{18}$) and 36 ($O^{18}O^{18}$) [8].

reactively sputtered iridium oxide. Here, the dissolution was order of magnitude lower with the negligible concentration of oxygen, evolved through the participation of lattice oxygen. This conclusion could however originate from the technical limitations, due to concentrations of evolved species below the detection limit. APT analysis of both oxides, used to correlate the difference in structure and its stability revealed, that hydrous oxide nanopores are covered with the layer consisting of Ir-O and OH in approximate ratio 1: 1. This suggests that hydrous iridium oxide consists of Ir^{III} -OOH species, which can by itself act as OER precursor. Indeed, it was found that the ratio between dissolution and evolution of oxygen through a recombination of two lattice oxygens was constant, which directly confirms their previously suggested correlation. Additionally, OH groups, present in the hydrous layer, stabilize the Ir^{III} species in the oxide and can serve as precursor for peroxide route, leading to evolution of $O^{16}O^{18}$. Based on the APT experiments it can be suggested, that Ir^{III} -OOH species could actually be the degradation intermediate $HIrO_2$ (Figure 5) and that its degradation may be accompanied by the release of oxygen molecule. In reactively sputtered oxide, presence of such species was however not detected, which is in line with its higher stability. Quantitatively, on hydrous iridium oxide approximately 0.05% of all oxygen molecules are produced via peroxide route, whereas only 0.01% of the oxygen molecules originate from the recombination of two oxygen atoms from the lattice.

4.2. Lattice oxygen evolution reaction and stability of rutile IrO_2

As aforementioned, the technical limitations of the techniques such as OLEMS can lead to inaccurate conclusions when investigating more stable oxides. The studies shown in this section have in general concluded that the rutile lattice is not participating in OER, which could explain its higher stability. However, to overcome the possible detection-related

limitations and test whether the exchange of oxygen anions is nevertheless possible in the case of more rigid structures, a different approach was used in the study published by Schweinar et al. [45]. Instead of detecting the evolved oxygen, the authors used the isotope labeled reactively sputtered iridium oxide thin film, anodically polarized it at 1 mA cm^{-2} for 10 minutes in a non-labeled electrolyte and afterwards estimated the proportion of exchanged oxygen atoms via APT. The analysis revealed a significant increase of O^{16} species in the top 2.5 nm of the film, which was a direct confirmation of active involvement of lattice in the reaction. The overall electrochemically active volume of catalyst was nonetheless significantly lower than in hydrous iridium oxide, which explains higher stability of rutile.

5. Concluding remarks and perspective

In this minireview, recent advances in the understanding of the degradation, more specifically dissolution of Ir-based catalysts for OER were presented. Ir-based materials are considered the best OER catalysts, as they combine both adequate activity and good stability. Crystalline analogue, i.e. rutile IrO_2 is known to be very stable, however, its activity is lower than the activity of amorphous Ir analogues and pure metallic Ir. On the contrary, these more active catalysts display lower resistance towards dissolution, which suggests that both parameters, activity and stability, are interrelated. In the first sections of the review, different OER mechanisms were discussed. Most often, the catalytic cycle is considering either redox changes of the cation, i.e. Ir or redox changes of the anion, i.e. oxygen ligand. As was shown in the review, different experimental and theoretical approaches are utilized for mechanistic studies. Understanding the reaction's pathway is of primordial importance as it can give an insight into the origin of different activities of Ir-based catalysts and can additionally direct the design of novel catalytic materials with improved performance. In the next sections of the review, mechanisms of OER were further correlated to the dissolution pathways that are directly related to different stabilities of Ir-based oxide analogues. First, a universal mechanism that links OER to dissolution via a common intermediate was presented. The proposed pathway suggests that the dissolution of Ir strongly depends on the nature of the catalyst. Based on this mechanism, active catalysts such as hydrous IrO_x and metallic Ir dissolve via $\text{Ir}^V\text{-Ir}^{III}$ cycle, with Ir^{III} intermediate generally assumed to be the origin of the instability. On the contrary, in the case of rutile, potentials are high enough for oxidation of Ir to IrO_3 intermediate, which was only recently experimentally confirmed for the first time. This intermediate was suggested to be kinetically stabilized, which explains the superior stability of rutile. Besides this, dissolution can occur also as a result of the destabilization of the oxide lattice after OER. Based on isotope labelling and on-line detection of evolved oxygen molecules or APT measurements, it was shown that lattice indeed participates in the reaction regardless of the nature of the oxide, however not to the same extent.

The processes that were discussed in the minireview are nicely summarized In Figure 7 [45]. Participation of either one (a) or two (b) lattice oxygen atoms in the OER result in the destabilization of the lattice. This occurs more frequently on amorphous oxides, as

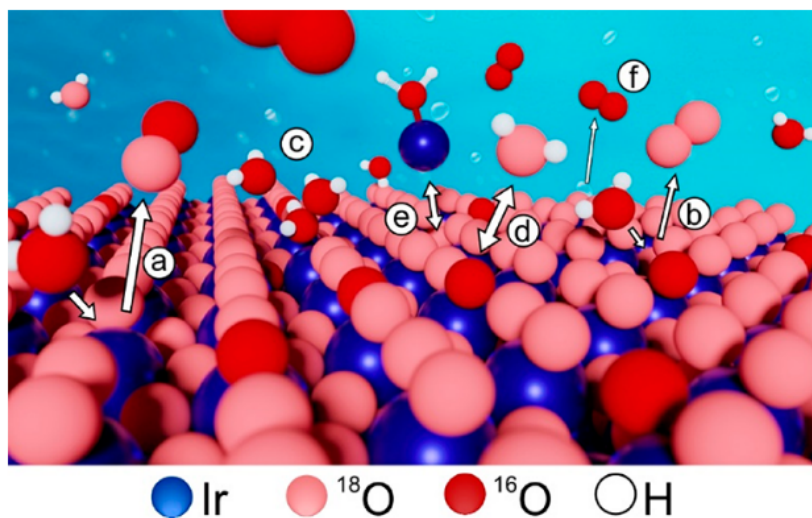


Figure 7: Processes on the surface of iridium oxide catalysts under OER conditions [45].

their structure is more flexible, with considerably larger catalytically active volume with intercalated water molecules and occupancy of activated oxygen atoms and $\text{Ir}^{III}\text{-OOH}$ species which can by themselves act as OER precursors. In reactively sputtered oxides the kinetics of lattice oxygen exchange is slower, but nevertheless present. It was previously suggested that the rate of oxygen exchange could potentially serve as a metric for the stability evaluation of different oxides [45]. The vacancies that are created after the removal of oxygen can be refilled either through the adsorption of a water molecule or the migration of bulk oxygen atoms. This inevitably results in surface reconstruction that can further enhance dissolution, e.g. through the oxidation of defects (c). Oxygen from the lattice can be also exchanged by oxygen from the water (d). This process is not expected to be particularly destructive, however, it still requires bond rupture and formation, which should lead to the destabilization of the surface. Formation of the unstable Ir^{III} species under OER conditions results in the dissolution of this intermediate. Afterwards, the dissolved species can be redeposited back to the surface (e) and thus boost the amorphization of the surface and increase the possibility for further dissolution. Despite the vigorous processes on the surface during OER, dissolution measurements have, however, shown that OER on iridium-based catalysts, regardless of the structure, occurs predominantly from the decomposition of water (f), which makes them the catalyst of choice for the OER in acidic media to date.

After almost a decade of fundamental dissolution-oriented studies performed on model systems, such as metallic iridium disk or thin films, the processes driving the degradation of OER catalysts are now generally well understood, however, a question remains whether

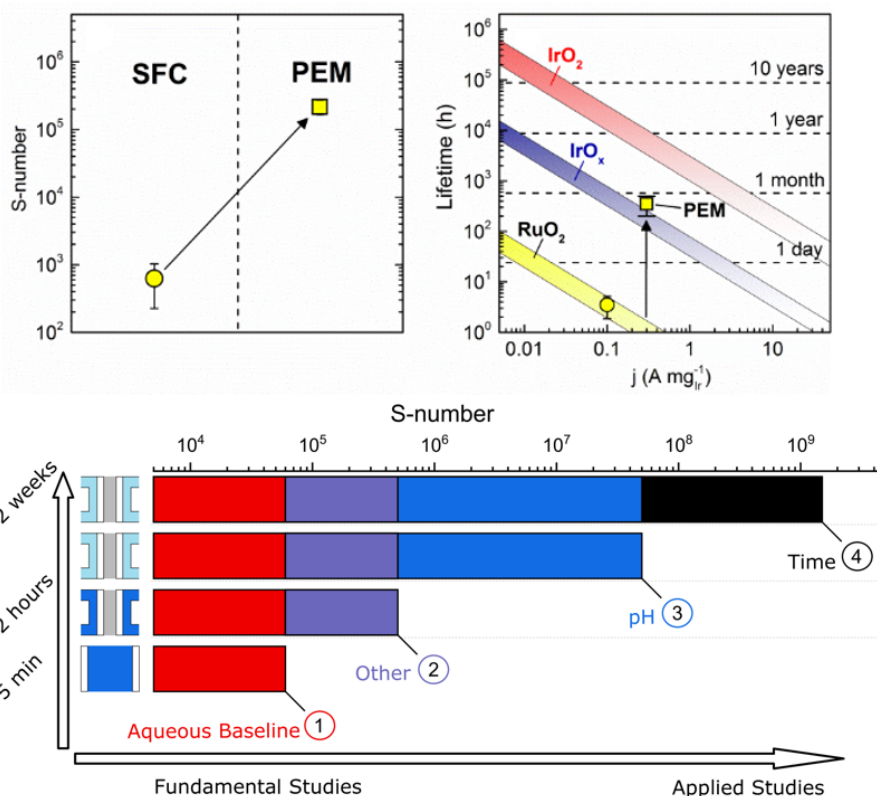


Figure 8: Comparison between S-numbers, obtained in aqueous electrolyte via SCF-ICP-MS measurements and via extraction from PEM stack (top) [10]; effect of pH and stabilization effect over time on the calculated S-number in aqueous model system and MEA (bottom) [46].

the acquired knowledge, presented by now can be transferred to the non-model systems. When comparing the S-numbers of anhydrous ruthenium oxide, measured in either aqueous electrolyte via SFC-ICP-MS or extracted from the PEM stack, the calculated lifetimes differed for more than two orders of magnitude, which suggests that dissolution measurements generally overestimate the dissolution of catalysts under OER (Figure 8) [10]. This could originate from different acidity in PEM stack, compared to the half-cell investigations, where electrolyte with pH 1 is usually used. Additionally, diffusivity of dissolved ions out of the membrane or their deposition in the membrane or cathode could result in lower dissolution of the catalyst. First attempts to evaluate the effect of different parameters on the dissolution rate were presented in the study, recently published by Knöppel et al. [46]. The aim of the study was to test different parameters that differ between the model aqueous system and membrane electrode assembly (MEA). The results revealed that the main source of the higher dissolution in model systems is overestimated acidity and stabilization overtime in real devices (Figure 8).

These results directly confirm the effect of pH on the dissolution of iridium under OER conditions. As was discussed above, the instability of Ir^{III} intermediate in the OER and dissolution pathways on more active catalysts, leads to the enhanced dissolution of these materials compared to rutile IrO₂. The observed suppressed dissolution at higher pH corroborates that stability of this intermediate is indeed pH-dependent. Future studies should thus focus on the effect of acidity on the stability and activity of iridium-based catalysts. While its effect on the activity was previously shown for various OER catalysts [47, 48, 49], stability was overlooked in this regard. Furthermore, understanding the effective pH under working conditions in PEM electrolyzer should be deepened.

Results, showing the discrepancies between model and real systems, dictate the direction of future studies on the topic, which should aim to close the gap between them. While the half-cell measurements in aqueous systems can be used as ideal systems for estimation of the stability of novel materials, techniques resembling MEA should be developed for the evaluation of parameters such as loading effect and binder content, that affect the performance of the catalyst. Setting up such as gas diffusion electrode (GDE) could be used for such studies [50, 51]. GDE was already used for the evaluation of ORR catalysts, however its application to the OER catalysis is still hindered by challenges, originating predominantly from the mass transport of generated oxygen molecules, that still need to be overcome in order to achieve realistic current densities.

It was shown that stability predominantly depends on the structure of the catalysts. This is especially crucial when nanoparticles with more surface defects such as vacancies, steps, kinks and grain boundaries are considered. Their effect on the dissolution should be therefore more thoroughly studied in future studies. Dissolution study by Jovanović et al. [52] on different iridium-based nanoparticles showed some discrepancy with the disk measurements obtained by Cherevko et al. [24, 35], which was related to the possible particle size effect. The long term stability of even crystalline IrO₂ nanoparticles could be potentially questioned, as Schweinar et al. [53] showed that the top 2.5 nm is actively involved in OER, which could be detrimental for nanoparticles. To observe compositional, structural and morphological changes of the nanoparticles under OER, advanced electron microscopy techniques like in-situ transmission electron microscopy (TEM) [54] and identical location (IL)-TEM [55] should be further developed. While in liquid in-situ TEM the unambiguous interpretation of the obtained data is limited predominantly by the interaction of the electron beam with the electrolyte, IL-TEM is now a generally well established technique for the atomic-scale observation of nanoparticulate electrocatalysts [56]. Only recently a novel methodology, namely modified floating electrode (MFE) was developed and applied to the ORR, which enables facile handling of the delicate TEM grids and operation under realistic current densities [57]. The challenge which still needs to be overcome in order to efficiently use MFE for OER is similarly as for GDE, efficient removal of generated oxygen bubbles.

References

- [1] K. Ayers, "Gigawatt-scale renewable hydrogen via water splitting as a case study for collaboration: The need to connect fundamental and applied research to accelerate solutions," *MRS Energy & Sustainability*, vol. 4, no. 1, pp. 1–10, 2017.
- [2] S. Cherevko, A. R. Zeradjanin, A. A. Topalov, N. Kulyk, I. Katsounaros, and K. J. Mayrhofer, "Dissolution of noble metals during oxygen evolution in acidic media," *ChemCatChem*, vol. 6, no. 8, pp. 2219–2223, 2014.
- [3] M. H. Miles and M. A. Thomason, "Periodic Variations of Overvoltages for Water Electrolysis in Acid Solutions from Cyclic Voltammetric Studies," *Journal of The Electrochemical Society*, vol. 123, pp. 1459–1461, oct 1976.
- [4] J. O. Bockris, "Kinetics of activation controlled consecutive electrochemical reactions: Anodic evolution of oxygen," *The Journal of Chemical Physics*, vol. 24, pp. 817–827, apr 1956.
- [5] S. Cherevko, "Stability and dissolution of electrocatalysts: Building the bridge between model and "real world" systems," *Current Opinion in Electrochemistry*, vol. 8, pp. 118–125, 2018.
- [6] A. A. Topalov, I. Katsounaros, J. C. Meier, S. O. Klemm, and K. J. Mayrhofer, "Development and integration of a LabVIEW-based modular architecture for automated execution of electrochemical catalyst testing," *Review of Scientific Instruments*, vol. 82, p. 114103, nov 2011.
- [7] O. Kasian, J. P. Grote, S. Geiger, S. Cherevko, and K. J. Mayrhofer, "The Common Intermediates of Oxygen Evolution and Dissolution Reactions during Water Electrolysis on Iridium," *Angewandte Chemie - International Edition*, vol. 57, no. 9, pp. 2488–2491, 2018.
- [8] O. Kasian, S. Geiger, T. Li, J. P. Grote, K. Schweinar, S. Zhang, C. Scheu, D. Raabe, S. Cherevko, B. Gault, and K. J. Mayrhofer, "Degradation of iridium oxides via oxygen evolution from the lattice: Correlating atomic scale structure with reaction mechanisms," *Energy and Environmental Science*, vol. 12, no. 12, pp. 3548–3555, 2019.
- [9] T. Binniger, R. Mohamed, K. Waltar, E. Fabbri, P. Levecque, R. Kötz, and T. J. Schmidt, "Thermodynamic explanation of the universal correlation between oxygen evolution activity and corrosion of oxide catalysts OPEN," *Scientific Reports* —, vol. 5, p. 12167, 2015.
- [10] S. Geiger, O. Kasian, M. Ledendecker, E. Pizzutilo, A. M. Mingers, W. T. Fu, O. Diaz-Morales, Z. Li, T. Oellers, L. Fruchter, A. Ludwig, K. J. Mayrhofer, M. T. Koper, and S. Cherevko, "The stability number as a metric for electrocatalyst stability benchmarking," *Nature Catalysis*, vol. 1, no. 7, pp. 508–515, 2018.

- [11] J. Rossmeisl, Z. W. Qu, H. Zhu, G. J. Kroes, and J. K. Nørskov, "Electrolysis of water on oxide surfaces," *Journal of Electroanalytical Chemistry*, vol. 607, no. 1-2, pp. 83–89, 2007.
- [12] A. Damjanovic, A. Dey, and J. O. Bockris, "Electrode Kinetics of Oxygen Evolution and Dissolution on Rh, Ir, and Pt-Rh Alloy Electrodes," *Journal of The Electrochemical Society*, vol. 113, no. 7, p. 739, 1966.
- [13] H. G. Sanchez Casalongue, M. L. Ng, S. Kaya, D. Friebel, H. Ogasawara, and A. Nilsson, "In Situ Observation of Surface Species on Iridium Oxide Nanoparticles during the Oxygen Evolution Reaction," *Angewandte Chemie International Edition*, vol. 53, pp. 7169–7172, jul 2014.
- [14] A. Minguzzi, O. Lugaresi, E. Achilli, C. Locatelli, A. Vertova, P. Ghigna, and S. Rondinini, "Observing the oxidation state turnover in heterogeneous iridium-based water oxidation catalysts," *Chemical Science*, vol. 5, no. 9, pp. 3591–3597, 2014.
- [15] V. Pfeifer, T. E. Jones, J. J. Velasco Vélez, C. Massué, M. T. Greiner, R. Arrigo, D. Teschner, F. Girgsdies, M. Scherzer, J. Allan, M. Hashagen, G. Weinberg, S. Piccinin, M. Hävecker, A. Knop-Gericke, and R. Schlögl, "The electronic structure of iridium oxide electrodes active in water splitting," *Physical Chemistry Chemical Physics*, vol. 18, no. 4, pp. 2292–2296, 2016.
- [16] V. A. Saveleva, L. Wang, D. Teschner, T. Jones, A. S. Gago, K. A. Friedrich, S. Zafeirotos, R. Schlögl, and E. R. Savinova, "Operando Evidence for a Universal Oxygen Evolution Mechanism on Thermal and Electrochemical Iridium Oxides," *Journal of Physical Chemistry Letters*, vol. 9, pp. 3154–3160, jun 2018.
- [17] N. Sivasankar, W. W. Weare, and H. Frei, "Direct observation of a hydroperoxide surface intermediate upon visible light-driven water oxidation at an Ir oxide nanocluster catalyst by rapid-scan FT-IR spectroscopy," *Journal of the American Chemical Society*, vol. 133, no. 33, pp. 12976–12979, 2011.
- [18] Z. Pavlovic, C. Ranjan, Q. Gao, M. Van Gastel, and R. Schlögl, "Probing the structure of a water-Oxidizing anodic iridium oxide catalyst using raman spectroscopy," *ACS Catalysis*, vol. 6, no. 12, pp. 0–7, 2016.
- [19] H. Ooka, Y. Wang, A. Yamaguchi, M. Hatakeyama, S. Nakamura, K. Hashimoto, and R. Nakamura, "Legitimate intermediates of oxygen evolution on iridium oxide revealed by in situ electrochemical evanescent wave spectroscopy †," *Phys. Chem. Chem. Phys.*, vol. 18, p. 15199, 2016.
- [20] I. C. Man, H. Y. Su, F. Calle-Vallejo, H. A. Hansen, J. I. Martínez, N. G. Inoglu, J. Kitchin, T. F. Jaramillo, J. K. Nørskov, and J. Rossmeisl, "Universality in Oxygen Evolution Electrocatalysis on Oxide Surfaces," *ChemCatChem*, vol. 3, no. 7, pp. 1159–1165, 2011.

- [21] Y. Ping, R. J. Nielsen, and W. A. Goddard, "The Reaction Mechanism with Free Energy Barriers at Constant Potentials for the Oxygen Evolution Reaction at the IrO₂ (110) Surface," *Journal of the American Chemical Society*, vol. 139, pp. 149–155, jan 2017.
- [22] A. Zagalskaya and V. Alexandrov, "Role of Defects in the Interplay between Adsorbate Evolving and Lattice Oxygen Mechanisms of the Oxygen Evolution Reaction in RuO₂ and IrO₂," *ACS Catalysis*, vol. 10, pp. 3650–3657, mar 2020.
- [23] S. Fierro, T. Nagel, H. Baltruschat, and C. Comninellis, "Investigation of the oxygen evolution reaction on Ti/IrO₂ electrodes using isotope labelling and on-line mass spectrometry," *Electrochemistry Communications*, vol. 9, no. 8, pp. 1969–1974, 2007.
- [24] S. Cherevko, S. Geiger, O. Kasian, A. Mingers, and K. J. Mayrhofer, "Oxygen evolution activity and stability of iridium in acidic media. Part 2. - Electrochemically grown hydrous iridium oxide," *Journal of Electroanalytical Chemistry*, vol. 774, pp. 102–110, 2016.
- [25] R. Kötz, H. Neff, and S. Stucki, "Anodic Iridium Oxide Films: XPS-Studies of Oxidation State Changes and," *Journal of The Electrochemical Society*, vol. 131, pp. 72–77, jan 1984.
- [26] M. Sathiya, G. Rousse, K. Ramesha, C. P. Laisa, H. Vezin, M. T. Sougrati, M.-L. Doublet, D. Foix, D. Gonbeau, W. Walker, A. S. Prakash, M. B. Hassine, L. Dupont, and J.-M. Tarascon, "Reversible anionic redox chemistry in high-capacity layered-oxide electrodes," *Nature Materials*, 2013.
- [27] P. Rozier, M. Sathiya, A. R. Paulraj, D. Foix, T. Desaunay, P. L. Taberna, P. Simon, and J. M. Tarascon, "Anionic redox chemistry in Na-rich Na₂Ru₁-YSnyO₃ positive electrode material for Na-ion batteries," *Electrochemistry Communications*, vol. 53, pp. 29–32, 2015.
- [28] A. Grimaud, O. Diaz-Morales, B. Han, W. T. Hong, Y. L. Lee, L. Giordano, K. A. Storzinger, M. T. Koper, and Y. Shao-Horn, "Activating lattice oxygen redox reactions in metal oxides to catalyse oxygen evolution," *Nature Chemistry*, vol. 9, no. 5, pp. 457–465, 2017.
- [29] V. Pfeifer, T. E. Jones, J. J. Velasco Vélez, C. Massué, R. Arrigo, D. Teschner, F. Girgsdies, M. Scherzer, M. T. Greiner, J. Allan, M. Hashagen, G. Weinberg, S. Piccinin, M. Hävecker, A. Knop-Gericke, and R. Schlögl, "The electronic structure of iridium and its oxides," *Surface and Interface Analysis*, vol. 48, no. 5, pp. 261–273, 2016.
- [30] A. Grimaud, A. Demortiere, M. Saubanere, W. Dachraoui, M. Duchamp, M. L. Doublet, and J. M. Tarascon, "Activation of surface oxygen sites on an iridium-based model catalyst for the oxygen evolution reaction," *Nature Energy*, vol. 2, no. 1, 2017.
- [31] A. Grimaud, W. T. Hong, Y. Shao-Horn, and J. M. Tarascon, "Anionic redox processes for electrochemical devices," *Nature Materials*, vol. 15, no. 2, pp. 121–126, 2016.

- [32] S. Cherevko, T. Reier, A. R. Zeradjanin, Z. Pawolek, P. Strasser, and K. J. Mayrhofer, "Stability of nanostructured iridium oxide electrocatalysts during oxygen evolution reaction in acidic environment," *Electrochemistry Communications*, vol. 48, pp. 81–85, 2014.
- [33] S. Geiger, O. Kasian, B. R. Shrestha, A. M. Mingers, K. J. J. Mayrhofer, and S. Cherevko, "Activity and Stability of Electrochemically and Thermally Treated Iridium for the Oxygen Evolution Reaction," *Journal of The Electrochemical Society*, vol. 163, no. 11, pp. F3132–F3138, 2016.
- [34] S. Cherevko, S. Geiger, O. Kasian, N. Kulyk, J. P. Grote, A. Savan, B. R. Shrestha, S. Merzlikin, B. Breitbach, A. Ludwig, and K. J. Mayrhofer, "Oxygen and hydrogen evolution reactions on Ru, RuO₂, Ir, and IrO₂ thin film electrodes in acidic and alkaline electrolytes: A comparative study on activity and stability," *Catalysis Today*, vol. 262, pp. 170–180, 2016.
- [35] S. Cherevko, S. Geiger, O. Kasian, A. Mingers, and K. J. Mayrhofer, "Oxygen evolution activity and stability of iridium in acidic media. Part 1. - Metallic iridium," *Journal of Electroanalytical Chemistry*, vol. 773, pp. 69–78, 2016.
- [36] O. Kasian, S. Geiger, M. Schalenbach, A. M. Mingers, A. Savan, A. Ludwig, S. Cherevko, and K. J. J. Mayrhofer, "Using Instability of a Non-stoichiometric Mixed Oxide Oxygen Evolution Catalyst As a Tool to Improve Its Electrocatalytic Performance," *Electrocatalysis*, vol. 9, pp. 139–145, mar 2018.
- [37] F. D. Speck, A. Zagalskaya, V. Alexandrov, and S. Cherevko, "Periodicity in the Electrochemical Dissolution of Transition Metals," *Angewandte Chemie International Edition*, p. anie.202100337, mar 2021.
- [38] A. Zagalskaya and V. Alexandrov, "Mechanistic Study of IrO₂ Dissolution during the Electrocatalytic Oxygen Evolution Reaction," *Journal of Physical Chemistry Letters*, vol. 11, pp. 2695–2700, apr 2020.
- [39] N. Dubouis, A. Serva, E. Salager, M. Deschamps, M. Salanne, and A. Grimaud, "The Fate of Water at the Electrochemical Interfaces: Electrochemical Behavior of Free Water Versus Coordinating Water," *Journal of Physical Chemistry Letters*, vol. 9, pp. 6683–6688, dec 2018.
- [40] G. Wan, J. W. Freeland, J. Kloppenburg, G. Petretto, J. N. Nelson, D.-Y. Kuo, C.-J. Sun, J. Wen, J. T. Diulus, G. S. Herman, Y. Dong, R. Kou, J. Sun, S. Chen, K. M. Shen, D. G. Schlom, G.-M. Rignanese, G. Hautier, D. D. Fong, Z. Feng, H. Zhou, and J. Suntivich, "Amorphization mechanism of SrIrO₃ electrocatalyst: How oxygen redox initiates ionic diffusion and structural reorganization," *Science Advances*, vol. 7, p. eabc7323, jan 2021.

- [41] P. Steegstra, M. Busch, I. Panas, and E. Ahlberg, "Revisiting the redox properties of hydrous iridium oxide films in the context of oxygen evolution," *Journal of Physical Chemistry C*, vol. 117, pp. 20975–20981, oct 2013.
- [42] P. E. Pearce, C. Yang, A. Iadecola, J. Rodriguez-Carvajal, G. Rousse, R. Dedryvère, A. M. Abakumov, D. Giaume, M. Deschamps, J.-M. Tarascon, and A. Grimaud, "Revealing the Reactivity of the Iridium Trioxide Intermediate for the Oxygen Evolution Reaction in Acidic Media," *Chemistry of Materials*, vol. 31, pp. 5845–5855, aug 2019.
- [43] E. Willinger, C. Massué, R. Schlögl, and M. G. Willinger, "Identifying Key Structural Features of IrO_x Water Splitting Catalysts," *Journal of the American Chemical Society*, vol. 139, no. 34, pp. 12093–12101, 2017.
- [44] T. Li, O. Kasian, S. Cherevko, S. Zhang, S. Geiger, C. Scheu, P. Felfer, D. Raabe, B. Gault, and K. J. Mayrhofer, "Atomic-scale insights into surface species of electrocatalysts in three dimensions," *Nature Catalysis*, vol. 1, no. 4, pp. 300–305, 2018.
- [45] K. Schweinar, B. Gault, I. Mouton, and O. Kasian, "Lattice Oxygen Exchange in Rutile IrO₂ during the Oxygen Evolution Reaction," *Journal of Physical Chemistry Letters*, vol. 11, no. 13, pp. 5008–5014, 2020.
- [46] J. Knöppel, M. Möckl, D. Escalera-López, K. Stojanovski, M. Bierling, T. Böhm, S. Thiele, M. Rzepka, and S. Cherevko, "On the limitations in assessing stability of oxygen evolution catalysts using aqueous model electrochemical cells," *Nature Communications*, vol. 12, p. 2231, dec 2021.
- [47] L. Giordano, B. Han, M. Risch, W. T. Hong, R. R. Rao, K. A. Stoerzinger, and Y. Shao-Horn, "pH dependence of OER activity of oxides: Current and future perspectives," *Catalysis Today*, vol. 262, pp. 2–10, 2016.
- [48] K. A. Stoerzinger, R. R. Rao, X. R. Wang, W. T. Hong, C. M. Rouleau, and Y. Shao-Horn, "The Role of Ru Redox in pH-Dependent Oxygen Evolution on Rutile Ruthenium Dioxide Surfaces," *Chem*, vol. 2, pp. 668–675, may 2017.
- [49] T. Takashima, K. Hashimoto, and R. Nakamura, "Mechanisms of pH-Dependent Activity for Water Oxidation to Molecular Oxygen by MnO₂ Electrocatalysts," *Journal of the American Chemical Society*, vol. 134, pp. 1519–1527, jan 2012.
- [50] K. Ehelebe, D. Seeberger, M. T. Y. Paul, S. Thiele, K. J. J. Mayrhofer, and S. Cherevko, "Evaluating Electrocatalysts at Relevant Currents in a Half-Cell: The Impact of Pt Loading on Oxygen Reduction Reaction," *Journal of The Electrochemical Society*, vol. 166, no. 16, pp. F1259–F1268, 2019.
- [51] J. Schröder, V. A. Mints, A. Bornet, E. Berner, M. Fathi Tovini, J. Quinson, G. K. H. Wiberg, F. Bizzotto, H. A. El-Sayed, and M. Arenz, "The Gas Diffusion Electrode Setup as Straightforward Testing Device for Proton Exchange Membrane Water Electrolyzer Catalysts," *JACS Au*, vol. 1, pp. 247–251, mar 2021.

- [52] P. Jovanovič, N. Hodnik, F. Ruiz-Zepeda, I. Arčon, B. Jozinovič, M. Zorko, M. Bele, M. Šala, V. S. Šelih, S. Hočevar, and M. Gaberšček, "Electrochemical Dissolution of Iridium and Iridium Oxide Particles in Acidic Media: Transmission Electron Microscopy, Electrochemical Flow Cell Coupled to Inductively Coupled Plasma Mass Spectrometry, and X-ray Absorption Spectroscopy Study," *Journal of the American Chemical Society*, vol. 139, no. 36, pp. 12837–12846, 2017.
- [53] K. Schweinar, R. L. Nicholls, C. R. Rajamathi, P. Zeller, M. Amati, L. Gregoratti, D. Raabe, M. Greiner, B. Gault, and O. Kasian, "Probing catalytic surfaces by correlative scanning photoemission electron microscopy and atom probe tomography," *Journal of Materials Chemistry A*, vol. 8, no. 1, pp. 388–400, 2020.
- [54] N. Hodnik, G. Dehm, and K. J. J. Mayrhofer, "Importance and Challenges of Electrochemical in Situ Liquid Cell Electron Microscopy for Energy Conversion Research," *Accounts of Chemical Research*, vol. 49, pp. 2015–2022, sep 2016.
- [55] N. Hodnik and S. Cherevko, "Spot the difference at the nanoscale: identical location electron microscopy in electrocatalysis," *Current Opinion in Electrochemistry*, vol. 15, pp. 73–82, 2019.
- [56] L. J. Moriau, A. Hrnjić, A. Pavlišić, A. R. Kamšek, U. Petek, F. Ruiz-Zepeda, M. Šala, L. Pavko, V. S. Šelih, M. Bele, P. Jovanovič, M. Gatalo, and N. Hodnik, "Resolving the nanoparticles' structure-property relationships at the atomic level: a study of Pt-based electrocatalysts," *iScience*, vol. 24, no. 2, 2021.
- [57] A. Hrnjić, F. Ruiz-Zepeda, M. Gaberscek, M. Bele, L. Suhadolnik, N. Hodnik, and P. Jovanovič, "Modified Floating Electrode Apparatus for Advanced Characterization of Oxygen Reduction Reaction Electrocatalysts," *Journal of the Electrochemical Society*, 2020.

Implementation of an optical compressor on a free-electron-laser as a new concept for generation of a few-femtosecond pulses in extreme ultra-violet spectral region

Luka Novinec

Laboratory of Quantum Optics, University of Nova Gorica, Vipavska 13, SI-5000 Nova Gorica

Elettra-Sincrotrone Trieste, Strada Statale 14-km 163,5, 34149 Trieste, Italy

Abstract

The free-electron lasers (FELs) are becoming cutting edge research tools with the ability to provide ultra-short and very intense pulses in the spectral range from extreme ultraviolet to soft X-ray. Such pulses are of great interest for their promising applications in ultra-fast time resolution studies of various disciplines, ranging from physics and chemistry to biology and material sciences. Here we present the concept of implementing an optical compressor on FEL, for generating few-femtosecond pulses in extreme-ultraviolet (EUV) spectral region. A proposed solution enabled the researchers to achieve a relevant reduction of the FEL pulse duration, compared to that obtained in standard operation mode thus giving way to the generation of fully coherent, ultra-short, close to transform-limited pulses with gigawatt power.

Keywords: free-electron laser, femtosecond, compressor, chirped pulse amplification

1. Introduction

Over the past decades, the development of FELs enabled users to expand the field of research into areas previously out of reach with synchrotron and tabletop laser sources. An FEL is a source of coherent radiation that uses the interaction between an electromagnetic wave and a bunch of relativistic electrons to amplify this wave as the electrons pass through a periodic magnetic array of an undulator. In the simplest arrangement, the so-called self-amplified spontaneous emission (SASE) generates a high-intensity beam, with very good lateral coherence while limited longitudinal and temporal coherence [1]. To overcome such limitations, an external (coherent) source as a trigger can be used. Such scheme, used in FERMI FEL facility in Trieste, is based on the generation of FEL light at the harmonics of an external seed laser (high-gain harmonic generation, HGHG) [2]. The use of HGHG allows us to generate pulses with high longitudinal and transverse

Email address: luka.novinec0008@student.ung.si (Luka Novinec)

coherence, low power fluctuations together with unprecedented spectral stability at wavelengths reaching deep into EUV.

While these light characteristics alone offer new insights into a wide range of scientific research, some of the most intriguing open problems in materials science arise from phenomena taking place at faster time scales, in the few-femtosecond range. This includes physical processes, such as the collapse and recovery of metallic or magnetic states, electron hopping, screening phenomena, or charge transfer mechanisms. Coherent, ultra-short pulse duration also allows the imaging of single molecules and, working like a high-speed camera, enables the creation of molecular movies, potentially revealing the details of physical, chemical, and biological dynamics on an ultra-short timescale.

Several different methods have been proposed and implemented to generate ultra-short pulses in short-wavelength FELs. It is worth noting that pulses in the soft and hard X-ray spectral region have Fourier transform-limited pulse duration shorter compared to pulses in the EUV spectrum. At SASE-based FEL [1], with electron beam formation system based on longitudinal compression, local charge concentration in electron bunch is created after each compressor. It is the leading edge of the bunch, with its high peak current, that is capable of driving the high-intensity lasing process. The longitudinal space charge induces a strong chirp in the bunch and along the high-current spike, which is the lasing portion of the electron bunch. The effect of the energy chirp in the regime of exponential growth leads to shortening of the lasing part of the electron bunch and hence the FEL pulse length with the consequence of the suppression of the FEL gain.

To overcome FEL gain suppression, a self-seeded scheme was proposed [3]. Because of the difficulty of carrying out external seeding at very short wavelengths, the idea of self-seeding the FEL by using X-rays from the first half of the undulator to seed the second half was proposed. The self-seeded mode is established by inserting the diamond crystal in the SASE X-ray beam path to generate the monochromatic, ultra-short seed pulse after the first half of the undulator. Using this pulse to seed the second half of the undulator resulted in pulse bandwidth and temporal duration reduction compared to conventional SASE operation. While this scheme provides higher FEL peak power, pulse power stability and longitudinal coherence remain to be improved.

Another proposed scheme to preserve FEL gain while using the phase-space manipulation method is by combining electron beam energy chirp with a judiciously chosen undulator field taper with a smooth variation of peak magnetic field along the beam propagation axis [4]. The energy chirp is detuning the beam's local resonant frequency which forces the bunch, as is propagating through the undulator, to fall out of the local gain bandwidth. This effect can be compensated, by choosing the undulator taper to allow the continuous gain of a high-current spike initiated in the bunch. Generated radiation maintained high pulse energy and efficiency due to the involvement of the entire beam in the FEL gain while accompanied by a narrowing of the spectral width.

The drawbacks of the above-mentioned methods can be overcome by implementing chirped pulse amplification (CPA) [5] set-up on FEL with an external seed laser. By using coherent external seed, we can generate light at the n th harmonic [6] of the laser wave-

length while preserving a high degree of transverse and longitudinal coherence. Despite the necessity of an additional optical stage, namely CPA, this solution allows the use of the whole electron beam charge obtaining high pulse power with ultra-short duration.

Here we present the use of CPA as broadband and tunable EUV compressor for chirped pulses generated by FEL, together with experimental results obtained on FERMI FEL-1. We will discuss the refurbishment of CPA for the planned experiment on the FERMI FEL-2 and what are the expected results.

2. CPA applied to FEL pulses

The CPA system is a well-known technique in laser physics and can be used to generate extremely high power ultra-short pulses by utilising solid-state lasers [8]. With the capability to produce laser pulses of well over 100 TW of peak power, this system enabled many important areas of scientific research. However, strong absorption of the materials used in conventional laser amplifiers presents one of the technical challenges, limiting the extension in the wavelength below 200 nm.

Since FELs have shown the capability of producing high-power radiation down to the X-ray spectrum, it has been suggested to combine the CPA technique with FEL to generate intense pulses with ultra-short temporal duration at shorter wavelengths. An experiment has been carried out at BNL using a direct seeding scheme producing 800 nm pulses [9]. It was shown that the radiation pulse had larger bandwidth compared to seed while it was compressed to a duration shorter than the seed pulse.

As the CPA-HGHG generated radiation pulses inherit the properties of the seed, a grazing-incidence double-grating compressor, responsible for reducing pulse time duration, is introducing nonzero group delay dispersion to it. The minimal pulse duration, $(\Delta t)_{FEL}^{min}$, after compression can be expressed as:

$$(\Delta t)_{FEL}^{min} = \frac{(\Delta t)_{seed}^{TL}}{n^{1-\alpha}} \quad (1)$$

Where $(\Delta t)_{seed}^{TL}$ is the seed pulse duration at the transform limit in the absence of chirp, n is the harmonic number and α (positive and smaller than 1/2) is a factor depending on the FEL operating regime. From this equation, one may easily find that the transform-limited pulse duration is mainly determined by the duration of the seed laser. For n th harmonic radiation, the transform-limited pulse duration would be n times shorter than that of the seed.

3. Experimental results

3.1. The setup

The CPA system implemented in FERMI FEL facility in Trieste [10] is exploiting classical-diffraction mount (CDM) geometry. It consists of four optical elements: two gratings (G1 and G2 in Fig. 1) and two plane folding mirrors (M1 and M2 in Fig. 1), which steer the

beam back to its original propagation axis. With the variation of the FEL incident angles (δ_1 and δ_2 in Fig. 1) on the gratings, the optical delay between different FEL spectral components can be precisely controlled. The two angles can be varied independently which allows the wave-front tilt compensation, due to the divergence of the FEL beam.

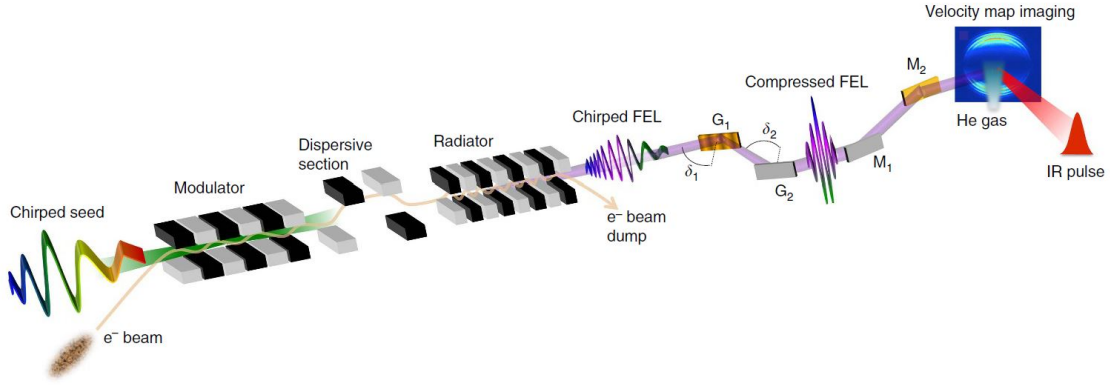


Figure 1: The schematics of CPA mode on FERMI FEL facility. For operating the FEL in the CPA regime, the Gaussian seed laser is modulated to carry linear frequency chirp. After the seed-electron interaction in the modulator, the bunch experiences energy modulation which, when passing the magnetic field of a dispersive section, is transformed into density modulation or micro bunching. In this process, the significant harmonic content and its higher harmonics of the seed frequency are transferred to micro bunches. By tuning the radiator to the n th harmonic of the seed, the passing electrons emit coherently at the frequency $\omega_{FEL} = n\omega_{seed}$. When properly tuned, the FEL harmonic pulse generated at the end of the radiator is carrying the frequency chirp transmitted from the seed pulse. This chirp is compensated by an optical compressor. The compressor consists of four optical elements: two gratings (G1 and G2) in classical diffraction geometry and two plane mirrors (M1 and M2), which steer the beam back to its original propagation axis. The compressed beam is then directed towards the experimental chamber where the FEL pulse duration is measured [10].

The FEL pulse duration was measured using a cross-correlation scheme [7], which relies on the ionisation of a He gas sample by the FEL in the field of an intense infrared laser with variable time delay and known duration (90 fs, FWHM). The measured photoelectron energy spectrum consists of a main line, associated to the direct photoemission process, and of sideband lines, indicating the interaction with the infrared field. The sideband lines are sensitive to the temporal overlap of the FEL and infrared pulses. The cross-correlation curves associated to different sidebands are obtained by integrating the electron signal over all emission angles and plotting the area under the corresponding peaks as a function of the FEL-infrared delay. From resulting area, one can deconvolve the FEL pulse profile.

3.2. The measurements

Initially, the FEL spectrum and pulse duration were characterised under standard working conditions, meaning, no seed stretching and FEL compression. Provided seed laser had a wavelength of $\lambda_{seed}=261$ nm, full width at half-maximum (FWHM) bandwidth was 0.7 nm and its initial, before stretching, FWHM duration was 170 fs. Resulting FEL radiation

FWHM spectral width and pulse duration were, respectively, 3.8×10^{-2} nm and 91 fs (in very good agreement with theoretical prediction, $\simeq 89$ fs).

To operate FEL in the CPA regime, the positive linear chirp has been introduced to seed pulse while stretching it up to 290 fs. The FEL pulse has been characterised before and after the compression. In both cases the average FWHM spectral width was 4.46×10^{-2} nm. For the case of no-compression, the obtained FWHM pulse duration was ~ 143 fs (again, in good agreement with the theoretical prediction of ~ 152 fs, Fig. 2(b)). The increase of the FEL pulse bandwidth with respect to that of the seed, which is the essence of CPA in seeded FELs, enabled obtaining, after compression, a significant shortening of the FEL pulse with respect to the no-CPA case. The FWHM pulse duration after the compression was $\simeq 50$ fs (Fig. 2(c)). This value is quite close to the predicted one by equation (1), that is ~ 40 fs.

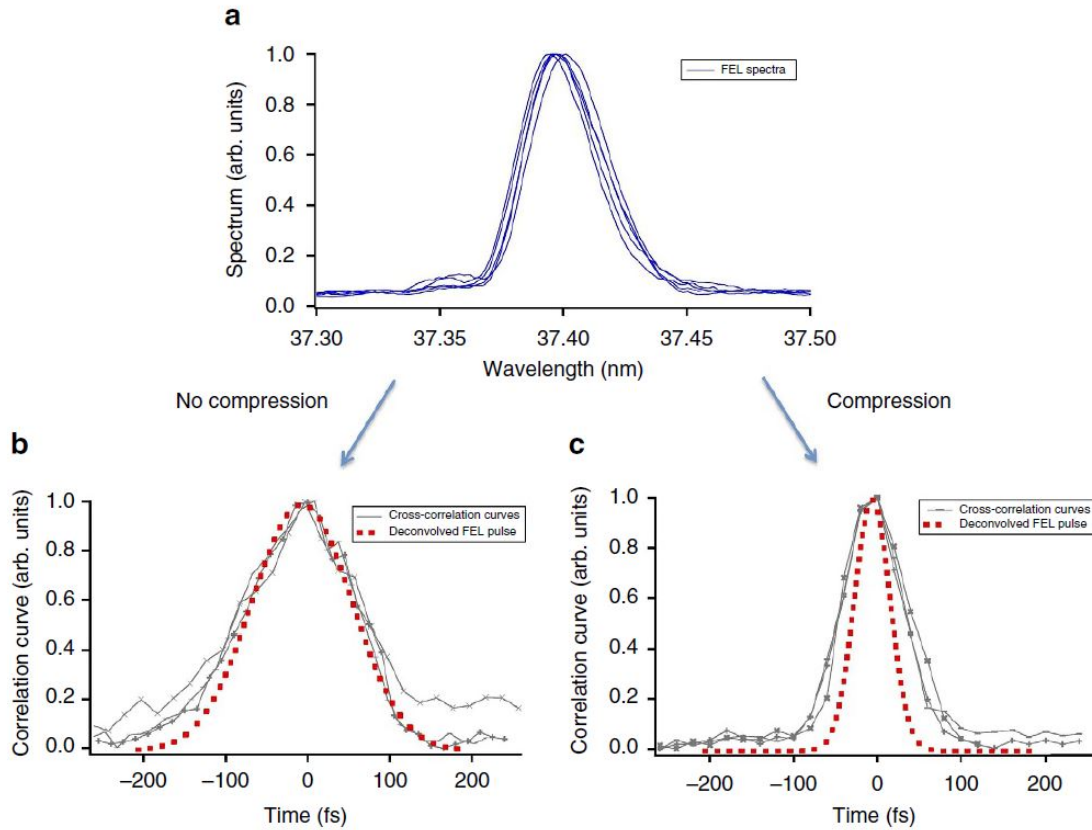


Figure 2: FEL spectro-temporal characterisation. (a) Normalised single-shot spectra of the free-electron laser (FEL) pulse generated after stretching the seed pulse. (b) Three cross-correlation curves associated to the second side-band for three independent FEL-infrared delay scans. The dotted curves represent the deconvolved FEL pulse. (c) Same as b for the FEL operated in CPA mode and the grating angles optimised for maximum compression [10].

These positive results are supporting the predicted application of the CPA to a EUV seeded FEL. The proposed technique enabled the researchers to achieve a relevant reduction of the FEL pulse duration, compared to that obtained in standard operation mode. By adopting the CDM geometry with low transmission ($\sim 5\%$) and relatively small harmonic number ($n = 7$) of generated pulses, limited the obtained peak power to a fraction of a gigawatt.

4. Future experiment

As a natural continuation of the presented experiment, it is proposed to operate FERMI in CPA mode using FEL-2. FEL-2 is a second undulator branch at FERMI, adopting a double cascade HGHG scheme, capable of producing radiation in 4 nm to 20 nm spectral range. This will allow us to generate coherent FEL radiation at high harmonics of the seed ($n = 20$, 13.05 nm), together with a positive energy chirp. In order to optimise the transmission of the CPA set up for a shorter wavelength, new gratings are chosen, based on simulations using ray-tracing code. Two different sets of seed parameters are proposed, where one set would be similar to the parameters used in the above-described experiment, while the other set would be state of the art performance of seed laser system applied at FERMI.

Seed parameters, set 1	Seed parameters, set 2
$(\Delta t_1)_{seed} = 140$ fs (1.2 x transform limit, FWHM)	$(\Delta t_2)_{seed} = 50$ fs (1.2 x transform limit, FWHM)
$(\Delta \lambda_1)_{seed} = 0.7$ nm	$(\Delta \lambda_2)_{seed} = 2$ nm

Table 1: Two sets of seed parameters, to be used in the proposed experiment. First set of parameters with initial FWHM seed-pulse duration of 140 fs and 0.7 nm FWHM bandwidth, while second parameters, representing the state of the art seed laser system performance, with 50 fs of FWHM seed-pulse duration and 2 nm FWHM bandwidth.

From the theoretical calculation, we got the predicted FEL pulse duration and bandwidth after the CPA compression, for two different sets of seed parameters. For the first set of seed parameters, we are expecting the resulting FEL radiation to have FWHM bandwidth of 1.3×10^{-2} nm and 15 fs - 20 fs FWHM pulse duration. In the case of the second seed, with state of the art seed laser system performance, we are expecting to reach 3.7×10^{-2} FWHM bandwidth at 6 fs of FWHM pulse duration.

Since FEL-2 operates in a double cascade HGHG scheme, for every radiator we are seeding a fresh portion of the electron bunch. For this reason, the electron bunch has to be temporally quite long in respect to the one used in the previous experiment. This imposes a challenge since controlling the quality of such beam in terms of current distribution and residual energy chirp, is not trivial at all. Apart from this, there are still some unknowns on how does the chirp imposed by the seed propagate, when the fresh portion of the electron bunch is used. With double cascade HGHG we are lacking information on how does the quality of the radiation, produced by the first stage of FEL-2, influence the pulse properties

and its compression. And with pulse temporal duration in a few-femtosecond time scale, beam diagnostics becomes certainly very demanding.

5. Conclusions

Presented experimental results and proposed improvements are showing the potential to produce, with existing technology, coherent few-femtosecond gigawatt laser pulses. With further studies, fully coherent sub-femtosecond FEL pulses at wavelengths close to the K-absorption edge of oxygen (2.3 nm) are very feasible. This would open new possibilities for using laser-like light with unprecedented temporal resolution for X-ray imaging in the water window.

References

- [1] Ackermann, W. et al., *Operation of a free-electron laser from the extreme ultraviolet to the water window*, Nat. Photonics 1, 336–342 (2007).
- [2] Allaria, E. et al., *Highly coherent and stable pulses from the FERMI seeded free-electron laser in the extreme ultraviolet* Nat. Photonics 6, 699–704 (2012).
- [3] Amann, J. et al., *et al.*, *Demonstration of self-seeding in a hard-X-ray free-electron laser*, Nat. Photonics 6, 693–698 (2012).
- [4] Giannessi, L. et al., *Self-amplified spontaneous emission free-electron laser with an energy-chirped electron beam and undulator tapering*, Phys. Rev. Lett. 106, 144801 (2011).
- [5] Strickland, D. & Mourou, G., *Compression of amplified chirped optical pulses*, Opt. Commun. 56, 219–221 (1985).
- [6] Yu, L. H. et al., *High-gain harmonic-generation free-electron laser*, Science 289, 932–934 (2000).
- [7] Maquet, A. & Taieb, R. *Two-colour IR-XUV spectroscopies: the soft-photon approximation*, J. Mod. Opt. 54, 1487–1857 (2007).
- [8] P. Maine, D. Strickland, P. Bado, M. Pessot, G. Mourou, *Generation of Ultrahigh Peak Power Pulses by Chirped Pulse Amplification*, IEEE Journal of Quantum Electronics QE-24, p.398, (1988).
- [9] L. Yu, T. Shaftan, D. Liu, T. Tsang, J. Rose, X.J. Wang, and T. Watanabe, *Proceedings of FEL 2006*, Berlin, Germany, 2006.
- [10] Gauthier, D., Allaria, E., Coreno, M. et al., *Chirped pulse amplification in an extreme-ultraviolet free-electron laser*, Nat Commun 7, 13688 (2016).

Activation of Methane: Overview of the State-of-the-Art Activation, Electrification, Conversion and Coupling Reactions

Alen Rupnik

*University of Nova Gorica, Vipavska 13, SI-5000 Nova Gorica
National Institute of Chemistry, Hajdrihova 19, SI-1000 Ljubljana*

ABSTRACT: Methane is the main component of natural gas and has a major impact on the environment, so the conversion of methane into more valuable chemicals is of great importance. Activation, conversions and further coupling reactions are means of methane consumption, but also reducing the energy demand for bespoke reactions would improve the final environmental footprint. In general, we know 4 different pathways for methane activation, namely halogenation, dry reforming, dehydrogenation and carbon coupling reactions. Since methane is the hydrocarbon with the highest hydrogen to carbon ratio, it has four strong and localized C-H bonds which makes it difficult for methane to easily participate in chemical reactions. But recently, new reaction mechanisms are emerging where electrocatalysis could present better methane activation mechanisms or reduce the energy required for methane conversion.

1 Introduction

Natural gas is naturally occurring hydrocarbon gas mixture consisting primarily of methane, but also including various other alkenes and sometimes other gases such as carbon dioxide, nitrogen and hydrogen sulfide. Since methane is the main component, it has major impact on the environment and its conversion into higher valuable chemicals is of great importance [1]. Most of methane is burned for heating and generation of electricity, and some small fraction is used for fueling vehicles. In chemical industry the carbon and hydrogen sources are not fully utilized. This is due to fact that methane is the hydrocarbon with the highest hydrogen to carbon ratio, it has four strong and localized C-H bonds which makes it difficult for methane to easily participate in chemical reaction. Nowadays, in industry methane is converted into other chemicals by indirect routes, these processes are mainly steam reforming, dry reforming, and partial carbon oxidation of methane where we get as a reaction product syngas, gas composed of CO and H₂, most often through method of elevated temperatures with pyrolysis at more than 970 K[2,3].

Furthermore syngas is used to make a wide spectrum of hydrocarbons or alcohols with use of catalysts through different power sourced mechanisms [4,5]. Methanol, ethanol and other higher hydrocarbons are more reactive than methane and thermodynamically feasible, the slow kinetics in some cases may be key factor into inhibiting cost efficiency of methanol conversion, so new methods using direct conversion or activation of methane are proposing new, more economically feasible processes. The ultimate goal of recent studies is development of new reaction mechanisms or just using different power sources and reactors to exploit methane resources more efficiently and if possible more clean methodologies. On the other hand, there is a growing interest in non-oxidative methane conversions and coupling reactions, as one bypasses the formation of CO₂ [6]. In the absence of oxygen, methane can be converted to higher hydrocarbons with the release of H₂. All the carbon and hydrogen atoms in the methane molecule are utilized in the form of more valuable added chemicals, so that the carbon and hydrogen atoms are fully utilized. The main methods for non-oxidative methane activation are electrocatalysis, electric field

induced conversion, magnetic field and plasma powered activation, halogenation and thermal dry reforming. This paper will cover more insights into newest reaction mechanisms, catalysts and other processes for activation of methane.

2 Methane activation through electrolysis mechanisms

Electrocatalysis could present better methane activation mechanisms or reduce the energy required for methane conversion. Even just finding the reaction pathways reducing the needed activation energy for H-C bond breaking or hydrogen substitution would benefit the overall natural gas/methane conversion or cost efficiency and through that reduce the greenhouse gas effect. Different up to date researches will be presented in the following chapter.

2.1 Electrocatalysis of methane

PdZn/C electrocatalysts are one of the plausible catalysts for methane electrification and are prepared by sodium borohydride utilized as reducing agent for activation of methane in an acidic medium at room temperature and in a proton exchange membrane fuel cell (PEMFC) at 80°C. The experiments at 80°C in PEMFC showed that the addition of 10% Zn into Pd/C electrocatalyst promote methane activation. Pd(90)Zn(10)/C showed superior performance for methane oxidation, while Zn/C and Pd(70)Zn(30)/C indicated a decrease in kinetics reaction [7].

However, methane conversion and utilization under ambient conditions remains a challenge. Here in this study authors designs a $\text{Co}_3\text{O}_4/\text{ZrO}_2$ nanocomposite for electrochemical oxidation of methane gas using a carbonate electrolyte at room temperature. Co_3O_4 activated the highly efficient oxidation of methane under mild electric energy with the help of carbonate oxidant, which is delivered by ZrO_2 . Based on presented experimental results, is the key intermediate acetaldehyde. During reaction few products are reported: methanol, formaldehyde, ethanol, acetaldehyde, 1-propanol, 2-propanol, and

acetone. After operating at potential of 2.0 V, that being most suitable for methane oxidation, and after 12h of operation, there was almost 40 % conversion of methane achieved. In summary, researchers designed a $\text{ZrO}_2/\text{Co}_3\text{O}_4$ nanocomposite that aids in the regional selective oxidation of CH_4 to 1-propanol and 2-propanol via an electrochemical method. After tracking the products for different reaction times, acetaldehyde was found to be the key intermediate. To convert acetaldehyde to 1-propanol with the participation of CH_4 , a free radical addition reaction was conducted by an electrochemical reaction, with Co_3O_4 as the catalyst and carbonate as the electrolyte. Finally, as a result of competition between reactions, both 1-propanol and 2-propanol were the main product alcohol presented in Fig. 1. This electrochemical partial oxidation of CH_4 may aid in the synthesis of other oxygenates and long-chain hydrocarbons [8].

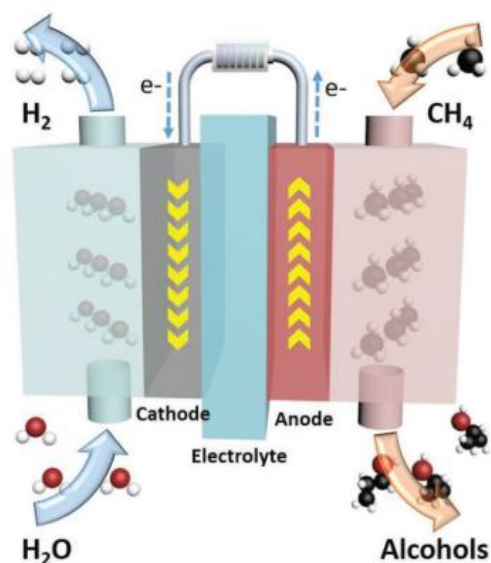


Fig. 1: The electrolytic reaction oxidation reaction of methane. Acquired from [8].

The direct conversion of methane to methanol would enable better utilization of abundant natural gas resources. In the presence of stoichiometric Pt^{IV} oxidants, Pt^{II} ions are capable of catalyzing this reaction in aqueous solutions at modest temperatures. Practical implementation of this chemistry requires a viable strategy for replacing or regenerating the expensive Pt^{IV} oxidant. Herein, R. Soyoung *et. al.*

established an electrochemical strategy for continuous regeneration of the Pt^{IV} oxidant to furnish overall electrochemical methane oxidation. Authors showed that Cl-adsorbed Pt electrodes catalyze facile oxidation of Pt^{II} to Pt^{IV} at low overpotential. Cl-adsorbed Pt surfaces were shown to be competent for the inner-sphere two-electron oxidation of Pt^{II} to Pt^{IV} while inert toward parasitic oxidation of the methanol product [9].

A new method is starting to emerge, possibly based on the idea of solid-state batteries, same for the methane activation when using solid state electrolytes. The application of solid electrolyte reactors for methane oxidation to co-generation of power and chemicals could be interesting, mainly with the use of materials that could come from renewable sources and abundant metals, such as the [6,6'-(2,2'-bipyridine-6,6'-diyl)bis(1,3,5-triazine-2,4-diamine)](nitrate-O)copper(II) complex. The authors searched for the best catalyst composition and methanol producing rates. What they presented is, that the optimal ratio between this complex and carbon was for 2.5 % of carbon, which produces rates of methanol greater than 1 mol L⁻¹ h⁻¹ and decreases from 0.2 to 0 V [10].

2.2 Ionic Liquids as electrolytes

Ionic Liquids (ILs) or as often referred to molten or liquid salts are defined as compounds completely composed of ions and for the last two decades have been the object of intense interest in chemical research. Their main property is melting point and is usually in temperature ranges below 100 °C. The first IL was reported by Paul Walden in 1914, who at the time had no idea how major scientific area will ILs be nowadays. More than 5000 articles have been published in last two decades indicating the exponentially growing interest in ILs, especially multidisciplinary studies including chemistry, materials science, chemical engineering and environmental science [11].

J. Cheng *et al.* demonstrate a versatile method to prepare highly active ternary systems that involve ionic liquids (ILs), inorganic Pt compounds and sulfuric acid (98% and below) for direct methane

conversion to methanol. Main problem arises as many inorganic platinum compounds, such as PtCl₂ or PtO₂, are rarely used in homogeneous catalysis because they are insoluble in typical organic or aqueous solutions, and even in concentrated acids. Authors found that these Pt compounds could be readily dissolved in a variety of ILs upon heating, and were subsequently soluble in concentrated sulfuric acid, forming a homogeneous solution. Suitable ILs found so far include imidazolium, pyridinium, pyrazolium and triazolium-based examples, with chloride (Cl₂) or bisulfate (HSO₄) as the anion. In the case of PtCl₂ + [1-mim][Cl] in 96% H₂SO₄ a methanol concentration of 0.17 M was achieved, which was about 5 times higher than using well known catalytic reaction using (bpy)PtCl₂ [12].

More recent work was done by Z. Whang *et al.* where they showed that at the ionic liquid (IL)/Pt electrode interface, the C–H bond in methane can be activated and abstracted in situ to form methyl radical by electrochemically generated bis((trifluoromethyl)sulfonyl)-amide ([NTf₂]) radicals from the ionic liquid, 1-butyl-1-methylpyrrolidinium bis((trifluoromethyl)sulfonyl)amide ([Bmpy][NTf₂]). Results in this work demonstrate electrochemical anaerobic oxidation of methane to the methyl radical in NTf₂-based ionic liquids at the platinum–[Bmpy][NTf₂] interface. A mechanism is proposed involving multiple steps: (1) electrochemical oxidation of the NTf₂⁻ anion to generate the NTf₂ radical; (2) formation of the Pt-NTf₂• radical adsorbate at the Pt electrode surface; (3) abstraction of the hydrogen atom from methane by the Pt-NTf₂• radical adsorbate to form the methyl radical; and (4) the methyl radical further attacks the NTf₂⁻ anion to form CF₃• which generates additional fragmentation products. ILs not only can be solvents, electrolytes, or reaction media but also can be explored as a precursor for the formation of metal catalysts by electrochemistry. For example, the CF₃• radical generated is important for organofluorination [13].

Ionic liquids unlocked many new reaction pathways and mechanisms for methane conversion. But ILs can not only work as an effective electrolyte or precursor for catalyst formation, but also as an effective

methane soluble media for methane trapping or transporting (Fig. 2). Recently there was work published of spectroscopic evidence of methane dissolution in ionic liquids. From the structural perspective, ILs containing long alkyl chains and C–F bonds showed higher CH₄ solubility. The common properties of these ILs are lower surface tension and molar density, indicating that weaker interactions between cations and anions in the IL network favored CH₄ dissolution. The absorption and desorption energies of CH₄ in the space of IL's network during the dissolution process depend on the strength of the cation–anion network interaction. Reducing the surface tension by adding 0.1 and 0.16 mol of FC-134 with respect to [Bmim][NTf₂] resulted in 39.3% improvement in CH₄ solubility, respectively [14].

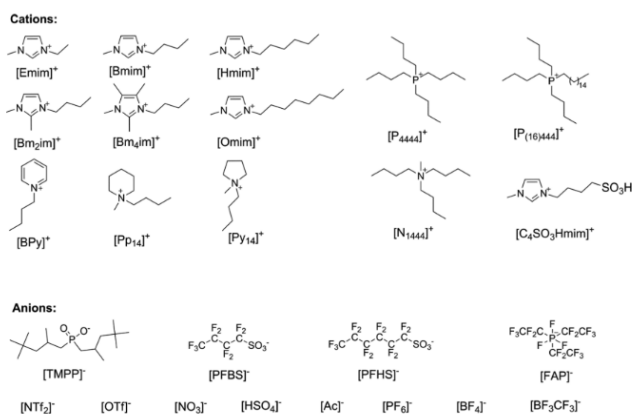


Fig. 2: Ionic liquids for methane dissolution. Acquired from [14].

Ionic liquids present interesting future in electrocatalysis and other electrochemical applications as one can extrapolate from the above presented examples. Their ability for possible engineering of properties makes them perfect for specific systems and processes where unique properties are desirable. Also, their ‘greener’ nature and easy recovery or regeneration gives them big advantage against conventional solvent-like systems. We can only look forward in seeing further development using ILs for methane conversions.

3 Methane activation using electric field source

The form of methane activation is formation of methyl radicals from CH₄, which has a high activation energy due to the high H–C bond dissociation energy (435 kJ mol⁻¹). The oxidative coupling of methane at a low temperature under application of an electric field may be induced by the O₂ activation via electrons running through the surface of TiO₂ located at the interface of TiO₂ and zeolite particles. The TiO₂/ZSM-5 composite and the related samples were exposed to the CH₄/O₂ gas flow in an electric field to evaluate the catalytic properties for the oxidative coupling of methane (OCM) reaction. During the reaction, a certain amount of H₂O was detected as reported by Q. Han *et al.* This strongly supports that the OCM reaction successfully occurred in this catalytic system. In addition, they also observed the production of H₂. It may be caused by the partial oxidation of CH₄ to give H₂ and CO, however, the selectivity to H₂ from CH₄ was still low, which was less than 30%. The OCM reaction is thus pointed out as the main reaction in this catalytic system. In conclusion at constant current of 4.0–8.0 mA applied to the catalyst bed of TiO₂(mc)/ZSM-5_800 at a low reaction temperature of 150 °C, which resulted in high methane conversion (18.4%) with selectivity 8.5% toward C₂H₆ and 15.7% towards C₂H₄, whereas the selectivity toward CO and CO₂ was relatively low at 64.2% and 3.4%, respectively [15].

Further along, there were experiments done, where authors proposed simultaneous activation of two strong H–C bonds with the cationic copper carbide, [Cu⁻C]⁺. In this work, authors report an unprecedented, mechanistically unique Cu⁺-mediated insertion of a carbon atom into two C–H bonds of methane to form ethylene in a single, barrier-less step.

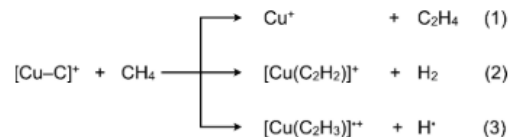


Fig. 3: Branch reaction mechanism for [Cu⁻C]⁺ reaction with methane. Acquired from [16].

In contrast, only a stepwise mechanism was found for the related $[\text{Au}^-\text{C}]^+/\text{CH}_4$ couple. The root cause of this switch from a concerted to a stepwise mechanism can be attributed to the rather different bond dissociation energies of $[\text{M}^-\text{C}]^+$ ($\text{M} = \text{Cu}$ and Au). In addition, arguments are provided showing that the copper ion in the ethylene forming reaction of $[\text{Cu}^-\text{C}]^+$ with methane can be replaced by a positive point charge, hence the term “charge-induced catalysis” is suggested [16].

The role of the electric field and surface protonics on low temperature catalytic dry reforming of methane is investigated by T. Yabe *et. al.* over 1 wt. % Ni/10 mol %La-ZrO₂ catalyst, which shows very high catalytic activity even at temperatures as low as 473 K. Reaction of carbon dioxide and methane offers great decrease of greenhouse gases as we combine two troubling gases and produce more useful product as named before, that being syngas. To implement dry reforming of methane (DRM) reaction as promising process at mild reaction conditions, i.e., lower reaction conditions, electrically promoted DRM, a strongly endothermic reaction, using renewable power is useful as a power-to-gas technology. Based on calculations from CH₄ and CO₂ consumption rate from dry reforming, authors present that activation energy was much lower when the electric field was applied, that being 8.2 kJ mol⁻¹ for CH₄ and 12.1 kJ mol⁻¹ for CO₂, compared to the value without the electric field applied the values were 66.1 kJ mol⁻¹ for CH₄ and 62.3 kJ mol⁻¹ for CO₂. Results show that the apparent activation energy decreased with the electric field, indicating that the reaction mechanisms with the electric field differ considerably. Results of the TOF study demonstrate that DRM activities in the electric field exhibit strong dependence on the Ni perimeter, rather than on the Ni specific surface area, which indicates that activation for CH₄ and CO₂ dissociation in the electric field proceeds mainly at the Ni–La-ZrO₂ interface [17].

Step further in electric field assisted catalysis is powering or heating the catalyst using electromagnetic, microwave (MW) heating power source. Reactor system consisting of a SiC structured reactor coated with Mo-ZSM5 catalyst, heated in a

cylindrical microwave cavity was presented by the authors. They have demonstrated that the temperature control of the catalytic monolith under MW-heating is possible despite the change of its dielectric properties due to eventual coking. The catalytic activity of the Mo-ZSM5@SiC structured was evaluated under MW and conventional heating at the same temperature, 700 °C, resulting in similar conversion but totally different product distribution. The coke formation under conventional heating is twice as big as the amount observed under MW heating. Results of methane conversion and selectivity are presented in Fig. 4 [18].

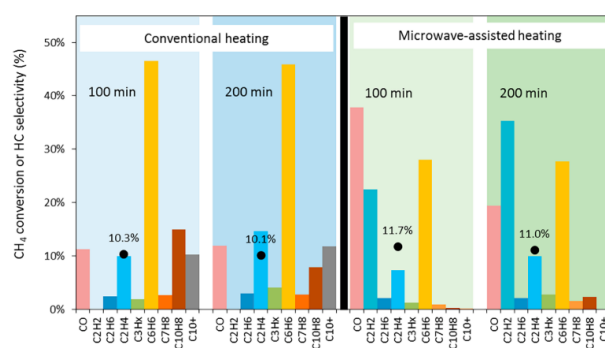


Fig. 4: Methane conversion and selectivity towards hydrocarbon products. Acquired from [18].

As we can see there are many different methodologies being developed for electric field assisted/powering methane conversion. Some of them resulted in new reaction pathways, reducing the activation energies resulting in similar or better conversion to classical well-known methods, but resulting in smaller energy consumption to do so. The key ingredient for even better conversion and efficiency would be combining right reactor set-up with the use of the right catalyst.

4 Methane activation using induction heating power source

Dry reforming of methane represents the lowest cost route to the production of syngas from biogas with reaction $\text{CH}_4 + \text{CO}_2 \leftrightarrow 2\text{CO} + 2\text{H}_2$ with enthalpy of $\Delta H^\circ = 247 \text{ kJ mol}^{-1}$ whereas steam reforming applied catalytic process used to date is the most industrially used process today. The main obstacle to the

industrial implementation of DRM is the absence of commercial catalysts with a proven high activity and stability and reduced coke formation. The most active metals for the DRM are those from transition metals Ni being the most commonly used because of its availability and price. Recent studies have focused on the development of complex mixed metallic oxides with a perovskite structure as they are suitable for methane conversion with dry reforming. M. Pérez-Camacho *et. al.* presented metal reactor with induction heating (IH) mechanism for heating the catalyst at a rate up to 100 °C/min. High conversions are reached as presented in table below:

Tab. 1: Methane and carbon dioxide conversions and H₂/CO ratio for the catalytic experiment of dry reforming of methane using IH. Acquired from [19].

Actual P (kW)	Current (A)	T _{catalytic bed} (°C)	CH ₄ conversion	CO ₂ conversion	H ₂ /CO ratio
121.92	69.5	557	20%	25%	0.48
142.21	75.4	624	30%	40%	0.50
189.28	86.4	707	60%	70%	0.90
245.74	98.1	785	80%	85%	0.95
312.43	110.5	863	90%	94%	0.98

Not only that the IH dry reforming is more effective and reaching high conversions, but also the authors presented data that indicates slower rates of carbon producing when using induction heated catalyst is around 4 times smaller than in comparison to carbon formation when using classical thermal heating of catalyst [19].

Work done by F. Varsano *et. al.* presents experimental results on the catalytic activation of dry reforming powered by induction heating. Energy is supplied by a radiofrequency alternating magnetic field to Ni₆₀Co₄₀ alloy that works at the same time as catalyst for the reforming reaction and heat generator by dissipation of the electromagnetic energy. This way the heat of reaction is directly provided by the catalytic bed, avoiding dissipation due to inefficient transfer from outside of the reactor. Temperatures higher than 850 °C are easily reached using Ni₆₀Co₄₀ pellets as heat mediators in a continuous-flow fixed-bed reactor. At this temperature methane conversion and hydrogen production occurred with yield comparable to those obtained by conventional heating. As expecting, with increasing power to

induction heater, the conversion and temperature are also increasing. The conversions of methane higher than 70 % were reached at yields of CO and H₂ reaching also almost up to 70 % at temperatures of 850 °C. The effect of size and shape of packed powdered catalyst was also presented, where the authors concluded that disc shaped packed bed (300 mg) reached almost 90 % conversion of methane with yield of CO reaching up to 90 %. The results obtained for this catalyst are very promising for the application of magnetic induction in dry reforming, particularly considering that the alloy is not dispersed nor supported on an inert substrate and that annealing phenomena could in principle deactivate it [16,17].

Magnetic field acceleration of CO₂ reforming of methane over a novel hierarchical Co/MgO catalyst in fluidized bed reactor is reported by J. Li *et. al.* The hierarchical Co/MgO catalyst shows good fluidization quality and is suitable for efficient CO₂-CH₄ reforming in fluidized-bed reactor. Compared to the conventional fluidized bed reactor (CFB), the hierarchical Co/MgO catalyst shows better conversions of CO₂ and CH₄, higher turnover rate, and higher resistance to coke deposition in the magnetic assisted fluidized bed (MFB) reactor. In the temperature range of 700–900 °C, the calculated apparent activation energy (E_a) values were 78.1 kJ mol⁻¹ and 80.4 kJ mol⁻¹ for MFB reactor and CFB reactor respectively. The E_a value obtained from MFB reactor was slightly lower than the one from CFB reactor. These results indicated that the apparent activation energy of the CH₄-CO₂ reforming reaction is reduced by the magnetic field. The hierarchical Co/MgO catalyst in the MFB reactor exhibited higher turnover rates than the CFB reactor at the same condition. Compared to the CFB reactor, the conversions of CO₂ and CH₄ were improved by 22% and 30% respectively in the MFB reactor at 800 °C with high gas hourly space velocity (GHSV) of 15×10⁴ h⁻¹. The hierarchical Co/MgO catalyst in the MFB reactor showed not only higher resistance to coke deposition than that in the CFB reactor, but also restrained the transformation of Co nanoparticles from surface of MgO to carbon tubes [22].

5 Conclusions and Outlook for the future

A lot of work has been done in the fields of methane activation and conversion, we can see few interesting and promising methods, but in order for one method to take place in all the abundant methane conversion a lot is still to be done. Combining dry reforming or partial oxidation of methane to produce syngas with other thermo-electrical methods is a promising field, that could be the one in the future especially combining green electricity from renewable sources to produce more power from natural gas sources.

New forms of providing power for methane conversion/activation reactions such as electric field induced conversion, magnetically induced reaction, microwave power source and electrolysis are promising methods, for better or cleaner conversion of natural gas, or more primarily methane and CO₂ conversion into syngas. A lot is still to be done and researched, but above presented researches give good and promising results towards greener, better world. The key next step could be combining few of the mentioned above technologies or catalysts, to achieve the best possible process for natural gas conversion into more valuable added products. We can only look forward to what will happen in the future.

1. Literature

- [1] E. McFarland, "Unconventional chemistry for unconventional natural gas," *Science*, vol. 338, no. 6105. American Association for the Advancement of Science, pp. 341–342, Oct. 19, 2012.
- [2] "Hydrogen and Syngas Production and Purification Technologies - Ke Liu, Chunshan Song, Velu Subramani - Google Knjige.(accessed from web on Jun. 04, 2021).
- [3] K. Göransson, U. Söderlind, J. He, and W. Zhang, "Review of syngas production via biomass DFBGs," *Renewable and Sustainable Energy Reviews*, vol. 15, no. 1. Pergamon, pp. 482–492, Jan. 01, 2011.
- [4] W. Zhou *et al.*, "Direct conversion of syngas into aromatics over a bifunctional catalyst: Inhibiting net CO₂ release," *Chem. Commun.*, vol. 56, no. 39, pp. 5239–5242, May 2020.
- [5] L. Liu *et al.*, "Conversion of syngas to methanol and DME on highly selective Pd/ZnAl₂O₄ catalyst," *J. Energy Chem.*, vol. 58, pp. 564–572, Jul. 2021.
- [6] K. Sun, D. M. Ginosar, T. He, Y. Zhang, M. Fan, and R. Chen, "Progress in Nonoxidative Dehydroaromatization of Methane in the Last 6 Years," *Industrial and Engineering Chemistry Research*, vol. 57, no. 6. American Chemical Society, pp. 1768–1789, Feb. 14, 2018.
- [7] J. Nandeha, "Activation of Methane on PdZn/C Electrocatalysts in an Acidic Electrolyte at Low Temperatures," *Int. J. Electrochem. Sci.*, pp. 10819–10834, Dec. 2019.
- [8] M. Ma *et al.*, "Ultrahigh Electrocatalytic Conversion of Methane at Room Temperature," *Adv. Sci.*, vol. 4, no. 12, Dec. 2017.
- [9] R. S. Kim and Y. Surendranath, "Electrochemical Reoxidation Enables Continuous Methane-to-Methanol Catalysis with Aqueous Pt Salts," *ACS Cent. Sci.*, vol. 5, no. 7, pp. 1179–1186, Jul. 2019.
- [10] L. M. S. Garcia *et al.*, "Conversion of Methane into Methanol Using the [6,6'-(2,2'-Bipyridine-6,6'-Diyl)bis(1,3,5-Triazine-2,4-Diamine)](Nitrate-O)Copper(II) Complex in a Solid Electrolyte Reactor Fuel Cell Type," *ACS Omega*, vol. 5, no. 26, pp. 16003–16009, Jul. 2020.
- [11] Z. Lei, B. Chen, Y. M. Koo, and D. R. Macfarlane, "Introduction: Ionic Liquids," *Chemical Reviews*, vol. 117, no. 10. American Chemical Society, pp. 6633–6635, May 24, 2017.
- [12] J. Cheng, Z. Li, M. Haught, and Y. Tang, "Direct methane conversion to methanol by ionic liquid-dissolved platinum catalysts," *Chem. Commun.*, no. 44, p. 4617, 2006.
- [13] Z. Wang, A. Kumar, M. D. Sevilla, and X. Zeng, "Anaerobic Oxidation of Methane to Methyl Radical in NTf₂-Based Ionic Liquids," *J. Phys. Chem. C*, vol. 120, no. 25, pp. 13466–13473, Jun. 2016.
- [14] T. Huang *et al.*, "Structural Dependence and Spectroscopic Evidence of Methane Dissolution in Ionic Liquids," *J. Phys. Chem. B*, vol. 122, no. 22, pp. 6007–6016, Jun. 2018.
- [15] Q. Han, A. Tanaka, M. Matsumoto, A. Endo, Y. Kubota, and S. Inagaki, "Conversion of methane to C₂ and C₃ hydrocarbons over TiO₂/ZSM-5 core-shell particles in an electric field," *RSC Adv.*, vol. 9, no. 60, pp. 34793–34803, 2019.

- [16] C. Geng, J. Li, T. Weiske, M. Schlangen, S. Shaik, and H. Schwarz, "Electrostatic and charge-induced methane activation by a concerted double C-H bond insertion," *J. Am. Chem. Soc.*, vol. 139, no. 4, pp. 1684–1689, Feb. 2017.
- [17] T. Yabe *et al.*, "Role of Electric Field and Surface Protonics on Low-Temperature Catalytic Dry Reforming of Methane," *ACS Sustain. Chem. Eng.*, vol. 7, no. 6, pp. 5690–5697, Mar. 2019.
- [18] I. Julian, H. Ramirez, J. L. Hueso, R. Mallada, and J. Santamaria, "Non-oxidative methane conversion in microwave-assisted structured reactors," *Chem. Eng. J.*, vol. 377, Dec. 2019.
- [19] M. N. Pérez-Camacho, J. Abu-Dahrieh, D. Rooney, and K. Sun, "Biogas reforming using renewable wind energy and induction heating," *Catal. Today*, vol. 242, no. Part A, pp. 129–138, Mar. 2015.
- [20] F. Varsano, M. Bellusci, A. La Barbera, M. Petrecca, M. Albino, and C. Sangregorio, "Dry reforming of methane powered by magnetic induction," *Int. J. Hydrogen Energy*, vol. 44, no. 38, pp. 21037–21044, Aug. 2019.
- [21] F. Varsano, M. Bellusci, A. Provini, and M. Petrecca, "NiCo as catalyst for magnetically induced dry reforming of methane," *IOP Conf. Ser. Mater. Sci. Eng.*, vol. 323, no. 1, p. 012005, Mar. 2018.
- [22] J. Li, J. Li, Q. Zhu, and H. Li, "Magnetic field acceleration of CO₂ reforming of methane over novel hierarchical Co/MgO catalyst in fluidized bed reactor," *Chem. Eng. J.*, vol. 350, pp. 496–506, Oct. 2018.

*This exact paper was written as an illustrative method of scientific paper writing skill for subject and learning purposes only and it's not publishable under any circumstances.

Processing experimental data on Coil-helix-coil transitions in a polypeptide chain in solution using Zimm-Bragg model

Knarik Yeritsyan

University of Nova Gorica, Vipavska 13, SI-5000 Nova Gorica

Abstract

For the description of conformational transitions in biopolymers and for processing experimental data the simplest approach is Zimm-Bragg(ZB) model, first represented in the late 1950s. Different methods were used to take into account water effects or other factors and complete the theory. At the same time simplifications in the partition function were done for this model to be convenient for numerical calculations of experimental data processing. We review the model and study a number of works done in this field and try to analyze different extensions and variations of this model.

Keywords: Zimm-Bragg model, helix-coil transition, thermal unfolding

1. Introduction

Polymers are macromolecules made of covalently bonded elementary repetitive units called monomers. A polypeptide molecule is made from a long unbranched sequence of amino acids. Amino acids are organic compounds that contain amino ($-\text{NH}_2$) and carboxyl ($-\text{COOH}$) functional groups, along with a side chain (R group) specific to each amino acid. The key elements of an amino acid are carbon (C), hydrogen (H), oxygen (O), and nitrogen (N) [1]. Proteins execute the majority of the cell's functions which may contain one or more polypeptide chains. Proteins in cells have fixed 3D structure that determines their function. The protein folding and unfolding is of one of the most important topics of biophysics. During the folding process the string of amino acids interacts with itself to form a stable three-dimensional structure. One of the folding substructures of protein is α -helix. The helical structure of polypeptides is mainly stabilized by H-bonding between the N-H and C amide and carbonyl groups of the main chain. H-bond attractions can occur between different molecules, which is called intermolecular H-bonding, or within different parts of a single molecule, which is called intra-molecular H-bonding [2]. When the biopolymer is immersed into the H-bonding network made by the solvent molecules, there apparently exists the competition between the inter- and intramolecular H-bonds. At a certain temperature, the intrapolypeptide H-bond will be substituted by the polypeptide-solvent one and vice

Email address: knarik.yeritsyan@ung.si (Knarik Yeritsyan)

versa. These changes are referred as helix-coil transition or cold denaturation. The helix coil transition is not a real phase transition but is a cooperative transition between a molecule being in a mostly helical state, and a mostly coiled state.

Polypeptides form a helical structure which is stable because of the stacking of the amine bases and of the hydrogen bonding between them. The helical structure is effective at "hiding" the hydrophobic sugar groups from contact with water. DNA macromolecules form helical structures in their active form and melt to a random coil phase in their denatured form. The denaturation transition consists in a helix-to-coil transition. In order to describe these phenomena a number of models are developed. Helix-coil transition models are statistical mechanics techniques to describe conformations of linear polymers in solution. One of the most common transition models is the Zimm-Bragg (ZB) [3] model with its extensions and variations.

To describe the thermal unfolding of proteins Seelig et al [7] used ZB α -helix-to-random coil transition theory for synthetic polypeptides and the two-state model which predicts only two types of protein molecules in solution: native and unfolded. Measurements were done for apolipoprotein A-1 and lysozyme by differential scanning calorimetry (DSC) and CD spectroscopy and based on experimental data differences between the two-state model and the Zimm-Bragg theory are investigated. For all proteins the experimental data of calorimetric unfolding transitions was perfectly fit on Zimm-Bragg model but the enthalpies and transition curves from two-state model are not in agreement with experimental results. This states that the unfolding of proteins can also be analyzed with ZB transition theory.

Murza and Kubelka [14] investigated the helix-coil transitions of 21-residue alanine peptide with ZB model using different numbers (up to 4) of nearest neighbor approximation. For calculations is used matrix method that considers combinations of any number of helical sections of any length. The model parameters were determined by global fitting the temperature-dependent circular dichroism and Fourier transform infrared experimental spectra. The four nearest neighbor variants of ZB model is used to describe the helix-coil transition in alanine-based peptides and they are compared with each other. The consequences of long-range interactions predictions are discussed for ZB model. All nearest-neighbor variants of the model are capable of fitting the experimental data equally well however probability distributions, free energy and ZB model parameters differ by the change of range of interactions.

Qian and Schellman [11] studied different helix-coil transition theories for finite length polypeptides and compared with each other. The physical parameters of helix-coil theory are examined and represented from the newer point of view. The primary focus is on Lifson-Roig [4] and Zimm-Bragg models, for both theories the physical assumptions are examined and was found a relationship between them. There was developed some more details for helix-coil model which will be useful for experiments.

Ren et al [18] did experiments were synthesized synthetic homopolypeptide samples with different lengths and helix-coil transitions were observed for different lengths. The results were compared with Schellman and ZB models. For short chains the ZB model gave a good global fit while for long chains it didn't fit the data. The inaccuracy may be due to the

approximations used in ZB model in order to simplify calculations. But the inaccuracy mostly comes from non-local intramolecular interactions which are not considered in the model. In case of longer chains the entropic effect causes interrupted helix conformation and these conformations also need to be considered in the partition function.

Doig [13] reviewed Zimm-Bragg and Lifson-Roig helix-coil transition theories. There was discussed newly known structural features of helices and including of that features in helix-coil models. There are number of ways to develop helix-coil models:

- (1) including additional interactions, such as side chain interactions, or more structurally complex C-capping motifs
- (2) including conformations in addition to helix and coil
- (3) including quaternary, tertiary structure of proteins
- (4) improvement of the treatment of the random coil

These developments give arise to the complex and unwieldy form of the partition function which makes it difficult for calculations.

Our goal is to study ZB model and its usage on different experimental profiles and estimate its validity in different situations.

2. Classical definition of Zimm-Bragg model

2.1. The Model

The helix-coil transition of a polypeptide chain Zimm and Bragg [3] discussed by referring to a simple model which allows bonding only between each group and the third preceding group. Two model parameters are taken into account: stability parameter s and cooperativity parameter σ . Stability parameter s has both enthalpic and entropic contributions. It has the meaning of a statistical weight, and is usually represented in terms of a (Gibbs or Helmholtz) free energy change between the helix and coil states:

$$s = e^{-\beta(G_{helix} - G_{coil})}. \quad (1)$$

The cooperativity parameter σ has entropic contribution and describes how much is the original probability of helix growth. There is also a third parameter k specifying the minimum number of segments in a random section between two helical parts which is considered to be unity in order to have a simple representation. Since this consideration is valid for only one unbroken helical sequence in the chain, the formulation is useful for short chains as it has a minor effect to the results. Using the fact that every repeat unit is in helical or coil state, for estimation of partition function Zimm and Bragg made specific assumptions about the statistical weights related to the particular state of the chain:

- (1) For every repeat unit in coil state a statistical weight is 1
- (2) For every helical segment following another helical segment is s
- (3) For every helical segment following two or more coil segments is σs
- (4) For every helical segment following less than two coil segments is 0

A number of methods can be used to calculate the partition function in this model:

- (*) Single sequence approximation suitable for short chains
- (*) Kramers and Wannier Transfer Matrix method
- (*) Generating function method (Ising method)

2.2. The Transfer Matrix Method

It appears, that any attempt to use all the terms in partition function will lead to very complicated expressions for large chain length N . Fortunately, there are several well-known approaches to simplify expressions. One of the important simplification is to consider that H-bonding affects only on first nearest neighbour. Taking into account only nearest neighbor interactions and following the transfer-matrix approach of Kramers and Wannier, the matrix of statistical weights of ZB model was constructed as:

$$\widehat{M}_{ZB} = \begin{array}{|c|cc|} \hline & i+1 & \\ \hline i & h & c \\ \hline h & s & 1 \\ c & s\sigma & 1 \\ \hline \end{array} = \begin{pmatrix} s & 1 \\ s\sigma & 1 \end{pmatrix} \quad (2)$$

The ZB model allows derivation of the thermodynamic properties of the system from the solutions of the characteristic equation for the transfer matrix Eq. (2)

$$|\widehat{M}_{ZB} - \widehat{I}\lambda| = 0, \quad (3)$$

where \widehat{I} is the unit matrix

$$\widehat{I} = \begin{pmatrix} 1 & 0 \\ 0 & 1 \end{pmatrix}. \quad (4)$$

Combining (2),(3) and (4) equations, we will get

$$\begin{vmatrix} s - \lambda & 1 \\ s\sigma & 1 - \lambda \end{vmatrix} = 0. \quad (5)$$

Solving Eq. (5) determinant we will arrive at the explicit expression for the characteristic equation in the form of second order polynomial in λ

$$\lambda^2 - (s + 1)\lambda + s(1 - \sigma) = 0. \quad (6)$$

From Eq. (6), the eigenvalues are:

$$\lambda_{1,2} = \frac{1}{2} \left[1 + s \pm \sqrt{(1 - s)^2 + 4\sigma s} \right]. \quad (7)$$

By assigning values (from the experimentally justified range) to the temperature-independent parameter σ we can plot the dependence of eigenvalues over parameter s .

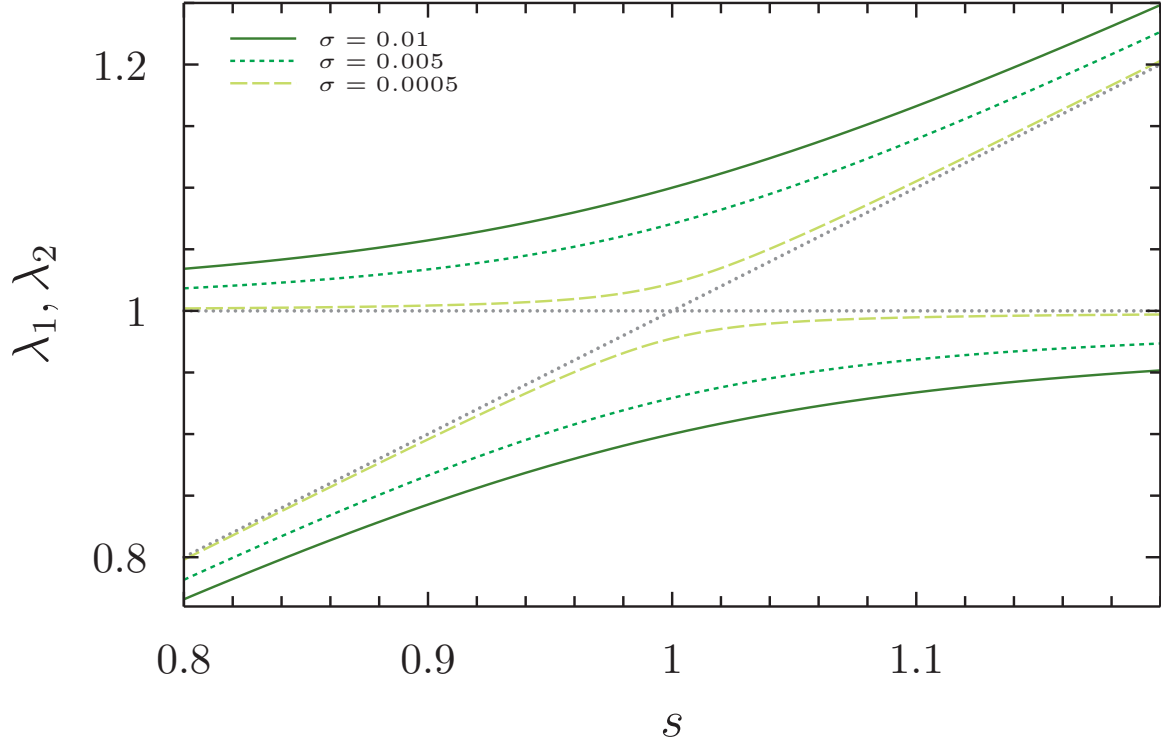


Figure 1: Eigenvalues dependence over parameter s for different values of parameter σ . Gray dotted lines show asymptotes s and 1 .

Eigenvalues come closest together at a point where the asymptotes cross. This happens because the transition takes place at the point where entropy and energy compensate each other. The partition function is

$$Z(\sigma, s) = C_1 \lambda_1^N(\sigma, s) + C_2 \lambda_2^N(\sigma, s), \quad (8)$$

where N is the number of repeat units in the entire chain, $C_1 = \frac{1-\lambda_2}{\lambda_1-\lambda_2}$, $C_2 = \frac{\lambda_1-1}{\lambda_1-\lambda_2}$. The degree of helicity in ZB model is defined through the partition function and eigenvalues, and in terms of model parameters s and σ reads as:

$$\theta(\sigma, s) = \frac{1}{N} \frac{\partial \ln Z}{\partial \ln s}, \quad (9)$$

For very large N the partition function reads $Z = \lambda_1^N$ and is clearly dominated by the largest eigenvalue, λ_1 . The degree of helicity is then given approximately by

$$\theta(\sigma, s) = \frac{1}{N} \frac{\partial \ln \lambda_1^N}{\partial \ln s} = \frac{\partial \ln \lambda_1}{\partial \ln s} = \frac{s}{\lambda_1} \frac{\partial \lambda_1}{\partial s} \quad (10)$$

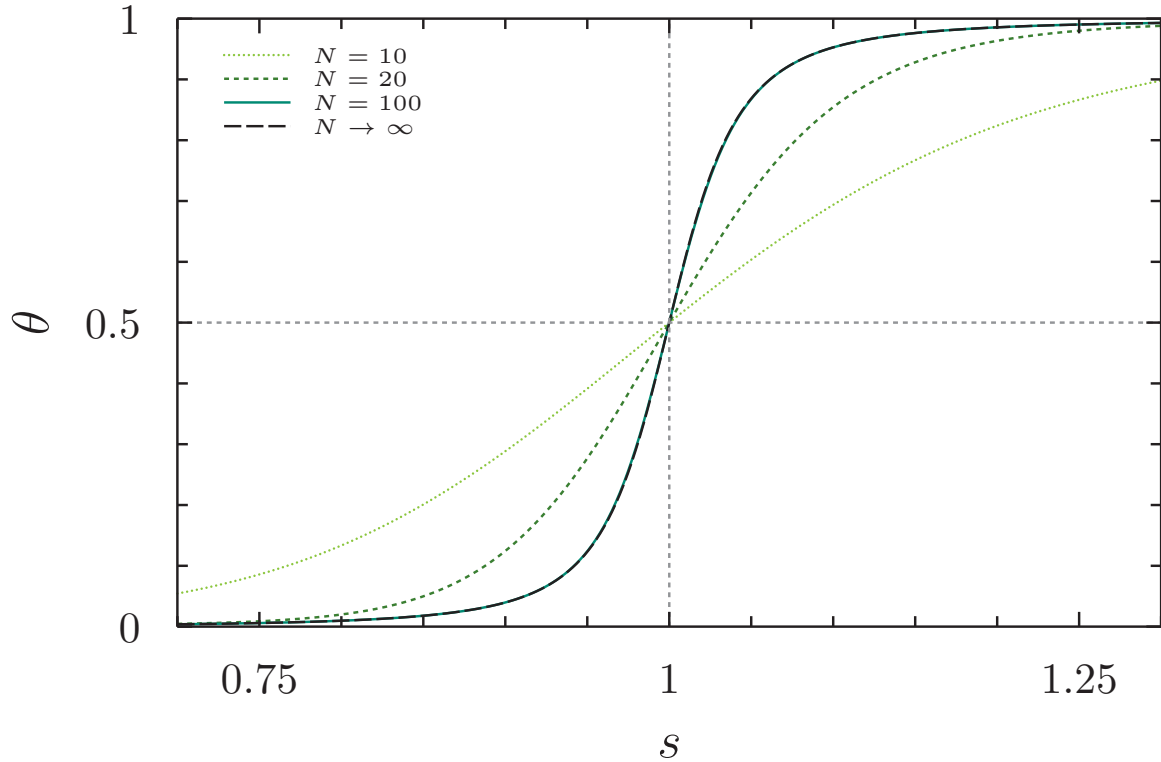


Figure 2: The degree of helicity dependence over parameter s for different values of number of repeat units N and fixed $\sigma = 5 \times 10^{-4}$. The curves for $N = 10, 20, 100$ are plotted from the exact expression Eq. 9, and the $N \rightarrow \infty$ curve is from the approximate Eq.10.

As we see from the Figure 2 when the number of repeat units becomes more than 100, the helicity degree curves overlap with those for $N \rightarrow \infty$ case. It means that for the study of helix-coil transition in natural proteins, the care should be always taken with respect to the length of polypeptides, and for the systems shorter than 100 repeat units, it may be meaningful to apply the exact formula Eq. (9), which is anyway not that difficult to implement.

After studying the dependence of the helicity degree over chain length N , it is also interesting to study, how will the curves look like at infinite chain length, but different values of σ . In principle, Figure 1 suggests, that when σ becomes smaller, the eigenvalues come closer and closer to each other. For the helicity degree smaller σ s result in sharper transitions, as is clearly visible in Figure 3.

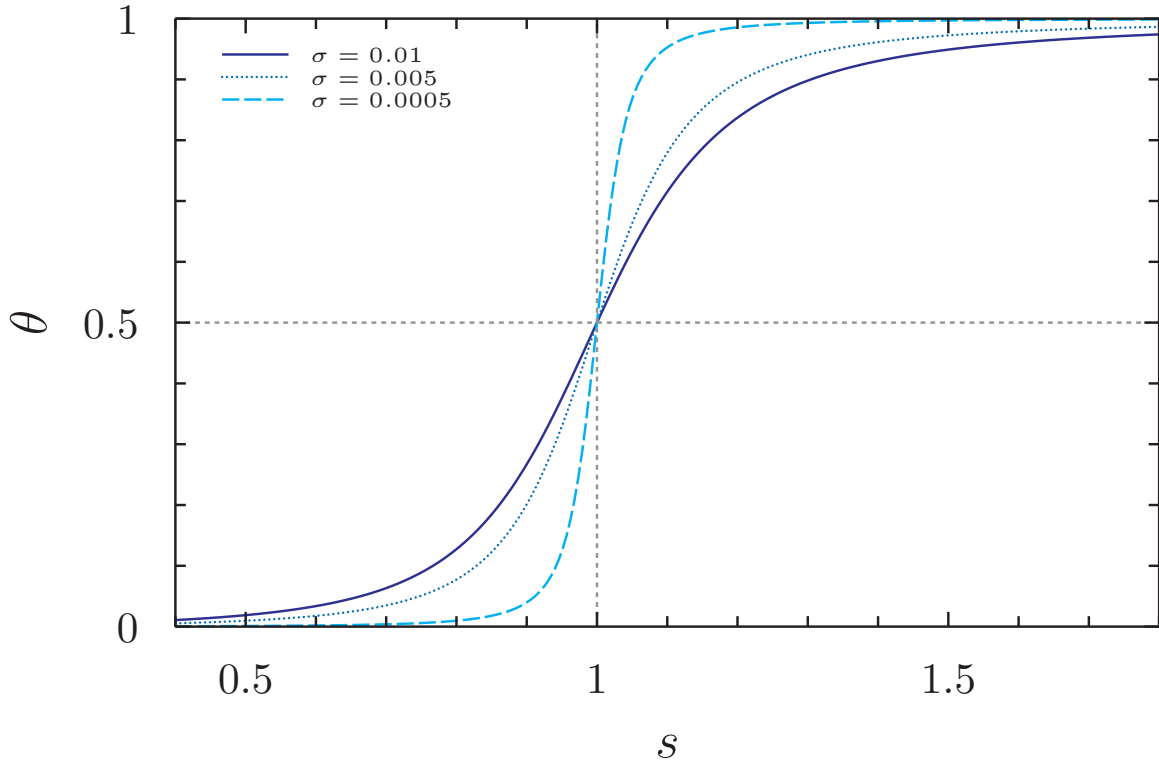


Figure 3: The degree of helicity dependence over parameter s for different values of parameter σ and for $N \rightarrow \infty$. Plotted from Eq. (10).

By changing the value of bonding parameter for short chains we will have different configurations of the chain: random coils or single helices occasionally disordered at the ends. For longer chains we will have helices occasionally broken by random sections.

Zimm and Bragg used published experimental data for polyhenzyl-glutamate to compare with theory. Fair agreement is found between the model results and the experiment.

2.3. The Generating Function Method

Applequist [9] presented one of the first studies where helix-coil transition theory was applied to experimental results. Zimm, Doty and Iso [5] demonstrated methods of obtaining theoretical fitting parameters from experimental data. The goal was to derive an equation in a way that will have simpler relationships between the basic parameters and observable quantities. For this purpose the partition function described by Zimm and Bragg is chosen and the relatively simpler terms of molecular states distribution of helix-coil transition is used. The matrix method was used by Zimm and Bragg to derive a partition function for a particular case while Applequist used the same mathematical method as Ising [6] used to discuss ferromagnetism of one-dimensional system. To find the sum he wrote a power series

in an arbitrary variable x as:

$$F(x) = \sum_{N=0}^{\infty} Z_N x^N, \quad (11)$$

where $F(x)$ is the grand partition function. Z_N can be obtained by finding the general coefficient of the power series expansion. Doing modifications we will get the following characteristic equation:

$$\lambda^{\mu-1}(\lambda-1)(\lambda-s) = \sigma s \quad (12)$$

Eq. (12) is identical to Eq. (6) which was solved by Zimm and Bragg with the transfer matrix method. By this approach a general formula is derived in which the partition function is reduced for the simplest case. Then the application of this formula is discussed for long chains. For the chains of any length an exact closed expression of the partition function is obtained as a result.

$$Z = \sigma s \sum_{i=0}^{\mu} \frac{\lambda_i^{N+\mu+1}}{(\lambda_i-1)[(1+s)\lambda_i^{\mu} - 2s\lambda_i^{\mu-1} + (\mu+1)\sigma s]}, \quad (13)$$

where parameter μ specifies the minimum possible number segments involved in a break in the helix. Some experimental data of helix-coil transition is used to compare with the theoretical results. This states that the matrix method used by Zimm and Bragg is not the only solution and the Ising method can also be adapted to derive a partition function.

2.4. Single Sequence Approximation of the Partition Function

A representation of the partition function Z for a chain of N repeat units may be obtained from the above assumptions 2.1 by direct enumeration of the number of ways of arranging a given number of bonded and unbonded states in a chain always starting with three unbonded. For short chains the conditions under which the helix will be formed is when $N\sigma$ is small and s is appreciably greater than unity. Physically, this corresponds to conditions under which only one helical section (unbroken sequence of bonded sections) would be expected. It is easy to show that the expression $d \ln Z / d \ln s$ is the average number of hydrogen bonds formed in the chain at a given value of s , since the number of hydrogen bonds in any state is equal to the power of s in the corresponding term in the partition function. The degree of helicity θ is defined as the fraction of possible hydrogen bonds formed,

$$\theta = \frac{1}{(N-4)} \frac{d \ln Z}{d \ln s}. \quad (14)$$

Keeping only the first term of the summation the final expression for helicity degree will be following:

$$\theta = \frac{(N-4)(s-1) - 2 + [(N-4)(s-1) + 2s]s^{1-N}}{(N-4)(s-1)1 + (s-1)^2 s^{-N} / \sigma - [(N-4)(s-1) + s]s^{1-N}}. \quad (15)$$

Eq. (15) is useful for calculation for small values of N (for short chains). Since they are valid only when there is one unbroken helical sequence in the chain, they are independent of the parameter μ .

3. Hamiltonian formulation of ZB model

Hamiltonian formulation of ZB model is presented in [16]. Model is based on three parameters: the energy parameter $W = V + 1 = e^{U/T}$, where U is the energy of the H-bond and T is the temperature; the parameter Q of entropic origin which is the ratio between the number of all accessible states versus the number of states in the helical conformation; and a geometric parameter Δ , that describes the geometry of H-bond formation. Assume that the spin variable γ_i describes the state of the i th repeated unit and can take one of Q values, where $\gamma_i = 1$ describes the repeat unit in ordered, helical state, while the other $Q - 1$ identical values are for the coil state. $Q \geq 2$ condition describes the degeneracy of the coil state. The Hamiltonian of this model is

$$-\beta H(\{\gamma_i\}) = J \sum_{i=1}^N \delta_i^{(\Delta)}. \quad (16)$$

where $\beta = 1/k_B T$, N is the number of repeat units, and $J = U/T$ is the temperature-reduced energy of H-bonding between polymeric units, $\delta_i^{(\Delta)} = \prod_{k=0}^{\Delta-1} \delta(\gamma_{i+k}, 1)$ stands for the Kronecker symbol.

We will consider only a nearest-neighbor interaction, $\Delta = 2$, so the the Hamiltonian of ZB model will write

$$-\beta H(\{\gamma_i\}) = J \sum_{i=1}^N \delta(\gamma_i, 1) \delta(\gamma_{i+1}, 1). \quad (17)$$

The partition function Z can be obtained as

$$Z(V, Q) = \sum_{\{\gamma_i=1\}}^Q e^{-\beta H(\{\gamma_i\})} = \sum_{\{\gamma_i=1\}}^Q \prod_{i=1}^N [1 + V \delta(\gamma_i, 1) \delta(\gamma_{i+1}, 1)] = \sum_{\{\gamma_i=1\}}^Q \prod_{i=1}^N (\widehat{M})_{\gamma_i, \gamma_{i+1}}, \quad (18)$$

where $(\widehat{M})_{\gamma_i, \gamma_{i+1}}$ are the elements of the $Q \times Q$ matrix

$$\widehat{M}(Q \times Q) = \begin{array}{c|cccc} & \begin{array}{c} i+1 \\ \hline i \end{array} & 1 & 2 & \cdots & Q \\ \hline 1 & & g(1, 1) & g(1, 2) & \cdots & g(1, Q) \\ 2 & & g(2, 1) & g(2, 2) & \cdots & g(2, Q) \\ \vdots & & \cdots & \cdots & \cdots & \cdots \\ Q & & g(Q, 1) & g(Q, 2) & \cdots & g(Q, Q) \end{array} \quad (19)$$

$$= \begin{pmatrix} W & 1 & \cdots & 1 \\ 1 & 1 & \cdots & 1 \\ \cdots & \cdots & \cdots & \cdots \\ 1 & 1 & \cdots & 1 \end{pmatrix},$$

where $g(\gamma_i, \gamma_{i+1}) = e^{J\delta(\gamma_i, 1)\delta(\gamma_{i+1}, 1)}$. From the structure of transfer-matrix Eq. (19), it is obvious that there are only two linearly independent eigenvalues, so the number of nontrivial eigenvalues λ and the order of the characteristic equation is also equal to two. The characteristic equation can be written as determinant (see Eq. (3)). Successively subtracting the second row from the first, third row from the second, etc., until all rows have been accounted for, similarly, successively adding column Q with column $Q - 1$, $Q - 1$ with $Q - 2$ etc., we will arrive at a final expression for this determinant:

$$\lambda^{Q-2} \times \begin{vmatrix} W - 1 - \lambda & W - 1 \\ 1 & Q - \lambda \end{vmatrix} = 0 \quad (20)$$

Neglecting the $Q - 2$ trivial eigenvalues, a simple change of variables

$$\Lambda = \frac{\lambda}{Q}; \sigma = \frac{1}{Q}; s = \frac{W - 1}{Q}. \quad (21)$$

yields

$$\begin{vmatrix} s - \Lambda & s \\ \sigma & 1 - \Lambda \end{vmatrix} = \Lambda^2 - \Lambda(s + 1) + s(1 - \sigma) = 0, \quad (22)$$

which exactly coincides with the characteristic equation for the ZB model given in Eq. (6). Therefore, the Hamiltonian in Eq. (17) provides exactly the same thermodynamics of the ZB model, hence, can be considered equivalent to it.

The helicity degree for ZB model can be written as:

$$\theta = \frac{1}{N} \frac{\partial \ln Z}{\partial \ln s} \frac{s + \sigma}{s}, \quad (23)$$

As we see the degree of helicity of ZB model in the Hamiltonian representation in Eq. (23) differs from the classical representation in Eq. (9) by the term of $\frac{s + \sigma}{s}$ which is very close to 1 only when the parameter $\sigma \rightarrow 0$.

4. Solvent effects within the ZB model

Although Zimm and Bragg [3] formulated their model in 1950s, it appeared to be so successful, that is widely used till nowadays, especially for fitting experimental data [20, 21, 22]. Together with its strength, the original model formulation also contains an essential weakness due to the absence of microscopic Hamiltonian. Namely, when attempting to incorporate the influence of solvent into the approach, it is not clear, how should the parameters s and σ be adjusted to describe solvent effects. For the solvent mostly water is used but can be used also others which can have H-bonding with the polypeptide chain. On the other hand, there have been a spin-based Hamiltonian approach to solvent reported in the literature [15]. Coupling the approach of Ref. [15] with the recently suggested microscopic formulation of ZB model [16] allowed to show that such interaction renormalizes parameter s only.

An example of studying solvent effects in ZB model is done by Badasyan et al [19]. They proposed a simplified and explicit model for water-polypeptide interactions for Hamiltonian formulation of the Zimm-Bragg helix-coil transition model. So the description of water was also included into a partition function. It was shown that for both heat and cold denaturation the model fits well with circular dichroism (CD) experimental data. Inter- and intra-molecular H-bonding energies can be found by this model which are unavailable in other models. The final expression for helicity degree is:

$$\theta_{ZB}(\tilde{s}, \sigma) = \frac{\tilde{s} + \sigma}{1 + \tilde{s} + \sqrt{(1 - \tilde{s})^2 + 4\sigma\tilde{s}}} \left(1 + \frac{2\sigma - 1 + \tilde{s}}{\sqrt{(1 - \tilde{s})^2 + 4\sigma\tilde{s}}} \right), \quad (24)$$

where \tilde{s} is the renormalised non linear parameter, which in the absence of solvent is equal to s defined in Eq. (21).

5. Conclusion

By discussing different approaches and applications of ZB model we saw that this model can be used not only for description of standard helix-coil transition but also for cold denaturation and for thermal unfolding of short peptides. Different technics can be used to derive the partition function of this model depending on convenience of numerical calculations. ZB model can also be extended to include water or other external effects or considering different number of nearest neighbor interactions. To include the solvent effects it's suitable to use the Hamiltonian definition of microscopic spin model.

References

- [1] Bruce Alberts et al., *Molecular Biology of the Cell (6th edition)*, Garland Science (2015).
- [2] Branden and J.Tooze, *Introduction to Protein Structure*, Garland Publishing (1998).
- [3] B. H. Zimm & J. K. Bragg, *Theory of the Phase Transition between Helix and Random Coil in Polypeptide Chains*, J. Chem. Phys. 31, 526 (1959).
- [4] S. Lifson and A. Roig, *On the Theory of Helix-Coil Transition in Polypeptides*, J. Chem. Phys. 34(6) (1961).
- [5] B. H. Zimm, P. Doty, & K. Iso, *Determination of the parameters for helix formation in poly- γ -benzyl-L-glutamate*, Proceedings of the National Academy of Sciences, 45(11), 1601–1607 (1959).
- [6] E. Ising, *Beitrag zur Theorie des Ferromagnetismus*, Zeitschrift Für Physik, 31(1), 253–258 (1925).

- [7] J. Seelig, H.-J. & Schönfeld, *Thermal protein unfolding by differential scanning calorimetry and circular dichroism spectroscopy Two-state model versus sequential unfolding*, Quarterly Reviews of Biophysics 49 (2016).
- [8] J. M. Scholtz, H. Qian, E. J. York, J. M. Stewart, & R. L. Baldwin, *Parameters of helix-coil transition theory for alanine-based peptides of varying chain lengths in water*, Biopolymers 31(13), 1463–1470 (1991).
- [9] J. Applequist, *On the Helix-Coil Equilibrium in Polypeptides*, J. Chem. Phys. 38(4), 934–941 (1963).
- [10] M. Gō, N. Gō, & H. A. Scheraga, *Molecular Theory of the Helix–Coil Transition in Polyamino Acids. III. Evaluation and Analysis of s and σ for Polyglycine and Poly-L-alanine in Water*, J. Chem. Phys. 54, 4489 (1971).
- [11] H. Qian and J. A. Schellman, *Helix-Coil Theories: A Comparative Study for Finite Length Polypeptides*, J. Phys. Chem. 96, 3987–3994 (1992).
- [12] J. W. Bryson, J. R. Desjarlais, T. M. Handel, & W. F. Degrado, *From coiled coils to small globular proteins: Design of a native-like three-helix bundle*, Protein Science 7:1404-1414 (1998).
- [13] Andrew J. Doig, *Recent advances in helix–coil theory*, Biophysical Chemistry 101–102, 281–293 (2002).
- [14] A. Murza, & J. Kubelka, *Beyond the nearest-neighbor Zimm-Bragg model for helix-coil transition in peptides*, Biopolymers 91(2), 120–131 (2009).
- [15] A. V. Badasyan, A. Giacometti, Y. Sh. Mamasakhlishov, V. F. Morozov, and A. S. Benight, *Microscopic formulation of the Zimm-Bragg model for the helix-coil transition*, Phys. Rev. E 81, 021921 (2010).
- [16] A. V. Badasyan, A. Giacometti, Y. S. Mamasakhlishov, V. F. Morozov, & A. S. Benight, *Microscopic formulation of the Zimm-Bragg model for the helix-coil transition*, Physical Review E, 81(2) (2010).
- [17] M. Aznauryan, D. Nettels, A. Holla, H. Hofmann, & B. Schuler, *Single-Molecule Spectroscopy of Cold Denaturation and the Temperature-Induced Collapse of Unfolded Proteins*, Journal of the American Chemical Society 135(38), 14040–14043 (2013).
- [18] Y. Ren, R. Baumgartner, H. Fu, van der P. Schoot, J. Cheng, & Y. Lin, *Revisiting the Helical Cooperativity of Synthetic Polypeptides in Solution*, Biomacromolecules 18(8), 2324–2332 (2017).
- [19] A. Badasyan, S. Tonoyan, M. Valant, J. Grdadolnik, *Implicit water model within the Zimm-Bragg approach to analyze experimental data for heat and cold denaturation of proteins*, Communications Chemistry volume 4(57) (2021).

- [20] Gregory G. Wood, Drew A. Clinkenbeard, and Donald J. Jacobs, *Nonadditivity in the alpha-helix to coil transition*, Biopolimers Volume 95, 4 (2011) 240-253.
- [21] S. Neelamraju, Mark T. Oakley, and Roy L. Johnston, *Chiral effects on helicity studied via the energy landscape of short (D, L)-alanine peptides*, J. Chem. Phys., Volume 143, 16 (2015).
- [22] Schreck JS. and Yuan JM., *A statistical mechanical approach to protein aggregation*, J. Chem. Phys., Volume 135, 23 (2011).

Photocatalytic nitrogen fixation to ammonia: A Review of Multiscale Modeling Simulations

Taja Žibert

*University of Nova Gorica, Vipavska 13, SI-5000 Nova Gorica
National Institute of Chemistry, Department of Catalysis and Chemical Reaction Engineering, Hajdrihova 19, 1001
Ljubljana*

Abstract

Haber-Bosch process is considered to be environmentally unfriendly, due to the high energy consumption and CO₂ emissions produced during methane steam reforming. Photocatalytic nitrogen fixation as a greener and sustainable alternative to the conventional Haber-Bosch process enables to perform nitrogen reduction reaction (NRR) under mild conditions. Recently, increasing computational power provides the opportunity to perform theoretical calculations and gain insight into the properties obtained at different levels of modeling. Herein, much attention is paid to first-principles calculations used to determine the electronic and optical properties of photocatalysts, N₂ adsorption and to expound possible NRR mechanisms. The most commonly reported photocatalysts for nitrogen fixation are TiO₂, g-C₃N₄ and bismuth oxyhalides. The catalyst structure is usually modified by dopants, defects (oxygen, nitrogen vacancies, ...), co-catalysts and Z-scheme heterojunctions to prevent charge carrier recombination, improve charge separation efficiency and adjust a band gap to be able to utilize a broader light spectrum. Most studies at the atomistic level of modeling are grounded upon density functional theory (DFT) calculations, however, there is still a need to consider methods beyond DFT to study the excited state properties more accurately. Furthermore, a few studies have been examined to include kinetics and macro-scale simulations, however, there is still room for such calculations, which empower to build a multiscale model for photocatalytic nitrogen fixation. A review is concluded with concluding remarks and future prospects.

Keywords: photocatalysis, nitrogen fixation, density functional theory, multiscale modeling

Email address: taja.zibert@ung.si (Taja Žibert)

Table of Contents

1	Introduction	3
2	Fundamentals of nitrogen photofixation	4
2.1	Adsorption configurations and reaction mechanisms	6
3	Multiscale modeling - theoretical description	7
3.1	Density Functional Theory	8
3.2	<i>ab initio</i> Molecular Dynamics	9
3.3	Kinetic Modeling	9
3.4	Computational Fluid Dynamics	10
4	A Review of properties calculated by density functional theory and <i>ab initio</i> molecular dynamics	10
4.1	Electronic properties	10
4.2	Adsorption	23
4.3	Reaction mechanism	33
5	Review of kinetics and macroscale modeling	40
6	Conclusion	42
7	References	44

1. Introduction

Artificial ammonia plays a remarkable role as a fertilizer, explosive [1], chemical [1, 2], energy [1] and hydrogen storage with the hydrogen density up to 17 % [2]. In the early years of the last century, Fritz Haber and Carl Bosch made a major breakthrough in ammonia synthesis. Fritz Haber succeeded in converting gaseous nitrogen and hydrogen into ammonia in the presence of a catalyst at high temperatures and pressures [3], and was awarded a Nobel Prize for his discovery in 1918 [4]. In 1931, Carl Bosch received a Nobel Prize for raising a process to the industrial level [4, 5]. In the synthesis of ammonia, the so-called Haber-Bosch process is still inevitable, but ammonia production on thermal catalysts requires high temperatures and pressures in the vicinity of 500 °C and 200 atm [6, 7]. Therefore, scientists are constantly looking for improvements in nitrogen fixation and ammonia synthesis, especially to reduce the input energy required to break a very strong triple bond in the nitrogen molecule (941 *kJ/mol*) [8] and to perform the reaction under mild conditions, thus avoiding high temperatures and pressures [6, 7].

The original Haber-Bosch process requires a hydrogen molecule as feedstock, typically produced from the methane steam reforming process ($\text{CH}_4 + 2\text{H}_2\text{O} \rightarrow 4\text{H}_2 + \text{CO}_2$) [9, 10]. The use of fossil fuels (methane) as a viable energy source for hydrogen production contributes significantly to CO₂ emissions (~ 1.2 %) [1, 7]. To avoid the noteworthy carbon footprint resulting from hydrogen production, the water molecule can be used as a feasible proton source. [7, 11].

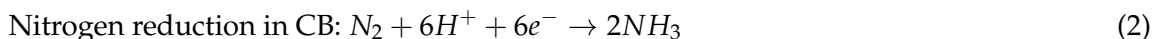
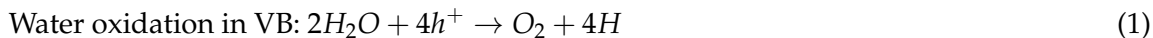
The first photocatalytic fixation and reduction of nitrogen to ammonia was reported by Schrauzer and Guth in 1977. They performed photocatalytic nitrogen reduction over TiO₂ based photocatalyst and detected ammonia as a main product and hydrazine as a possible by product [12]. Since then, numerous photocatalysts have been explored to perform nitrogen fixation, activation, and reduction to ammonia under mild conditions. Most promising reported groups of photocatalyst are metal oxides, bismuth oxyhalides, carbonaceous materials, metal sulfides and bio-mimicking photocatalysts [8].

Although a major advantage of photocatalytic reactions is the environmentally friendly use of sustainable and clean light sources as input energy [8, 11], the attention must be paid on the appropriate choice of the photocatalyst to fixate nitrogen molecule effectively. Nitrogen molecule is very stable and a high energy input is required to activate it, when it is adsorbed at the active sites of the photocatalyst. [8, 9] It is therefore common to modify the catalyst structure by incorporating dopants, introducing defects, loading co-catalysts or constructing heterojunctions and therefore provide more promising active sites for N₂ adsorption [7]. Modifications affect on the structure of the catalyst, which is undoubtedly connected to their electronic properties [13]. The fundamentals of photocatalytic activity, mechanisms and modifications of semiconductor photocatalysts are discussed in more detail in the following sections.

This review article aims to describe the photocatalytic nitrogen reduction reaction (NRR) focusing on its theoretical description using a multiscale modeling approach, with an emphasis on first-principles studies. In Section 2, the fundamentals of the photocatalytic NRR, together with brief explanation of adsorption, reaction mechanisms and catalyst modifications are presented. The theoretical methods within a multiscale modeling approach in Section 3 are followed by the electronic properties, adsorption and reaction mechanisms calculated using a DFT approach in Section 4. Section 5 gives an overview of the NRR kinetics and also the results performed on the macro-scale manner. Lastly, the findings and future prospects are presented in the last section.

2. Fundamentals of nitrogen photofixation

The nitrogen molecule is considered to be inert and very stable, due to a high ionization potential of 15 eV, a negative electron affinity of -1.8 eV and a large energy band gap of 22 eV. Thus, the activation of the nitrogen molecule remains challenging, mainly because of the cleavage of a very strong triple bond in the nitrogen molecule. The cleavage of the first bond in the nitrogen molecule, which is crucial for activation and represents a rate-limiting step in nitrogen reduction, requires a dissociation enthalpy of 410 kJ mol⁻¹ [8, 9]. Its activation therefore requires harsh conditions or an appropriate (photo)catalyst, even though the nitrogen reduction reaction to ammonia is alone exothermic with a ΔH (298K) of -92.2 kJ/mol [14]. After N₂ and other representative reactants (hydrogen or water) adsorb at the active sites of the semiconductor surface, the photocatalyst is illuminated by a light source. The solar irradiation provides the elimination and migration of the electron from the valence band (VB) to the conduction band (CB), consequently creating a hole in the valence band. The photogenerated electrons and holes must migrate to the active sites of the photocatalyst for the reaction to proceed. Ideally, the electrons and holes move directly to the active sites, but if the structure of the photocatalyst is not optimized, the probability of electron-hole recombinations is higher. This leads to the recombination of the electron-hole pairs and significantly lowers the photocatalytic activity. When the electron is excited from the valence band, the metal traps it at the active site where the photooxidation and photoreduction reactions occur. In the valence band, the holes react with hydrogen or water and in the conduction band, the electrons react with the nitrogen molecule. The photoreduction of nitrogen molecule requires 6 electrons and 6 protons to convert one nitrogen molecule into two ammonia molecules ($N_2 + 6 H^+ + 6 e^- \leftrightarrow 2 NH_3$) [8, 13]. Water oxidation and nitrogen reduction as well as corresponding reduction potentials are displayed in Eq. 1 and 2, respectively, and shown in Fig. 1.



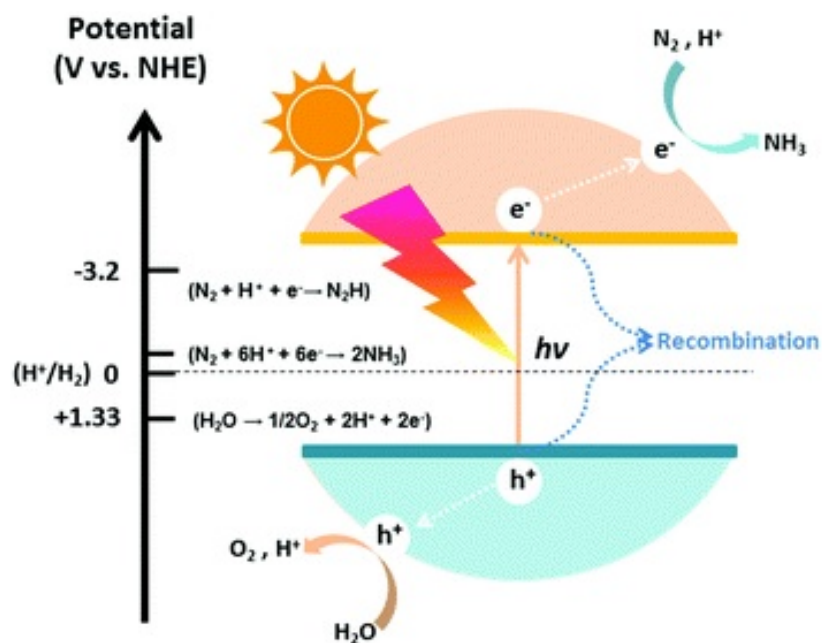


Figure 1: Schematic representation of semiconductor photocatalyst showing reduction potentials for nitrogen reduction and water oxidation reactions. Potentials are presented at pH 0 [15].

When considering photocatalytic reactions, a few features should be taken into consideration. The positions of the band edges as well as the width of the band gap affect the wavelength (or energy) of the light used as the input light source. The energy of the band gap must match the energy of the light source to provide a desired amount of energy to excite the electrons. Therefore, semiconductors with large band gaps require ultraviolet (UV) light to generate charge carriers (electrons and holes), while those with smaller band gaps can utilize visible (VIS) or even infrared (IR) light. However, the band gap should be kept reasonably small, while too narrowed band gap leads to the electron-hole recombination and hence unavailability of charge carriers for the reactions to proceed. The availability of electron-hole pairs can be controlled by introducing defects, such as vacancies, or doping with heteroatoms, while they act as electron trappers and thus prevent electron-hole recombination. In addition, photocatalytic reactions struggle with small product selectivity and poor quantum yields, which is an additional stimulation to improve the properties of the photocatalyst and consequently the photocatalytic activity and selectivity [7, 8, 13]. Photocatalytic activity can be improved by combining two different photocatalysts, i.e. creating a heterojunction photocatalyst. Low et al. reported three common types of heterojunctions, i.e. type-I, type-II and type-III, which are explained in detail in reference [16]. In photocatalytic NRR, Z-scheme heterojunctions are popular and very common. The re-

duction potentials of NRR vs a normal hydrogen electrode (NHE) at pH 0 are shown in Tab. 1.

Table 1: Reduction potentials of NRR at pH 0 [9].

Reaction	Potential vs NHE [V]
$\text{N}_2 + \text{e}^- \rightarrow \text{N}_2^- (\text{aq})$	-4.20
$\text{N}_2 + \text{H}^+ + \text{e}^- \rightarrow \text{N}_2\text{H}$	-3.20
$\text{N}_2 + 2\text{H}^+ + 2\text{e}^- \rightarrow \text{N}_2\text{H}_2$	-1.10
$\text{N}_2 + 4\text{H}^+ + 4\text{e}^- \rightarrow \text{N}_2\text{H}_4$	-0.36
$\text{N}_2 + 5\text{H}^+ + 4\text{e}^- \rightarrow \text{N}_2\text{H}_5^+$	-0.23
$\text{N}_2 + 6\text{H}^+ + 6\text{e}^- \rightarrow 2\text{NH}_3$	+0.55
$\text{N}_2 + 8\text{H}^+ + 8\text{e}^- \rightarrow 2\text{N}_2\text{H}_4^+$	+0.27

2.1. Adsorption configurations and reaction mechanisms

The first step in nitrogen photofixation is an adsorption of the nitrogen molecule on the active sites of the semiconductor photocatalyst. The nitrogen adsorption can be achieved via an end-on or side-on configuration [9]. The configurations are explained below when describing the principles of the reaction mechanisms.

Nitrogen reduction at the active sites of a heterogeneous catalyst occurs under one of two proposed pathways, namely dissociative and associative. During dissociative pathway, the triple bond in the nitrogen molecule is broken before successive hydrogenation steps occur on nitrogen atoms, hence a high input energy is required to cleavage the triple bond. The said pathway is therefore less common in photocatalytic nitrogen fixation. After adsorption and triple bond dissociation, the hydrogenation occurs on the two separated nitrogen atoms and the protons are successively added to form two ammonia molecules.

The associative mechanism is reported to be more common in nitrogen photofixation, and three possible associative pathways are proposed, namely distal, alternating and enzymatic. In both the alternating and distal pathways, the nitrogen molecule is adsorbed onto the surface of the catalyst such that one nitrogen atom is adsorbed onto the surface (denoted as the first nitrogen atom, N1), while the other (denoted as the second nitrogen atom, N2) is bonded to the N1 and is not directly adsorbed onto the catalyst surface. The said nitrogen fixation refers to the end-on configuration of the nitrogen molecule and is typical for alternating and distal associative mechanisms. After nitrogen adsorption via the end-on configuration, the first hydrogenation occurs at the distant nitrogen atom (N2). After this step, the pathway can be divided into the alternating or distal pathway. In side-on configuration both nitrogen atoms are simultaneously adsorbed on the catalyst surface and favor the enzymatic pathway [8, 9, 14]. All mentioned pathways are in detail presented in Fig. 2.

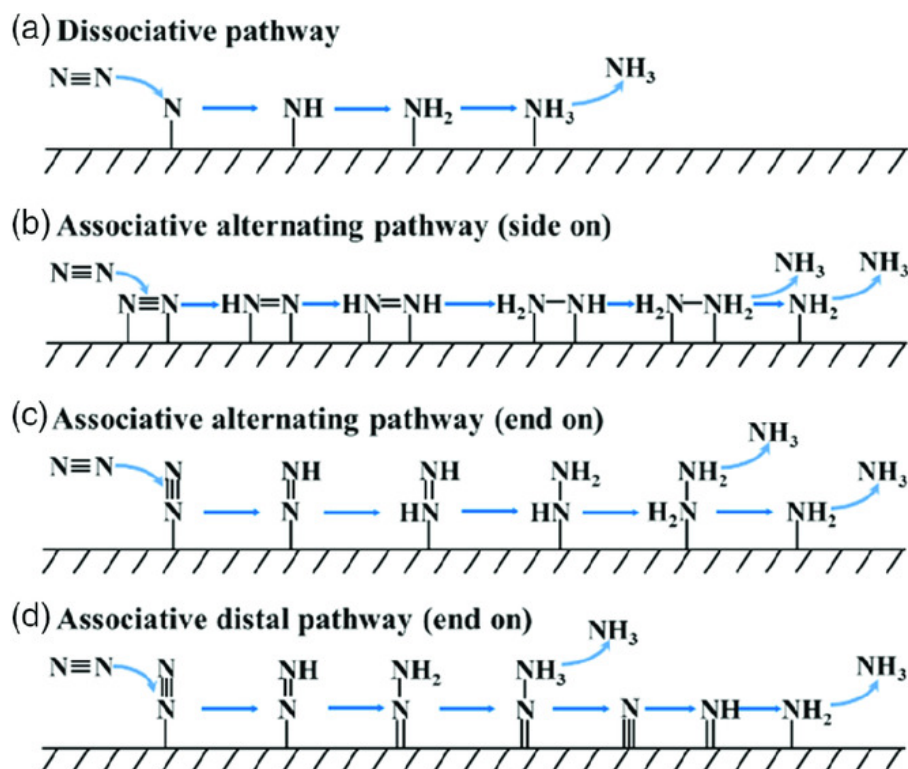


Figure 2: Proposed dissociative and associative mechanisms for nitrogen reduction process. a) dissociative pathway b) associative alternating/enzymatic (side-on) pathway c) associative alternating (side-on) pathway d) associative distal (end-on) pathway [14].

3. Multiscale modeling - theoretical description

The basic idea of a multiscale modeling approach is to study the system of interest at different modeling levels, i.e., at different length and time scales. Calculations at the atomistic level are in materials computational science usually performed using the DFT method, which can be followed by a (Ab Initio) Molecular Dynamics simulations (MD). Kinetics is studied using a mean-field microkinetic modeling (MM) or kinetic Monte Carlo (kMC) methods at the meso level, and reactor modeling is performed using a Computational Fluid Dynamics (CFD) at the macro level of modeling [17–20]. Multiscale modeling approach is graphically presented in the Fig. 3 [19].

This section introduces the basics of commonly used theoretical methods in computational materials science, i.e. DFT, Ab Initio Molecular Dynamics (AIMD), MM, kMC and CFD.

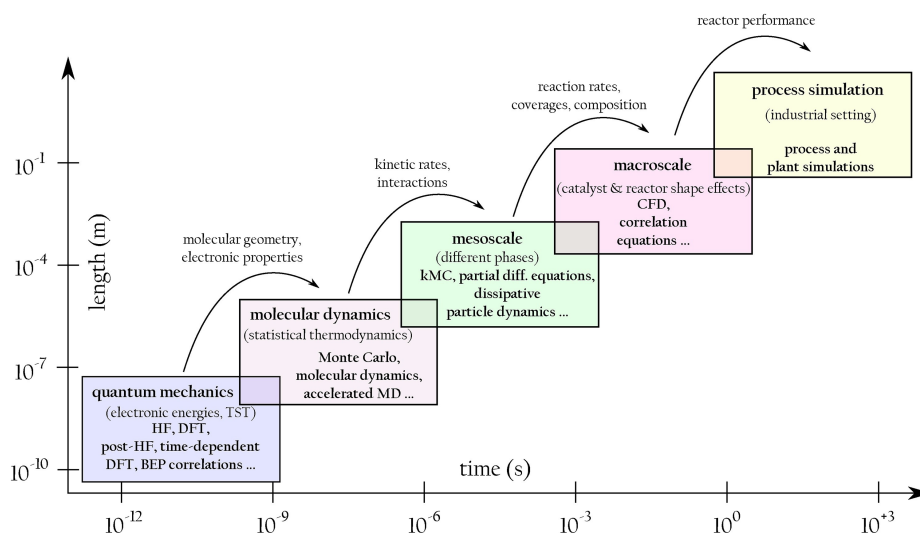


Figure 3: Multiscale model at different time and length scales [21].

3.1. Density Functional Theory

In 1964 P. Hohenberg and W. Kohn [22] laid the foundations of DFT and mathematically proved the Hohenberg-Kohn theorem [23, 24]. The latter states that all ground-state properties depend on electron density, i.e. the total energy of the system is a functional of electron density, and that the correct density is density with the minimum of the total energy [22, 23]. In DFT, great attention must be paid to the choice of the exchange-correlation functional (a suitable approximation), since the solution of the KS equations depend on the accuracy of the exchange-correlation energy [23].

To effectively study the photocatalytic properties, time-dependent density functional theory (TD-DFT) must also be considered, as the DFT is normally used to calculate the ground-state properties. On the other hand, TD-DFT enables to study the excited-state properties in a linear-response or real-time regime. The latter empower to determine and analyze the linear absorption spectrum of excited system, a time-dependent dipole moment and a non-linear emission spectra. Excitation energies are calculated in a linear-response regime and TD-DFT calculations yields also photoelectron spectra (PES). It is important to bear in mind that the ground state and excitation energies can be calculated using both DFT and TD-DFT, but considering the time evolution tends to describe the excited state properties more accurately [25, 26].

DFT as an attractive ab-initio method enables to investigate various material properties, i.e. electronic, mechanical, magnetic, dielectric and structural properties, crystal structures, phase diagrams, vibrational spectroscopy, surfaces and adsorption, reactions and electronic transport [17, 18]. Along with TD-DFT it can be used as a promising tool to calculate photocatalytic properties at the atomistic level of modeling.

3.2. *ab initio* Molecular Dynamics

AIMD does not rely on force fields to account for the interactions, as is typical for classical molecular dynamics simulations [19], but rather on forces obtained from first-principles calculations [20]. In AIMD simulation, the dynamic trajectories at finite temperature are generated, the bonds are allowed to break, therein polarization effects are also taken into account. Most commonly used first-principle method is DFT with a plane wave basis set approach (Bloch theorem is considered) and the total energy is defined as a functional of orthonormal single particle electron orbitals. It is of great importance to choose the appropriate functional for the exchange-correlation part, since the latter have a strong influence on the quality of the electronic structure. The total dipole moment and IR spectra can be calculated. In (photo)catalytic systems, AIMD is usually employed to confirm thermodynamic stability of the systems studied [27–32].

3.3. *Kinetic Modeling*

The data obtained from first principle DFT calculations can be further used to study the kinetics of heterogeneous reactions using mean-field microkinetic modeling (MM) or kinetic Monte Carlo (kMC) simulations.

Kinetic Monte Carlo is a stochastic method that can be used to describe different surface processes, such as adsorption, diffusion, reaction and desorption by solving the master equation. First, the initial configuration at the initial time is generated and all possible surface processes are specified. Then, the reaction rates for all the specified reaction processes are calculated and a particular surface process is randomly selected. After this step, the time is advanced by a random number between 0 and 1. The next configuration is considered and the system is modernized to this new configuration. All processes occurring in the new configuration are specified and the simulation is repeated until the system converges, i.e. reaches a steady-state.

In contrast to kMC, microkinetic modeling provides the determination of deterministic solutions by numerically solving the differential rate equations. These equations are integrated until the steady-state values converge and the turnover frequencies (TOF) are determined. Heat conduction, viscosity and diffusivity as representatives of transport processes can be studied as well as reactions in the gas, liquid and gas-solid (surface) phases. After the reaction model is proposed, the kinetics of the given processes can be described and solved by the macroscopic rate equations mentioned above, which include the rate coefficients related to the reaction rates. It is noteworthy that the mean-field approximation is considered, which means that the adsorbates are not correlated. Microkinetic simulations are less computationally expensive compared to kMC, but the catalytic activity is overestimated [33].

3.4. Computational Fluid Dynamics

On a macro-scale manner, Computational Fluid Dynamics (CFD) is applied to provide an insight into reactor-related properties, i.e. the hydrodynamics of multi phases, light intensity distribution and reaction kinetics. Within the CFD framework, optical properties, such as the scattering coefficients, absorption coefficients, phase function parameter and optical parameters can be calculated. When studying photocatalytic systems, the radiative transport equation (RTE) is employed to describe the light absorption of the illuminated light in the photoreactor as well as out- and in-scattering irradiation. In the slurry reactors, RTE equation includes light absorption, in- and out-scattering, while in some immobilized systems (coated plates, monoliths, optical fibers), RTE equation is reduced to the Beer-Lambert law due to negligible scattering effects, since only light absorption is presented in the reactor system [34, 35].

4. A Review of properties calculated by density functional theory and *ab initio* molecular dynamics

This section aims to give an overview of the electronic properties of semiconductors, adsorption (modes and energies) and proposed reaction mechanisms for photocatalytic NRR calculated using a DFT and AIMD approaches.

4.1. Electronic properties

Tab. 2 shows the theoretically calculated and experimentally determined band gaps.

Table 2: Experimentally determined and theoretically calculated band gaps of some promising photocatalysts for nitrogen fixation.

Catalyst	Functional	Theoretical band gap [eV]	Experimental band gap [eV]	References
pristine TiO ₂	GGA-PBE, DFT+U	3.15	3	[36]
OV-doped TiO ₂	/	2.79	/	
Cu-doped OV-TiO ₂	/	/	3	
SrTiO ₃	GGA-PBE, DFT+U	2.2	3.26	[37]
SrTiO ₃ -OV, strain	/	bandgap for strain	/	/
B-decorated g-CN	PBE, DFT+D2	Bandgap of prisitne melone based CN: 2.49 eV	/	[28]
g-C ₃ N ₄	GGA-PBE, DFT-D2	3.21 eV	/	[29]
B-doped g-C ₃ N ₄	/	0.63 eV	/	
g-C ₃ N ₅	B3LYP/6-31G(d) functional and basis set	3.76 (energy gap); 4.77 eV (HOMO-LUMO gap)	/	[38]
NV-g-C ₃ N ₅	/	3.05 eV (energy gap); 4.06 eV (HOMO-LUMO gap)	2.08	
pristine g-CN	HSE06	2.7	/	[31]
FeMo/CN	/	/	/	
MoW/CN	/	1.2	/	
NiMo/CN	/	0.8	/	
TiMo/CN	/	0.9	/	
M ₄ @B ₃₆ N ₃₆	HSE06 (DFT-D3)	0.54–1.60	/	[39]
pristine CuCr-LDH	DFT+U	1.6	/	[40]
MgAl-NS	/	/	5	
ZnCr	GGA-PBE, DFT+U	2.4	/	[41]
ZnCr-LDH	/	/	2.51	
ZnCr-LDH-OV	/	2.19	ZnCr-1h: 2.32	
ZnCr-OV-Zn	/	2.18	/	

Gd-IHEP-7 (2D MOF)	PBE, UPBE-D3	0.714	/	[42]
Gd-IHEP-8 (3D MOF)	/	0.691	/	
Gd-IHEP-7 ligand gr replaced with CH ₃	/	2.126	/	
Gd-IHEP-8 ligand gr replaced with CH ₃	/	1.904	/	
Zn ₃ In ₂ S ₆ (S-TA)	GGA-PBE	1.28	2.78	[43]
Zn-defective Zn ₃ In ₂ S ₆ (S-TAA)	/	1.56	/	
S-Cys (Zn ₃ In ₂ S ₆ from L-CYS)	/	/	2.89	
S-TA (Zn ₃ In ₂ S ₆ from TA)	/	/	2.81	
OV-S rich TiO ₂ -xSy (101) - Ti32O52S8	GGA-PBE, DFT-D3, HSE06 for bandgap	/	1.18	[44]
OV-S poor TiO ₂ -xSy (101) - Ti32O61S2	/	/	3.22	

Zhao et al. [36] calculated the band gap, density of states (DOS) and electron density diagram of pristine TiO₂, oxygen vacancy (OV) rich-TiO₂ (OV-TiO₂) and Cu-doped TiO₂. The calculations were performed using DFT+U and the results revealed that the presence of OV significantly decreases the band gap of TiO₂ and introduces additional defect states in the middle of the band gap. On the other hand, Cu doping divides the band gap of OV-TiO₂-strain (Cu-doped TiO₂) into two sections due to the increased electron density around O atoms. The band gap, DOS and projected density of states (PDOS) were calculated also for Au₄Ru₂ clusters by Sun et al. [45]. DOS and PDOS showed discrete electronic levels and single electron excitations. Moreover, PDOS showed that LUMO (the lowest unoccupied molecular orbital) and LUMO+1 states are mainly composed of Ru atoms, implying that Ru atoms could serve as active sites for N₂ adsorption. Ye et al. [46] studied MoS₂@TiO₂ nanojunctions as a promising catalyst for nitrogen photofixation and calculated the charge transfer between TiO₂ and MoS₂ by Frontier orbital analysis. The results showed that electrons are transferred from TiO₂ to MoS₂, while the HOMO (the highest occupied molecular orbital) orbital of the photocatalyst is mainly composed of TiO₂ and the LUMO is composed of MoS₂, especially Mo atoms. According to the latter results, N₂ is adsorbed and activated on TiO₂ MoS₂@TiO₂. DOS, PDOS and band gap of SrTiO₃ were calculated by Huang et al. [37]. The results showed that VBM consists of occupied O 2p states and CBM consists of Ti 3d states. To improve the photocatalytic activity, OVs and pressure deformation were introduced. When OVs were introduced, the Fermi level was pushed toward CBM (metallic ground state) and more O 2p states appeared, while a compressive strain of 2.5 %, moved VBM and CBM from 0.12 to 0.28 and 1.78 to 1.46 eV, respectively. It can be concluded that compressive strain enhances nitrogen activation.

Shiraishi et al. [47] conducted DFT calculations (B3LYP/6-31G(d)) to determine the HOMO and LUMO energies of pristine and P-doped NV (nitrogen vacancy)-C₃N₄. Calculated energies are -6.01 eV and -1.03 eV, while HOMO and LUMO+1 energies of NV-P-G-C₃N₄ add up to 4.14 and 8.46 eV, respectively. Nitrogen photofixation on a honeycombed Fe³⁺-doped graphitic carbon nitride and pristine g-C₃N₄ was studied by Shaotheng Hu et al. [48]. Charge density differences, DOS, Mulliken charges and adsorption energies were

calculated. The DOS graph revealed that the orbitals of physically adsorbed N_2 on pristine $g-C_3N_4$ are very similar to the orbitals in an isolated N_2 , implying that the activation of the nitrogen molecule on Fe free $g-C_3N_4$ is impoverished. On the other hand, when nitrogen is adsorbed on Fe^{3+} -doped $g-C_3N_4$, it is observed that the sigma 2p orbital (HOMO) of N_2 becomes delocalized, indicating nitrogen activation. The Bader charge analysis, PDOS and charge density difference of B_{int4} -melon based CN were theoretically investigated and calculated by Zheng et al. [28]. PDOS of side-on nitrogen adsorption at the B_{int4} active site revealed the hybridization of the B-2p and N-2p orbitals. The possible side reaction HER was also considered, although the selectivity of the NRR reaction is relatively high. It was confirmed that at the B_{int4} active site the NRR reaction is predominant and that it is energetically more favorable to adsorb N_2 than the water molecule. Incorporated B atom lowers the band gap thus provides the utilization of light in broader spectrum (visible and even IR-light) and enables efficient charge separation. The stability of the photocatalyst was also confirmed by an AIMD simulation performed for 20 ps at 300 K with a time step of 0.5 fs. DFT calculations (B3LYP functional, 6-311++G(d,p), LANL2DZ basis sets) were used to study the interaction energies between $FeCl_3$ and urea, and $FeCl_3$ /urea and melamine, as a promising photocatalysts for nitrogen photofixation [49]. They concluded that the interaction energy of $FeCl_3$ /urea/melamine (-250.1 kJ/mol (-2.59 eV)) is higher than that of $FeCl_3$ /urea (-203.1 kJ/mol (-2.10 eV)), indicating that the presence of melamine is favorable. Mulliken charges, DOS and charge density differences (Fig. 4) were calculated also for N_2 adsorption on pristine and Cu^+ doped $g-C_3N_4$ by Hu et al. [50]. They also confirmed a negligible N_2 activation over pristine CN, while Cu^+ doping induced the delocalization of electrons in HOMO (sigma g 2p) (from -0.2 to -0.3), which causes the imminent overlap of HOMO and LUMO orbital ($\pi g^* 2p$). Regarding the LUMO orbitals of N_2 , the electron states are decreased from 6.9 eV for free N_2 to 1.0 eV for N_2 adsorbed on $Cu^+-C_3N_4$, and consequently the band gap decreases (the electrons in the valence gap are easily excited).

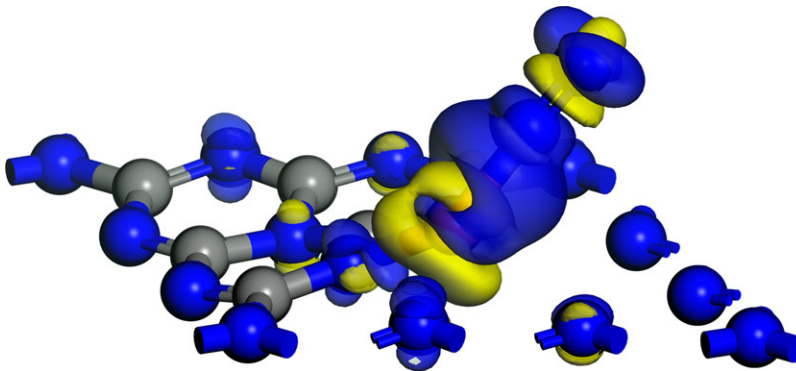


Figure 4: Charge density difference of the N_2 adsorbed on the Cu^+ active site (yellow denotes charge accumulation and blue color denotes charge depletion [50]).

Lv et al. [29] performed spin-polarized DFT calculations using PBE-D2 to study nitrogen activation on a metal-free B@g-CN. The binding energy of the B atom incorporated into a g-CN structure was calculated to be -5.67 eV, indicating that the adsorption of the B atom on the hole edge of g-CN is favorable, thus the aggregation of the B is prohibited. AIMD simulations at 800 K confirmed the thermodynamic stability of B@g-CN. B@g-CN has a centralized spin moment of $1.00 \mu_B$, which contributes to efficient nitrogen activation. The band gap structures revealed that B atom lowers the band gap sufficiently (hybridization of B and N 2p orbitals is observed), thus allows the irradiation of the photocatalyst in the visible and even in the IR spectrum compared to the pristine catalyst. The B atom acts as an electron trapping center, helps to reduce the electron-hole recombination and promoted N_2 fixation. Wang et al. [51] calculated Hirshfeld charges, charge density difference analysis and DOS of N_2 adsorbed on Co-doped g- C_3N_4 . Charge density difference analysis revealed the electron-back donation process and electron transfer from Co d-orbitals to the antibonding orbital in N_2 , resulting in activation of nitrogen molecule, which was also confirmed by DOS, i.e. strong hybridization between the d-orbital of Co and p-orbital of nitrogen was observed. Bader charge, charge density difference calculations and Ab Initio Molecular Dynamics (AIMD) simulations of N_2 fixation over Pt-SACs/CTF were performed by J. Li et al. [30]. The latter were carried out at 300 K and confirmed the thermodynamic stability of the catalyst and nitrogen adsorption on the catalyst surface. Wang et al. [31] investigated MM/g- C_3N_4 (M = Cr, Ti, Fe, Mn, Co, Mo, Ni and W). Among all the energetically feasible catalysts, FeMo/g- C_3N_4 , TiMo/g- C_3N_4 , MoW/g- C_3N_4 and NiMo/g- C_3N_4 were chosen as promising catalysts for NRR. Their thermodynamic and kinetic stability were confirmed by AIMD simulations at 400 K. The optical absorption spectra and the electronic band structures of the aforementioned most promising catalysts were calculated using a HSE06 functional. Based on the calculated band gap values, it was determined that pristine catalyst can absorb the light in the UV spectrum, which was also confirmed by absorption spectra. On the other hand, NiMo/-, TiMo/-, MoW/g- C_3N_4 can utilize VIS and IR light. The calculated band edge positions revealed that the VB positions of all three catalysts lie lower than the redox potential of N_3NH_3 and the CBs lie higher, which is feasible for NRR. The Bader charges were also calculated. Yang et al. [39] made an extensive theoretical study of 11 transition metals incorporated into the $B_{36}N_{36}$ clusters to form $M_4@B_{36}N_{36}$ as a photocatalyst for nitrogen photoreduction. The formation energies of the $M_4@B_{36}N_{36}$ were reported to be exothermic, namely in the range from -1.25 to -5.15 eV, indicating energetically favorable formation. The band gap obtained from the calculation of HOMO and LUMO energies was reported to be 0.54–1.60 eV and about 0.05 to 0.14 eV was transferred from the metal to the B atom due to the ability of electrons to fill the p orbitals of B. AIMD at 300 K for 10 ps in water environment confirmed the stability of clusters, as the structure changes were negligible.

Sun et al. [52] calculated PDOS of BiO quantum dots which showed that the valence bands of BiO consist of Bi p-electrons, suggesting that Bi atoms behave as active sites for nitro-

gen activation. On the other hand, Xu et al. [53] calculated DOS of pristine and OV-rich BOC ($\text{Bi}_2\text{O}_2\text{CO}_3$) which showed that the valence states consists mainly of O 2p orbitals, while the conduction states consists of Bi 6p orbitals. After OV formation, additional defect levels are introduced, which has also been confirmed by UV-VIS experiments. Di et al. [54] studied SUC (single unit cell) $\text{Bi}_3\text{O}_4\text{Br}$ photocatalyst and obtained DOS of pristine, OV-, BiV- and BiOV (bismuth and oxygen vacancy)-SUC $\text{Bi}_3\text{O}_4\text{Br}$. DOS showed that OVs introduce a new defect level in the middle of the band gap, while, on the other hand, several additional defect levels were observed when Bi vacancy was present. BiV and OV together introduced new defect levels especially near the valence and conduction bands, providing easier excitation of electrons from the valence to the conduction band. BiOBr (102) photocatalyst, including the incorporation of OVs, and Fe, Mo and Ni transition metals, was investigated by Chen et al. [55], who calculated the band gaps and DOS. Pristine BiOBr exhibited an indirect band gap of 2.67 eV, and OV and metal doping introduced additional defect levels in the middle of the band gap. DOS showed that the CBM of pristine catalyst consists mainly of Bi 6p states, while VBM of Br states. It was found that the introduction of OV has an effect on the Bi 6p states, namely it improves the electron-hole separation. Similar considerations can be made for doping with metal atoms, as their presence affects the CBM and VBM levels. The effect of OVs and compressive strain has also been studied for CuCr-LDH and ZnAl-NS photocatalysts. Zhao [40] obtained similar results as [55] and suggested that OVs act as electron trapping sites, while they introduce a new defect level. On the other hand, compressive strain introduces several additional defect levels in the middle of the band gap. The band structure and electron density difference of pristine ZnCr, OV-ZnCr-LDH, Zn-OV-ZnCr-LDH were studied by Zhao et al. [41], who determined that introduced OV and unsaturated Zn sites improve the charge separation and lower the band gap.

Zhang et al. [56] calculated DOS and electron transfer using DFT+U. DOS showed that the valence band states consist of O 2p, C 2p orbitals, while Ce 4f orbitals are abundant in the conduction band states. Upon adsorption of N_2 at the active sites of Ce-CUS, the Ce 4f orbitals overlap with the π anti-bonding orbital of N_2 , indicating that electron transfer occurs from Ce to N_2 , resulting in nitrogen activation and extension of triple bond to 1.117 Å. Kong-Qiu Hu [42] studied nitrogen activation on the surfaces of Gd-IHEP-7 (2D metal organic framework (MOF)) and Gd-IHEP-8 (3D MOF). They calculated band structures, DOS, PDOS and Mulliken charges and revealed that 3D MOF exhibits narrower band gap compared to a MOF with a 2D structure. The band gaps of modified Gd-IHEP-7 and Gd-IHEP-8 were also calculated, implying that the ligand substitution is not beneficial due to the significantly increased band gaps. Time dependent DFT (TD-DFT) calculations were also examined to verify the stability of the ground state optimized structures of Gd-IHEP-7 and Gd-IHEP-8.

Azofra et al. [32] generated three 4-membered FeSMoS rings by Fe deposition on the surface of MoS_2 and favorable Fe-S binding energy was determined. NVT MD simulations

confirmed the stability of Fe-S bonds near the water monolayer at room temperature. DOS of pristine MoS₂ and Fe-deposited MoS₂ revealed additional states around Fermi level, which appeared due to Fe doping. Han et al. [43] performed DFT calculations to investigate the band gap, DOS and PDOS of pristine and Zn-defective Zn₃In₂S₆. It was found that a pristine catalyst exhibits a direct band gap of 1.28 eV calculated in the gamma point. The band gap in the Z-point of a Zn-defective Zn₃In₂S₆ (S-TAA) was calculated to be 1.56 eV. DOS and PDOS revealed that the CBM (conduction band minimum) consists mainly of Zn 4s, 3p states, S 2p and In 5s states, while CBM consists of S 3p and Zn 3d states. Moreover, Zn vacancies increase the width of CB gap. studied nitrogen activation under ambient conditions (room T) using spin-polarized GGA-PBE approach, however, the band structure was calculated using HSE06 functional. The authors calculated the band gap, charge, molecular orbitals and spin density distribution of P and Fe-P (Fe-doped) monolayer phosphorene were calculated by Wei et al. [57]. The band gap of P was calculated to be 1.5-1.6 eV, which is in agreement with the previously reported experimental results. TiO_{2-x}S_y with rich and poor amount of oxygen vacancies and sulfur dopants were constructed and band structures were calculated by Xue et al. [44] using spin-polarized DFT-PBE calculations. The results suggest a beneficial presence of OV and S dopants, as the band structures showed that both types defects help in narrowing the band gap.

As seen in this section, TiO₂, g-C₃N₄ and bismuth oxyhalides are most commonly reported catalysts for photocatalytic NRR, however, sulfides, metal organic frameworks (MOF) and layered double hydroxide (LDH) should not be neglected. Theoretically calculated and experimentally determined band gap values of some promising photocatalysts for NRR are summarized in this section. It can be discern that electronic properties of semiconductor photocatalysts depend strongly on the atomic structure, while some pristine catalysts exhibit smaller band gap than others. For instance, pristine CuCr-LDH has the band gap of 1.6 eV [40], while pristine TiO₂ [36] and g-C₃N₄ [29] have 3.15 and 3.21 eV, respectively. Moreover, the electronic properties can be altered by modifying the structure of the photocatalyst. The introduction of defects, such as vacancies, or doping of heteroatoms into the bulk structure cause additional mid-gap states, which act as electron trappers and reduce charge carrier recombination. It is also worth mentioning that the electronic properties are determined by calculating the band structure, density of states and projected density of states. Band gap and the energies of band edges (valence band maximum and conduction band minimum) are discerned from the band structure and total density of states. On the other hand, projected density of states gain the insight into the orbital composition of CBM and VBM. For instance, Huang et al. [37] calculated electronic properties of SrTiO₃ using DFT-PBE and DFT+U approach. PDOS results showed that the VBM of SrTiO₃ consists mainly of O 2p states, while CBM consists of Ti 3d states. This indicates a possible electron excitation from O 2p to Ti 3d orbitals, suggesting that Ti atoms are active sites for adsorption of N₂. The band gap of 2.2 eV was also determined

from DOS calculations. Furthermore, additional mid-gap states were observed in DOS and PDOS graphs after OVs were introduced and the VBM and CBM levels also moved after a compressive strain of 2.5 % was induced.

The calculated results can also differ depending on the functional selected. Most of the calculations of electron properties are performed using GGA-based functionals (PBE or PW91), even though they struggle with the underestimation of such properties [58]. Hybrid functionals would be a better choice for electronic property calculations, however, the articles published so far generally do not consider them. The choice to add the Hubbard U-correction or Grimme's corrections is much more common. The calculated electronic, adsorption properties and mechanisms are gathered in Tab. 3.

Table 3: Properties calculated for N₂ activation over most promising photocatalysts by first-principles.

Catalyst	Functional	Adsorption energy [eV]	Mechanism	Calculated properties	References
OV-rutile TiO ₂ (110)	HSE06 +D3//PBE+U+D3 GGA-PBE	end-on: Ti5c atom: 0.40, OV:0.31 eV; side-on: Ti5c atom: 0.05, OV:0.10 eV	distal	N ₂ adsorption energies, N ₂ bond prolongation, charge transfer, reaction mechanism	[59]
P25 (anatase TiO ₂)	GGA-PBE	-0.621	alternating (end-on to side-on adsorption conf... /	N ₂ adsorption energy	[60]
Fe-TiO ₂		/	/		
Rutile TiO ₂ (110)	GGA-PBE	/	associative	(Electron density, ad- sorption energies), free energy diagram	[61]
a (amorphous) TiO ₂ on r-TiO ₂ (110)		/	/		
VO-doped TiO ₂		-0.25			
Cu-doped TiO ₂ with OV - TiO ₂ -OV-strain		-0.37			
pristine TiO ₂ (010) facet	DOPSI	/	working in tandem mechanism /	charge density differ- ence, electron transfer	[62]
OV-TiO ₂		/	/		
pristine rutile TiO ₂ (110)	BEEF-vdW		dissociative and associa- tive	surface free energy, cov- erage, coverage proba- bility, mechanism	[63]
VO-rutile TiO ₂ (110)		/	associative		
Fe-doped rutile (110)		/	associative		
pristine anatase TiO ₂ (101)	PBE, DFT+U	negative adsorption en- ergy		Bader charge, differen- tial charge densities, N ₂ adsorption energy, bond prolongation	[64]
OV-anatase TiO ₂ (101)		end-on: -1.0915	/		
anatase TiO ₂ (101)	PBE, GGA+U	-0.18	/	N ₂ adsorption energies, charge density differ- ence	[65]
VO-anatase TiO ₂ (101)		-0.62	/		
Ti ₃ C ₂ O ₂		-0.34	/		
Ti ₃ C ₂ O ₂ -VO		-0.38	/		
pristine TiO ₂ (001)	PBE, DFT+U	/	/	band structure, band gap, PDOS, Ru adsorp- tion energies	[66]
Ru-defected TiO ₂ (001) - D-O-2v and D-O-3v de- fects		/	/		
Rutile TiO ₂ (110)	BEEF-vdW	/	distal	surface coverage proba- bilities, N ₂ binding free energies	[67]
carbon-TiO ₂		-1.89	/		
TiO ₂ (101) anatase	GGA-PBE, DFT-D2	0.17		N ₂ adsorption energies, bond prolongation	[68]
OV-TiO ₂ (101)		0.342	/		
Ti ₃ C ₂ Mxene		2.731	/		
TiO ₂ (101)	PBE + Grimme-D2	-0.25	distal-alternating	N ₂ adsorption energies, bond prolongation, free energy profiles	[69]
OV-TiO ₂ (101)		-0.47	/		

Fe capped OV-TiO ₂ Fe-OV-TiO ₂ (101)		-0.29 -0.31	/		
anatase TiO ₂ (101)	PBE, DFT+U	/	/	band structure, CBM and VBM, DOS, electron density difference, N ₂ adsorption, mechanism	[70]
OV-anatase-TiO ₂ (101)		end-on: -0.44	/		
	PBE, DFT+U, DFT-D3	-3.18	/	N ₂ adsorption energies, N ₂ bond prolongation, free energy profiles	[71]
TiO ₂ (101)		-0.36	/		
TiO ₂ /Co		-0.86	/		
TiO ₂ /Fe		-1.34	/		
TiO ₂ /Ni		-0.38	/		
TiO ₂ /Pt		-0.34	/		
TiO ₂	/	-0.25	/	PDOS, N ₂ adsorption, Bader charge, density difference	[72]
Ni-TiO ₂		-0.53	/		
anatase OV-TiO ₂ (101)	GGA-PBE, DFT-D3	/	distal, alternating, enzymatic	band gap, DOS, PDOS, H binding energy, N ₂ adsorption energies, bond prolongation, mechanism	[45]
Au ₄ Ru ₂ Ag ₄ Ru ₂ /OV-TiO ₂ (101)		/ end-on: -0.07, side-on: -1.33	/		
Au ₄ Ru ₂ (SCH ₃) ₈ (P(CH ₃) ₃) ₂ /TiO ₂		/	/		
OV-TiO ₂	GGA-PBE	/	distal-alternating-enzymatic	mechanism	[73]
MoS ₂ @TiO ₂	PW91-GGA	/	/	Frontier orbital analysis, electron density distribution	[46]
SrTiO ₃	GGA-PBE, DFT+U	/	/	DOS, PDOS, bandgap, VBM and CBM positions	[37]
SrTiO ₃ -OV, strain		/	/		
BaTiO ₃ (110)-OV	PBE	side-on: -4.60	/	N ₂ adsorption energy, N ₂ bond prolongation, charge density difference, free energy profiles	[74]
g-C ₃ N ₄ -NV (nitrogen vacancy)	/	-1.72 (-166.2 kJ/mol)	/	N ₂ adsorption, N ₂ bond prolongation	[75]
g-C ₃ N ₄ -NV (nitrogen vacancy)	/	NV1: -166.2, NV2: -2.4	dissociative	N ₂ adsorption, N ₂ bond prolongation	[76]
pristine g-C ₃ N ₄	/	/	/	electron transitions (HOMO to LUMO and LUMO+1)	[47]
P-doped CN-NV		/	/		
g-C ₃ N ₄ -NV (bulk)	/	/	/	N ₂ bond prolongation	[77]
g-C ₃ N ₄ -NV (001)	/	/	/		
pristine g-C ₃ N ₄	/	-14.6 kJ/mol	/	DOS, N ₂ adsorption energies, charge density difference, Mulliken charge	[48]
Fe-g-C ₃ N ₄		-134.8 kJ/mol	/		
bulk SCNN	GGA	-0.335	/	N ₂ adsorption energies, charge density difference	[27]
SCNN (sulfur doped g-CN)-C vacancies		CV active site: -0.665	/		
pristine melon-based g-CN	PBE, DFT+D2	/	distal, alternating, enzymatic	Bader charge, PDOS, charge density difference, N ₂ adsorption	[28]
B-decorated g-CN		-0.10 (B _{N3}), -0.12 (B _{C3}), -0.11 (B _{C4}), -1.67 (B _{int4}), -1.52 (B _{int5}), -0.96 (B _{N3}), -1.37 (B _{N5}), -1.72 (B _{N2})	associative distal alternating and enzymatic		
FeCl ₃ /urea	B3LYP, 6-311++G(d,p) basis set, LANL2DZ basis set	/	/	interaction energies of FeCl ₃ /urea and FeCl ₃ /urea/melamine	[49]
FeCl ₃ /rea/melamine cyano defective g-C ₃ N ₄	GGA-PBE	/	/	charge density difference for catalyst	[78]

pristine g-C ₃ N ₄	GGA-PW91	pristine g-CN: -0.162 eV	/	DOS, N ₂ adsorption energies, bond length, Mulliken charges, charge density difference, HOMO-LUMO	[50]
Cu+-doped g-C ₃ N ₄		Ms-Cu-CN: -1.196	/		
g-CN /osheet	GGA-PBE	-0.26	/	N ₂ adsorption energies	[79]
EDTA-g-CN /osheet		-0.29	/		
Fe-EDTA g-CN /osheet		-0.99	/		
g-CN	GGA-PBE	-0.0299	/	N ₂ adsorption energy, bond prolongation, Mulliken charge analysis, mechanism	[80]
NV-g-CN		-0.1003	/		
BNUCNx (two adsorption sites- B1 and B2)		(-0.2143), -0.8063 (B2 - most favorable)	/		
g-CN	GGA-PBE, DFT-D2	distal, alternating and enzymatic pathway.	AIMD, band gap, binding energy of B-g-CN, N ₂ , CO ₂ , H ₂ O, O ₂ adsorption energies, Bader charge, magnetic properties	[29]	
B@g-CN		/	/		
g-CN	GGA-PW91	(-6.6 kJ/mol)	/	DOS, N ₂ adsorption, Hirshfeld charges, charge density difference, triple bond prolongation	[51]
Co-doped g-CN		(-156.5) kJ/mol	non-dissociative mechanism		
g-CN	Wb97x-d/6-31G(d)* functional and basis set	/	/	N ₂ adsorption energies, Gibbs free energies.	[81]
V-rich g-CN		/	/		
pristine g-C ₃ N ₄	PW91, DFT-D, HSE06	/	/	band structures, absorption spectra, electron transitions, Fermi level, electron density difference, Hirshfeld charge, DOS, ELF (electron localization function), NV formation energies, N ₂ adsorption, mechanism, free energy diagram, HER	[82]
planar NV (central)-g-C ₃ N ₄		/	distal, alternating, enzymatic		
planar NV(2-fold coordinated)-g-C ₃ N ₄		/	distal		
corrugated NV(central)-g-C ₃ N ₄		/	/		
corrugated NV(2-fold coordinated)-g-C ₃ N ₄		end-on: -2.56	alternating		
g-C ₃ N ₅	B3LYP/6-31G(d) functional and basis set	/	/	HOMO-LUMO gaps, energy gaps (from TDOS)	[38]
NV-g-C ₃ N ₅		/	/		
VN-CN	GGA-PW91, OBS for DFT-D corrections	chemisorption: -3.52	/	N ₂ adsorption energies, N ₂ bond prolongation, charge density difference	[83]
VN-SCN		chemisorption: -4.54	/		
g-CN	GGA-PBE, PAW, DFT-D3	end-on: physical	distal, alternating	N ₂ adsorption energies, N ₂ bond prolongation, energy barrier	[84]
Mo single atom-g-CN		end-on: chemical: -1.31	end-on configuration: distal and alternating		
GaN	PW, GGA-PBE, PAW, optB86 exchange functional	physical adsorption		N ₂ adsorption energies, charge density difference, Bader charge, triple bond prolongation	[85]
GaN-NV (nitrogen vacancies)		chemical adsorption	/		

Pt-SACs/CTF	PW, GGA-PBE, PAW; DFT-D3 dor AIMD	-0.97	distal and alternating mechanism	AIMD, Bader charge, charge density difference, N ₂ adsorption energies, binding energies, Gibbs free energy of Pt incorporated into SACs/CTF, electron transfer	[30]
pristine g-CN	GGA-PBE; DFT-D3, HSE06 (electronic prop)	end-on: -1.01, side-on: - 2.09	alternating, distal, enzy- matic	AIMD, Bader charge, N ₂ adsorption energy, charge density difference, Gibbs free energies, energy bar- riers, H ₂ adsorption	[31]
FeMo/CN MoW/CN NiMo/CN TiMo/CN		/	/		
pristine C ₂ N	GGA-PBE functional, Grimmes's DFT-D2	/	/	optical absorption spec- trum, band structures, AIMD, phonon disper- sion spectrum, N ₂ ad- sorption, bond prol- ongation, mechanism	[86]
B/C ₂ N		end-on: -1.44, side-on: - 0.58	distal, alternating, enzy- matic		
VN-gCN	GGA-PW91, OBS for DFT-D corrections	-3.52	/	charge density differ- ence, N ₂ adsorption en- ergy, electron density	[87]
VN-P-gCN		-4.72	/		
Ru/E-g-CN	PBE-GGA, DFT+U	-2.18	dissociative, associative	CINEB for TS and barriers, Ru adsorption ener- gies, N ₂ adsorption en- ergies, work functions, mechanism, energy bar- riers	[88]
Ru/B-g-CN		-1.31	dissociative, associative		
Fe(III)-g-C ₃ N ₄	GGA-PBE	/	/	Fe adsorption on g-CN	[89]
B/g-C ₃ N ₄	PBE (PBE), HSE06	end-on: -1.28; side-on: - 1.04	distal, alternating, enzy- matic	AIMD, band structures, optical absorption spec- tra, N ₂ adsorption en- ergies, charge density dif- ference, free energy dia- grams	[90]
O ₂ /C	GGA-PBE	-0.12	hydride distal, alternat- ing pathway	N ₂ adsorption energies, mechanism, Gibbs free energies	[91]
Fe ₁ O ₄ /C Fe ₁ O ₄ /C Fe ₁ O ₄ /C-PPH ₃ /NaI		end-on: -1.59 side-on: -1.46 -0.17	/		
Ti ₃ C ₂ (001)	GGA-PBE	end-on: -3.16; -2.75, side-on: -5.20	/	N ₂ adsorption, charge density difference, bond prolongation	[92]
Mo ₂ C, W ₂ C, Ta ₂ C, Ta ₂ N, Ti ₂ C and Ti ₂ N	PBE-GGA	/	distal, enzymatic	N ₂ adsorption energies, mechanism, Gibbs free energies, charge density difference	[93]
11 transition metals, M ₄ @B ₆ N ₃ 6	DFT-D3, HSE06	/	/	AIMD, Bader charge, HOMO-LUMO en- ergies, average bond prolongation, adsorp- tion energies, differ- ential charge density difference, Gibbs free energy diagrams, onset potentials	[39]
BiO(010) surface	GGA-PBE, PW, PAW	/	mechanism was ex- plored experimentally (side-on...	charge density, N ₂ bond prolongation, partial charge density	[52]
pristine BiOCl (001)	PBE, DFT+U, PAW	/	/	N ₂ adsorption energies, N ₂ bond prolongation, charge density differ- ence, Bader charge	[94]
pristine BiOCl (010) OV-pristine BiOCl (001) OV-pristine BiOCl (010)		/ chemisorption chemisorption	/		

BiOBr(001)-OV facet	PBE, DFT+U, PW	via side-on configuration, chemical adsorption	/	Bader charge, charge density difference, adsorption, triple bond prolongation	[95]
BiOCl	GGA-PBE, DFT-D3, HSE06 (electronic)	/	/	NAMD, band structures, optical absorption spectra, Nader charge, N ₂ adsorption, HER	[96]
BiOBr		/	/		
BiOI		/	/		
Mo-BiOCl		distal mechanism: different dopants	/		
Mo-BiOCl/BiOBr heterojunction		/	/		
Bi ₃ FeMo ₂ O ₁₂ (150)	PBE	/	associative, dissociative pathway	mechanism	[97]
Bi ₂ O ₂ CO ₃ (110) (pristine BOC)	GGA-PBE	/	/	DOS	[53]
OV-BOC		/	/		
BiOCl-OV (001) - 5 OV positions!	GGA-PBE	/	/	N ₂ bond prolongation	[98]
BMO	GGA-PBE, DFT+U	-1.91	distal	N ₂ adsorption energies, N ₂ bond prolongation, mechanism	[99]
VO-BMO (010)	/	-3.95	/		
Bi ₃ O ₄ Br	GGA-PBE, DFT+U	-0.087	/	DOS for SUC BiOBr, N ₂ adsorption energies	[54]
SUC Bi ₃ O ₄ Br (defective)		-0.241	/		
(Bi _x M _y) ₂ MoO ₆ , m=Fe, La, Yb; Bi	GGA-PBE, PAW, PW	/	dissociative for M=Fe, La, Yb	mechanism	[100]
c-PAN /Bi ₂ WO ₆	GGA-PBE	/	/	N ₂ bond prolongation, electron transfer	[101]
pristine BiOBr	GGA-PBE	/	/	formation energy of OV InFe-BiOBr, charge density map	[102]
Fe-BiOBr + OV		/	/		
pristine BiOBr (001)	GGA-PBE, DNP 4,4 basis set	thermodynamically unfavorable (N ₂ adsorption)	distal /	adsorption energies, mechanism, Gibbs free energies	[103]
OV-BiOBr (001)		/	distal:		
pristine Bi ₅ O ₇ Br	GGA-PBE	-0.008	distal	for all: mechanism, N ₂ adsorption energies, ads. en. of intermediates, energy barrier	[104]
OV-Bi ₅ O ₇ Br		-0.017	/		
Bi ₅ O ₇ Br+O atom		-0.001	/		
pristine BiOBr	DFT-D3, DFT+U	-0.12	/	band structure, CBM, VBM positions, DOS, PDOS, N ₂ adsorption energies	[55]
OV-BiOBr		-0.14	/		
Fe-BiOBr		-0.29	/		
Mo-BiOBr		-0.14	/		
Ni-BiOBr		-0.12	/		
Mo-OV-BiOBr		-0.32	/		
Ni-OV-BiOBr		-0.26	/		
/		-0.45	/		
pristine CuCr-LDH	DFT+U	-0.453	/	band structures, DOS, PDOS, N ₂ adsorption energies	[40]
CuCr-LDH-OV		-0.81	/		
CuCr-LDH-OV,1% strain		-0.886	/		
ZnAl-NS		/	/		
ZnAl-LDH	GGA-PBE, DFT+U	-0.03	/	Band gap, charge density difference, Bader charge, electronegativity difference, flat band potentials, N ₂ adsorption energies	[105]
ZnAl-LDH-OV		-0.54	/		
Cu-doped ZnAl-LDH-OV		-0.94	/		

ZnCr	GGA-PBE, DFT+U	/	/	Band gaps, N ₂ adsorption energies, energy barrier for RDS, formation energy of OV	[41]
ZnCr-LDH		(-0.45 eV unsaturated Zn, -0.17 eV saturated Zn)	/		
ZnCr-LDH-OV		/	/		
ZnCr-OV		/	/		
CdS@LDHs-1	GGA-PBE	/	mechanism: energy barriers: 2.24 eV	mechanism, energy barriers	[106]
CdS@LDHs-2		/	1.69		
CdS@LDHs-3		/	1.38		
Ce-CUS (loaded on MOF-76 Ce)	DFT+U	/		DOS, charge transfer	[56]
MIL-101(Fe)	DFT+U	-0.48	distal, alternating /	charge density difference, N ₂ adsorption energy, Gibbs free energies for first and second hydrogenation	[107]
MIL-101(Ce)		-0.43	/		
Gd-IHEP-7 (2D MOF)	PBE, UPBE-D3	end-on: -0.26	distal, alternating associative	TD-DFT, Mullikan charges, DOS, band structure, N ₂ adsorption energies, CI NEB, Gibbs free energies	[42]
Gd-IHEP-8 (3D MOF)		end-on: -0.29	distal, alternating associative		
Gd-IHEP-7 ligand gr replaced with CH ₃		/	/		
Gd-IHEP-8 ligand gr replaced with CH ₃		/	/		
MoS ₂	GGA-PBE, D3, HSE06	/	distal /	DOS (both), Bader charge, Fe-MoS ₂ binding energy, NBO: MD, Gibbs free energies	[32]
Fe-MoS ₂ (Fe is deposited)		/	/		
SV-IT MoS ₂ /CsS composite	/	/	distal, alternating	Gibbs free energies	[108]
CdS	//	-0.033 (-3.2 kJ/mol)	/	N ₂ adsorption energies	[109]
CdS-SV		-1.31 (-126.5 kJ/mol)	/		
W ₁₈ O ₄₉ (001)	GGA-PBE	-1.65	/	charge density difference, N ₂ adsorption energies	[110]
Mo-doped W ₁₈ O ₄₉		-2.48	enzymatic mechanism		
FeMoS-FeS-SnS		/	/	binding energies	[111]
BPNS/CdS (0001) facet	GGA-PBE	/	distal	charge density difference, mechanism	[112]
CdS (002)	PBE	1.16	/	N ₂ adsorption energies	[113]
NiS (211)		-0.26	/		
Ni-doped CdS		-0.55	/		
Zn ₃ IN ₂ S ₆ (S-TA)	GGA-PBE	/	alternating	bandgap, DOS, PDOS, mechanism	[43]
ZN-defective Zn ₃ IN ₂ S ₆ (S-TAA)		/	/		
Ru(001)	GGA-PBE, DFT-D	end-on: -0.83	enzymatic	N ₂ adsorption, charge density difference, mechanism	[114]
CoS		end-on: -0.58	/		
CoS _r (101)		end-on on SV: -0.98	/		
CoS _r (101)/Ru(001)		side-on: -1.01	/		
WS ₂ monolayer	GGA-PBE	/	dissociative, associative	dopant formation energies, Hirshfeld charges, charge transfer, N ₂ adsorption energies, energy evolution profiles of N ₂ adsorption, reaction energy diagrams	[115]
WS ₂ -SV		-0.04	/		
Ni-WS ₂ -SV		end-on: -0.92, side-on: -0.69	end-on associative (distal, alternating)	Hirshfeld charge analysis, S vacancy formation, N ₂ adsorption, reaction barrier, mechanism	

Au(111)/TS	GGA-PBE, PBE-D3	/	dissociative, associative	solvent effect on adsorbates: Poisson-Boltzmann explicit solvation model, Gibbs free energies for first hydrogenation, charge density difference, H adsorption	[116]
Au(111)-PTFE/TS		/	/		
OV-S rich TiO ₂ -xSy (101) - Ti32O52S8	GGA-PBE, DFT-D3, HSE06	(-0.76 -- -2.1)	/	band structures, N ₂ adsorption energies	[44]
OV-S poor TiO ₂ -xSy (101) - Ti32O61S2	/	/	/	/	
beta Ga ₂ O ₂ (111) facet	GGA-PBE	-0.975	/	N ₂ adsorption energies, N ₂ bond prolongation, mechanism	[117]
LaFeO ₃ (121)	GGA-PBE	/	/	N ₂ bond prolongation	[118]
beta-Sb(001)	PBE-D3, PBE-BJ	/	/	first hydrogenation in mechanism, binding free energy of first hydrogenation	[119]
beta-Sb(100)		/	/		
Sb ₂ O ₃ (001)		/	/		
Sb(001)-SB vacancy		/	/		
Sb(100)-Sb vacancy		/	/		
Sb ₂ O ₃ (001)-O vacancy		/	/		
Bi ₂ WO ₆ (010) (Bi and W active sites)	PBE	/	distal, alternating, enzymatic	formation energies of OV-catalyst, activation, free energy profiles	[120]
Bi ₂ WO ₆ (010)-OV		/	/		
B-antite (BNNTs)	WB97X-D functional, 6-31G* basis set	end-on: -1.06 (-24.4 kcal/mol), side-on: 0.22 (5.15 kcal/mol)	dissociative (excluded), associative (alternating, distal)	BNNTs formation energies, N ₂ adsorption modes, bond prolongation, free energy diagrams, transition states, NBO, Hirshfeld charge, charge density difference	[121]
N-antite (BNNTs)		/	/		
OV-BiOBr	PBE, PBE-sol, DFT-D	end-on: -1.90, side-on: -1.34, side-on N ₂ : -...	distal (adsorption on OV-O-ter+H), alternating...	charge transfer, Hirshfeld charge analysis, N ₂ adsorption, O ₂ and H ₂ O adsorptions, Gibbs free energy diagram	[122]
Bi ₂ MoO ₆	GGA-PBE	/	/	work functions	[123]
Fe-Bi ₂ MoO ₆		/	/		
Pal	GGA-PBE+U	/	/	band structure, DOS, work functions	[124]
Fe ₂ O ₃		/	/		
30 % Fe-Pal		/	/		
MoO ₃ (001) and (100)	PBE+U, DFT-D2	/	/	DOS, Bader charge, Mulliken charge, binding energies (Mo-O), bond elongation	[125]
OV-MoO ₃		/	/		
BiVO ₄ (010/040)	PW91,DFT-D	-0.75	/	electrostatic potentials, band gap, charge density difference, Bader charge, N ₂ adsorption, reaction mechanism	[126]
black phosphorene (BP)	GGA-PBE, HSE06	/	/	NAMD, formation energies of vacancy defects, band gaps, band edges, DOS, PDOS, N ₂ adsorption energies, bond prolongation	[127]
DV-BP		0.25-1.86	/		
blue phosphorene (BuP)		/	/		
DV-BuP		0.25-1.86	/		

4.2. Adsorption

W. Zhao et al. [60] examined the adsorption of nitrogen on Fe³⁺ doped anatase TiO₂ (101). The authors concluded that nitrogen adsorption over the studied catalyst is feasible, as the adsorption energies of N₂ and intermediates vary from -0.621 to -4.666 eV, which is in agreement with the prolongation of triple bond from 1.937 to 2.252 Å when it is broken to the single bond during successive hydrogenation steps. The adsorption energies for pristine TiO₂, OV-TiO₂ and Cu-doped TiO₂ were calculated by Y. Zhao et al. [36] using DFT+U. The adsorption is the most feasible over Cu-doped TiO₂, however all three catalysts exhibit promising results. Defects (OV and strain) enhance electron transfer from defective TiO₂ (OV-TiO₂, Cu-doped TiO₂) to empty π anti-bonding orbital of the adsorbed N₂, as the triple bond is weakened to 1.160 Å for adsorption on OV-TiO₂ and 1.163 Å for Cu-doped TiO₂ compared to pristine TiO₂ (1.155 Å). N₂ adsorption over pristine and OV-TiO₂ was also studied by Yang et al. [62] who obtained similar results. They determined physical adsorption over pristine catalyst and chemical adsorption over defective catalyst. A negligible electron transfer from TiO₂ to N₂ was determined by calculating charge density difference at an isovalue of 0.01 e Å⁻³. On the other hand, a notable charge density difference at an isovalue of 0.05 e Å⁻³ was observed upon adsorption on the OVs, indicating sufficient electron transfer from the OV to N₂ via back donation process, resulting in bond elongation from 1.109 to 1.162 Å. G. Zhang et al. [64] also confirmed a suitability of OVs, since the adsorption energies of all intermediates are calculated to be negative and N₂ is chemically adsorbed. Ti atoms located near OVs gather electrons, which are then transferred to unoccupied π orbital in N₂, leading to triple bond elongation and thus activation of N₂ (determined by calculating Bader charge and differential charge density). The activation of adsorbed N₂ is reflected in the elongation of triple bond from 1.113 to 1.138 Å. Another study, involving OV-defective TiO₂ was done by Hou et al. [65], who studied N₂ activation over pristine TiO₂ (101), OV-TiO₂ (101), Ti₃C₂O₂ and OV-Ti₃C₂O₂ by calculating adsorption energies and charge density differences. Nitrogen is adsorbed on Ti atoms and the adsorption energies are all negative. Both the charge density difference and negative adsorption energies of N₂ over Ti atom of TiO₂-based catalysts indicate favorable nitrogen adsorption, especially over OV-defective TiO₂.

Comer et al. [67] investigated the role of carbon in TiO₂ photocatalyst using BEEF-vdW DFT approach. A substitution of carbon by bridging oxygen atom was performed. A carbon radical (C*), considered as an active site for N₂ adsorption, is formed from hydrocarbon, namely CH₄, via a photooxidative mechanism. A C* active sites have a notably strong N₂ binding free energy of -1.89 eV, but surface carbons have been reported to be unstable. Liao et al. [68] proposed anatase TiO₂ (101) facet, OV-TiO₂ (101) and Ti₃C₂ MXene as an attractive co-catalyst to the P25 TiO₂ photocatalyst for nitrogen fixation. Adsorption energy calculations revealed a much stronger adsorption of N₂ on the surface of Ti₃C₂ MXene compared to pristine and OV-TiO₂ (101) catalysts. Upon the adsorption on the corresponding catalyst, N₂ was activated and the triple bond prolonged to 1.351,

1.156 and 1.113 Å when fixation occurred over Ti_3C_2 MXene, OV-TiO₂ (101) and TiO₂ (101), respectively. The results indicate that oxygen vacancy defects and Ti_3C_2 MXene as a co-catalyst both promote nitrogen photofixation compared to pristine TiO₂, however, MXene exhibits better photocatalytic adsorption properties. Nitrogen adsorption and its activation on a OV-TiO₂ (101) and F-modified TiO₂ (101) were studied by Guan et al. [69]. Nitrogen was chemically adsorbed on the OV active site and the electrons are transferred from the OV to the N₂, while the latter receives 0.52 e and the triple bond is prolonged from 1.09 to 1.18 Å. N₂ adsorption over F defective TiO₂ is more favorable compared to the pristine catalyst, however OVs exhibit the best fixation ability. Sun et al. [45] examined DFT calculations to study N₂ photoreduction over anatase TiO₂ (101), Au₄Ru₂/TiO₂ (101) and Au₄Ru₂(SCH₃)₈(P(CH₃)₃)₂/TiO₂ (101) photocatalysts. The adsorption of N₂ is more feasible when it occurs via end-on adsorption configuration. Upon electron transfer from Ru to the N₂, N-N bond is prolonged from 1.13 to 1.14–1.16 Å, confirming nitrogen activation. The authors perceived no significant effect of Au₄Ru₂(SCH₃)₈(P(CH₃)₃)₂ in N₂ activation as the distance between the Au₄Ru₂ cluster and the substrate added up to 2.57 Å and the binding energy of -0.28 eV per Au(Ru). Adsorption energies and charge density differences of N₂ adsorption over OV-BaTiO₃(110) were determined by Zhao et al. [74] using DFT-PBE approach. Upon the side-on adsorption of molecular nitrogen on the active sites of the catalyst with the energy of -4.60 eV, the triple bond in N₂ is prolonged from 1.117 to 1.314 Å, indicating its activation. The charge density difference exhibited an electron transfer from the catalyst to the nitrogen atoms based on the accumulation and depletion of electrons.

Nitrogen adsorption modes were calculated on the surface of NV-g-C₃N₄. Ma et al. [75] reported that only one of the investigated NV active sites is suitable for N₂ adsorption. The latter is activated on NV, while a sigma bond is formed between nitrogen atom and C atom and the nitrogen bond is elongated from 1.107 to 1.242 Å. Nitrogen adsorption on NV-g-C₃N₄ was also studied by Li et al. [76]. In this study, adsorption on two nitrogen vacancy sites on the surface of g-C₃N₄ was investigated. One NV exhibited physical (NV2) and the other one chemical adsorption (NV1). Upon chemisorption of the nitrogen molecule at position 1, the bond length increases from 1.107 to 1.242 Å, while no significant change in the triple bond length was observed upon physisorption at position 2. DFT calculations were performed by Dong [77] to explore the nitrogen adsorption on NV-g-C₃N₄ (bulk and (001) surface). The results showed that chemical adsorption occurs directly on the OV and the triple bond in N₂ is prolonged from 1.117 to 1.214 Å. Hu et al. [48] studied nitrogen adsorption on pristine and Fe³⁺-g-C₃N₄. The results showed that Fe³⁺ acts as an active site for the chemisorption of nitrogen and that a coordinative Fe-N bond is formed with a length of 1.82 Å and the triple bond in nitrogen is prolonged from 1.157 to 1.181 Å, which confirms nitrogen activation. On the other hand, nitrogen is physically adsorbed on the surface of pristine g-C₃N₄ no change in bond length between two nitrogen atoms is observed during adsorption. The charge density difference

and Mullikan charge value confirm the electron transfer from the Fe^{3+} active site to N_2 . N_2 fixation over SCNN-550 (sulfur-doped $\text{g-C}_3\text{N}_4$ with carbon vacancies) was performed by Cao et al. [27]. They determined carbon vacancies (CV) as active sites for N_2 adsorption and by calculating charge density difference confirmed electron transfer from CV to adsorbed N_2 . Furthermore, the formation of $-\text{N}_2\text{H}$ and HN-NH intermediates has been proposed, but the full mechanism has not been investigated.

Zheng et al. [28] performed DFT -PBE-D2 calculations to study nitrogen photofixation over a boron-decorated melon-based carbon nitride. B was interstitially incorporated into the melon-based C_3N_4 structure, replacing N or C atoms (B_N or B_C , respectively). Side-on adsorption is the most feasible on B_{int4} , while end-on on B_{int5} active site. The Bader charge analysis revealed that 1.35 e is transferred from B to the melon-based CN, indicating that the B atom is a suitable active site for nitrogen adsorption and activation. The electron transfer from B active site to adsorbed N_2 was confirmed by charge density difference. The magnetic spin moment of the B atom is calculated to be $1.01 \mu_B$, indicating that spin-polarization also contributes to substrate activation. The adsorption energies for the chemical adsorption of nitrogen on the surface of $\text{g-C}_3\text{N}_4$ (CN) and Ms-Cu-CN were calculated by Hu et al. [50] using GGA-PW91 approach. When adsorbed on Ms-Cu-CN (Cu-N bond length is 2.943 \AA), the nitrogen triple bond was extended from 1.157 to 1.17 \AA , confirming nitrogen activation. On the other hand, no significant change in length of triple bond was observed upon adsorption on pristine g-CN compared to the free nitrogen molecule. The charge density difference analysis and calculated Mullikan charges revealed that electrons are transferred from the Cu^+ active sites to the nitrogen molecule. DFT method with the GGA-PBE functional was used to calculate the free energy change for the HER process and the adsorption energies of nitrogen photofixation on the Fe-EDTA graphitic carbon nitride nanosheets [79]. The adsorption energies showed that nitrogen molecule is physically adsorbed on the surface of CNNS and EDTA-CNNS and chemically on the surface of Fe-EDTA-CNNS. Liang et al. [80] used DFT calculations to study adsorption energies of nitrogen on boron-doped ultrathin carbon nitride and concluded that adsorption is the most feasible over BNUCNx-B2. The triple bond is in the latter case prolonged to 1.256 \AA , implying its activation. Both NVs and boron-doping affect promote N_2 fixation. The Mulliken charge analysis revealed that the cyano group ($-\text{CN}$) acts as an electron acceptor and that the B atom as a dopant enables electron transfer to the nitrogen molecule. The end-on and side-on adsorptions of the nitrogen molecule on a metal-free B@g-CN were considered by X. Lv et al. [29]. Since the photocatalyst can be exposed to impurities, the adsorption of the CO_2 molecule was also investigated and excluded as a possible impurity. Even though, water and oxygen molecules can be reduced, enough active sites for N_2 adsorption is provided. The Bader charge analysis showed that $1.42 |e|$ is transferred from the B atom to the g-CN. K. Wang et al. [51] calculated Hirshfeld charges, charge density difference analysis and DOS of N_2 activation over pristine and Co-doped $\text{g-C}_3\text{N}_4$. The results show that nitrogen adsorption is more

feasible over Co-doped catalyst, which provides chemical adsorption and prolongation of triple bond from 1.175 to 1.178 Å when adsorption occurs on Co active site. On the other hand, physical adsorption is possible over pristine catalyst. The total Hirshfeld charge analysis show lower charge carrier flow from the bulk catalyst to N_2 compared to charge transfer from Co-doped catalyst to the adsorbed N_2 . Another study of N_2 activation over pristine and vacancy rich g- C_3N_4 was carried out by Shi et al. [81]. Three active sites were predicted and explored for nitrogen fixation on vacancy rich g- C_3N_4 , namely on oxygen atom, hydroxyl group and on undoped g- C_3N_4 active site. The aforementioned active sites were depicted as A, B and C, respectively (Fig. 5). It was reported that adsorption at the C adsorption site is the most feasible. It was also observed that the adsorption energies increased (at the site A for 3-times, at the site B for 2.3 times and at the site C it remained unchanged) when O atoms or OH groups were introduced into the g-CN structure.

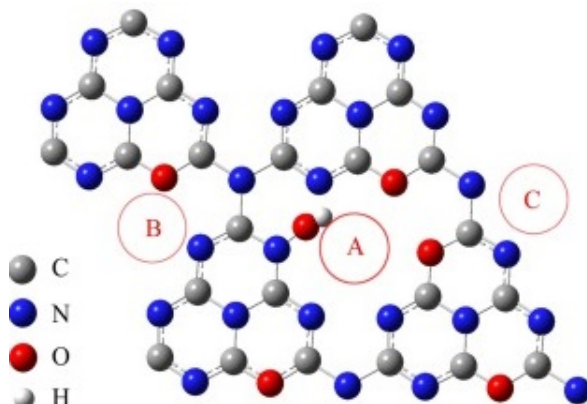


Figure 5: Three adsorption modes on vacancy-rich g- C_3N_4 for N_2 adsorption, denoted as A, B and C [81].

Li et al. [83] confirmed that N_2 is chemisorbed on the surface of VN-CN and VN-SCN, however the adsorption is more feasible over VN-SCN, implying a significant role of sulfur dopant. In the latter case triple bond is prolonged from 1.157 to 1.415 Å. The electron transfer from NV to the antibonding orbital of nitrogen was confirmed by charge density difference analysis. Guo et al. [84] also confirmed a beneficial role of doping, as they investigated N_2 fixation over pristine and Mo-immobilized g- C_3N_4 . For the latter, chemical adsorption of N_2 via end-on adsorption configuration on a Mo active center was determined with significantly lower adsorption energy compared to adsorption on pristine catalyst and bond prolongation from 1.11 to 1.15 Å. Water adsorption was also studied, however its adsorption energy is much higher (-0.391 eV) and does not endanger N_2 fixation. Liu et al. [85] theoretically investigated nitrogen adsorption over NV-GaN, which was chosen due to its high surface activity and stability. The results show that the nitrogen molecule is physically adsorbed on the surface of pristine GaN, while it is chemically adsorbed on the surface of nitrogen vacancy rich GaN. In the latter case, N_2 is adsorbed

on NV active site and the triple bond is prolonged from 1.11 to 1.28 Å, implying its activation. Differential charge density (calculated at the isosurface of 0.002 e/Å³) and Bader charges revealed that electrons are transferred from Ga to the antibonding orbital in N₂ upon adsorption on the surface of GaN.

J. Li et al. [30] confirmed side-on adsorption of N₂ at the N₃ site of the Pt-SACs/CTF catalyst. AIMD simulations were performed to simulate and determine the thermodynamic stability of the Pt-SACs/CTF and N₂-Pt-SACs/CTF. The results revealed that both structures are stable under simulation conditions and reaction temperature of 300 K. The Bader charge analysis showed that electrons are transferred from the Pt atom (active site) to the CTF framework, as the calculated Bader charge for Pt atom adds up to +0.43 e. Charge density difference of the Pt-SACs/CTF showed that the change in the electron density occurs due to the formation of the Pt-N bond upon Pt introduction into the SACs/CTF catalyst. Wang et al. [31] studied N₂ adsorption on dual-metals (M1M2) loaded on the surface of g-C₃N₄. End-on and side-on nitrogen adsorption configurations were proposed and results showed that FeMo, MoW, NiMo and TiMo can be considered as efficient photocatalysts. On the latter photocatalysts, the adsorption occurs on Fe, W, Ni and Ti active sites. Electrons are transferred from Mo to Fe (0.43 e), W (0.38 e), Ni (0.36 e) or Ti (0.33 e) and then further to antibonding orbital of N₂. The authors investigated adsorption on a FeMo dual-metal deposited on N-doped graphene, which thermodynamic stability was confirmed by AIMD simulations. Charge density difference analysis showed the accumulation of charge on N₂ and its depletion on a FeMo active site, confirming electron transfer from the dual metal to the adsorbed nitrogen molecule. Nitrogen adsorption together with the charge transfer between the VN-g-C₃N₄ and VN-P-g-C₃N₄ photocatalysts and N₂ were studied by Wang et al. [87]. The adsorption energy was much smaller when it occurred on a phosphorus doped photocatalyst compared to the P-free catalyst (-3.52 eV), suggesting that the P atom promotes nitrogen fixation ability. Feasibility of P doping is reflected also in prolongation of triple bond from 1.157 to 1.399 Å. The charge density difference confirmed that electrons are transferred from NV to the N₂, which are generated upon P doping. Liu et al. [88] investigated adsorption energies of Ru₁₁ clusters loaded on E-g-CN layer and on the edges of two layers of B-g-C₃N₄, respectively. Ru₁₁ cluster was especially attractive as it contains B₅ sites, which are considered as active sites for nitrogen adsorption and activation. Nitrogen adsorption on Ru₁₁/B-g-C₃N₄ was found to be more feasible than over Ru₁₁/E-g-C₃N₄. N₂ is adsorbed via side-on configuration which was determined to be more stable than -on configuration. Work functions were also calculated and revealed a possible electron transfer from E-g-CN and B-g-CN to Ru clusters with the values of work functions of 5.4, 4.13 and 3.93 eV for Ru₁₁, E-g-CN and B-g-CN, respectively.

Hou et al. [91] investigated N₂ adsorption on the surface at the three active sites of Fe₁O₄/C-PPH₃/Na, however, they also calculated adsorption energies on the surfaces of O₂/C and Fe₁O₄/C and revealed that the adsorption is the most feasible on Fe₁O₄/C

when N_2 is adsorbed via end-on configuration. Qin et al. [92] studied different N_2 adsorption modes on the Ti_3C_2 (001) surface, which was found to be more feasible when it occurred via side-on configuration. The latter was determined based on lower adsorption energy and higher bond prolongation (to 1.334 Å). Electron transfer from d-orbital of Ti to N_2 was confirmed by charge density difference. Shao et al. [93] made an extensive study of various MXenes, M_2X ($M=Mo, Ta, Ti, W$ and $X = C$ and N), as promising catalysts for NRR. N_2 adsorption was proposed on the top of the metal atom (TM), the hexagonal center (HC), top of X atom (TX), namely in perpendicular, parallel (Ta, Ti based MXenes) or tilted (Mo_2C, W_2C) mode. The calculated binding energies (adsorption energies) were all negative, indicating that nitrogen adsorption was favorable on all MXenes, however it is the most feasible over Ta_2C, Ta_2N, Ti_2C and Ti_2N . Charge density calculations showed that photogenerated electrons are transferred from M_2X to N_2 which is activated and triple bond prolonged to $\sim 1.20 - 1.95$ Å.

Nitrogen activation was explored by Yang et al. [39] and $M_4@B_36N_36$ clusters were considered as photocatalysts for N_2 activation. They proposed 11 metals to be caged into the B_36N_36 structure, however Sc, Ti, V, Cr, Y, Zr, Mo and W were chosen to be included in the cluster structures due to their ability to perform side-on adsorption of nitrogen molecule. Nitrogen was adsorbed on the aforementioned clusters and the electron transfer from cluster to N_2 was confirmed by charge density difference and N_2 activation by prolongation of triple bond in the range between 0.09 and 0.12 Å. $Y_4@B_36N_36$ exhibited the lowest adsorption energy of -0.76 eV and depleted the highest amount of electrons (0.72 eV). Songmei Sun et al. [52] confirmed N_2 activation over BiO quantum dots, as the triple bond is prolonged from 1.09 to 1.12 Å. The coverage of water molecules is high and is found to enhance nitrogen activation, as N_2H_n is readily desorbed from the surface when water molecules were added.

N_2 end-on chemisorption was suggested over OV-defective (001) and (010) BiOCl facets by Li et al. [94]. Upon nitrogen adsorption on the (001) surface, the triple bond is elongated from 1.078 to 1.137 Å, whereas upon the adsorption on the (010) surface it is elongated to 1.198 Å, indicating (010) surface is more favorable for nitrogen activation. Charge density difference calculations showed that electron transfer from OV of OV-BiOCl (010) to N_2 is more efficient than transfer from OV-BiOCl (001) to N_2 , which was confirmed also by Bader charge analysis, implying higher activation over (010) surface. Li et al. [95] attempted to perform chemical adsorption of N_2 on H-stabilized BiOBr(001), but the latter was excluded due to the weak interaction between the nitrogen molecule and the photocatalyst. When considering the OV-BiOBr (001) photocatalyst, N_2 was adsorbed via a side-on configuration and was associated with two nearest-neighbor OV defects. Activation of the nitrogen molecule during adsorption on OV-BiOBr (001) was confirmed by charge density differences and Bader charge calculations. Electron transfer along with elongation of triple bond upon the adsorption on BiOCl-OV was studied by Wu et al. [98] who reported that nitrogen is adsorbed on the OV of OV-BiOCl via end-on configuration

and activated while triple bond is prolonged to 1.173 Å. Higher activation is observed when Br atom is doped, which is consistent with bond prolongation to 1.184 Å.

Li et al. [99] studied nitrogen adsorption on BMO (Bi_2MoO_6) and OV-BMO-OH (010) surfaces. DFT+U calculations using GGA-PBE showed that nitrogen was activated upon adsorption on both photocatalysts, but the activation was higher when adsorbed on the OV-rich BMO (010). The adsorption energy of nitrogen on OV-BMO 010 is lower and the triple bond is elongated to 1.209 Å, indicating more favorable adsorption over OV-defective catalyst. Jun Di et al. [54] conducted DFT+U calculations to study the adsorption on the pristine and defective $\text{Bi}_3\text{O}_4\text{Br}$ catalyst. The results showed that nitrogen adsorption on BiOV-defective $\text{Bi}_3\text{O}_4\text{Br}$ is more feasible than adsorption on the pristine catalyst. [101] C. Zhang et al. performed spin-polarized DFT calculations of N_2 fixation over c-PAN (cyclized polyacrylonitrile) / Bi_2WO_6 . The nitrogen atoms in c-PAN act as active sites for nitrogen adsorption and its activation which occurs upon electron transfer from the unsaturated N atom in to the antibonding orbital in N_2 (determined by Bader charge analysis). Xue et al. [103] studied N_2 adsorption on the pristine and OV-rich BiOBr (001) surface. Nitrogen is activated upon adsorption on the OV-BiOBr, as the triple bond in N_2 is prolonged from 1.11 to 1.24 Å. P. Li et al. [104] investigated nitrogen adsorption over pristine $\text{Bi}_5\text{O}_7\text{Br}$, OV- $\text{Bi}_5\text{O}_7\text{Br}$ and $\text{Bi}_5\text{O}_7\text{Br} + \text{O}$ (additional O atom).using DFT-PBE. Adsorption is the most feasible over OV- $\text{Bi}_5\text{O}_7\text{Br}$. Ni-OV-BiOBr exhibited the lowest adsorption energy of N_2 among all investigated photocatalysts (BiOBr, OV-BiOBr, Fe-BiOBr, Mo-BiOBr, Ni-BiOBr, Fe-O-BiOBr, Mo-O-BiOBr and Ni-O-BiOBr). Even though Chen et al. [55] determined Ni-doped catalyst (Fig. 6) as a catalyst with the lowest adsorption energy of N_2 , Bader charge analysis shows more efficient electron transfer from Fe-OV-BiOBr (102) to N_2 . Both catalyst are therefore considered as promising for nitrogen activation.

Zhao et al. [40] examined adsorption energy calculations over a pristine, OV-defective and OV-strain-CuCr-LDH and -ZnAl-LDH. Introduced defects (OVs) lowered the adsorption energy of N_2 on both CuCr-LDH and ZnAl-LDH catalysts. Similar conclusion was made by Zhang et al. [105] who studied adsorption over pristine ZnAl-LDH, OV-ZnAl-LDH and Cu-doped ($\text{Cu}^{\sigma+}$) -OV-ZnAl-LDH. Cu doping exhibited the lowest adsorption energy and the most feasible electron transfer from unsaturated Cu active site to N_2 (confirmed by charge density difference and Bader charge). Another study was done by Zhao [41] who observed stronger adsorption of N_2 over unsaturated Zn active sites of ZnCr-LDH compared to adsorption over saturated Zn active sites.

Zhang et al. [56] calculated DOS and electron transfer for N_2 fixation over Ce-CUS photocatalyst. It was observed that Ce 4f orbitals overlap with the pi anti-bonding orbital of N_2 , indicating that electron transfer occurs from Ce to N_2 and prolongs triple bond to 1.117 Å. G. Li et al. [107] studied the adsorption and electron transfer from Cr and Fe active sites of MIL-101(Cr) and MIL-101(Fe), respectively, to the adsorbed N_2 molecule. Adsorption energy is lower over Fe active sites, whose feasibility was confirmed by calculating charge density difference. The latter show a negligible transfer from the Cr to N_2 and a

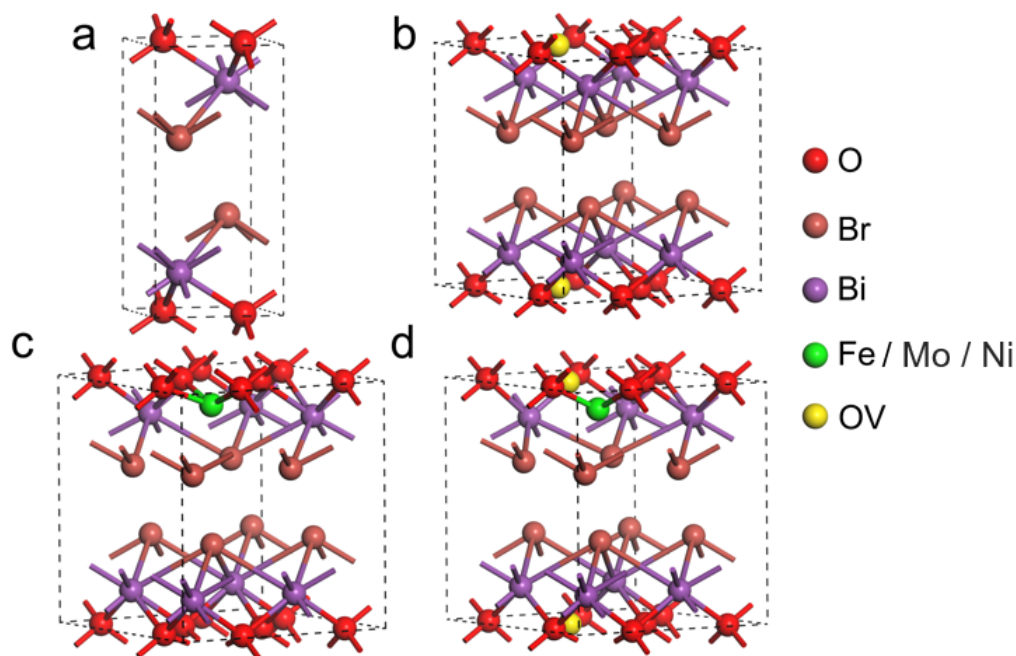


Figure 6: Optimized structures of: a) pristine BiOBr, b) OV-BiOBr (2x2x1) supercell, Fe/Mo/Ni-BiOBr (2x2x1) supercell d) OV-Fe/Mo/Ni-BiOBr (2x2x1) supercell [55].

significant transfer from Fe active site to N_2 . Chemical adsorption of N_2 over Gd-IHEP-7 and Gd-IHEP-8 surfaces was studied by Hu et al. [42]. The adsorption via end-on configuration is lower over Gd-IHEP-8, which is also consistent with bond prolongation to 1.106 Å.

The adsorption of N_2 and H_2O on the Fe active site of FeSMoS was theoretically examined by Azofra [32]. Adsorption of N_2 is compared to adsorption of H_2O more spontaneous (negative Gibbs free energy). Bader charge analysis shows electron transfer from Fe to MoS_2 , indicating that Fe could be a suitable active site for N_2 fixation. Furthermore, NBO (Natural Bonding Orbital Analysis) was performed to investigate the N-Fe interaction when the nitrogen is chemically adsorbed on the Fe atom. S. Hu et al. [109] studied N_2 adsorption on pristine and SV-CdS (111) facet. Lower adsorption energy and larger bond prolongation (from 1.164 to 1.213 Å of N_2 adsorbed on SV of CdS (111) indicate favorable presence of SV.

N. Zhanf et al. [110] explored N_2 adsorption on pristine W_18O_49 and Mo-doped W_18O_49 . N_2 approaches toward W-W dimer in pristine catalyst via end-on configuration and exhibits lower adsorption energy when it is adsorbed on Mo active site of Mo-doped W_18O_49 . The charge density difference shows that N_2 is polarized when adsorbed on the Mo active

site, as the charge difference increased from 0.45 to 0.58 e.

Liu et al. [111] conducted broken symmetry DFT to study the binding energies between N_2 and the precursors of FeMoS-FeS-SnS, FeMoS-SnS and FeS-SnS. These chalcogels were selected as local fractions for nitrogen adsorption. It was observed that N_2 is adsorbed on Mo or 4-coordinated Fe active site. Binding of N_2 to the Mo active site required 9.6 kcal/mol, while binding to 4- reduced $Mo_2Fe_6S_8(SPh)_3$ was slightly thermodynamically feasible (-0.8 kcal/mol) and binding to 5- reduced photocatalyst was more feasible for -7.3 kcal/mol. The triple bond in the nitrogen molecule was extended to 1.098 Å when nitrogen was adsorbed on the 5-state. When nitrogen was adsorbed on the Fe atom in $Mo_2Fe_6S_8(SPh)_3$, δ of the binding energies were 27.3, -1.6, and -8.6 for the 3-, 4-, and 5-states, respectively. The length of the nitrogen triple bond was 1.111 Å when the nitrogen is adsorbed in the 5-state. This indicates that the Fe active site was best for nitrogen adsorption, while the binding energies were lower compared to adsorption at the Mo active site. When nitrogen interacted with the Mo active site, the sulfur bridging ligand left the Mo atom and moved to the opposite Mo atom. On the other hand, when nitrogen interacted with the Fe atom, the chloride ligand was removed and the Fe-S-Sn bridge was disrupted. The predominant interactions were van der Waals forces. When nitrogen was adsorbed onto $[Fe_4S_4Cl_4]^{2-}$, the binding was similar to the binding of nitrogen to the Fe atom as the chloride ligand was removed. The binding energies for adsorption of N_2 in the 2-, 3-, and 4-states were thermodynamically less favorable and were (δ) 27.4, 19, and 5.4 kcal/mol for the 2-, n3-, and 4-states, respectively. The triple bond was extended from 1.098 to 1.116 Å when nitrogen was adsorbed on the 4-state of $[Fe_4S_4Cl_4]^{2-}$.

Shen et al. [112] studied a BPNS/CdS (0001) photocatalyst and calculated a charge density difference. It was observed that BPNSs accumulate electrons that are transferred from the CdS and that the Fermi level of the CdS (-0.06 V vs RHE) lies lower than of the BPNS (0.46 V vs RHE). Gao et al. [113] examined DFT calculations using PBE functional to study nitrogen adsorption on CdS (002), NiS (211) surfaces and on Ni-doped CdS surface. Among them, Ni-doped CdS exhibited the lowest adsorption energy and Ni dopant is therefore considered as promising for N_2 activation, which was also confirmed by charge density difference calculations.

Yuan et al. [114] investigated the adsorption on single Ru, Co atoms, S-vacancies in CoS_x , and on Ru-Co center in Ru/ CoS_x , which was found to be the most feasible over Ru-Co center in Ru/ CoS_x , which is consistent with the longest width of extended triple bond in N_2 compared to the activation on other catalysts. Ru loaded on SV-CoS/CN reduces sulfur vacancies and accepts electrons from CoS_x . The excitons are dissociated and transferred from CN and CoS_x to Ru in Ru/ CoS_x and further to N_2 . WS_2 monolayer with S-vacancy was formed and studied by Ma et al. [115] Transition metal single atoms (Sc, Ti, V, Cr, Fe, Co, Ni, Cu, Nb, Mo, Te, Ru, Rh, Pd, Ag, Cd, W, Pt, Au) were anchored on S-vacancy (SV) and SV formation was determined to be a spontaneous process. They concluded that Ni is the most promising transition metal for nitrogen chemisorption, which occurs via

end-on configuration, alluding on a distal or alternating mechanism to be predominant. Electron transfer from Ni-catalyst to N_2 was determined by Hirshfield charge analysis, revealing N_2 activation and triple bond prolongation to 1.19 Å. Hue et al. [44] examined spin-polarized DFT calculations with PBE functional to study nitrogen adsorption over OV-S rich- and OV-S-poor $TiO_{2-x}S_y$ (101). The results show that N_2 adsorption over OV-S-rich $TiO_{2-x}S_y$ is more feasible due to lower adsorption energy, however, S doping was found to be more feasible compared to OVs. Oshikiri et al. [117] investigated the adsorption on β Ga_2O_2 (111) facet. Nitrogen is adsorbed over Ga active site with an energy of -0.975 eV and the triple bond is prolonged to 1.159 Å. Electrons are transferred directly (photogenerated electrons) or through carbonaceous radicals that are formed during the reaction. DFT-PBE approach was applied to study nitrogen photofixation on $LaFeO_3$ (121) surface [118]. Upon chemical adsorption at the Fe active site of the catalyst, the nitrogen molecule is activated and the triple bond prolonged from 1.081 to 1.167 Å. The activation is explained as a pull and push process, since Fe^{3+} is considered as an adsorption site for N_2 . Furthermore, hydrogen bonding group is proposed as a second (additional) active site for nitrogen activation. 'Pull and push' process is explained in the Fig. 7.

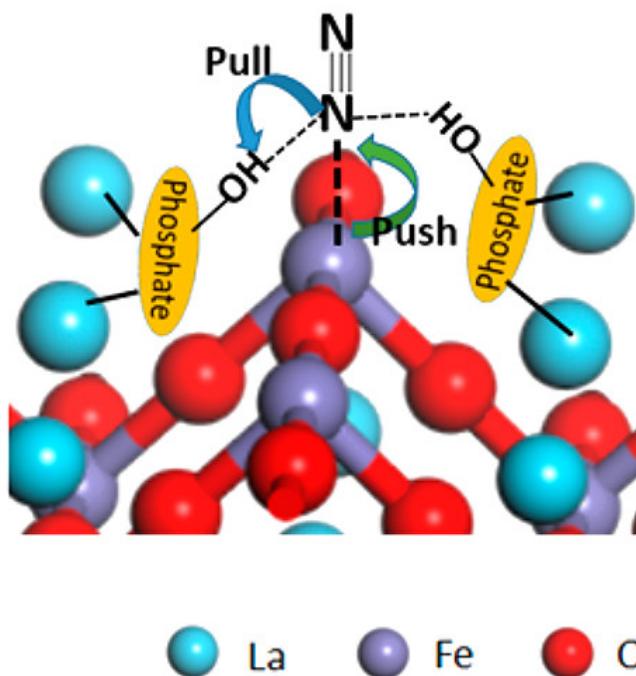


Figure 7: Pull and push process of N_2 activation over $LaFeO_3$ [118].

Nitrogen activation was studied by Wang et al. [120] on the Bi_2WO_6 (010) surface. The

attention is paid to the active sites of Bi and W near oxygen vacancies, since the triple bond in N_2 is prolonged from 1.155 to 1.189 and 1.159 Å in the presence of low valence W and Bi sites, respectively. Liu et al. [122] investigated charge transfer from Bi-Br facet and O-ter+H+OV to adsorbed N_2 . The Hirshfeld charge analysis shows that the electrons are transferred from Bi-Br facet to the nitrogen adsorbed via end-on, side-on and bridge-on configurations. N_2 is also activated upon charge transfer from O-ter+H+OV facet to the π antibonding orbital in N_2 .

In Section 2.2 we summarized the principles of N_2 adsorption. In this section we reviewed N_2 adsorption and activation properties, such as adsorption modes, energies, adsorption configurations and activation, which was determined by calculating Bader or Hirshfeld charges, charge density differences and prolongation of triple bond in N_2 . Generally, nitrogen is adsorbed via end-on or side-on configuration. Adsorption modes depend on the catalyst structure, however, it can be summarized that vacancies and dopant atoms (cocatalyst) are considered as active sites for N_2 adsorption. Upon the adsorption, electrons are transferred from the catalyst to the π antibonding orbital in N_2 and the triple bond in N_2 is prolonged, resulting in activation of the adsorbed molecule [7–9, 14]. Electron transfer can be accompanied by calculating charge density differences and Bader or Hirshfeld charges. In addition, it is important to be cognizant to the strength of adsorption. Physisorption is too weak for the chemical reaction to occur, while on the other hand too strong adsorption leads to the poisoning of the catalyst surface with intermediates and products, which affects negatively on the photocatalytic activity [128]. The latter was demonstrated in the study of N_2 adsorption performed on dual-metals loaded on the surface of g- C_3N_4 . Wang et al. [31] reported that nitrogen adsorption via end-on configuration on CrCo, FeCo and MnMo/gCN occurred via physisorption, as the adsorption energy added up to ~ -0.50 eV. On the other hand, adsorption over CrFe and TiW/gCN occurred too strongly (~ -2.00 eV) and the ammonia molecule was difficultly desorbed from the catalyst surface. Other considered dual metals were found to be suitable for N_2 adsorption and further reduction, as the adsorption energies were calculated in the range from -1.01 to -2.09 eV.

4.3. Reaction mechanism

The mechanism of nitrogen reduction over Fe-doped TiO_2 (101) was proposed by W. Zhao et al. [60]. They proposed an alternating pathway for N_2 reduction to NH_3 . $\cdot H$ required for reduction is provided from water, which accepts electrons from TiO_2 surface and yields $\cdot H$. Y. Zhao et al. [36] calculated Gibbs free energies for first and second hydrogenation of N_2 on pristine, OV and Cu-doped TiO_2 . They concluded that the adsorption and activation of nitrogen is the most favorable on TiO_2 -OV-strain photocatalyst. Comer et al. [63] theoretically investigated nitrogen photoreduction and oxidation on pristine, OV defective and Fe-doped rutile TiO_2 (110). They calculated the surface free energy, coverage and

coverage probability for H₂O, N₂, O₂ and OH adsorbed on the aforementioned photocatalysts. Dissociative and associative pathways were proposed for nitrogen adsorption on pristine rutile TiO₂ (110) and free energy diagrams were calculated, indicating unfavorable nitrogen reduction while the energy barriers are too high. However, the associative pathway is found to be more favorable compared to the dissociative pathway. G. Zhang et al. [64] calculated adsorption energies for all intermediates formed during hydrogenation of nitrogen on OV-anatase TiO₂(101). The mechanism of reduction was not fully described, but only energy values for photocatalyst, nitrogen and intermediates (N₂H, N₂H₂, N₂H₃, N₂H₄, NH₂ + NH₃ and NH₃) were presented. Comer et al. [67] examined photooxidation of CH₄ hydrocarbon to form C* radicals, that are incorporated into the structure of TiO₂. Specifically, bridging oxygen atoms are replaced by carbon radicals. The photooxidation of CH₄ to C* is thermodynamically feasible since it is exothermic. The researchers proposed distal mechanism for nitrogen reduction on carbon active sites in C-TiO₂. The potential-limiting step for nitrogen reduction is first hydrogenation of C*-N₂ to C*-N₂H. After desorption of second ammonia molecule, C*H₃ must be regenerated to generate C*. It is worth mentioning that carbon rich TiO₂ provide nitrogen photoreduction to ammonia, although the reductive driving force for CH₄ oxidation is relatively small (> 1eV).

Guan et al. [69] calculated adsorption energies over pristine, OV defective and F-defective TiO₂ (101) photocatalyst. The desorption of a second ammonia molecule with an energy barrier of 1.65 eV is calculated as a rate-determining step for NRR over OV-TiO₂ (101). On the other hand, for the adsorption of N₂ on F-OV-TiO₂ (101), the formation of NNH* with an energy barrier of 1.61 eV is determined as the rate-determining step. Proposed reaction pathway over OV-TiO₂ can be written as follows: *N₂ → NNH* → NNH₂* → NHNH₂* → NHNH₃* → NH* + NH₃ → NH₂* → NH₃* → NH₃. The authors suggested that NRR occurs preferentially over F-OV-TiO₂, because both OVs and hydrophobic F promote nitrogen fixation and activation. Sun et al. [45] examined DFT calculations to investigate nitrogen photofixation over OV-TiO₂ (101) and Ag₄Ru₂/OV-TiO₂ (101) photocatalysts. Firstly, they suggested water photolysis to provide hydrogens as the proton source for nitrogen reduction. They proposed OV defects on the surface and on the subsurface of TiO₂ and calculated kinetic barriers of 0.09 and 0.02 eV for water oxidation on the surface and subsurface OV-defective TiO₂ (101). Moreover, the authors exhibited three reaction pathways for nitrogen reduction, namely distal, alternating and enzymatic. They concluded that nitrogen photoreduction is more likely to occur on Ru active site of Au₄Ru₂/TiO₂ (101) through alternating and distal pathways.

Qian et al. [73] explored a reaction mechanism for nitrogen photoreduction over a OV-TiO₂ photocatalyst. They suggested to start the NRR with a distal mechanism, proceed with alternating and finish with enzymatic pathway. Based on the calculated results, it can be concluded that the formation of the second ammonia is considered as a potential limiting step for NRR. Moreover, OVs facilitate nitrogen reduction. Free energy profiles

for N₂ adsorption on oxygen vacancy rich-BaTiO₃ (110) were calculated by Zhao et al. [74]. The results show that the rate-determining step of NRR is desorption of the first ammonia molecule formed by successive hydrogenation of adsorbed N₂. After a Lorentz force of 0.01 q was applied, the magnetic field was induced and the reaction energy of the rate-determining step decreased from 1.66 eV to 1.39 eV. The results suggest a favorable ferromagnetic properties of BaTiO₃, as the spontaneous polarization electric field promotes charge carrier separation and thus enhances the photocatalytic activity. Li et al. [76] proposed a dissociative mechanism for NRR over NV-P-doped g-C₃N₄. The water molecule is adsorbed on the P atom, whereas dissociation of nitrogen triple bond occurs on the C³⁺ atom, which contains 2 unpaired electrons and meleme center. In addition, no adsorption centers for N₂ adsorption are located next to the nitrogen vacancy.

Zheng et al. [28] theoretically studied nitrogen activation over boron-decorated melon-based carbon nitride. A reaction mechanism at the B_{int4} active site was investigated. Distal, alternating and enzymatic pathways were proposed to study the nitrogen photoreduction process, and Gibbs free energies were calculated for all intermediates formed during the reduction process. The required potentials for distal and alternating pathways are higher than the potential of B/g-C₃N₄ (-1.21 V), indicating that the distal and the alternating pathways are not the most feasible for NRR. In the enzymatic side-on pathway the nitrogen adsorption requires the ΔG of -1.16, which is lower than in the both end-on pathways. The enzymatic pathway is considered to be most feasible among all three pathways studied. Yao et al. [79] applied DFT calculations to study nitrogen fixation and hydrogen evolution reaction on Fe-EDTA-CNNS catalyst. The free energy diagram for the HER reaction process showed a significant change in the free energy of the intermediate H* (0.94 eV), indicating that the HER reaction occurs at the surface of the photocatalyst. Guo et al. [84] proposed distal and alternating reaction mechanisms for nitrogen adsorption on the Mo-immobilized CN with the end-on configuration. The formation of the N₂H* intermediate is a rate-determining step. Li et al. [30] proposed distal and alternating mechanisms to explain the nitrogen photoreduction over Pt-SACs/CTF catalyst. Gibbs free energy profiles for nitrogen reduction on the Pt-SACs/CTF catalyst were calculated to explore which of the above mechanisms is thermodynamically more favorable. In the alternating mechanism only the first hydrogenation process is endergonic, while the others are exergonic, indicating that alternating mechanism is thermodynamically more favorable compared to distal pathway (Fig. 8).

Wang et al. [31] studied 16 dual-metal graphitic carbon nitrides as a promising catalysts for photo(electro) NRR. They compared alternating, distal and enzymatic mechanisms based on calculated Gibbs free energies and energy barriers for individual steps. It was observed that among all photocatalysts studied, FeMo/gCN possesses the best charge transfer ability. Multiple metal active centers enhance nitrogen reduction process. The HER reaction (H adsorption) was also studied. The adsorption energies for nitrogen reduction on 4 photocatalysts were compared to adsorption energies of H adsorption. It

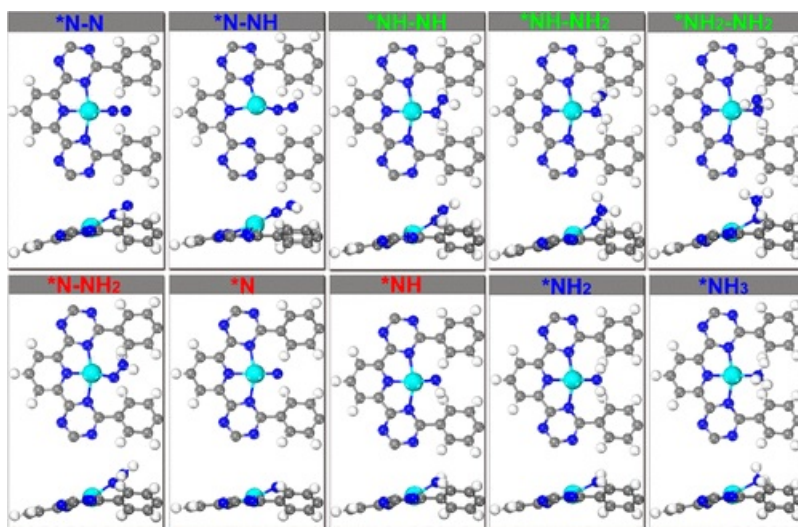


Figure 8: Intermediates formed during the distal and alternating pathways [30]

was observed that on FeMo, TiMo and NiMo nitrogen rather than hydrogen adsorption prevails, while adsorption energies for nitrogen and hydrogen adsorption are very similar in the case of MoW. Liu et al. [88] examined spin-polarized DFT calculations with a PBE-GGA+U approach to examine NRR on Ru/E-g-C₃N₄ and Ru/B-g-C₃N₄. It was found that N₂ reduction could undergo an associative pathway over a Ru/E-g-C₃N₄ photocatalyst and a dissociative mechanism over a Ru/B-g-C₃N₄ photocatalyst. NRR over both photocatalysts showed the same rate determining step, namely the transformation of end-on to side-on adsorption configuration of N₂. Based on the adsorption results, Hou et al. [91] investigated NRR via hybrid distal to alternating pathway, when N₂ is adsorbed via end-on configuration at Fe active sites of Fe₁O₄/C. However, they also proposed an enzymatic pathway (Fig. 9) and calculated Gibbs free energies of the intermediates. The rate-limiting step of NRR via a hybrid distal to alternating pathway is the first hydrogenation of N₂. HER (hydrogen evolution reaction) was also studied and the H adsorption energy of Fe₁O₄/C was lower than the N₂ adsorption (-0.80 eV), confirming the preferential adsorption of nitrogen. Among all proposed pathways, alternating was defined as the most promising.

The reduction of N₂ on different MXens (M₂X (M=Mo, Ta, Ti, W and X = C and N)) was theoretically studied by Shao et al. [93]. They proposed a distal and an enzymatic pathway for NRR. It was found that reaction on Mo₂C and W₂C is more feasible compared to Ta- and Ti-based carbides and nitrides. Yang et al. [39] carried out spin-polarized DFT-D3 calculations to reveal the NRR mechanism over M₄@B₃₆N₃₆, where considered metals were Sc, Ti, V, Cr, Y, Zr, Nb, Mo, Hf, Ta and W. Due to side-on nitrogen adsorption configuration, only enzymatic pathway was theoretically explored. Gibbs free energy calcula-

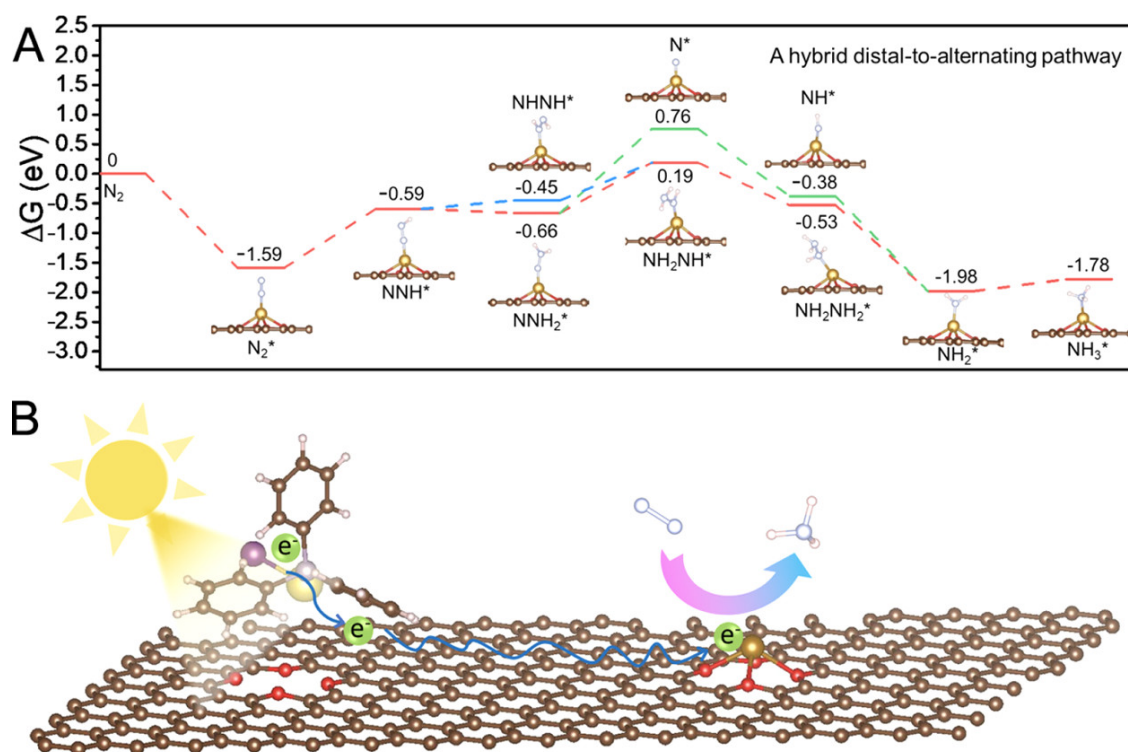


Figure 9: A) A hybrid pathway proposed for N_2 fixation over the $\text{Fe}_1\text{O}_4/\text{C}$ catalyst. B) A schematic representation of photocatalytic NRR over the $\text{Fe}_1\text{O}_4/\text{C}$ catalyst [91].

tions of NRR over $\text{Mo}_4@\text{B}_{36}\text{N}_{36}$ showed that a rate-determining step is the hydrogenation of $^*\text{NH}_2$ to $^*\text{NH}_3$. On the other hand, when Ti, V, Cr and W metals were considered in clusters, the rate-determining step is the formation of $^*\text{NH}_2\text{-NH}_2$. Furthermore, for Sc, Y and Zr-containing photocatalyst, the rate determining step is reported to be the protonation of $^*\text{NH-NH}$ to $^*\text{NH-NH}_2$. It can be seen that the step, which is considered as rate-determining, strongly depend on the transition metal chosen. Li et al. [94] studied a mechanism for nitrogen reduction to ammonia on OV-BiOCl (001) and (010) facets by means of DTF+U. Relative energies of the intermediates formed during distal and alternating pathways were calculated. It was proposed that nitrogen reduction on OV-BiOCl (001) follows the distal pathway, while the NRR on BiOCl (010) follows the alternating pathway. The nitrogen reduction reaction was theoretically predicted by Liu et al. [97] on the surface of $\text{Bi}_3\text{FeMo}_2\text{O}_{12}$. They investigated an associative and dissociative pathways and found that the limiting step for nitrogen reduction on OV-free catalyst are the formations of 2NH_2 and 2N^* , respectively. It was also observed that a small amount of OV enhances nitrogen activation, as the stability of the N-OV- $\text{Bi}_3\text{FeMo}_2\text{O}_{12}$ is observed to be higher. Furthermore, the presence of OVs on the photocatalyst surface result in higher sta-

bilization of adsorbed intermediates (N, H, NH). DFT calculations using GGA-PBE were performed to study a reaction mechanism of nitrogen reduction over OV-BiOBr (001) facet [103]. The authors proposed a distal pathway for this investigated NRR, while the first hydrogenation occurs at the distal N atom. Li et al. [104] theoretically explored a possible mechanism for NRR over the pristine Bi₅O₇Br, OV-Bi₅O₇Br and Bi₅O₇Br+O. A reaction step in distal mechanism from *N-NH₂ to *N-NH₃ proved to be the one with the largest energy barrier and is therefore considered as a rate-determining step. It was concluded that among all three photocatalysts, Bi₅O₇Br-OV is the most promising for nitrogen photoreduction.

Zhao [41] proposed and explored a possible reaction mechanism of NRR at the saturated and unsaturated Zn active sites of ZnCr-LDH. The rate-determining step is the cleavage of the nitrogen triple bond. Li et al. [107] studied a mechanism for ammonia synthesis on MIL-101(Cr) and MIL-101(Fe), and calculated Gibbs free energies for the first and second hydrogenations of N₂. They suggested that two successive hydrogenations occur at the distal N atom. Reported Gibbs free energy values reconfirm that the Fe active site can be considered more promising compared to the Cr active site. The mechanism of photocatalytic NRR on the surfaces of Gd-IHEP-7 and Gd-IHEP-8 was explored by Hu et al. [42] and the free energy diagram was calculated. The authors proposed alternating and a distal pathways and found an endothermic first hydrogenation of N₂ on Gd-IHEP-7 and an exothermic one on Gd-IHEP-8.

Azofra et al. [32] studied a possible pathway for N₂ reduction on Fe-deposited MoS₂. Upon the first hydrogenation, Fe-NNH· is formed and converted into NNH₂ intermediate ($\Delta G = 0.85$ eV and $\Delta G = 0.13$ eV), suggesting a distal pathway for the reaction studied. DFT calculations were carried out to reveal a possible reaction mechanism of nitrogen photoreduction on SV-1T-MoS₂/CdS composite [108]. The first hydrogenation on the distal N atom was determined as an exergonic process. The second hydrogenation was suggested to occur on the distal and the binding N atoms, resulting in a 0.4 eV lower free energy of the *NHNH intermediate compared to *NNH₂, suggesting that the NRR undergoes alternating pathway. Shen et al. [112] suggested two possible reaction pathways for photocatalytic NRR on the surface of BPNSs/CdS. In this study, they proposed a distal reaction pathway for the photocatalytic nitrogen reduction at the surface P active sites and calculated the associated Gibbs free energies for all intermediates. Han et al. [43] proposed a possible reaction pathway of NRR on the ZnV-Zn₃In₂S₆. Zn-vacancies as cationic defects were considered as active sites for nitrogen adsorption. End-on adsorption of N₂ and its activation was followed by first hydrogenation by H⁺ delivered from the methanol (the hole sacrificial agent used in the reaction). ALternating mechanism was proposed and investigated. Zn-deficient Zn₃In₂S₆ increase nitrogen activation compared to untreated Zn₃In₂S₆, indicating a favorable existence of Zn vacancies. Yuan et al. [114] propounded an enzymatic pathway (Fig. 10) for nitrogen reduction on the Ru(001)/CoS_x(101) catalyst. The rate-limiting step is the formation of *NH-NH₂ from

*NH-NH. When N was first hydrogenated on the Co atom, the overall change in free energy for the formation of *NH-NH₂ was calculated to be 0.27 eV (from 0.0 to +0.27 eV), indicating that Ru is more favorable for first hydrogenation compared to Co in Ru-Co active site.

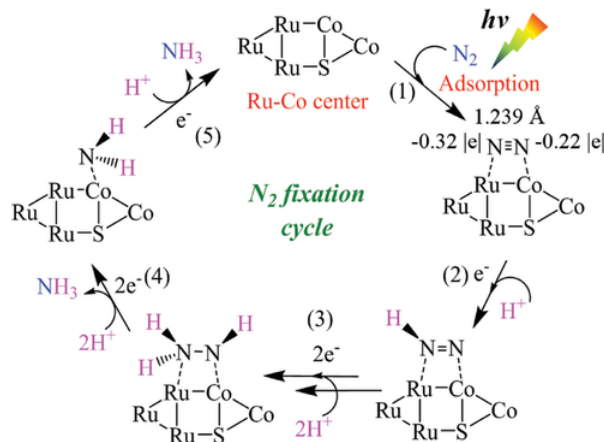


Figure 10: A reaction mechanism of NRR over Ru-Vs-CoS/CN [114].

S vacancy defective WS₂ monolayer with transition metal single atoms loaded on its surface, was theoretically studied by Ma et al. [115] using spin-polarized DFT calculations. Of all the transition metals studied, Ni was found to be the most auspicious to be anchored on SV-WS₂ and to serve as an active site for N₂ chemical adsorption. Associative and enzymatic pathways were considered for photo-NRR. The dissociative and enzymatic pathways were excluded because N₂ is not dissociated and the side-on adsorption configuration is less favorable, respectively. Therefore, it was concluded that the studied reaction proceeds via an alternating mechanism. Wang et al. [120] examined DFT calculations using PBE functional to study nitrogen activation on the Bi₂WO₆ (010) surface. They proposed three reaction mechanisms, namely one for N₂ reduction on W site, and two for reduction on Bi site with two OV's. They concluded that the reaction could undergo an alternating pathway when Bi with two OV's is considered with the rate-determining step being the cleavage of the N-N bond. A distal pathway for nitrogen adsorption on Bi and Bi with two OV's was ruled out due to the non-stability of *NNH₂ intermediate. The latter pathway was eliminated also for W site. On the other hand, for the nitrogen activation on the W site, the alternating pathway was calculated to be feasible with the ammonia desorption determined as a rate-determining step. NRR could not proceed through alternating pathway when N₂ was adsorbed on Bi and Bi site.

A reaction pathway for photocatalytic NRR is closely associated with N₂ adsorption configurations. As it was described in this section and Section 2, end-on adsorption configurations follow distal or alternating associative mechanisms and side-on adsorption

follows enzymatic associative mechanism. Articles that include the investigation of dissociative mechanisms are rare, as the activation and the following reaction steps occur preferably via associative mechanisms. As discussed in the previous sections, water is commonly used as a proton source, especially at the laboratory level of photocatalytic NRR investigation. With regard to theoretical calculations, hydrogen or water molecules are considered as a reductants for NRR [8]. On the other hand, products that were observed to be formed at the laboratory scale are ammonia as a main product, as well as hydrazine and in some cases nitrate. Theoretically predicted products are ammonia and the hydrazine that might be formed as a by product during the alternating or enzymatic associative pathway.

5. Review of kinetics and macroscale modeling

In order to build a multiscale model, the meso- and macro-level calculations come to the fore. In this section, attention is paid to the microkinetic and kinetic Monte Carlo simulations at the mesoscale and to computational fluid dynamics at the macroscale of modeling. Since the calculations of photocatalytic nitrogen fixation are rarely performed at higher levels of modeling, we report some results involving thermocatalytic NRR over metal catalysts.

Gouveia et al. [129] coupled spin polarized DFT studies with a microkinetic model to study nitrogen fixation over a 2D inorganic MXene catalyst. First-principles calculations were performed in a PBE approach including Grimme's D3 corrections. First-principles calculations were used to determine nitrogen adsorption modes on M_2C and M_2N MXen (0001) surfaces where M denotes Ti, Zr, Hf, V, Nb, Ta, Cr, Mo and W metals and reaction mechanism over Nb_2C , Mo_2N and W_2N MXenes. It was found that Nb_2C , Mo_2N and W_2N show the lowest dissociation energy barriers for N_2 dissociation determined via dissociative pathway. Among all the aforementioned MXenes, W_2N exhibited the lowest dissociation energy barrier of 0.28 eV and was therefore used in a microkinetic model carried out at maximum of 1075 K for ammonia synthesis. Calculated reaction order results revealed that the reaction orders of reactants increase with increasing temperature. The third hydrogenation, i.e. ammonia formation was determined to be the rate-limiting step. Surface coverages and ammonia production and reverse reactions were calculated.

Nakao et al. [130] studied nitrogen fixation and reduction to ammonia over a Ru/Ca_2NH (100) catalyst within the framework of DFT method and GGA-PBE functional. The structure of Ru_5/Ca_2NH catalyst was confirmed by AIMD simulations at 673 K. They investigated N_2 adsorption, formation of NH_x intermediates and H migration from Ru to the $Ru/Ca_2NH_{1-x}e_x^-$. NH_x intermediates were formed faster from the lattice H^- than from H adatoms adsorbed on the Ru site. The activation barriers and vibrational frequencies calculated by means of DFT were incorporated as input parameters into the microkinetic model. For each elementary step, TOF (turnover frequency) were calculated, considering

edge site of Ru particles of Ru/Ca₂NH to be the active sites for adsorption of intermediates. The lowest TOF value corresponded to the rate-determining step, which was found to be the formation of ammonia molecule from NH₂ and H₅. The coverages of N and H atoms were also calculated at temperature in the range between 300 and 400 °C and pressure of 0.1 MPa.

First-principles calculations coupled with kinetic Monte Carlo were examined to investigate thermocatalytic ammonia synthesis over a Fe (111) surface [131]. For all elementary reaction steps, DFT calculations were employed to calculate Gibbs free energies and reaction barriers for 17 steps, and through transition state theory (the climbing image NEB method) determine the input parameters that were entered into the kMC model. kMC simulations were performed at temperature of 673 K and pressure of 20 atm, as well as under the conditions characteristic for Haber-Bosch process, i.e. temperature of 723 K and pressure of 200 atm. Former conditions (single-crystal experiments) yielded the turnover frequency of 17.7 /s at the steady state, which was in good agreement with experimentally determined TOF of 9.7 /s per 2x2 Fe (111) site.

Another study over Fe-based catalyst was performed by Liu et al. [132] who were interested in calculating the mechanism for NRR, supported by microkinetic modeling to determine kinetic properties. Nitrogen adsorption and then mechanism elucidation were studied over Fe₃/θ-Al₂O₃ (010). DFT calculations within the framework of PBE yielded DOS, which showed the overlapping of Fe₃ β spin d orbitals and π anti-bonding N₂ orbitals, suggesting an electron transfer from Fe₃ cluster to the adsorbed N₂ molecule. The latter electron transfer was confirmed also by electron density difference and Bader charge calculations. Reaction mechanism investigations confirmed that NRR was more likely to occur via associative mechanism. Furthermore, microkinetic analysis of NRR over Fe₃ cluster, Fe₃/θ-Al₂O₃ (010) and Ru clusters was done. The simulations were carried out in the temperature range of 1-100 bar and temperatures of 300–1000 K. It was concluded that nitrogen adsorption exhibits a linear BEP relation to the transition state energies when N₂ was adsorbed on the metal surface. Furthermore, calculated TOF for NRR over Fe₃/θ-Al₂O₃ (010) exhibited similar values to ones calculated on the Ru catalyst (Ru B5 site). These results indicate that loading of Fe cluster on the surface of Al₂O₃ (010) display favorable results and thus consider Fe clusters as promising for the thermocatalytic NRR.

Another theoretical study of thermocatalytic NRR encompassing first-principles calculations using B2LYP approach and kinetic modeling was done by Ghoshal et al. [133]. They proposed distal, alternating and enzymatic mechanisms for side-on N₂ adsorption and further reduction with H₂O over TiO₂ doped-Ru_n (n=5,6) clusters. Electron transfer from Ru to N₂ was confirmed by Bader charge analysis. When N₂ reduction occurred over TiO₂ doped-Ru_n (n=5,6), ammonia was found to be formed more favorable via the distal mechanism, while hydrazine was formed as a main product via the alternating pathway. On the other hand, enzymatic mechanism turned out to be less feasible to yield ammonia or hydrazine. The formation of *N-NH₂ intermediate was determined as a rate-determining

step with a negligible reaction barrier. In addition, the authors investigated water oxidation and proposed a hydrogen molecule as a co-reactant in the reaction. Kinetic modeling calculations revealed that TiO₂ doping reduced the kinetics compared to Ru clusters, based on the calculations of rate coefficients.

Another study on the Ru-based catalyst for thermocatalytic nitrogen reduction was explored by Dahl et al. [134]. In this study, experimentally determined data were used to build a microkinetic model. Rates of ammonia synthesis and TOF over Ru single catalyst and Ru/MgAl₂O₄ catalyst were predicted in a continuously stirred tank reactor. The number of active sites and the coverages of reactants and intermediates were also calculated. A proposed model was in good agreement with the rates obtained experimentally for NRR over both catalysts. The mechanism that was proposed, was also confirmed to be a good choice based on the kinetic simulations.

Another microkinetic analysis along with CFD simulations was examined by Deshmukh et al. [135]. The authors were focusing more on ammonia desorption than on ammonia synthesis.

Kinetic and reactor modeling simulations are very scarce in photocatalytic nitrogen fixation, indicating the low chances of creating a complete multiscale model that includes all levels of modeling. In contrast to photocatalysis, calculations of meso- and macroscale simulations are somewhat more common for thermocatalytic ammonia synthesis. Although the coupling of DFT with the microkinetic model [129, 130, 132–135] is more widely used compared to kMC and CFD, the coupling of DFT with kMC or kinetics with CFD remains relatively unexplored.

6. Conclusion

Photocatalytic nitrogen fixation has recently received considerable attention as a sustainable and eco-friendly alternative to the conventional Haber-Bosch process. The latter results in high energy consumption and notable carbon footprint, corresponded to hydrogen production from methane via methane steam reforming [8]. Light-driven ammonia synthesis has yet been well explored at the laboratory level, however, theoretical studies are slowly coming to the fore. The aim is to theoretically study nitrogen photofixation at different modeling levels, thus effectively encapsulating atomistic-level calculations, kinetics, and macroscale simulations [19]. It is worth mentioning the growing number of theoretical studies that go hand in hand with increasing computational power, making it possible to perform such calculations and obtain the results.

DFT calculations are thus far the most widely used in computational materials science for performing atomistic-level modeling calculations. They are usually carried out in a plane-wave approach with a GGA-PBE (or less likely PW91) functional, but now and then some hybrid functionals (PBE0, HSE06) are employed to predict electronic properties more precisely. More commonly, Hubbard-U corrections (DFT+U) are applied in the systems with

strong Coulomb interactions and Grimme's corrections (D2 and D3) to consider dispersion corrections.

TiO₂, g-C₃N₄, sulfides and bismuth oxyhalides are reported to be the most aspiring photocatalysts for nitrogen fixation with the corresponding characteristics. Modifications of the catalyst structures were found to have a favorable effect on the nitrogen fixation ability. Dopants, cocatalysts, introduced defects (most commonly oxygen and nitrogen vacancies) and heterojunctions (two photocatalysts combined together) tend to decrease the band gap width, prevent electron-hole recombination, thus improve charge separation, and increase ammonia production yields and rates. In addition, doping and vacancy formation introduce new defect levels in the middle of the band gap, resulting in less charge carrier recombination as defects act as recombination centers. Researchers are frequently interested in calculating the band structure (valence band maximum, conduction band minimum), band gap energy, density of states and projected density of states.

The electronic properties of the semiconductor photocatalysts are a good springboard to consider nitrogen adsorption at the active sites of the photocatalyst. Active sites are commonly introduced defects that facilitate nitrogen adsorption. The latter can occur via end-on or side-on configuration, followed by a proton-electron coupled (PEC) process, resulting in N₂ activation and prolongation of triple bond [8]. At this juncture, the calculations of adsorption energies, Bader or Hirshfeld charge analysis, and electron density difference become prominent. It is important to stress the importance of the strength of adsorption, as if physical adsorption occurs and N₂ binds too weakly, no chemical reaction is perceived. On the other hand, the reactants, intermediates or products should not bind too strongly to the catalyst surface, as the latter results in surface poisoning and thus lowers the product yield [31, 128].

Together with the adsorption configurations, a possible mechanism can be predicted. Although nitrogen fixation on a heterogeneous catalyst can proceed via dissociative and associative mechanisms, most articles dealing with photocatalytic ammonia synthesis do not consider the dissociative pathway or exclude it based on the calculated Gibbs free energies. Indeed, for the latter, it is typical that the triple bond is cleaved upon adsorption and before the first hydrogenation. Therefore, a high energy input is required to dissociate a very strong triple bond, which is not feasible in photocatalytic reactions. Instead of dissociative, three associative pathways are commonly described in photocatalytic NRR, namely, distal, alternating and enzymatic pathways [8]. Among all three, the distal and alternating pathways are the most regularly reported to proceed. The researchers suggested possible reaction mechanisms based on experimentally determined intermediates and products formed during the reaction or, more likely, based on DFT calculations of N₂ adsorption that occurred via an end-on or side-on configuration. Namely, it was shown that end-on adsorption boost distal or alternating mechanism, while, on the other hand, side-on configuration favored enzymatic pathway. Most of the DFT studies are coupled with experimental work, which generally use water as a proton source, due to its envi-

ronmental friendlies. On the other hand, hydrogen is considered as one of the reactants in the majority of DFT studies. Regarding the products, ammonia, hydrazine and nitrate (NO_3^-) are likely to be detected experimentally, however, DFT calculations yield ammonia and in some cases hydrazine.

Meso- and macroscale simulations by means of microkinetic or kinetic Monte Carlo modeling and computational fluid dynamics were found to be in the field of photocatalytic nitrogen fixation considerably uncharted. Ever so often, first-principles are coupled with microkinetic [129, 130, 132–135] and barely with kinetic Monte Carlo [131] when considering ammonia synthesis under thermocatalytic conditions. Furthermore, reactor modeling at the macro level [135] is even more scarce.

Meso- and macroscale simulations using microkinetic or kinetic Monte Carlo modeling and computational fluid dynamics have been largely unexplored in the field of photocatalytic nitrogen fixation. Time and again, when considering ammonia synthesis under thermocatalytic conditions, first-principles are coupled with microkinetics [129, 130, 132–135] and hardly with kinetics Monte Carlo [131]. Moreover, reactor modeling at the macro level [135] is even rarer.

This review primarily includes most first-principles studies that have been conducted in the field. However, it should be emphasized that the ground-state level calculations have been performed using DFT, neglecting the excited-state properties that are crucial for capturing the essence of the photocatalytic reactions. Few and far between, electron excitations are modeled and time-dependent DFT is employed, but not in the matter of excited state calculations. On the other hand, multiscale modeling of photocatalytic nitrogen fixation is still in its infancy, especially due to the deficiency of meso- (kinetics) and macro-level (reactor modeling) calculations. These considerations show that photocatalytic nitrogen fixation and reduction to ammonia is relatively uncharted in terms of multiscale modeling, but has great potential to be explored more intensively in the future, including the properties of the excited states calculated in the multiscale manner.

7. References

- [1] C. Smith, A. K. Hill, L. Torrente-Murciano, Current and future role of haber-bosch ammonia in a carbon-free energy landscape, *Energy & Environmental Science* 13 (2) (2020) 331–344. doi:10.1039/c9ee02873k.
- [2] V. Kyriakou, I. Garagounis, A. Vourros, E. Vasileiou, M. Stoukides, An electrochemical haber-bosch process, *Joule* 4 (1) (2020) 142–158. doi:10.1016/j.joule.2019.10.006.

- [3] F. Haber, The synthesis of ammonia from its element – nobel lecture, accessed on October 28, 2021 (1932).
URL <https://www.nobelprize.org/prizes/chemistry/1918/haber/lecture/>
- [4] J. W. Erisman, M. A. Sutton, J. Galloway, Z. Klimont, W. Winiwarter, How a century of ammonia synthesis changed the world, *Nature Geoscience* 1 (10) (2008) 636–639. doi:10.1038/ngeo325.
- [5] C. Bosch, The development of the chemical high pressure method during the establishment of the new ammonia industry – nobel lecture, accessed on October 28, 2021 (1920).
URL <https://www.nobelprize.org/prizes/chemistry/1931/bosch/lecture/>
- [6] H. Li, C. Mao, H. Shang, Z. Yang, Z. Ai, L. Zhang, New opportunities for efficient N_2 fixation by nanosheet photocatalysts, *Nanoscale* 10 (33) (2018) 15429–15435. doi:10.1039/c8nr04277b.
- [7] R. Shi, Y. Zhao, G. I. N. Waterhouse, S. Zhang, T. Zhang, Defect engineering in photocatalytic nitrogen fixation, *ACS Catalysis* 9 (11) (2019) 9739–9750. doi:10.1021/acscatal.9b03246.
- [8] K. Ithisuphalap, H. Zhang, L. Guo, Q. Yang, H. Yang, G. Wu, Photocatalysis and photoelectrocatalysis methods of nitrogen reduction for sustainable ammonia synthesis, *Small Methods* 3 (6) (2018) 1800352. doi:10.1002/smt.d.201800352.
- [9] M. Li, H. Huang, J. Low, C. Gao, R. Long, Y. Xiong, Recent progress on electrocatalyst and photocatalyst design for nitrogen reduction, *Small Methods* 3 (6) (2018) 1800388. doi:10.1002/smt.d.201800388.
- [10] R. Shi, X. Zhang, G. I. N. Waterhouse, Y. Zhao, T. Zhang, The journey toward low temperature, low pressure catalytic nitrogen fixation, *Advanced Energy Materials* 10 (19) (2020) 2000659. doi:10.1002/aenm.202000659.
- [11] R. Li, Photocatalytic nitrogen fixation: An attractive approach for artificial photocatalysis, *Chinese Journal of Catalysis* 39 (7) (2018) 1180–1188. doi:10.1016/s1872-2067(18)63104-3.
- [12] G. N. Schrauzer, T. D. Guth, Photolysis of water and photoreduction of nitrogen on titanium dioxide, *Journal of the American Chemical Society* 99 (22) (1977) 7189–7193. doi:10.1021/ja00464a015.

- [13] Z. Wang, Y. Liu, B. Huang, Y. Dai, Z. Lou, G. Wang, X. Zhang, X. Qin, Progress on extending the light absorption spectra of photocatalysts, *Physical Chemistry Chemical Physics* 16 (7) (2014) 2758. doi:10.1039/c3cp53817f.
- [14] S. Chen, D. Liu, T. Peng, Fundamentals and recent progress of photocatalytic nitrogen-fixation reaction over semiconductors, *Solar RRL* 5 (2) (2020) 2000487. doi:10.1002/solr.202000487.
- [15] X. Chen, N. Li, Z. Kong, W.-J. Ong, X. Zhao, Photocatalytic fixation of nitrogen to ammonia: state-of-the-art advancements and future prospects, *Materials Horizons* 5 (1) (2018) 9–27. doi:10.1039/c7mh00557a.
- [16] J. Low, J. Yu, M. Jaroniec, S. Wageh, A. A. Al-Ghamdi, Heterojunction photocatalysts, *Advanced Materials* 29 (20) (2017) 1601694. doi:10.1002/adma.201601694.
- [17] J. Hafner, C. Wolverton, G. Ceder, Toward computational materials design: The impact of density functional theory on materials research, *MRS Bulletin* 31 (9) (2006) 659–668. doi:10.1557/mrs2006.174.
- [18] P. J. Hasnip, K. Refson, M. I. J. Probert, J. R. Yates, S. J. Clark, C. J. Pickard, Density functional theory in the solid state, *Philosophical Transactions of the Royal Society A: Mathematical, Physical and Engineering Sciences* 372 (2011) (2014) 20130270. doi:10.1098/rsta.2013.0270.
- [19] T. Karakasidis, C. Charitidis, Multiscale modeling in nanomaterials science, *Materials Science and Engineering: C* 27 (5-8) (2007) 1082–1089. doi:10.1016/j.msec.2006.06.029.
- [20] R. Iftimie, P. Minary, M. E. Tuckerman, Ab initio molecular dynamics: Concepts, recent developments, and future trends, *Proceedings of the National Academy of Sciences* 102 (19) (2005) 6654–6659. doi:10.1073/pnas.0500193102.
- [21] M. Huš, M. Grilc, A. Pavličič, B. Likozar, A. Hellman, Multiscale modelling from quantum level to reactor scale: An example of ethylene epoxidation on silver catalysts, *Catalysis Today* 338 (2019) 128–140. doi:10.1016/j.cattod.2019.05.022.
- [22] P. Hohenberg, W. Kohn, Inhomogeneous electron gas, *Physical Review* 136 (3B) (1964) B864–B871. doi:10.1103/physrev.136.b864.
- [23] X. Meng, N. Yun, Z. Zhang, Recent advances in computational photocatalysis: A review, *The Canadian Journal of Chemical Engineering* 97 (7) (2019) 1982–1998. doi:10.1002/cjce.23477.

- [24] N. Argaman, G. Makov, Density functional theory: An introduction, *American Journal of Physics* 68 (1) (2000) 69–79. doi:10.1119/1.19375.
- [25] J. Enkovaara, C. Rostgaard, J. J. Mortensen, J. Chen, M. Duřak, L. Ferrighi, J. Gavnholt, C. Glinsvad, V. Haikola, H. A. Hansen, H. H. Kristoffersen, M. Kuisma, A. H. Larsen, L. Lehtovaara, M. Ljungberg, O. Lopez-Acevedo, P. G. Moses, J. Ojanen, T. Olsen, V. Petzold, N. A. Romero, J. Stausholm-Møller, M. Strange, G. A. Tritsarlis, M. Vanin, M. Walter, B. Hammer, H. Häkkinen, G. K. H. Madsen, R. M. Nieminen, J. K. Nørskov, M. Puska, T. T. Rantala, J. Schiøtz, K. S. Thygesen, K. W. Jacobsen, Electronic structure calculations with GPAW: a real-space implementation of the projector augmented-wave method, *Journal of Physics: Condensed Matter* 22 (25) (2010) 253202. doi:10.1088/0953-8984/22/25/253202.
- [26] C. Adamo, D. Jacquemin, The calculations of excited-state properties with time-dependent density functional theory, *Chem. Soc. Rev.* 42 (3) (2013) 845–856. doi:10.1039/c2cs35394f.
- [27] S. Cao, B. Fan, Y. Feng, H. Chen, F. Jiang, X. Wang, Sulfur-doped g-c₃n₄ nanosheets with carbon vacancies: General synthesis and improved activity for simulated solar-light photocatalytic nitrogen fixation, *Chemical Engineering Journal* 353 (2018) 147–156. doi:10.1016/j.cej.2018.07.116.
- [28] M. Zheng, Y. Li, K. Ding, Y. Zhang, W. Chen, W. Lin, A boron-decorated melon-based carbon nitride as a metal-free photocatalyst for n₂ fixation: a DFT study, *Physical Chemistry Chemical Physics* 22 (38) (2020) 21872–21880. doi:10.1039/d0cp03824e.
- [29] X. Lv, W. Wei, F. Li, B. Huang, Y. Dai, Metal-free b@g-CN: Visible/infrared light-driven single atom photocatalyst enables spontaneous dinitrogen reduction to ammonia, *Nano Letters* 19 (9) (2019) 6391–6399. doi:10.1021/acs.nanolett.9b02572.
- [30] J. Li, P. Liu, Y. Tang, H. Huang, H. Cui, D. Mei, C. Zhong, Single-atom pt-n₃ sites on the stable covalent triazine framework nanosheets for photocatalytic n₂ fixation, *ACS Catalysis* 10 (4) (2020) 2431–2442. doi:10.1021/acscatal.9b04925.
- [31] S. Wang, L. Shi, X. Bai, Q. Li, C. Ling, J. Wang, Highly efficient photo/electrocatalytic reduction of nitrogen into ammonia by dual-metal sites, *ACS Central Science* 6 (10) (2020) 1762–1771. doi:10.1021/acscentsci.0c00552.
- [32] L. M. Azofra, C. Sun, L. Cavallo, D. R. MacFarlane, Feasibility of n₂ binding and reduction to ammonia on fe-deposited MoS₂ 2d sheets: A DFT study, *Chemistry – A European Journal* 23 (34) (2017) 8275–8279. doi:10.1002/chem.201701113.

- [33] H. Prats, F. Illas, R. Sayós, General concepts, assumptions, drawbacks, and misuses in kinetic monte carlo and microkinetic modeling simulations applied to computational heterogeneous catalysis, *International Journal of Quantum Chemistry* 118 (9) (2017) e25518. doi:10.1002/qua.25518.
- [34] D. Drikakis, M. Frank, G. Tabor, Multiscale computational fluid dynamics, *Energies* 12 (17) (2019) 3272. doi:10.3390/en12173272.
- [35] Y. Boyjoo, M. Ang, V. Pareek, Some aspects of photocatalytic reactor modeling using computational fluid dynamics, *Chemical Engineering Science* 101 (2013) 764–784. doi:10.1016/j.ces.2013.06.035.
- [36] Y. Zhao, Y. Zhao, R. Shi, B. Wang, G. I. N. Waterhouse, L.-Z. Wu, C.-H. Tung, T. Zhang, Tuning oxygen vacancies in ultrathin TiO_2 nanosheets to boost photocatalytic nitrogen fixation up to 700 nm, *Advanced Materials* 31 (16) (2019) 1806482. doi:10.1002/adma.201806482.
- [37] B. Huang, Y. Liu, Q. Pang, X. Zhang, H. Wang, P. K. Shen, Boosting the photocatalytic activity of mesoporous $SrTiO_3$ for nitrogen fixation through multiple defects and strain engineering, *Journal of Materials Chemistry A* 8 (42) (2020) 22251–22256. doi:10.1039/d0ta08678a.
- [38] M. Li, Q. Lu, M. Liu, P. Yin, C. Wu, H. Li, Y. Zhang, S. Yao, Photoinduced charge separation via the double-electron transfer mechanism in nitrogen vacancies $g\text{-}c_3n_5/BiOBr$ for the photoelectrochemical nitrogen reduction, *ACS Applied Materials & Interfaces* 12 (34) (2020) 38266–38274. doi:10.1021/acscami.0c11894.
- [39] X. Yang, S. Zhou, S. Huang, J. Zhao, Metal-encapsulated boron nitride nanocages for solar-driven nitrogen fixation, *The Journal of Physical Chemistry C* 124 (43) (2020) 23798–23806. doi:10.1021/acs.jpcc.0c07968.
- [40] Y. Zhao, Y. Zhao, G. I. N. Waterhouse, L. Zheng, X. Cao, F. Teng, L.-Z. Wu, C.-H. Tung, D. O'Hare, T. Zhang, Layered-double-hydroxide nanosheets as efficient visible-light-driven photocatalysts for dinitrogen fixation, *Advanced Materials* 29 (42) (2017) 1703828. doi:10.1002/adma.201703828.
- [41] Y. Zhao, L. Zheng, R. Shi, S. Zhang, X. Bian, F. Wu, X. Cao, G. I. N. Waterhouse, T. Zhang, Alkali etching of layered double hydroxide nanosheets for enhanced photocatalytic N_2 reduction to NH_3 , *Advanced Energy Materials* 10 (34) (2020) 2002199. doi:10.1002/aenm.202002199.
- [42] K.-Q. Hu, P.-X. Qiu, L.-W. Zeng, S.-X. Hu, L. Mei, S.-W. An, Z.-W. Huang, X.-H. Kong, J.-H. Lan, J.-P. Yu, Z.-H. Zhang, Z.-F. Xu, J. K. Gibson, Z.-F. Chai, Y.-F. Bu, W.-Q. Shi, Solar-driven nitrogen fixation catalyzed by stable radical-containing

- MOFs: Improved efficiency induced by a structural transformation, *Angewandte Chemie International Edition* 59 (46) (2020) 20666–20671. doi:10.1002/anie.202009630.
- [43] H. Han, Y. Yang, J. Liu, X. Zheng, X. Wang, S. Meng, S. Zhang, X. Fu, S. Chen, Effect of zn vacancies in zn₃in₂s₆ nanosheets on boosting photocatalytic n₂ fixation, *ACS Applied Energy Materials* 3 (11) (2020) 11275–11284. doi:10.1021/acsaem.0c02202.
- [44] X. Xue, H. Chen, Y. Xiong, R. Chen, M. Jiang, G. Fu, Z. Xi, X. L. Zhang, J. Ma, W. Fang, Z. Jin, Near-infrared-responsive photo-driven nitrogen fixation enabled by oxygen vacancies and sulfur doping in black TiO₂-xSy nanoplatelets, *ACS Applied Materials & Interfaces* 13 (4) (2021) 4975–4983. doi:10.1021/acsaem.0c17947.
- [45] Y. Sun, W. Pei, M. Xie, S. Xu, S. Zhou, J. Zhao, K. Xiao, Y. Zhu, Excitonic au₄ru₂(PPh₃)₂(SC₂H₄Ph)₈ cluster for light-driven dinitrogen fixation, *Chemical Science* 11 (9) (2020) 2440–2447. doi:10.1039/c9sc06424a.
- [46] W. Ye, M. Arif, X. Fang, M. A. Mushtaq, X. Chen, D. Yan, Efficient photoelectrochemical route for the ambient reduction of n₂ to NH₃ based on nanojunctions assembled from MoS₂ nanosheets and TiO₂, *ACS Applied Materials & Interfaces* 11 (32) (2019) 28809–28817. doi:10.1021/acsaem.9b06596.
- [47] Y. Shiraishi, S. Shiota, Y. Kofuji, M. Hashimoto, K. Chishiro, H. Hirakawa, S. Tanaka, S. Ichikawa, T. Hirai, Nitrogen fixation with water on carbon-nitride-based metal-free photocatalysts with 0.1% solar-to-ammonia energy conversion efficiency, *ACS Applied Energy Materials* 1 (8) (2018) 4169–4177. doi:10.1021/acsaem.8b00829.
- [48] S. Hu, X. Chen, Q. Li, F. Li, Z. Fan, H. Wang, Y. Wang, B. Zheng, G. Wu, Fe³⁺ doping promoted n₂ photofixation ability of honeycombed graphitic carbon nitride: The experimental and density functional theory simulation analysis, *Applied Catalysis B: Environmental* 201 (2017) 58–69. doi:10.1016/j.apcatb.2016.08.002.
- [49] H. Mou, J. Wang, D. Zhang, D. Yu, W. Chen, D. Wang, T. Mu, A one-step deep eutectic solvent assisted synthesis of carbon nitride/metal oxide composites for photocatalytic nitrogen fixation, *Journal of Materials Chemistry A* 7 (10) (2019) 5719–5725. doi:10.1039/c8ta11681d.
- [50] S. Hu, X. Qu, J. Bai, P. Li, Q. Li, F. Wang, L. Song, Effect of cu(i)-n active sites on the n₂ photofixation ability over flowerlike copper-doped g-c₃n₄ prepared via a novel molten salt-assisted microwave process: The experimental and density functional theory simulation analysis, *ACS Sustainable Chemistry & Engineering* 5 (8) (2017) 6863–6872. doi:10.1021/acssuschemeng.7b01089.

- [51] K. Wang, G. Gu, S. Hu, J. Zhang, X. Sun, F. Wang, P. Li, Y. Zhao, Z. Fan, X. Zou, Molten salt assistant synthesis of three-dimensional cobalt doped graphitic carbon nitride for photocatalytic N_2 fixation: Experiment and DFT simulation analysis, *Chemical Engineering Journal* 368 (2019) 896–904. doi:10.1016/j.cej.2019.03.037.
- [52] S. Sun, Q. An, W. Wang, L. Zhang, J. Liu, W. A. G. III, Efficient photocatalytic reduction of dinitrogen to ammonia on bismuth monoxide quantum dots, *Journal of Materials Chemistry A* 5 (1) (2017) 201–209. doi:10.1039/c6ta09275f.
- [53] C. Xu, P. Qiu, L. Li, H. Chen, F. Jiang, X. Wang, Bismuth subcarbonate with designer defects for broad-spectrum photocatalytic nitrogen fixation, *ACS Applied Materials & Interfaces* 10 (30) (2018) 25321–25328. doi:10.1021/acsmi.8b05925.
- [54] J. Di, J. Xia, M. F. Chisholm, J. Zhong, C. Chen, X. Cao, F. Dong, Z. Chi, H. Chen, Y.-X. Weng, J. Xiong, S.-Z. Yang, H. Li, Z. Liu, S. Dai, Defect-tailoring mediated electron-hole separation in single-unit-cell $\text{Bi}_3\text{O}_4\text{Br}$ nanosheets for boosting photocatalytic hydrogen evolution and nitrogen fixation, *Advanced Materials* 31 (28) (2019) 1807576. doi:10.1002/adma.201807576.
- [55] X. Chen, X. Zhang, Y.-H. Li, M.-Y. Qi, J.-Y. Li, Z.-R. Tang, Z. Zhou, Y.-J. Xu, Transition metal doping BiOBr nanosheets with oxygen vacancy and exposed {102} facets for visible light nitrogen fixation, *Applied Catalysis B: Environmental* 281 (2021) 119516. doi:10.1016/j.apcatb.2020.119516.
- [56] C. Zhang, Y. Xu, C. Lv, X. Zhou, Y. Wang, W. Xing, Q. Meng, Y. Kong, G. Chen, Mimicking π backdonation in ce-MOFs for solar-driven ammonia synthesis, *ACS Applied Materials & Interfaces* 11 (33) (2019) 29917–29923. doi:10.1021/acsmi.9b08682.
- [57] Z. Wei, Y. Zhang, S. Wang, C. Wang, J. Ma, Fe-doped phosphorene for the nitrogen reduction reaction, *Journal of Materials Chemistry A* 6 (28) (2018) 13790–13796. doi:10.1039/c8ta03989e.
- [58] P. Mori-Sánchez, A. J. Cohen, The derivative discontinuity of the exchange-correlation functional, *Phys. Chem. Chem. Phys.* 16 (28) (2014) 14378–14387. doi:10.1039/c4cp01170h.
- [59] X.-Y. Xie, P. Xiao, W.-H. Fang, G. Cui, W. Thiel, Probing photocatalytic nitrogen reduction to ammonia with water on the rutile TiO_2 (110) surface by first-principles calculations, *ACS Catalysis* 9 (10) (2019) 9178–9187. doi:10.1021/acscatal.9b01551.

- [60] W. Zhao, J. Zhang, X. Zhu, M. Zhang, J. Tang, M. Tan, Y. Wang, Enhanced nitrogen photofixation on Fe-doped TiO₂ with highly exposed (101) facets in the presence of ethanol as scavenger, *Applied Catalysis B: Environmental* 144 (2014) 468–477. doi:10.1016/j.apcatb.2013.07.047.
- [61] C. Li, T. Wang, Z.-J. Zhao, W. Yang, J.-F. Li, A. Li, Z. Yang, G. A. Ozin, J. Gong, Promoted fixation of molecular nitrogen with surface oxygen vacancies on plasmon-enhanced TiO₂ photoelectrodes, *Angewandte Chemie International Edition* 57 (19) (2018) 5278–5282. doi:10.1002/anie.201713229.
- [62] J. Yang, Y. Guo, R. Jiang, F. Qin, H. Zhang, W. Lu, J. Wang, J. C. Yu, High-efficiency 'working-in-tandem' nitrogen photofixation achieved by assembling plasmonic gold nanocrystals on ultrathin titania nanosheets, *Journal of the American Chemical Society* 140 (27) (2018) 8497–8508. doi:10.1021/jacs.8b03537.
- [63] B. M. Comer, A. J. Medford, Analysis of photocatalytic nitrogen fixation on rutile TiO₂(110), *ACS Sustainable Chemistry & Engineering* 6 (4) (2018) 4648–4660. doi:10.1021/acssuschemeng.7b03652.
- [64] G. Zhang, X. Yang, C. He, P. Zhang, H. Mi, Constructing a tunable defect structure in TiO₂ for photocatalytic nitrogen fixation, *Journal of Materials Chemistry A* 8 (1) (2020) 334–341. doi:10.1039/c9ta10471b.
- [65] T. Hou, Q. Li, Y. Zhang, W. Zhu, K. Yu, S. Wang, Q. Xu, S. Liang, L. Wang, Near-infrared light-driven photofixation of nitrogen over Ti₃C₂Tx/TiO₂ hybrid structures with superior activity and stability, *Applied Catalysis B: Environmental* 273 (2020) 119072. doi:10.1016/j.apcatb.2020.119072.
- [66] S. Liu, Y. Wang, S. Wang, M. You, S. Hong, T.-S. Wu, Y.-L. Soo, Z. Zhao, G. Jiang, J. Qiu, B. Wang, Z. Sun, Photocatalytic fixation of nitrogen to ammonia by single Ru atom decorated TiO₂ nanosheets, *ACS Sustainable Chemistry & Engineering* 7 (7) (2019) 6813–6820. doi:10.1021/acssuschemeng.8b06134.
- [67] B. M. Comer, Y.-H. Liu, M. B. Dixit, K. B. Hatzell, Y. Ye, E. J. Crumlin, M. C. Hatzell, A. J. Medford, The role of adventitious carbon in photo-catalytic nitrogen fixation by titania, *Journal of the American Chemical Society* 140 (45) (2018) 15157–15160. doi:10.1021/jacs.8b08464.
- [68] Y. Liao, J. Qian, G. Xie, Q. Han, W. Dang, Y. Wang, L. Lv, S. Zhao, L. Luo, W. Zhang, H.-Y. Jiang, J. Tang, 2d-layered Ti₃C₂ MXenes for promoted synthesis of NH₃ on p25 photocatalysts, *Applied Catalysis B: Environmental* 273 (2020) 119054. doi:10.1016/j.apcatb.2020.119054.

- [69] R. Guan, D. Wang, Y. Zhang, C. Liu, W. Xu, J. Wang, Z. Zhao, M. Feng, Q. Shang, Z. Sun, Enhanced photocatalytic n_2 fixation via defective and fluoride modified TiO_2 surface, *Applied Catalysis B: Environmental* 282 (2021) 119580. doi:10.1016/j.apcatb.2020.119580.
- [70] Y. Zhang, X. Chen, S. Zhang, L. Yin, Y. Yang, Defective titanium dioxide nanobamboo arrays architecture for photocatalytic nitrogen fixation up to 780~nm, *Chemical Engineering Journal* 401 (2020) 126033. doi:10.1016/j.cej.2020.126033.
- [71] W. Gao, X. Li, S. Luo, Z. Luo, X. Zhang, R. Huang, M. Luo, In situ modification of cobalt on MXene/ TiO_2 as composite photocatalyst for efficient nitrogen fixation, *Journal of Colloid and Interface Science* 585 (2021) 20–29. doi:10.1016/j.jcis.2020.11.064.
- [72] J. Li, D. Wang, R. Guan, Y. Zhang, Z. Zhao, H. Zhai, Z. Sun, Vacancy-enabled mesoporous TiO_2 modulated by nickel doping with enhanced photocatalytic nitrogen fixation performance, *ACS Sustainable Chemistry & Engineering* 8 (49) (2020) 18258–18265. doi:10.1021/acssuschemeng.0c06775.
- [73] J. Qian, S. Zhao, W. Dang, Y. Liao, W. Zhang, H. Wang, L. Lv, L. Luo, H.-Y. Jiang, J. Tang, Photocatalytic nitrogen reduction by Ti_3C_2 MXene derived oxygen vacancy-rich c/TiO_2 , *Advanced Sustainable Systems* 5 (4) (2021) 2000282. doi:10.1002/adsu.202000282.
- [74] Z. Zhao, D. Wang, R. Gao, G. Wen, M. Feng, G. Song, J. Zhu, D. Luo, H. Tan, X. Ge, W. Zhang, Y. Zhang, L. Zheng, H. Li, Z. Chen, Magnetic-field-stimulated efficient photocatalytic n_2 fixation over defective BaTiO_3 perovskites, *Angewandte Chemie International Edition* 60 (21) (2021) 11910–11918. doi:10.1002/anie.202100726.
- [75] H. Ma, Z. Shi, Q. Li, S. Li, Preparation of graphitic carbon nitride with large specific surface area and outstanding n_2 photofixation ability via a dissolve-regrowth process, *Journal of Physics and Chemistry of Solids* 99 (2016) 51–58. doi:10.1016/j.jpcs.2016.08.008.
- [76] S. Li, X. Chen, S. Hu, Q. Li, J. Bai, F. Wang, Infrared ray assisted microwave synthesis: a convenient method for large-scale production of graphitic carbon nitride with outstanding nitrogen photofixation ability, *RSC Advances* 6 (51) (2016) 45931–45937. doi:10.1039/c6ra08817a.
- [77] G. Dong, W. Ho, C. Wang, Selective photocatalytic n_2 fixation dependent on $\text{g-c}_3\text{n}_4$ induced by nitrogen vacancies, *Journal of Materials Chemistry A* 3 (46) (2015) 23435–23441. doi:10.1039/c5ta06540b.

- [78] Y. Kong, C. Lv, C. Zhang, G. Chen, Cyano group modified g-c₃n₄: Molten salt method achievement and promoted photocatalytic nitrogen fixation activity, *Applied Surface Science* 515 (2020) 146009. doi:10.1016/j.apsusc.2020.146009.
- [79] C. Yao, R. Wang, Z. Wang, H. Lei, X. Dong, C. He, Highly dispersive and stable fe³⁺ active sites on 2d graphitic carbon nitride nanosheets for efficient visible-light photocatalytic nitrogen fixation, *Journal of Materials Chemistry A* 7 (48) (2019) 27547–27559. doi:10.1039/c9ta09201c.
- [80] C. Liang, H.-Y. Niu, H. Guo, C.-G. Niu, D.-W. Huang, Y.-Y. Yang, H.-Y. Liu, B.-B. Shao, H.-P. Feng, Insight into photocatalytic nitrogen fixation on graphitic carbon nitride: Defect-dopant strategy of nitrogen defect and boron dopant, *Chemical Engineering Journal* 396 (2020) 125395. doi:10.1016/j.cej.2020.125395.
- [81] A. Shi, H. Li, S. Yin, Z. Hou, J. Rong, J. Zhang, Y. Wang, Photocatalytic NH₃ versus h₂ evolution over g-c₃n₄/cs x WO₃: O₂ and methanol tipping the scale, *Applied Catalysis B: Environmental* 235 (2018) 197–206. doi:10.1016/j.apcatb.2018.04.081.
- [82] C. Ren, Y. Zhang, Y. Li, Y. Zhang, S. Huang, W. Lin, K. Ding, Whether corrugated or planar vacancy graphene-like carbon nitride (g-c₃n₄) is more effective for nitrogen reduction reaction?, *The Journal of Physical Chemistry C* 123 (28) (2019) 17296–17305. doi:10.1021/acs.jpcc.9b03511.
- [83] Z. Li, G. Gu, S. Hu, X. Zou, G. Wu, Promotion of activation ability of n vacancies to n₂ molecules on sulfur-doped graphitic carbon nitride with outstanding photocatalytic nitrogen fixation ability, *Chinese Journal of Catalysis* 40 (8) (2019) 1178–1186. doi:10.1016/s1872-2067(19)63364-4.
- [84] X.-W. Guo, S.-M. Chen, H.-J. Wang, Z.-M. Zhang, H. Lin, L. Song, T.-B. Lu, Single-atom molybdenum immobilized on photoactive carbon nitride as efficient photocatalysts for ambient nitrogen fixation in pure water, *Journal of Materials Chemistry A* 7 (34) (2019) 19831–19837. doi:10.1039/c9ta06653e.
- [85] M. Liu, Y. Wang, X. Kong, L. Tan, L. Li, S. Cheng, G. Botton, H. Guo, Z. Mi, C.-J. Li, Efficient nitrogen fixation catalyzed by gallium nitride nanowire using nitrogen and water, *iScience* 17 (2019) 208–216. doi:10.1016/j.isci.2019.06.032.
- [86] K. Bhattacharyya, A. Datta, Visible light driven efficient metal free single atom catalyst supported on nanoporous carbon nitride for nitrogen fixation, *Physical Chemistry Chemical Physics* 21 (23) (2019) 12346–12352. doi:10.1039/c9cp00997c.

- [87] H. Wang, Y. Bu, G. Wu, X. Zou, The promotion of the photocatalytic nitrogen fixation ability of nitrogen vacancy-embedded graphitic carbon nitride by replacing the corner-site carbon atom with phosphorus, *Dalton Transactions* 48 (31) (2019) 11724–11731. doi:10.1039/c9dt01261c.
- [88] H. Liu, P. Wu, H. Li, Z. Chen, L. Wang, X. Zeng, Y. Zhu, Y. Jiang, X. Liao, B. S. Haynes, J. Ye, C. Stampfl, J. Huang, Unravelling the effects of layered supports on ru nanoparticles for enhancing n₂ reduction in photocatalytic ammonia synthesis, *Applied Catalysis B: Environmental* 259 (2019) 118026. doi:10.1016/j.apcatb.2019.118026.
- [89] H. Zeng, L. Liu, D. Zhang, Y. Wang, Z. Li, C. Liu, L. Zhang, X. Cui, Fe(III)-c₃n₄ hybrids photocatalyst for efficient visible-light driven nitrogen fixation, *Materials Chemistry and Physics* 258 (2021) 123830. doi:10.1016/j.matchemphys.2020.123830.
- [90] C. Ling, X. Niu, Q. Li, A. Du, J. Wang, Metal-free single atom catalyst for n₂ fixation driven by visible light, *Journal of the American Chemical Society* 140 (43) (2018) 14161–14168. doi:10.1021/jacs.8b07472.
- [91] T. Hou, H. Peng, Y. Xin, S. Wang, W. Zhu, L. Chen, Y. Yao, W. Zhang, S. Liang, L. Wang, Fe single-atom catalyst for visible-light-driven photofixation of nitrogen sensitized by triphenylphosphine and sodium iodide, *ACS Catalysis* 10 (10) (2020) 5502–5510. doi:10.1021/acscatal.0c00920.
- [92] J. Qin, X. Hu, X. Li, Z. Yin, B. Liu, K. ho Lam, 0d/2d *AgInS₂/MXene* z-scheme heterojunction nanosheets for improved ammonia photosynthesis of n₂, *Nano Energy* 61 (2019) 27–35. doi:10.1016/j.nanoen.2019.04.028.
- [93] M. Shao, Y. Shao, W. Chen, K. L. Ao, R. Tong, Q. Zhu, I. N. Chan, W. F. Ip, X. Shi, H. Pan, Efficient nitrogen fixation to ammonia on MXenes, *Physical Chemistry Chemical Physics* 20 (21) (2018) 14504–14512. doi:10.1039/c8cp01396a.
- [94] H. Li, J. Shang, J. Shi, K. Zhao, L. Zhang, Facet-dependent solar ammonia synthesis of BiOCl nanosheets via a proton-assisted electron transfer pathway, *Nanoscale* 8 (4) (2016) 1986–1993. doi:10.1039/c5nr07380d.
- [95] H. Li, J. Shang, Z. Ai, L. Zhang, Efficient visible light nitrogen fixation with BiOBr nanosheets of oxygen vacancies on the exposed {001} facets, *Journal of the American Chemical Society* 137 (19) (2015) 6393–6399. doi:10.1021/jacs.5b03105.
- [96] Y. Zhao, S. Zhou, J. Zhao, Y. Du, S. X. Dou, Control of photocarrier separation and recombination at bismuth oxyhalide interface for nitrogen fixation, *The Journal of Physical Chemistry Letters* 11 (21) (2020) 9304–9312. doi:10.1021/acs.jpcllett.0c02480.

- [97] B. Liu, A. S. Yasin, T. Musho, J. Bright, H. Tang, L. Huang, N. Wu, Visible-light bismuth iron molybdate photocatalyst for artificial nitrogen fixation, *Journal of The Electrochemical Society* 166 (5) (2019) H3091–H3096. doi:10.1149/2.0151905jes.
- [98] D. Wu, R. Wang, C. Yang, Y. An, H. Lu, H. Wang, K. Cao, Z. Gao, W. Zhang, F. Xu, K. Jiang, Br doped porous bismuth oxychloride micro-sheets with rich oxygen vacancies and dominating 0+0+1 facets for enhanced nitrogen photo-fixation performances, *Journal of Colloid and Interface Science* 556 (2019) 111–119. doi:10.1016/j.jcis.2019.08.048.
- [99] G. Li, W. Yang, S. Gao, Q. Shen, J. Xue, K. Chen, Q. Li, Creation of rich oxygen vacancies in bismuth molybdate nanosheets to boost the photocatalytic nitrogen fixation performance under visible light illumination, *Chemical Engineering Journal* 404 (2021) 127115. doi:10.1016/j.cej.2020.127115.
- [100] A. S. Yasin, B. Liu, N. Wu, T. Musho, Density functional theory evaluation of cation-doped bismuth molybdenum oxide photocatalysts for nitrogen fixation, *Computational Materials Science* 158 (2019) 65–75. doi:10.1016/j.commat.2018.08.039.
- [101] C. Zhang, G. Chen, C. Lv, Y. Yao, Y. Xu, X. Jin, Q. Meng, Enabling nitrogen fixation on Bi_2WO_6 photocatalyst by c-PAN surface decoration, *ACS Sustainable Chemistry & Engineering* 6 (9) (2018) 11190–11195. doi:10.1021/acssuschemeng.8b02236.
- [102] Y. Liu, Z. Hu, J. C. Yu, Fe enhanced visible-light-driven nitrogen fixation on BiOBr nanosheets, *Chemistry of Materials* 32 (4) (2020) 1488–1494. doi:10.1021/acs.chemmater.9b04448.
- [103] X. Xue, R. Chen, H. Chen, Y. Hu, Q. Ding, Z. Liu, L. Ma, G. Zhu, W. Zhang, Q. Yu, J. Liu, J. Ma, Z. Jin, Oxygen vacancy engineering promoted photocatalytic ammonia synthesis on ultrathin two-dimensional bismuth oxybromide nanosheets, *Nano Letters* 18 (11) (2018) 7372–7377. doi:10.1021/acs.nanolett.8b03655.
- [104] P. Li, Z. Zhou, Q. Wang, M. Guo, S. Chen, J. Low, R. Long, W. Liu, P. Ding, Y. Wu, Y. Xiong, Visible-light-driven nitrogen fixation catalyzed by $\text{Bi}_5\text{O}_7\text{Br}$ nanostructures: Enhanced performance by oxygen vacancies, *Journal of the American Chemical Society* 142 (28) (2020) 12430–12439. doi:10.1021/jacs.0c05097.
- [105] S. Zhang, Y. Zhao, R. Shi, C. Zhou, G. I. N. Waterhouse, L.-Z. Wu, C.-H. Tung, T. Zhang, Efficient photocatalytic nitrogen fixation over $\text{Cu}^{\delta+}$ -modified defective ZnAl-layered double hydroxide nanosheets, *Advanced Energy Materials* 10 (8) (2020) 1901973. doi:10.1002/aenm.201901973.

- [106] G. Zhang, T. Dai, Y. Wang, Y. Meng, B. Xie, Z. Ni, S. Xia, Modulation of photo-generated solvated electrons for ammonia synthesis via facet-dependent engineering of heterojunctions, *Applied Catalysis B: Environmental* 288 (2021) 119990. doi:10.1016/j.apcatb.2021.119990.
- [107] G. Li, F. Li, J. Liu, C. Fan, Fe-based MOFs for photocatalytic n₂ reduction: Key role of transition metal iron in nitrogen activation, *Journal of Solid State Chemistry* 285 (2020) 121245. doi:10.1016/j.jssc.2020.121245.
- [108] B. Sun, Z. Liang, Y. Qian, X. Xu, Y. Han, J. Tian, Sulfur vacancy-rich o-doped 1t-MoS₂ nanosheets for exceptional photocatalytic nitrogen fixation over CdS, *ACS Applied Materials & Interfaces* 12 (6) (2020) 7257–7269. doi:10.1021/acsami.9b20767.
- [109] S. Hu, X. Chen, Q. Li, Y. Zhao, W. Mao, Effect of sulfur vacancies on the nitrogen photofixation performance of ternary metal sulfide photocatalysts, *Catalysis Science & Technology* 6 (15) (2016) 5884–5890. doi:10.1039/c6cy00622a.
- [110] N. Zhang, A. Jalil, D. Wu, S. Chen, Y. Liu, C. Gao, W. Ye, Z. Qi, H. Ju, C. Wang, X. Wu, L. Song, J. Zhu, Y. Xiong, Refining defect states in W₁₈O₄₉ by Mo doping: A strategy for tuning n₂ activation towards solar-driven nitrogen fixation, *Journal of the American Chemical Society* 140 (30) (2018) 9434–9443. doi:10.1021/jacs.8b02076.
- [111] J. Liu, M. S. Kelley, W. Wu, A. Banerjee, A. P. Douvalis, J. Wu, Y. Zhang, G. C. Schatz, M. G. Kanatzidis, Nitrogenase-mimic iron-containing chalcogels for photochemical reduction of dinitrogen to ammonia, *Proceedings of the National Academy of Sciences* 113 (20) (2016) 5530–5535. doi:10.1073/pnas.1605512113.
- [112] Z.-K. Shen, Y.-J. Yuan, P. Wang, W. Bai, L. Pei, S. Wu, Z.-T. Yu, Z. Zou, Few-layer black phosphorus nanosheets: A metal-free cocatalyst for photocatalytic nitrogen fixation, *ACS Applied Materials & Interfaces* 12 (15) (2020) 17343–17352. doi:10.1021/acsami.9b21167.
- [113] X. Gao, L. An, D. Qu, W. Jiang, Y. Chai, S. Sun, X. Liu, Z. Sun, Enhanced photocatalytic n₂ fixation by promoting n₂ adsorption with a co-catalyst, *Science Bulletin* 64 (13) (2019) 918–925. doi:10.1016/j.scib.2019.05.009.
- [114] J. Yuan, X. Yi, Y. Tang, M. Liu, C. Liu, Efficient photocatalytic nitrogen fixation: Enhanced polarization, activation, and cleavage by asymmetrical electron donation to n≡n bond, *Advanced Functional Materials* 30 (4) (2019) 1906983. doi:10.1002/adfm.201906983.
- [115] X. Ma, J. Hu, M. Zheng, D. Li, H. Lv, H. He, C. Huang, N₂ reduction using single transition-metal atom supported on defective WS₂ monolayer as promis-

- ing catalysts: A DFT study, *Applied Surface Science* 489 (2019) 684–692. doi:10.1016/j.apsusc.2019.05.022.
- [116] J. Zheng, Y. Lyu, M. Qiao, R. Wang, Y. Zhou, H. Li, C. Chen, Y. Li, H. Zhou, S. P. Jiang, S. Wang, Photoelectrochemical synthesis of ammonia on the aerophilic-hydrophilic heterostructure with 37.8% efficiency, *Chem* 5 (3) (2019) 617–633. doi:10.1016/j.chempr.2018.12.003.
- [117] W. Zhao, H. Xi, M. Zhang, Y. Li, J. Chen, J. Zhang, X. Zhu, Enhanced quantum yield of nitrogen fixation for hydrogen storage with in situ-formed carbonaceous radicals, *Chemical Communications* 51 (23) (2015) 4785–4788. doi:10.1039/c5cc00589b.
- [118] X. Sun, D. Jiang, L. Zhang, S. Sun, W. Wang, Enhanced nitrogen photofixation over LaFeO_3 via acid treatment, *ACS Sustainable Chemistry & Engineering* 5 (11) (2017) 9965–9971. doi:10.1021/acssuschemeng.7b01912.
- [119] Z. Zhao, C. Choi, S. Hong, H. Shen, C. Yan, J. Masa, Y. Jung, J. Qiu, Z. Sun, Surface-engineered oxidized two-dimensional sb for efficient visible light-driven n_2 fixation, *Nano Energy* 78 (2020) 105368. doi:10.1016/j.nanoen.2020.105368.
- [120] T. Wang, C. Feng, J. Liu, D. Wang, H. Hu, J. Hu, Z. Chen, G. Xue, Bi_2WO_6 hollow microspheres with high specific surface area and oxygen vacancies for efficient photocatalysis n_2 fixation, *Chemical Engineering Journal* 414 (2021) 128827. doi:10.1016/j.cej.2021.128827.
- [121] C. V. S. Kumar, V. Subramanian, Can boron antisites of BNNTs be an efficient metal-free catalyst for nitrogen fixation? – a DFT investigation, *Physical Chemistry Chemical Physics* 19 (23) (2017) 15377–15387. doi:10.1039/c7cp02220d.
- [122] H. Liu, Z. Fang, Y. Su, Y. Suo, S. Huang, Y. Zhang, K. Ding, Different atomic terminations affect the photocatalytic nitrogen fixation of bismuth oxybromide: A first principles study, *Chemistry - An Asian Journal* 13 (7) (2018) 799–808. doi:10.1002/asia.201701670.
- [123] Q. Meng, C. Lv, J. Sun, W. Hong, W. Xing, L. Qiang, G. Chen, X. Jin, High-efficiency fe-mediated Bi_2WO_6 nitrogen-fixing photocatalyst: Reduced surface work function and ameliorated surface reaction, *Applied Catalysis B: Environmental* 256 (2019) 117781. doi:10.1016/j.apcatb.2019.117781.
- [124] X. Li, H. Shi, S. Zuo, B. Gao, C. Han, T. Wang, C. Yao, C. Ni, Lattice reconstruction of one-dimensional mineral to achieve dendritic heterojunction for cost-effective nitrogen photofixation, *Chemical Engineering Journal* 414 (2021) 128797. doi:10.1016/j.cej.2021.128797.

- [125] Y. Li, X. Chen, M. Zhang, Y. Zhu, W. Ren, Z. Mei, M. Gu, F. Pan, Oxygen vacancy-rich MoO_{3-x} nanobelts for photocatalytic n₂ reduction to NH₃ in pure water, *Catalysis Science & Technology* 9 (3) (2019) 803–810. doi:10.1039/c8cy02357c.
- [126] G. Zhang, Y. Meng, B. Xie, Z. Ni, H. Lu, S. Xia, Precise location and regulation of active sites for highly efficient photocatalytic synthesis of ammonia by facet-dependent BiVO₄ single crystals, *Applied Catalysis B: Environmental* 296 (2021) 120379. doi:10.1016/j.apcatb.2021.120379.
- [127] W. Pei, S. Zhou, J. Zhao, Y. Du, S. X. Dou, Optimization of photocarrier dynamics and activity in phosphorene with intrinsic defects for nitrogen fixation, *Journal of Materials Chemistry A* 8 (39) (2020) 20570–20580. doi:10.1039/d0ta08553g.
- [128] M. Králik, Adsorption, chemisorption, and catalysis, *Chemical Papers* 68 (12) (jan 2014). doi:10.2478/s11696-014-0624-9.
- [129] J. D. Gouveia, Á. Morales-García, F. Viñes, J. R. B. Gomes, F. Illas, Facile heterogeneously catalyzed nitrogen fixation by MXenes, *ACS Catalysis* 10 (9) (2020) 5049–5056. doi:10.1021/acscatal.0c00935.
- [130] T. Nakao, T. Tada, H. Hosono, First-principles and microkinetic study on the mechanism for ammonia synthesis using ru-loaded hydride catalyst, *The Journal of Physical Chemistry C* 124 (3) (2019) 2070–2078. doi:10.1021/acs.jpcc.9b10850.
- [131] J. Qian, Q. An, A. Fortunelli, R. J. Nielsen, W. A. Goddard, Reaction mechanism and kinetics for ammonia synthesis on the fe(111) surface, *Journal of the American Chemical Society* 140 (20) (2018) 6288–6297. doi:10.1021/jacs.7b13409.
- [132] J.-C. Liu, X.-L. Ma, Y. Li, Y.-G. Wang, H. Xiao, J. Li, Heterogeneous fe₃ single-cluster catalyst for ammonia synthesis via an associative mechanism, *Nature Communications* 9 (1) (apr 2018). doi:10.1038/s41467-018-03795-8.
- [133] S. Ghoshal, A. Pramanik, P. Sarkar, Towards h₂O catalyzed n₂-fixation over TiO₂ doped ru_n clusters (n = 5, 6): a mechanistic and kinetic approach, *Physical Chemistry Chemical Physics* 23 (2) (2021) 1527–1538. doi:10.1039/d0cp03507f.
- [134] S. Dahl, J. Sehested, C. Jacobsen, E. Tornqvist, I. Chorkendorff, Surface science based microkinetic analysis of ammonia synthesis over ruthenium catalysts, *Journal of Catalysis* 192 (2) (2000) 391–399. doi:10.1006/jcat.2000.2857.
- [135] S. Deshmukh, A. Mhadeshwar, D. Vlachos, Microkinetic modeling of ammonia synthesis and decomposition on ruthenium and microreactor design for hydrogen production, *ACS Division of Fuel Chemistry, Preprints* 48 (09 2003).